UNIVERSITY OF CALIFORNIA
RIVERSIDE

The Evolution of Star-Forming Galaxies using the Largest Narrowband Surveys

A Dissertation submitted in partial satisfaction
of the requirements for the degree of

Doctor of Philosophy

in

Physics

by

Ali Ahmad Khostovan

September 2018

Dissertation Committee:

Dr. Bahram Mobasher, Chairperson
Dr. Brian Siana
Dr. George Becker

The Dissertation of Ali Ahmad Khostovan is approved:

Committee Chairperson

University of California, Riverside

خیال من به تماشای آسمان بود است　　بدوش ماه و به آغوش کهکشان بود است
گمان مبر که همین خاکدان نشیمن ماست　　که هر ستاره جهان است یا جهان بود است

جاوید نامه، اقبال لاهوری

My mind awhile was gone about the heavens to pace,
High on the back of the moon, Fast in the stars' embrace.

Think not we are enfurled within this globe of clay;
Each separate star's world, Or was a world one day.

Javid Nameh, Iqbal Lahouri

Acknowledgements

I like to first begin by acknowledging the PhD Dissertation Committee members for spending their time to read this dissertation and also evaluate my 6 years of work here at UCR. I also would like to thank all members of the Astronomy Department. I have never seen such a wonderful department where faculty, postdocs, and students work so closely together and create a friendly and supportive atmosphere.

I like to thank my advisor, Prof. Bahram Mobasher, for his continuous support over these many years. You have helped me grow as a scientist and always made me see the big picture of what I do and the implications of my work. You gave me such great opportunities to expand and learn as a scientist. Thank you so much for all the support over these past several years.

I also like to thank Dr. David Sobral as both my co-advisor and also as a great friend. You always kept my head straight, taught me to keep things simple, and kept me from going on a 'safari' whenever I interpreted results. You always knew within 100σ that I would be 15 minutes late to our Skype sessions, but would still make the time to talk for 1 - 2 hours regarding my projects. I wouldn't be where I am today without your guidance and support. You always made the time to go over my projects, comment on many paper drafts, and host me on several visits. You have also been a great friend and a ruthless Ticket-to-Ride player (seriously, I think I only beat you once and that was probably dumb luck on my part). I really wouldn't be where I am without your guidance and support.

I like to acknowledge the great support of my parents and sister. This unit of four is by far

the most important unit in my life and I know that I would not be standing where I am today if I never had you all to love and support my dreams and aspirations throughout my life. I love you guys so much. I especially like to thank my dad as he is the one who strongly influenced me to pursue a career in science. When I was a kid, you would always show me these cool science documentaries, especially those based on space. You also showed me science experiments and got me involved in the school-wide and county-wide science fairs when I was growing up.

I like to thank my best friend, Nima Chartab Soltani. We met each other late in my PhD career, but the friendship that grew during those two years is something that I greatly cherish. We have done so many crazy things, such as driving late at night to Dana Point, making spontaneous road trips to San Diego and Las Vegas, and driving 2200 km in 6 days throughout Europe (I think that this was by far the most fun and also the craziest thing we have ever done). We both support each other when we are at our lowest and when we are at our best. I only wish that you were here during the full course of my time at UCR.

I also wish to acknowledge the great support from my dear friends. To list a few: Marziye Jafariyazani, Najmeh Emami, Saeed Rezaee, Hesam Abedini, Niloufar Shiri, Shahriyar Valielahiroshan, and many more. All of you had a great impact in my life and made my time here at UCR truly amazing. This list of friends is truly incomplete and all of you have positively influenced my life. I truly thank you all.

I thank the UCR hiking group for the weekly/biweekly programs that they always offered. Grad school life can often times be stressful and hiking is a great way to not only relieve that stress, but also meet new friends, especially those who you do not see on a daily basis. This group started when Sara Alaee and Amin Safdari came to UCR last year and started the group in conjunction with Amin Baniasadi, Joobin Gharibshah, Shakiba Hajisadeghi, Mohsen Karimi, and Fahimeh Arab. To you all, and all those who participate in this group, thank you so much for the great memories and adrenaline-pumping hikes (especially that one where we got caught in the snowstorm).

I want to greatly thank the whole Iranian community at UCR. As an Iranian born in the United States, I am so happy to have had the opportunity to not only experience my cultural heritage and language, but also to have done so with people my age. You all accepted me into the community and gave me such great and happy memories that I know I would never have found in any other place outside of Iran. I will truly miss this community now that I have completed my thesis work and am leaving UCR. Thank you.

I lastly would like to thank my grandmothers who I know would have wanted to be here and witness my great achievement. I lost both of you when I was just a teenager and I really miss you both. I have so many happy childhood memories with you both and I just wish that I could have shared many more. I love you both.

Dedication

In dedication to my loving parents, sister, grandparents, family, and friends who supported me all my life and given me reason to pursue my dreams. I especially dedicate this work to a man whom I never had the chance to meet and yet loved with all my heart, my dear grandfather, Ahmad Khostovan. I have always been told that I am very much like you and I know if we ever met we would have been more than family, but best friends. I especially dedicate all this work in your loving memory.

Ahmad Khostovan (1903 - 1972)

ABSTRACT OF THE DISSERTATION

Evolution of Star-Forming Galaxies using the Largest Narrowband Surveys

by

Ali Ahmad Khostovan

Doctor of Philosophy, Graduate Program in Physics
University of California, Riverside, September 2018
Dr. Bahram Mobasher, Chairperson

Observations of the star formation history of the Universe shows that galaxies have evolved considerably over the past 13 Gyrs, but what is causing such an evolution to occur? To answer this question is to delve deeper and ask more fundamental questions: How are the statistical properties of galaxies changing with time? What mechanisms/drivers are involved? How does the host halo influence the residing galaxy's evolution? What are the progenitors of the present-day galaxies?

To address these questions, I use unique, narrowband selected samples of **3475** Hβ+[OIII]- and **3298** [OII]-selected emission line galaxies from the High-z Emission Line Survey (HiZELS) and $\sim$**4000** Lyα-selected galaxies from the Slicing COSMOS 4K (SC4K) survey. The HiZELS survey covers samples divided in four discrete redshift slices ($\Delta z \sim 0.01-0.03$) between $z \sim 0.8-3.3$ and $z \sim 1.5-5$ for Hβ+[OIII] and [OII] emitters, respectively, and the SC4K covers Lyα samples divided in 15 discrete redshift slices ($\Delta z \sim 0.02-0.15$) between $z \sim 2.5-6$.

Measurements of the [OIII] and [OII] stellar mass and luminosity functions are presented for the first time up to $z \sim 3$ and 5, respectively. Both [OIII] and [OII] emitters show stellar mass and luminosity functions that strongly evolve with redshift with [OII] emitters observed to become rarer with increasing redshift. I present measurements of the star formation history of the Universe using only [OII] from the local Universe to $z \sim 5$. I confirm that star formation rates strongly increase from $z \sim 5$ to a peak around $z \sim 3$ and gradually decrease to the present-day. Stellar mass densities of [OIII] and [OII] emitters are found to trace the stellar mass buildup of

star-forming galaxies, but diverge at $z < 1$ from the global population of galaxies, suggesting a decreasing fraction of star forming galaxies due to quenching mechanisms.

I investigate the evolution of the equivalent widths of Hα, [OIII], and [OII] emitters and find different evolutions for both lines. Hα and [OIII] emitters are found to continuously increase with redshift, while [OII] equivalent widths increase up to $z \sim 4$ and decrease quickly at higher redshifts. Comparing the evolution of the [OIII] and [OII] equivalent widths suggests an increasingly energetic ionization state of the gas in the interstellar medium of star-forming galaxies. This explains the rapid drop in number densities of [OII] emitters in respect to [OIII]-selected emitters where due to higher [OIII]/[OII] line ratios, [OII] emitters become increasingly rare due to changes in the physical conditions of the interstellar medium.

I conclude my work by investigating the clustering and halo properties of [OIII], [OII], and Lyα emitters. Strong evolutions in the clustering lengths for all redshift samples is observed with galaxies being more clustered at higher redshifts. Applying models to convert clustering lengths to halo masses shows that galaxy properties and halo masses are tightly correlated with one another. Strong, redshift-independent trends between halo mass and line luminosity, stellar mass, rest-frame 1500Å luminosity, and UV star formation rate are observed. This signifies the important role that halos play in the overall evolution of star-forming galaxies. Lastly, I find that Lyα emitters at high-z are progenitors of a wide range of present-day galaxies, ranging from dwarf-like, to Milky Way, to large cluster galaxies making them ideal tools to study the formation of galaxies in the local Universe.

Table of Contents

List of Tables

List of Figures

Figure **Page**

CHAPTER 1

Introduction

Astronomers in all subfields of astrophysics ask the same fundamental question: why is the Universe the way it is? What caused all of this to happen? How did we go from an infinitesimal point to the complex structure that we see today? We all address these problems in our own unique ways, using different types of observations and samples ranging from solar system objects, to stars and exoplanets, to molecular clouds, to local group galaxies, to the large cosmic arena of galaxies, and to the Universe as a whole. With all this complexity, we all focus narrowly on small aspects of this grand problem, becoming experts on a tiny piece of a larger puzzle and, with our collaborative efforts, we start putting those pieces together. This thesis is the culmination of six years of work that I have done on a piece of this puzzle to better our understanding how galaxies evolve from the era of the earliest galaxies, to the peak of star formation activity in the Universe, and down to the present-day.

In this chapter, I will present a brief overview of the background material related to this thesis.

1.1 Galaxy Formation

Our understanding of galaxy formation and evolution has grown considerably over the past 20 years with the advent of many state-of-the-art observational facilities, both ground-based and space-based, and the increasing power of computers used in large cosmological simulations. The current consensus regarding galaxy formation is that it started from the small, minute perturbations that occurred during 'inflation' (Guth, 1981) right after the Big Bang (see Benson (2010) for a review). The perturbations first formed dark matter halos as dark matter is 'collisionless' such that it would not experience pressure during gravitational collapse, in comparison to baryonic matter. The deep potentials of these halos allowed for baryonic matter to fall in, become shock heated to expand and fill the halo with hot primordial gas in the form of hydrogen and helium. The gas eventually cools down radiatively and falls back into the center of halo becoming a dense cloud of gas that eventually collapses to form the first stars and galaxies.

1.2 Cosmic Star Formation

The fundamental properties of galaxies derive from these three main components: gas, stars, and dust. The cold gas that exists in a galaxy can collapse, if dense and cool enough, to form stars. These stars live out their lives and eventually die out releasing their materials into the interstellar medium (ISM) in the form of enriched metals and dust. The next generation of stars are then created from this enriched gas such that to characterize a galaxy requires a detailed understanding of these three components.

The famous 'Madau-Lilly' plot quantifies the cosmic evolution of star formation activity (Lilly et al., 1996; Madau et al., 1996; Hopkins & Beacom, 2006; Madau & Dickinson, 2014) by using observations of star forming galaxies over a wide range of cosmic time (up to $z \sim 8$ using UV-dropout galaxies). The main consensus based on the recent measurements of Madau &

Dickinson (2014), as shown in Figure 1.1, is that cosmic star formation activity increased rapidly by an order of magnitude during the first 2 Gyrs from the end of the epoch of reionization to cosmic noon ($z \sim 2-3$). This was then followed by about 2 Gyrs of peak star formation activity where galaxies were able to form stars at a rapid pace. The following 10 Gyrs up to the present-day shows star formation productivity in the Universe has gradually decreased by an order of magnitude. Reasons for this is still an open debate ranging from environmental (e.g., Boselli & Gavazzi 2006), halo (e.g., Birnboim & Dekel 2003), stellar (e.g., Hopkins et al. 2014), and AGN quenching/feedback (e.g., Fabian 2012).

Imprinted within Figure 1.1 is information regarding how galaxies were able to produce stars over 13 Gyrs. The processes that drive star formation activity are embedded within this plot making measurements of the cosmic star formation rate densities as fundamental measurements in understanding galaxy formation and evolution.

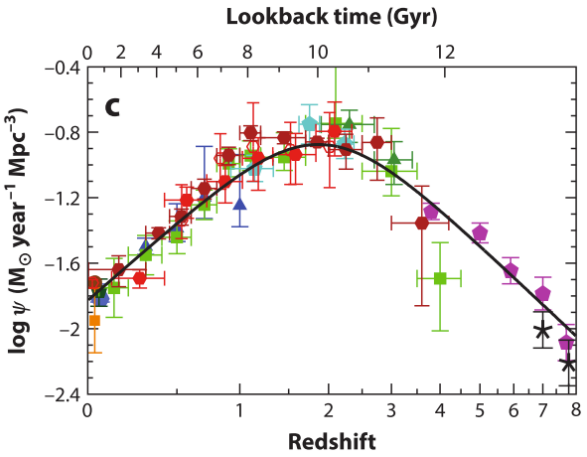

Figure 1.1: Cosmic Star Formation History of the Universe as measured by Madau & Dickinson (2014). The measurements shown here are based on far-infrared and UV observations along with their corresponding star formation rate calibrations (e.g., Kennicutt 1998). Observations shown are for a select population of galaxy selection types which correspond to average star formation timescales of $\sim 100-300$ Myrs.

Figure 1.1 shows observations of the luminosity densities converted to star formation rates using an empirical calibration (e.g., Kennicutt 1998) for only far-infrared (FIR) and UV-selected samples, with the $z > 3$ measurements only based on galaxies selected using the UV dropout technique (a combination of three broadband filters for which one filter observes the Lyman Limit at 912Å; Steidel et al. 1995; Giavalisco 2002). Several caveats ensue when using only limited selection types, as well as using varying types of galaxy selections in the 'Madau-Lilly' plot.

The first caveat is the star formation calibration used. Since stars can have different lifetimes, depending on their mass and luminosities, and have peak continuum emission at different wavelengths, the type of calibration used can correspond to a wide range in average star formation activity timescales (e.g., Kennicutt 1998; Hao et al. 2011; Murphy et al. 2011; Kennicutt & Evans 2012; Calzetti 2013). The closest calibration to an instantaneous star formation rate measurement is based on emission line calibrations, such as Hα, [OIII], and [OII], which can trace timescales of $\sim 5-10$ Myrs. This is because such emission lines trace the most massive, short-lived O type stars. UV based calibrations trace $\sim 100-200$ Myrs and trace the OB-type stars in dust-free galaxies. FIR calibrations trace a similar timescale but are biased to dusty systems as thermal dust emission peaks in the far-infrared. Radio based calibrations, such as the 1.4 GHz emission, traces timescales of ~ 100 Myr and come primarily from the synchrotron radiation produced by the supernovae of massive stars. Hopkins & Beacom (2006) showed that populating the 'Madau-Lilly' plot with measurements using varying star formation calibrations results in a spread in measured cosmic star formation rates for a given redshift. One reason for this scatter is due to the varying timescales probed.

The second caveat is the size and depth of the survey/sample. Small arcmin^2 surveys have the great advantage of probing the faintest galaxies in a field, but severely suffer from missing the rarest galaxies (i.e., the brightest, massive galaxies) and from observing unique parts of a region of the night sky (e.g., overdense regions, filaments, fields). In regards to measurements of the cosmic star formation rate densities, Sobral et al. (2015a) showed that surveys covering comoving volumes of $< 3\times10^5$ Mpc^3 can suffer from $15-30$ percent error due to sample variance alone. On the other hand, wide surveys cover larger areas that significantly reduce the effects of sample variance, but miss the faint galaxies that are detected in small area surveys.

Given these caveats, to properly measure the cosmic star formation history of the Universe requires that we use samples of star forming galaxies with simple, consistent selection functions over a wide range of redshifts and using a single calibration to measure instantaneous star

formation rates. We require that these samples cover a wide range of comoving volumes to probe different environments and rare, bright galaxies, but also be deep enough to observe the faint galaxies that forms the bulk of the galaxy population. With such samples, we can robustly constrain the history of cosmic star formation and also start to investigate the factors that shape this fundamental property.

1.3 Statistical Properties of Galaxy Populations

1.3.1 The Schechter Function

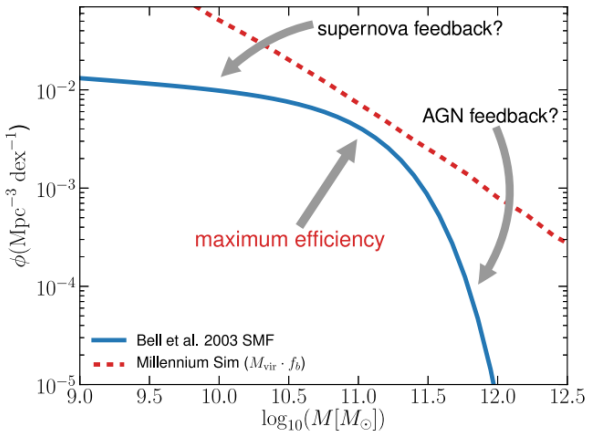

Figure 1.2: An example of the stellar mass function modeled as a Schechter function from Mutch et al. (2013). The *dash line* refers to the halo mass function from the Millennium simulation and the *blue line* refers to the observed $z = 0$ stellar mass function of Bell et al. (2003). Models suggest that feedback mechanisms are what give the shape of the Schechter function.

Measuring the cosmic star formation rates of galaxy populations requires that we understand their statistical properties. The range and distribution of luminosities and stellar mass are fundamental characteristics of a galaxy population and are shown in the form of luminosity and stellar mass functions. Schechter (1976) formed an analytical expression for the luminosity distribution as:

$$\Phi(L)\ \mathrm{d}L = \phi^\star \left(\frac{L}{L^\star}\right)^\alpha e^{-(L/L^\star)}\ \mathrm{d}L \qquad (1.1)$$

where $\Phi(L)$ is the luminosity function, α is the faint-end slope, and $\phi^\star$ and $L^\star$ are the characteristic number density and luminosity, respectively.

Figure 1.2 explains the physical reasoning behind the 'Schechter' function, as defined in Equation 1.1. The low-mass, faint-end consists of galaxies that reside in low-mass dark matter halos. The effects of supernova-driven winds causes the remaining gas in these galaxies to be

driven out of the galaxy due to the shallow potential of the host halo. The exponential-cutoff at the high-mass, bright end is thought to be caused by AGN feedback where material falls quickly and accretes into the central supermassive black hole resulting in radiation heating the surrounding gas. This causes a steep cut in the star formation activity of a galaxy and ultimately quenches all activity, resulting in the exponential cutoff seen in Figure 1.2. The 'knee' of the Schechter function is defined at the characteristic luminosity (or stellar mass). This is the point for which star formation efficiency is found to be at it's maximum where the effects of supernova and AGN feedback are not as strong (e.g., Behroozi et al. 2013b).

1.3.2 Luminosity Functions of Star-Forming Galaxies

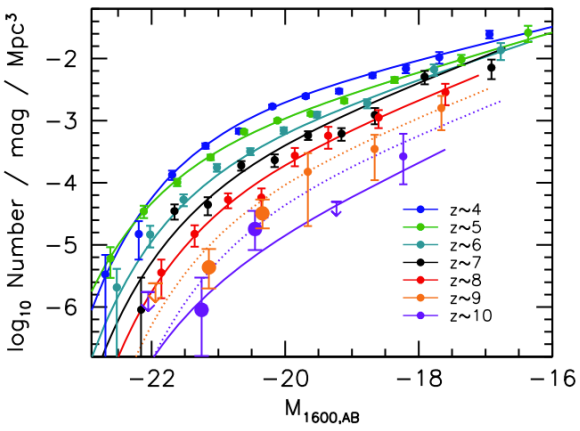

Figure 1.3: The rest-frame UV Luminosity Functions measured by Bouwens et al. (2016) between $z \sim 4-10$. Number densities of UV-selected galaxies decreases considerably to higher redshift, but are skewed towards fainter luminosities such that faint galaxies become increasingly important at high-z.

The past several decades have resulted in a wealth of luminosity function measurements of star-forming galaxies up to $z \sim 2$ using narrowband-selected Hα- (e.g., Ly et al. 2007; Sobral et al. 2009; Ly et al. 2011; Sobral et al. 2012, 2013a, 2015a; Matthee et al. 2017a), [OIII]- (e.g., Ly et al. 2007; Pirzkal et al. 2013; Colbert et al. 2013; Sobral et al. 2015a), and [OII]-selected samples (e.g., Gallego et al. 2002; Ly et al. 2007; Takahashi et al. 2007; Bayliss et al. 2011; Sobral et al. 2012; Ciardullo et al. 2013; Sobral et al. 2015a), as well as UV-selected samples (e.g., Arnouts et al. 2005; Reddy & Steidel 2009; Oesch et al. 2010; McLure et al. 2013; Alavi et al. 2014; Bouwens et al. 2015; Finkelstein et al. 2015; Alavi et al. 2016; Bouwens et al. 2016). As described above, the shape of the luminosity function is governed by physical processes that are occurring inside galaxies such that these measurements are crucial

in quantifying how the physical properties of populations of galaxies is changing over cosmic time. Measuring these properties are then crucial in understanding how galaxies evolve.

The luminosity function of star-forming galaxies selected using their UV luminosities is shown in Figure 1.3 as measured by Bouwens et al. (2016). The UV continuum luminosities measured trace the continuum emission of *OB*-type stars and correspond to star formation activity within a ~ 100 Myr timeframe. The main consensus found is that the UV luminosity functions strongly evolve with redshift with their number densities becoming decreasing with increasing redshift. Although such sources become increasingly rare with increasing redshift, the distribution becomes more skewed towards fainter sources with the faint-end slope becoming steeper ($\alpha \sim -2$ by $z \sim 6$; e.g., Oesch et al. 2010; Alavi et al. 2016) such that the faint, star-forming galaxies become of greater importance at higher redshifts (e.g., Robertson et al. 2013; Schenker et al. 2013a; Alavi et al. 2014; Finkelstein et al. 2015).

Hα luminosity functions trace the instantaneous star formation activity of galaxies and have been well constrained out to $z \sim 2$ for which Hα falls outside the scope of ground-based observations. Figure 1.4 shows the evolution of the Hα luminosity functions from $z \sim 0-2$ as measured by Sobral et al. (2013a). The luminosity functions strongly evolve with $L^\star$ increasing from $10^{41.9}$ erg s^{-1} to $10^{42.9}$ erg s^{-1} and the $\phi^\star$ relatively constant around $10^{-2.75}$ Mpc^{-3}. The faint-end slope is found to be constant at $\alpha = -1.6$ suggesting that bright and faint Hα-selected star forming galaxies evolve uniformly.

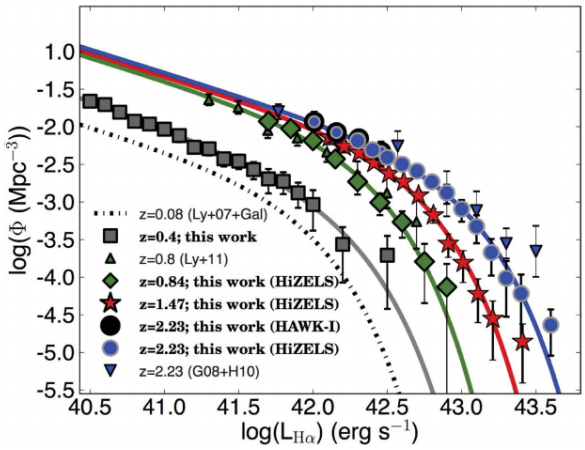

Figure 1.4: The evolution in the Hα Luminosity Function up to $z = 2.23$ as measured by Sobral et al. (2013a). A clear, strong evolution is shown in the luminosity function seen as an in increase in $L^\star$.

Since Hα directly traces the ionized gas (HII region) that is heated by the creation of new,

massive, short-lived stars, it is the best calibration of instantaneous star formation activity. Large samples of Hα emitters then allows us to directly select galaxies based on star formation activity and allow us to investigate the mechanisms that drive changes in typical Hα luminosities/star formation rates. Unfortunately, beyond $z \sim 2$, Hα falls into the infrared where it is no longer accessible from the ground. This requires that we focus our efforts on observing samples based on other emission lines that trace HII regions in star-forming galaxies. Such major accessible lines at $z > 2$ are [OIII], [OII], and Lyα, which can be observed up to $z \sim 3$, 5, and 16, respectively (up to K band).

1.4 Emission Line Strengths and the ISM

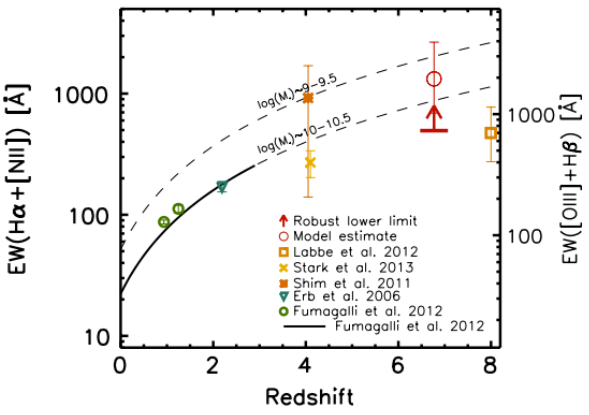

Figure 1.5: The rest-frame Equivalent Width evolution of Hα and [OIII]+Hβ emission as measured Smit et al. (2014). Emission line strengths are found to be considerably stronger at higher redshifts. The equivalent width is an observational proxy for the specific star formation rate (sSFR), such that higher sSFRs are found in high-z galaxies. This suggests that high-z star forming galaxies assemble their stellar populations in a shorter timescale.

As mentioned above, emission line-selected samples have the added advantage of directly selecting galaxies based on their instantaneous star formation activity. Comparing emission lines can also present us a great deal of information regarding the current physical conditions of the interstellar medium within galaxies.

Typical strong emission lines found in star-forming galaxies are Lyα, [OII], Hβ, [OIII], Hα, and [NII]. The strength of these lines are observed to change with cosmic time. Fumagalli et al. (2012) and Sobral et al. (2014) found that the equivalent widths of Hα anticorrelates with stellar mass, such that low-mass star-forming galaxies are typically the extreme emission-line galaxies several studies have reported

(e.g., Erb et al. 2006; Shim et al. 2011; van der Wel et al. 2011; Stark et al. 2013; Roberts-Borsani et al. 2016; Forrest et al. 2017). Recent work have found ubiquitous, high equivalent width [OIII] and Hα emission in $z \sim 6-7$ galaxies (Figure 1.5; e.g., Smit et al. 2014; Rasappu et al. 2016). The increasingly strong emission lines with increasing redshift are signatures of higher specific star formation rates (Fumagalli et al., 2012), which suggests that galaxies are rapidly building up their stellar mass at earlier times.

The physical conditions of the ISM in star forming galaxies is also found to evolve, although the cause is something that is still an open question. For example, the ionization state of the ISM can be measured by looking at the [OIII]/[OII] ratio as [OIII] requires ~ 35 eV and [OII] ~ 13 eV to ionize, respectively. Previous measurements find that high$-z$ galaxies have higher [OIII]/[OII] ratios, which has been attributed to a harder ionization field (e.g., Hayashi et al. 2015; Kewley et al. 2015), lower metallicities (e.g., Sanders et al. 2016), higher electron densities (e.g., Shirazi et al. 2014), geometry of the gas (e.g., Kewley et al. 2013), and also a combination of global properties (e.g., Nakajima & Ouchi 2014) at higher redshifts. Using large samples of emission-line selected samples can help in shedding light on the changing properties of the ISM in star-forming galaxies at different epochs of cosmic time.

1.5 Galaxies and their Host Halos

As discussed in §1.1, galaxies form inside their host dark matter halos. It has also been shown in the previous section that galaxy properties have changed considerably over the past 13 Gyrs. The main question that arises is how much of that evolution is related to changes in the host halo? How do galaxies and halos co-evolve? Addressing these questions involves using the angular/spatial clustering of galaxies in conjunction with prescriptions of the halo mass and bias functions, as well as the halo occupation distribution (HOD), to measure the host halo properties.

With the advent of large galaxy photometric and spectroscopic surveys, (e.g., SDSS: York et al. 2000, 2dFGRS: Colless et al. 2001, DEEP2: Davis et al. 2003, VVDS: Le Fèvre et al. 2005, PRIMUS: Coil et al. 2011, GAMA: Driver et al. 2011, BOSS: Dawson et al. 2013, VIPERS: Garilli et al. 2014, eBOSS: Dawson et al. 2016) in the last two decades, it has become possible to perform detailed analysis of clustering of galaxies as a function of their physical properties (e.g., colors, luminosities, star formation rates, and stellar masses). At low redshifts ($z \sim 0-1$), it has been found that red, passive galaxies are more clustered than blue, active galaxies (e.g., Norberg et al. 2002; Zehavi et al. 2005; Coil et al. 2008; Zehavi et al. 2011; Guo et al. 2013, 2014). Similar luminosity trends with clustering strength/halo mass are also observed at $z \sim 1-2$ (e.g., Hartley et al. 2008; McCracken et al. 2010; Marulli et al. 2013; Ishikawa et al. 2015) and, using primarily Lyman Break galaxies (LBGs), at $z \sim 2-7$ (e.g., Adelberger et al. 2005; Barone-Nugent et al. 2014; Harikane et al. 2016). Correlations between increasing stellar mass and increasing clustering strength/dark matter halo mass have also been reported in the literature (e.g., Meneux et al. 2008, 2009; Wake et al. 2011; Lin et al. 2012; Mostek et al. 2013; McCracken et al. 2015).

The significance of the results highlighted above suggests that dark matter halos have an important role in the star formation processes that occur within galaxies. Large narrowband and spectroscopic surveys have been able to study how the clustering properties of galaxies correlates with star formation activity directly. Recent narrowband measurements using Hα (tracing the instantaneous SFR) up to $z \sim 2$ find that the clustering signal strongly increases with increasing Hα line luminosity as shown in Figure 1.6 (Sobral et al., 2010; Stroe & Sobral, 2015; Cochrane et al., 2017). Surprisingly, Sobral et al. (2010) found that the dependency is also redshift-independent in terms of $L/L^{\star}(z)$, with $L^{\star}(z)$ being the characteristic Hα luminosity at each redshift, equivalent to a characteristic SFR (SFR*, Sobral et al. 2014). Other studies find similar line luminosity/SFR trends with clustering strength/halo mass up to $z \sim 2$ (e.g., Mostek et al. 2013; Dolley et al. 2014; Coil et al. 2017). The trends observed by Sobral et al. (2010)

also show a shallower/flat slope at $L > L^{\star}(z)$, which is suggested to be a signature of quenching processes within the most massive halos.

Current results are primarily based on samples of the nearby Universe and a handful of $z \sim 1-2$ studies. There are also a few Lyman Break Galaxy (LBG) selected samples up to $z \sim 7$, but such samples are severely biased against dusty systems (e.g., Oteo et al. 2015), have photometric redshifts that are uncertain, and complex selection functions. In order to effectively study the clustering properties of galaxies and understand how and when these galaxy-halo trends formed requires samples that are: 1) well-defined in terms of selection criteria, 2) cover a range of redshifts to trace the evolving parameters over cosmic time, 3) cover multiple and large comoving volumes to reduce the effects of cosmic variance, 4) span a wide range in physical properties to properly subdivide the samples, and 5) have known redshifts.

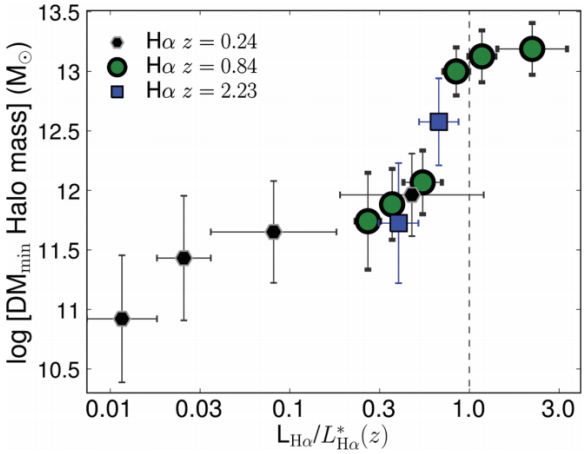

Figure 1.6: Halo Mass in terms of Hα luminosity normalized by the characteristic Hα luminosity, $L^{\star}(z)$, as measured by Sobral et al. (2010). The host halo mass of Hα-selected star forming galaxies is found to tightly scale with Hα luminosity independent of redshift. This implies that the host halo properties plays an important role in how the residing galaxies evolves, at least up to $z \sim 2$.

1.6 This Thesis

In this thesis, I will present all the work that I have done over the past 6 years in addressing several key questions in astrophysics. My work uses data from the High-z Emission Line Survey (HiZELS) and the recent Slicing COSMOS 4K (SC4K) survey, which are narrowband and intermediate band blind-surveys of three fields in the night sky: COSMOS, UDS, and SA22. The samples consist of several thousand Lyα, Hα, Hβ, [OIII], and [OII] emission line galaxies spanning a wide redshift range between $z \sim 0.4-6$ with typical survey sizes of ~ 2 deg^2.

The key questions that I address are:

1. How are the statistical properties and typical star formation activity of star-forming galaxies changing with cosmic time?

2. What can the buildup of stellar mass in emission line-selected galaxies tell us about the mechanisms that drive the galaxy growth?

3. How are emission line strengths changing with redshift? What can this tell us about the conditions of star-forming galaxies at high-z compared to the local Universe?

4. How are galaxies co-evolving with their host halos? What galaxy properties are closely related to changes in the host halo mass? How important are the host halos to the overall evolution of the residing galaxies?

5. What are the descendants of high-z star forming galaxies? Are local, extreme galaxies, such as 'Green Peas', related to typical star-forming galaxies seen at high-z?

Every chapter in this thesis attempts to address these key questions using unique samples of star-forming galaxies selected using emission lines that trace the ionized gas in the HII regions of galaxies. This thesis is organized as follows:

In Chapter 2, I present a sample of 3475 Hβ+[OIII] and 3298 [OII] emitters between $z \sim 0.8-3$ and $z \sim 1.5-5$, respectively, in four redshift slices per emission line corresponding to the four HiZELS narrowband filters. The Hβ+[OIII] and [OII] luminosity functions are presented and studied in detail, followed by measurements of the cosmic star formation rate densities (SFRDs). The cosmic star formation history is mapped out using the [OII] SFRDs along with local Universe measurements to present a detailed measurement of the 'Madau-Lilly' plot using a single calibration of star formation over 13 Gyrs of cosmic history.

In Chapter 3, I investigate the stellar mass functions for the Hβ+[OIII] and [OII] samples and measure stellar mass densities for each redshift slice. I also investigate the equivalent

width evolution of the lines to understand how the emission line strengths change over cosmic time. This is also compared to the local Universe to understand which local population of galaxies represents the typical [OIII] and [OII] galaxy found at $z > 2$. I conclude this chapter by investigating the [OIII]/[OII] ratio evolution and discuss what this means for the physical conditions of the ISM in star-forming galaxies.

In Chapter 4, I present a detailed study of the clustering properties of Hβ+[OIII]- and [OII]-selected galaxies. Converting the clustering lengths to halo masses, I investigate how both galaxy and halo properties changes over cosmic time. This is investigated in terms of stellar masses and line luminosities (trace star formation) to understand how and when these trends were set in place.

In Chapter 5, I extend the work from the previous chapter to Lyα emitters from the Slicing COSMOS 4K (SC4K) survey which combines 3 narrowband filters and 12 intermediate band filters to form 15 redshift samples spanning between $z \sim 2.5-6$ in the full 2 deg^2 COSMOS field. I investigate the connection between galaxies and halos in the same approach as used in Chapter 4, but also investigate the dependency between halo mass and rest-frame UV properties, such as the rest-frame 1500Å continuum luminosity and UV star formation rates. I conclude this chapter by analyzing the potential local Universe descendants of the high-z star-forming galaxies in my samples.

I present the main conclusions of this thesis in Chapter 6.

CHAPTER 2

Evolution of the Hβ+[OIII] and [OII] luminosity functions and the [OII] star-formation history of the Universe up to $z \sim 5$ from HiZELS

Abstract

We investigate the evolution of the Hβ+[OIII] and [OII] luminosity functions from $z \sim 0.8$ to ~ 5 in four redshift slices per emission line using data from the High-z Emission Line Survey (HiZELS). This is the first time that the Hβ+[OIII] and [OII] luminosity functions have been studied at these redshifts in a self-consistent analysis. This is also the largest sample of [OII] and Hβ+[OIII] emitters (3475 and 3298 emitters, respectively) in this redshift range, with large co-moving volumes $\sim 1 \times 10^6$ Mpc^{-3} in two independent volumes (COSMOS and UDS), greatly reducing the effects of cosmic variance. The emitters were selected by a combination of photometric redshift and color-color selections, as well as spectroscopic follow-up, including recent spectroscopic observations using DEIMOS and MOSFIRE on the Keck Telescopes and

FMOS on Subaru. We find a strong increase in $L^\star$ and a decrease in $\phi^\star$ for both Hβ+[OIII] and [OII] emitters. We derive the [OII] star-formation history of the Universe since $z \sim 5$ and find that the cosmic SFRD rises from $z \sim 5$ to ~ 3 and then drops towards $z \sim 0$. We also find that our star-formation history is able to reproduce the evolution of the stellar mass density up to $z \sim 5$ based only on a single tracer of star-formation. When comparing the Hβ+[OIII] SFRDs to the [OII] and Hα SFRD measurements in the literature, we find that there is a remarkable agreement, suggesting that the Hβ+[OIII] sample is dominated by star-forming galaxies at high-z rather than AGNs.

2.1 Introduction

Our understanding of the mass assembly and star-formation processes of the Universe has improved greatly over the past few decades (for in-depth reviews, see Kennicutt & Evans 2012 and Madau & Dickinson 2014). We currently have evidence to show that the cosmic star-formation rate (SFR) peaked at $z > 1$ and that about half of the current stellar mass density had been assembled by that time (e.g, Lilly et al. 1996; Hopkins & Beacom 2006; Karim et al. 2011; Sobral et al. 2013a). However, many open questions remain. How fast did the star-formation rate density (SFRD) drop at $z > 2$? How has the population of star-forming galaxies changed over cosmic time? How does the evolution depend on the enviroment over cosmic time? To answer these questions, it is imperative that we use samples of star-forming galaxies that are low in contaminants and are well-defined in terms of selection methodology.

There are many different star-formation indicators and calibrations in the literature. Each indicator traces the star-formation activity in galaxies independently and with different timescales. The ultraviolet (UV) light from bright, young stars with masses $> 5\ M_\odot$ traces the bulk of the young population with time scales of ~ 100 Myr. UV light of stars with masses $> 10\ M_\odot$ ionize the gas along the line-of-sight, resulting in the absorption and then re-emission of photons seen

as nebular (e.g., Lyman, Balmer, and Paschen series of the Hydrogen Atom) and forbidden emission lines (e.g., [OIII] & [OII]). The lifetimes for stars capable of ionizing the surrounding gas and dust to form the nebular and forbidden emission lines are on the scale of ~ 10 Myr, allowing for the measurement of the instantaneous star-formation rate. Other indicators include far-infrared emission coming from the heating of dust shrouding the hot, UV bright, young stars and the synchrotron emission in the radio coming from accelerated electrons in supernovae. For an in-depth review of the various indicators and calibrations, we refer the reader to reviews in the literature (e.g., Kennicutt 1998, Calzetti 2013).

Despite the different indicators that exist, one can not say that only one of the indicators is the "holy grail" of measuring the SFR of star-forming galaxies. However, using different tracers to map out the evolution of the cosmic SFR history is not the best solution either. This is because evolutionary studies based on samples selected in different ways and using different indicators/calibrations at different redshifts will be susceptible to complicated, strong biases and selection effects, which results in a significant scatter when combining all of them to probe the evolution of the cosmic SFR. Another issue is that most studies don't probe sufficiently large volumes to overcome the effects of cosmic variance. Furthermore, the effects of correcting for dust extinction, especially for UV and optical studies, can result in large systematic uncertainties. One requires an indicator that can be used to probe from the low-z to the high-z Universe using a robust and consistent methodology to reduce the effects and biases that come from making assumptions and differing selection techniques.

Emission lines observed using narrow-band imaging techniques can provide an accurate and reliable sample of star-forming galaxies (e.g., Bunker et al. 1995; Fujita et al. 2003; Glazebrook et al. 2004; Ly et al. 2007; Villar et al. 2008; Geach et al. 2008; Sobral et al. 2013a). The methodology utilizes two different images of the same field: one being from a broad-band filter and the other being from a corresponding narrow-band filter. The narrow-band image is dominated by emission-line galaxies and the continuum, while the broad-band image is

dominated by the continuum with a small contribution from the emission-line. When the two are subtracted, the result is the removal of the continuum and an image of galaxies with emission-lines. The advantage of narrow-band imaging surveys is that they allow for the selection of emitters with a clean selection function by emission line flux and within a known narrow redshift range. This is because the filter width is quite narrow, such that any source brighter than expected from its broad-band magnitude is an emitter. Emission-line surveys via grism spectroscopy on the *HST* (e.g., Colbert et al. 2013) are also great accompaniments to narrow-band studies, as they are area-limited (area of the grism) while emission-line surveys are redshift-limited.

Most narrow-band surveys have focused on Hα (e.g., Tresse et al. 2002; Fujita et al. 2003; Pascual 2005; Ly et al. 2007, 2011; Sobral et al. 2009, 2013a) as it is a reliable star-formation indicator which is well-calibrated in the local universe and is only mildly affected by dust attenuation. The latest results of the High-Emission Line Survey (HiZELS, Geach et al. 2008; Sobral et al. 2009, 2012, 2013a) have robustly traced the evolution of the cosmic SFR up to $z \sim 2$. This is the maximum redshift that Hα surveys can probe from the ground, as at higher redshifts Hα falls into the mid-IR and is blocked by water vapor and carbon dioxide in the atmosphere. To probe to higher-z using the same narrow-band technique would require another emission line. The other major emission lines associated with star-forming galaxies are Hβ4861, [OIII]4959, [OIII]5007, and [OII]3727 which can be probed up to $z \sim 3$ for Hβ+[OIII]and up to $z \sim 5$ for [OII].

In the past decade, several Hβ, [OIII], and [OII] studies have been carried out (e.g., Hammer et al. 1997; Hogg et al. 1998; Gallego et al. 2002; Hicks et al. 2002; Teplitz et al. 2003; Ly et al. 2007; Takahashi et al. 2007; Bayliss et al. 2011, 2012; Sobral et al. 2012; Ciardullo et al. 2013; Drake et al. 2013), the majority of which had small sample sizes and, hence, suffered from cosmic variance biases. The majority observed up to $z \sim 1$, while only the works of Bayliss et al. (2011) and Bayliss et al. (2012) measured the [OII] SFR densities at $z \sim 2$ and $z \sim 4.6$,

respectively. Both these works used small samples, with the $z \sim 4.6$ measurement having a sample size of only 3 [OII] emitters, greatly limiting any conclusion.

This paper presents, for the first time, the luminosity functions of Hβ+[OIII][1] and [OII] emitters up to $z \sim 5$ using the reliable selection techniques of Sobral et al. (2009, 2012, 2013a) on the combined COSMOS and UDS narrow-band publicly available catalogs[2]of HiZELS. The sample probes comoving volumes of up to $\sim 1 \times 10^6$ Mpc^3, which greatly reduces the effects of cosmic variance. This is also the largest sample of Hβ+[OIII] and [OII] emission line galaxies up to $z \sim 5$ to date in the literature and is used to effectively and robustly probe the evolution of the cosmic SFR density.

This paper is organized as follows: in Section 2, we outline the photometric and spectroscopic data sets that we use and the methodology utilized to effectively select Hβ+[OIII] and [OII] emitters. In Section 3, we outline our volume calculations and the completeness and filter profile corrections. Also in Section 3 are the results of the luminosity functions. In Section 4, we present the results and discuss our cosmic star-formation rate densities and the evolution of the stellar mass density based on [OII] emitters. Section 5 outlines the conclusion of this work and is followed by appendix A, which presents our color-color selection criteria, and appendix B, which presents our binned luminosity function data points, and appendix C, which presents our SFR density compilation.

Throughout this paper, we assume ΛCDM cosmology with $H_0 = 70$ km s^{-1} Mpc^{-1}, $\Omega_{\rm m} = 0.3$, and $\Omega_\Lambda = 0.7$ with all magnitudes presented as AB and the initial mass function is assumed to be a Salpeter IMF.

[1]Because the Hβ and [OIII] emission lines are close to each other, photo-z and color-color selections can not distinguish between them. The best way to fully differentiate the two is via spectroscopy. Based on line ratio studies, we can argue that most of the emitters will be [OIII] emitters, but to ensure we are not biasing our measurements based on such assumptions, we present the results as the combined measurement of Hβ+[OIII].

[2]The narrow-band catalogs are available on VizieR and are from Sobral et al. (2013a).

Table 2.1: A list of the narrow-band filters used (Sobral et al., 2013a), along with the central wavelength (μm) and the FWHM (Å) of each filter. Included is the expected redshift of each emission line within the range of the FWHM of the filter and the comoving volume that is observed.

			Hβ+[OIII]5007		[OII]3727	
Filter	$\lambda_{\rm obs}$ (μm)	FWHM (Å)	z	Volume (10^5 Mpc^3 deg^{-2})	z	Volume (10^5 Mpc^3 deg^{-2})
NB921	0.9196	132	0.84 ± 0.01	1.79	1.47 ± 0.02	3.75
NBJ	1.211	150	1.42 ± 0.01	3.11	2.25 ± 0.02	4.83
NBH	1.617	211	2.23 ± 0.02	5.05	3.34 ± 0.03	6.53
NBK	2.121	210	3.24 ± 0.02	4.87	4.69 ± 0.03	5.68

2.2 Data

2.2.1 Selection Catalogs

Our data consist of narrow-band and broad-band photometric data of the UDS (Lawrence et al., 2007) and COSMOS (Scoville et al., 2007) fields and spectroscopic follow-ups that are described in section 2.2.4. The catalogs that are described below are taken from Sobral et al. (2013a) and are publicly available.

The narrow-band catalogs are from the High-z Emission Line Survey (HiZELS, Geach et al. 2008; Sobral et al. 2009, 2012, 2013a). This project utilizes the narrow-band J, H, and K filters of the Wide Field CAMera (WFCAM) on the United Kingdom Infrared Telescope (UKIRT) and the NB921 filter of the Suprime-Cam on the Subaru Telescope. Previous uses of this data focused primarily on Hα emitting galaxies and their properties (e.g., Garn et al. 2010; Geach et al. 2012; Sobral et al. 2010, 2011, 2013a; Stott et al. 2013b,a; Swinbank et al. 2012b,a; Darvish et al. 2014), but HiZELS is able to pickup more than just this emission line as it can detect any line above the flux limit. In this paper, we focus on the Hβ+[OIII] and [OII] emitting galaxies found by HiZELS. The broad-band catalogs are from the Cosmological Evolution

Survey (COSMOS; Scoville et al. 2007) and the DR8 release of the Subaru-*XMM*-UKIDSS Ultra Deep Survey (UDS; Lawrence et al. 2007) catalog.[3]

2.2.2 Narrow-Band Selection of Potential Emitters

In this subsection, we will review the methodology of selecting potential emitters followed by Sobral et al. (2013a). We refer the reader to this paper for a detailed overview.

Potential emitters were selected by their color excess in terms of the parameter Σ (Bunker et al., 1995; Sobral et al., 2012), which quantifies the significance of the excess of a source with respect to the random scatter expected for a source to have a color excess > 0 in terms of their narrow-band magnitudes:

$$\Sigma = \frac{1 - 10^{-0.4(\mathrm{BB}-\mathrm{NB})}}{10^{-0.4(ZP-\mathrm{NB})}\sqrt{\pi r_{\mathrm{ap}}^2(\sigma_{\mathrm{NB}}^2 - \sigma_{\mathrm{BB}}^2)}} \tag{2.1}$$

where BB and NB are the broad-band and narrow-band magnitudes, respectively, r_{ap} is the aperture radius in pixels, and σ_{BB} and σ_{NB} are the rms per pixel for the broad-band and narrow-band, respectively (see e.g. Sobral et al. 2012, 2013a).

Emitters are selected on the basis that they have $\Sigma > 3$ and a rest-frame equivalent width $\mathrm{EW}_0 > 25$ Å. The second condition ensures that we select sources with a significant color excess for bright narrow-band magnitudes (see Figure 3 of Sobral et al. 2013a).

2.2.3 Photo-z Measurements

We initially used the photo-z measurements from Ilbert et al. (2009) and Cirasuolo et al. (2007) for COSMOS and UDS, respectively, that were provided in the corresponding catalogs. The main problem of using those measurements is that in the UDS catalog, more than $> 60\%$ of sources are without photometric redshifts. This raises issues when selecting emitters via

[3] We refer the reader to the respective papers for further details on the creation of these catalogs. We also refer the reader to the UKIDSS and COSMOS websites for further information of the multi-wavelength photometric and spectroscopic data sets. (COSMOS: http://irsa.ipac.caltech.edu/data/COSMOS; UDS: http://www.ukidss.org)

redshift selection. Although the color-color selection is effective alone in selecting Hβ+[OIII] and [OII] emitters (see below and appendices for discussion), we wish to have emitters selected by two independent methods to act as a check-and-balances to robustly select emitters. Therefore, we measured the photometric redshifts for all of the UDS and COSMOS narrow-band excess sources, using EaZY (Brammer et al., 2008) to ensure that (1) the majority of the UDS catalog had reliable photometric redshifts, and (2) that both COSMOS and UDS had their redshifts determined by the same code, models, and assumptions.

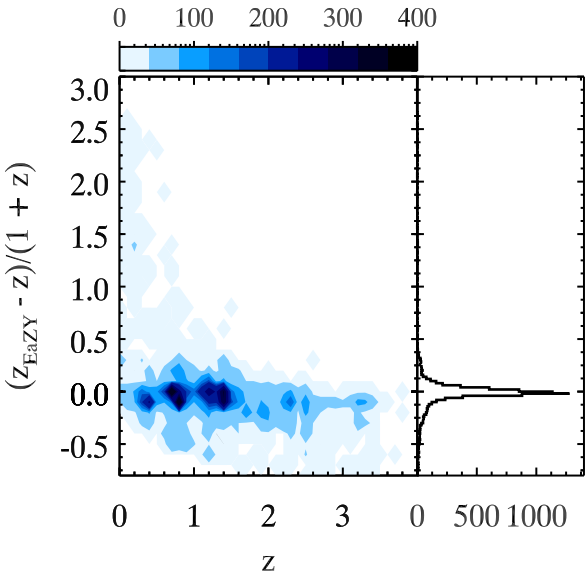

Figure 2.1: The 2D density distribution of the errors between the redshifts determined by EaZY and those of Ilbert et al. (2009) (COSMOS, Le Phare) and Cirasuolo et al. (2007) (UDS, Hyperz) for all narrow-band excess sources (full catalog). We find that $\sim$ 95% of our measurements are in agreement with the redshifts from the literature. The median error is measured as 0.038 without sigma-clipping. There are over-densities at $z \sim 0.4$, 0.8, and 1.5 that conform to redshifts for our major emission-lines. We find outliers with errors up to $\sim$ 2.5, but these are only 4% of our sample. In comparison to the wealth of spectroscopic data, we find a median photometric redshift error of $\Delta z/1+z_{spec} = 0.047$ in comparison to spectroscopic redshifts.

The filters we use for measuring photometric redshifts for our UDS sources are ***UBVRizYJHK*** + *Spitzer* IRAC Ch1 - 4 + narrow-band (NB) + broad-band (BB) filters. For our COSMOS sources, we combine our ***UBVgRizJK***+*GALEX* FUV & NUV+*Spitzer* IRAC Ch1 - 4 +NB+BB catalog with that of Ilbert et al. (2009). The benefit of this is that we include 12 Intermediate Subaru (e.g., IA427, IA464) bands and one Subaru NB711 band that were within the Ilbert et al. (2009) catalog. This results in a total of 29 filters to constrain the measurements. Furthermore, the benefit of using the narrow-band filters in measuring the redshifts is that these filters specifically capture emission-lines which are inherent in the SEDs. The Pegase13 spectral library that is used in EaZY includes a prescription for emission-lines, which makes the measurements more accurate

when including the narrow-band filters. Figure 2.2 shows the benefit of using narrow-band filters in the fitting process by the sharp peaks for which we expect the major emission lines to be located in terms of redshift.

Figure 2.1 shows the 2D density distribution of $\sigma_z = (z_{\mathrm{EaZY}} - z)/(1+z)$, where z are the redshifts measured by Ilbert et al. (2009) and Cirasuolo et al. (2007), and the original photometric redshifts in the catalog. We find a median error of 0.038 (all sources without sigma-clipping). Figure 2.1 also shows over-densities at $z \sim 0.4$, 0.8, and 1.5 which are expected as these are the most populated redshift slices in our sample, since they conform to major emission-lines. We find outliers up to $\sigma_z \sim 2.5$, but these only constitute a small fraction, such that $\sim 95\%$ of our sample are in agreement with Ilbert et al. (2009) and Cirasuolo et al. (2007).

2.2.4 Spectroscopic Redshifts

We make use of the vast array of spectroscopic observations from the literature, which greatly enhances the reliability of our sample. In the COSMOS catalog, spectroscopic measurements are drawn from various studies as listed on the COSMOS website, as well as the zCOSMOS measurements from Lilly et al. (2007). The UDS catalog also includes measurements from various publications that are highlighted on the UKIDSS UKIRT website, including the UDSz survey (Bradshaw et al., 2013; McLure et al., 2013). We also include FMOS measurements from Stott et al. (2013b), DEIMOS & MOSFIRE measurements from Nayyeri et al., in prep, PRIMUS measurements from Coil et al. (2011), and VIPERS measurements from Garilli et al. (2014). In total, we have 1269 emitters that have spectroscopic redshifts with 661, 350, 177, and 81 emitters in NB921, NBJ, NBH, and NBK, respectively. This allows us to enhance the reliability of our sample and to test our photo-z and color-color selections. In comparison to the spectroscopic redshifts, we have assessed the median errors of our photometric redshifts to be $\Delta z/1 + z_{\mathrm{spec}} = 0.047$ (without sigma-clipping).

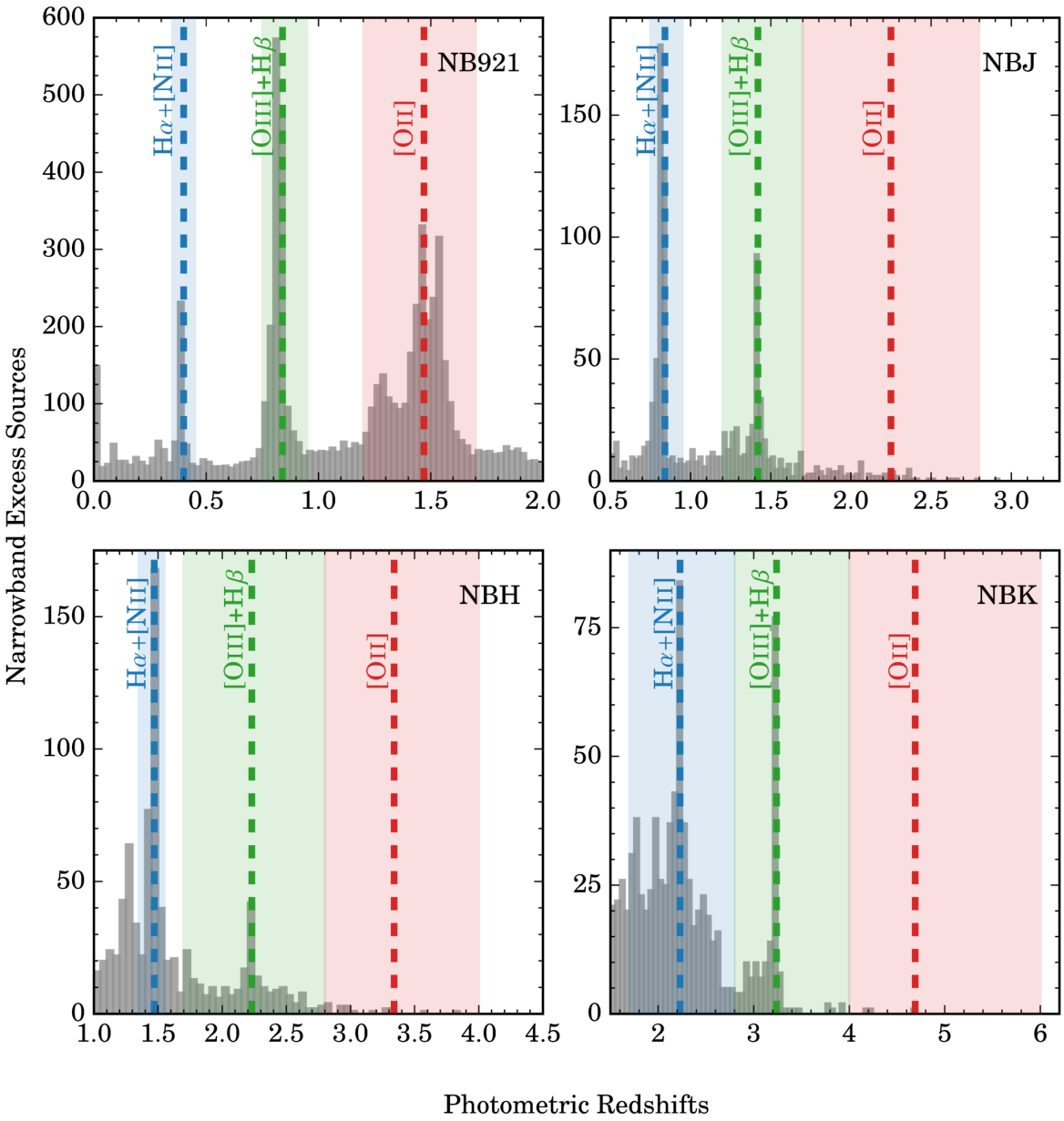

Figure 2.2: Log-scale photometric redshift distributions of the emitters selected in NB921(*upper left*), NBJ (*upper right*), NBH (*lower left*), and NBK (*lower right*). Each main peak is associated with a strong emission line, specifically Hα, Hβ+[OIII], and [OII]. The *dashed red* line is the expected redshift of Hα emitters. The *dashed blue* lines are the expected redshifts for Hβ+[OIII] emitters corresponding to Hβ4861, [OIII]4959, and [OIII]5007. It is clear then that differentiating these lines, even in narrow-band surveys, is quite difficult due to their close proximity to each other. Lastly, the *dashed green* line is the expected redshift of [OII] emitters. Highlighted in the corresponding, but lighter colors, are the photo-z selection regions. The Hα selection region is from Sobral et al. (2013a). The photo-z distributions are from our photo-z calculations using EaZY for the COSMOS and UDS fields.

Table 2.2: The number of emitters selected based on color-color, photo-z, spec-z, and dual/multi-emitters. We also include the total number of emitters found. It should be noted that an emitter can be selected by more than just one selection, such that by tallying up the number of emitters per column will result in a number larger than the number in the column that shows the total number of emitters. We also show the number of sources selected only based on color-color and only based on photo-z. This highlights the importance of having more than one selection technique. For example, if we solely relied on color-color selection, then we would have a loss of 21% in our $z = 1.42$ Hβ+[OIII] sample. Furthermore, we also include the number of emitters selected as dual/multi-emitters. These are sources that were detected in more than one narrow-band, resulting in two or more detected emission-lines complementing each other (e.g., Hα in NBH and [OII] in NB921 for $z \sim 1.47$).

Emission Line	Band	z	Color-Color	CC Only	Photo-z	Photo-z Only	Spec-z	Dual/Multi-Emitter	Total
Hβ+[OIII]									
	NB921	0.84	2005	1000	1262	257	213	160	2477
	NBJ	1.42	277	41	314	78	15	23	371
	NBH	2.23	208	52	212	56	3	44	271
	NBK	3.24	145	11	158	24	2	0	179
[OII]									
	NB921	1.47	3152	957	2211	16	97	213	3285
	NBJ	2.23	115	51	85	21	0	6	137
	NBH	3.30	29	18	16	5	1	0	35
	NBK	4.70	18	14	4	0	0	0	18

2.2.5 Selection of Hβ+[OIII] and [OII] Emitters

The selection of potential Hβ+[OIII] and [OII] emitters is done by a combination of three different methods: (1) photometric redshift; (2) color-color; and (3) spectroscopic redshift. In this section, we will present the general selection criteria that we used to select our sample. For more detailed information about the specific selection cuts applied in each case, we refer the reader to appendix 2.6.1.

With three different selection methods, conflicts can arise where one selection method provides a result that conflicts with another method. To solve the issue, we prioritize the selection methods as such: 1) spectroscopic redshifts, 2) photometric redshifts, and 3) color-color. If the emitter has a spectroscopic redshift, then it is selected based only on measurement. If it doesn't have a spectroscopic redshift, then we select it based on its photometric redshift.

Lastly, if the emitter has a photometric redshift but is not within the range of being selected as Hα (see photo-z selection criteria in Sobral et al. 2013a), Hβ+[OIII], or [OII] or if the emitter does not have photo-z measurements, then it is selected based on the color-color criterion. In most cases, we find that emitters with photo-z within the redshift selection range are also found within the color-color selection area. In such cases, the emitters are selected based on both selection methods.

As shown in figure 2.2, the local peaks in the photometric redshift distributions are located around the expected redshifts for Hβ+[OIII] and [OII] emitters. This signifies that we have many Hβ+[OIII] and [OII] emitters in our sample. We select our emitter candidates by defining a range in the distribution of z_{phot} that is centered on the expected redshift of the emission line, which is aligned with the peaks in figure 2.2. In most cases, the number of Hα emitters are the largest, followed by Hβ+[OIII] and [OII]. In NB921 (figure 2.2), Hβ+[OIII] and [OII] lines are the strongest, respectively, as these redshifts are near the peak of the cosmic star-formation history and also probe a much larger cosmic volume that Hα. Other populations of emission lines are found, such as Paschen series lines, HeI, and [SIII] (figure 2.2).

Color-color selections are also applied for each redshift. The selection criteria used for $z \sim 1-3$ are from Sobral et al. (2013a) as these are in perfect agreement with our large spectroscopic sample, while the criteria used for the Hβ+[OIII] and [OII] at $z = 3.3$ and [OII] at $z = 4.5$ are based on the dropout color-color selection known as the Lyman break technique (Dickinson 1998; Stark et al. 2009). For some redshifts, we use more than one color-color selection to reduce the contaminations from lower and higher-z sources. All color-color selection definitions are found in table 2.4.

Whenever available, we select sources based on their spectroscopic redshifts. Sources for which the spectroscopic redshift contradicts the photo-z and color-color selection are removed from the sample. By including spectroscopically confirmed sources, we increase the size of our sample. We also note that we use all our spectroscopic redshifts to confirm the robustness of

our photo-z and color-color selections.

Also in the selection process is selecting dual/multi-emitters. For some sources that are selected as emitters with some emission line, there also exists another emission line in another band. For example, an emitter that is selected in NBJ as an Hβ+[OIII] emitter ($z = 1.47$) can also be selected in NB921 as an [OII] emitter if observed in that narrow-band. Sobral et al. (2012) used this same technique in a double-blind study to find [OII] emitters in NB921 by using selected Hα emitters in NBH as a proxy. The benefit to this technique is that it confirms emitters if they are selected in at least two bands; corresponding to getting a redshift out of two emission lines. In cases where we find dual/multi-emitters, we treat them as spectroscopic measurements as it is similar to having a spectroscopically confirmed emitter and include them in the sample.

One major source of contamination that we may have is having selected a source as an [OII] emitter when it is an Hβ+[OIII] emitter and vice versa. Also, there are situations where a source is selected as one of the emitters of interest, but also falls into the color-color selection for another emission line, or even Hα (as these color-color selections were used by Sobral et al. (2009, 2012, 2013a) to find such emitters). To overcome this degeneracy, we look at the photo-z distributions shown in figure 2.2 as a probability distribution to assign the emission line based on the most probable line in the sample. In all cases, except for NB921, Hα is the most probable line. For NB921, Hβ+[OIII] is the most probable.

Another source of contamination is from misidentified lines. From the wealth of spectra that we have, the majority of misidentified lines are Hα. Further details on the types of misidentified lines can be found in appendix 2.6.1. Our total sample size is outlined in table 2.2.

2.3 Luminosity Functions and Evolution

We use the traditional V_{max} estimator to create our binned data. The binned data is defined such that:

$$\phi(L_j) = \frac{1}{\Delta \log L_{b,j}} \sum_{\log L_{c,j} - \Delta \log L_{b,j}/2.}^{N} \frac{1}{C(L_i) V_{max,i}} \tag{2.2}$$

where L_j is the j^{th} luminosity bin, $\Delta \log L_{b,j}$ is the bin-size, $\log L_{c,j}$ is the central luminosity of the j^{th} bin, $C(L_i)$ being the completeness of the i^{th} source described in section 2.3.1, and $V_{max,i}$ being the volume for which that source may be detected as described in section 2.3.2.

2.3.1 Line Completeness

To assess the completeness, we follow the methodology proposed in Sobral et al. (2012, 2013a). We start with the full catalog that has all the emitters and includes sources which did not make our emitter selection. To measure the recovery fraction based on the emission line flux, we input a mock line flux starting at 10^{-18} erg s^{-1} cm^{-2} to all sources in the catalog. We then apply the excess selection criteria (Σ and EW cuts) used in Sobral et al. (2013a) followed by our color-color selections. The recovery fraction is then defined as the number of sources recovered divided by the total number of sources in the catalog. This is then repeated after increasing the input mock line flux by small increments. The expected result is that at 10^{-18} erg s^{-1} cm^{-2} the recovered fraction will be low and will increase as the input line flux increases. Figure 2.3 shows the average completeness determined for our Hβ+[OIII] and [OII] sources in the different narrow bands. The advantage of this technique is that we are not limiting our determination of the completeness to a certain model, but actually using the observed data itself to get the completeness correction.

There are some important points to be noted. First, these simulations are run separately per image. This is because the depths of each image are not the same and thus can not be used together all at once to determine the completeness correction. Secondly, we apply an uncertainty

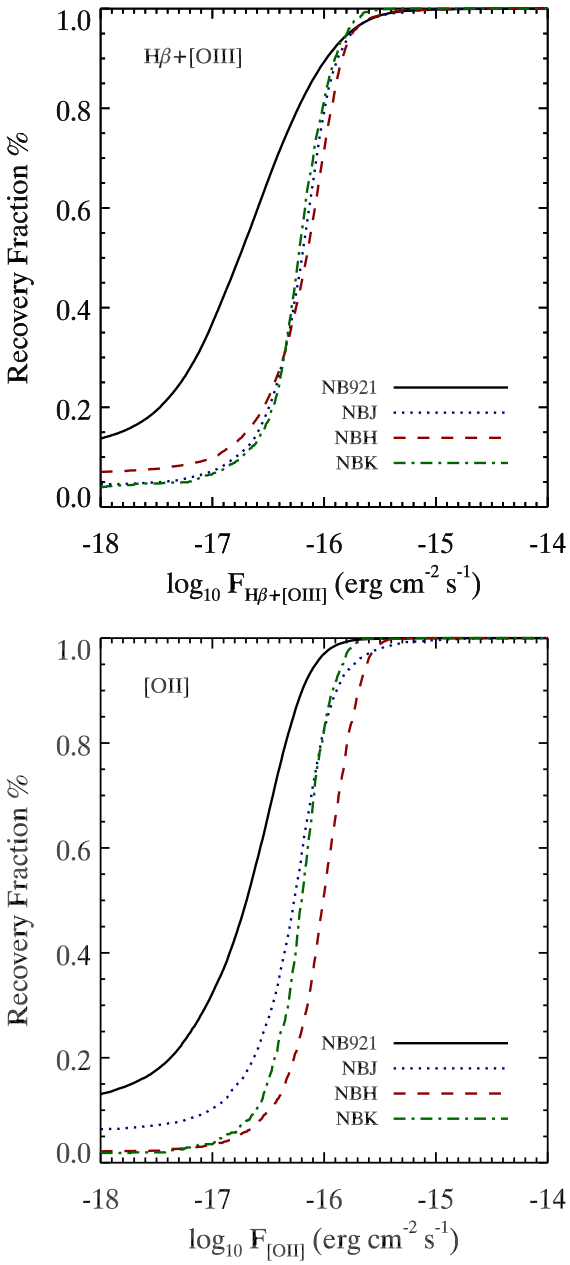

Figure 2.3: Average line completeness for the entire sample per band. Note that the completeness does vary between the COSMOS and UDS fields, as well as from image-to-image within each field. This is because each image has a different depth. We compute the completeness based on each image to account for this discrepancy.

of 20% of the completeness correction to the other uncertainties in quadrature in order to take into account the errors associated with this method of determining the corrections.

2.3.2 Volumes & Filter Profile Correction

We calculate the volumes assuming a top-hat filter that has the same range as the FWHM of the actual filter. We report the probed comoving volume per square degree in table 2.1. The volumes for each log-luminosity bins in the luminosity functions are reported in tables 2.5 and 2.6 for Hβ+[OIII] and [OII], respectively.

Although a top-hat filter makes our calculations easy, it is not a true representation of the throughput of the filter, which requires us to apply a filter profile correction. There are two main effects that the filter profile correction takes into account. The first is the *flux loss due to emitters that are close to the edge of the filter's FWHM*. Bright emitters at the wings will have a significant flux loss (close to 40%; depends on the filter) and would be considered as a faint source. This gives an overall bias in our sample population of faint

sources and a lack of bright sources. The second effect is *the volumes are corrected for the bright sources*. Any faint source that is close to the wings of the filter will most likely not be in our sample, but bright sources will be detected as faint emitters. This then implies that our bright emitters cover a wider range of the filter, meaning a wider range in redshift, and, therefore, a larger volume.

We use the method proposed in Sobral et al. (2009, 2012, 2013a). We correct for the filter by creating a mock sample of 10^5 fake emitters based on the luminosity function with the assumption of a top-hat filter. Random redshifts are assigned to each source and in a range covering the full filter profile, but not large enough that evolutionary effects of the luminosity function and cosmological structure biases the results. We assume a uniform redshift distribution. This mock sample will have the same distribution as the input top-hat luminosity function which we define as $\phi_{\rm TH}$. We then make a second mock sample with the same top-hat luminosity function but now apply the actual filter. This is done by:

$$L_{corr} = \frac{\int_{z_1}^{z_2} L_{in}(z) T(z) dz}{\int_{z_1}^{z_2} T(z) dz} \tag{2.3}$$

where $T(z)$ is the filter-response function in terms of redshift and $L_{in}(z)$ is the luminosity of the emitter which is defined as $L_{in}(z) = L\ \delta(z_{\rm rand} - z_{\rm filter})$, where $z_{\rm rand}$ is the randomly assigned redshift and $z_{\rm filter}$ is the matching redshift of the filter. This results in the loss of sources as some sources will have a redshift outside the range of the filter's FWHM. The luminosity function from this population is defined as $\phi_{\rm Filter}$ and is compared to $\phi_{\rm TH}$ in order to get the filter profile correction factor. The result shows that the bright sources are underestimated as expected, which changes the shape of the final luminosity function slightly. Specifically, it decreases the faint-end slope and increases the $L^\star$ and $\phi^\star$ slightly. This correction is applied to the LFs by dividing all the binned $\Phi(L)$ data points by the correction factor.

2.3.3 Luminosity Function Fitting

There are several different functions that have been proposed in the literature to describe the observed luminosity function of the Universe (see Johnston 2011 for an in-depth review). We adopt the most-widely accepted Schechter function to fit the observed luminosity function. The Schechter function is defined in its log-form as:

$$\Phi(L)\mathrm{d}L = \phi^\star \ \ln 10 \left(\frac{L}{L^\star}\right)^{1+\alpha} e^{-(L/L^\star)} \mathrm{d}\log_{10} L \tag{2.4}$$

where $\phi^\star$ is the normalization of the luminosity function, $L^\star$ is the characteristic luminosity, and α is the faint-end slope.

We fit each luminosity function using the MPFIT fitting routine (Markwardt, 2009), which utilizes the Levenberg-Marquardt least-squares minimization technique to find the best-fit for a given function. For each fit, we take the best-fit values as our fitted parameters. For the 1σ errors, we run a Monte Carlo simulation, similar to that of Ly et al. (2011). The simulation starts by selecting a random number that is drawn from a normal distribution that will perturb each data point, $\Phi(L)$, in the luminosity function within the 1σ error bars. We also vary the bin size and center of the bin by perturbing the original bin size and bin center by a uniform distribution. The fit is then run again and these steps are repeated for each iteration. A total of 10^5 iterations are done to get a probability distribution of the best-fit values from where the 1σ error bars are then calculated.

Our best-fit values are shown in table 2.3. We keep α fixed to a constant value of -1.6 and -1.3 for Hβ+[OIII] and [OII], respectively, as we are not able to fully constrain the faint-end. These values are drawn from looking at past work from previous narrow-band studies in order for our results to be comparable (e.g., Hβ+[OIII], Colbert et al. 2013; [OII], Bayliss et al. 2011). The drawback to this is that we are using low-z measurements of α as a proxy for the high-z universe, which can be an incorrect assumption. Low-z studies, such as Colbert et al. (2013), Ly et al. (2007), and Pirzkal et al. (2013) for Hβ+[OIII] and Ly et al. (2007), Ciardullo et al.

(2013), Takahashi et al. (2007), Bayliss et al. (2011), and Sobral et al. (2012) for [OII], have shown that the faint-end slope doesn't evolve up to $z \sim 1.5$, while Hα surveys such as Sobral et al. (2013a, 2014) have shown no evolution in the faint-end slope up to $z \sim 2.23$. Furthermore, UV studies (e.g., Oesch et al. 2010; Smit et al. 2012), have shown no evolution up to $z \sim 6-7$. Based on these results, we keep α fixed as we constrain the bright-end rather than the faint-end.

Lastly, the LF results are not corrected for dust extinction, except when measuring the star-formation rate densities. This is because many studies in the literature use very different extinction diagnostics, such that it becomes difficult to compare various studies. Furthermore, our knowledge of the role of dust on emission-lines for the high-z universe, especially for the emission-lines of interest in our study, is still in development and requires future detailed investigations. To simplify the use of our LFs by others in future studies, we present all the LF parameter results as uncorrected for dust and AGN contribution. When discussing the SFRDs in section 2.4, we will include the results with and without dust and AGN corrections.

2.3.4 Hβ+[OIII] Luminosity Function $z \sim$ 0.8, 1.5, 2.2, and 3.3

We present here the results of the fitted Schechter function to the Hβ+[OIII] observed luminosity function out to $z \sim 3.3$. This is the highest redshift determination of the Hβ+[OIII] LFs currently to date and is the first time that the luminosity function has been constrained out to these redshifts. We present the results in figure 2.4. From $z \sim 0.8$ to 3.3, we see a clear evolution in the shape of the LFs (figure 2.4, *left*). We also show on figure 2.4 the evolution of $\phi^\star$ and $L^\star$ with α fixed to -1.6. It should be noted that there is a degeneracy between the fitted Schechter parameters, as shown in figure 2.7. This needs to be borne in mind when interpreting the evolution of any single parameter, although figure 2.7 indicates that our results are relatively robust. Based on our results, we find that $\phi^\star$ has been decreasing from $z \sim 0.8$ to ~ 3.3. The opposite trend is seen in $L^\star$ where it is increasing from $z \sim 0.8$ to ~ 3.3.

Our results show a clear evolution in the luminosity function and are consistent with the

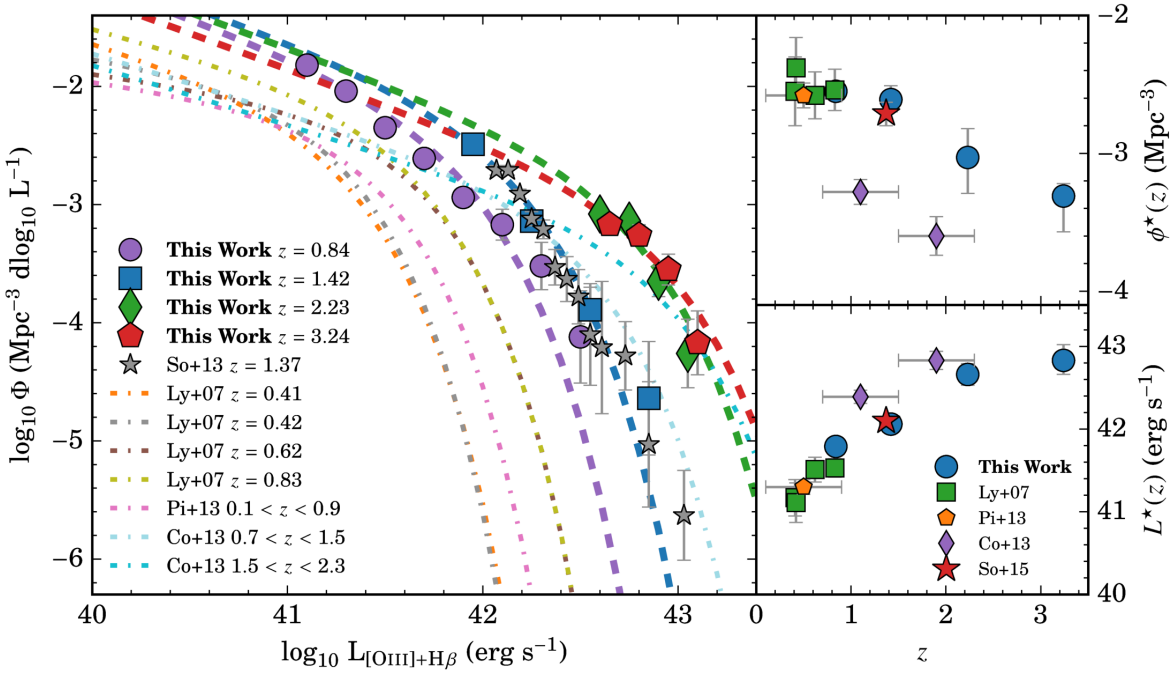

Figure 2.4: *Left:* Presented are our Hβ+[OIII] Luminosity Functions along with LFs from the literature. Included on the top horizontal axis is the $\log_{10}$ SFR that was derived via the Osterbrock & Ferland (2006) calibration (see section 2.4.2). The darker data points are color coded to match the lighter LF fit (*dashed lines*). There is a clear evolution in the LFs up to $z \sim 3$. We find that our $z = 1.42$ and 2.23 LFs are in reasonable agreement with the [OIII] grism spectroscopy study of Colbert et al. (2013) at the bright-end, suggesting that we are selecting a reliable sample of [OIII] emitters. The major difference between our $z = 0.84$ and the $z = 0.83$ LF of Ly et al. (2007) is probably due to sample size biases. Our sample is much larger, hence we are able to populate our brightest bins, causing a shift in $L^\star$ to higher luminosities. *Top Right:* The evolution of $\phi^\star$ from the Hβ+[OIII] luminosity function. A strong, decreasing evolution is seen in $\phi^\star$ from $z = 0$ to $z \sim 3$. This same evolution is seen by UV LF studies (see Oesch et al. 2010 for details). *Bottom Right:* The evolution of $L^\star$ from the Hβ+[OIII] luminosity function. We see a strong, increasing evolution in $L^\star$ up to $z \sim 3$.

same evolution seen in the results from the literature (Ly et al., 2007; Pirzkal et al., 2013; Colbert et al., 2013; Sobral et al., 2015a). We report our LF parameters in table 2.3. We find that our $z \sim 1.47$ and 2.23 LF agrees well with the LFs of Colbert et al. (2013) in the bright-end, but diverges at the faint-end. This matches with our discussion in the section below (see section 2.3.4.1) where we predict the bright-end to be dominated by [OIII] emitters. The Colbert et al. (2013) study was part of the *HST* WISP program, covering 29 fields (0.036 deg^2) in search of Hα, [OIII], and [OII] emission line galaxies using WFC3 grim spectroscopy. Because this was a

spectroscopic study and the fact that our LF matches (in the bright-end) with that of Colbert et al. (2013) gives us confirmation that we are picking up the [OIII] emitters in our sample. The rise in the faint-end can then be attributed to the Hβ emitters in our sample.

In comparison to Ly et al. (2007), we see a clear deviation of the fits between our $z \sim 0.84$ and their $z \sim 0.83$. Although we do agree in terms of $\phi^\star$, the main deviation in the LFs are in $L^\star$ and α (was $\alpha = -1.44 \pm 0.09$ in comparison to our -1.6 fixed faint-end slope). The study was based on deep optical imaging of the Subaru Deep Field (SDF) using the Suprime-Cam on the 8.2 m Subaru Telescope and was complemented with Subaru FOCAS and Keck DEIMOS spectroscopy. The deviation could be due to biases from sample sizes such that our sample consists of more bright emitters to populate the bright-end, hence shifting $L^\star$ higher. In comparison to Sobral et al. (2015a), for which this work was done in unison with, we find perfect agreement but our sample probes deeper by 0.1 dex.

Figure 2.4 shows the evolution of $L^\star$ along with the results from other studies. There is a strong trend in which $L^\star$ is increasing from $z = 0 - 2.23$ and then flattens. This trend is supported by Ly et al. (2007), Pirzkal et al. (2013), Colbert et al. (2013), and Sobral et al. (2015a). Prior to this work, the $z < 1$ studies hinted to a rising trend in $L^\star$, which with our measurements and the $z \sim 1.5$ measurements of Sobral et al. (2015a) has been confirmed up to $z \sim 3$.

For the normalization of the LF, we see an evolution (figure 2.4) such that $\phi^\star$ drops as redshift increase up to $z \sim 3$. This is consistent with the collection of UV LFs (i.e., Oesch et al. 2010), while our determination is based on a reliable Hβ+[OIII] sample. Note that prior to this study, the Hβ+[OIII] measurements in the literature paint the picture that the $\phi^\star$ evolution is flat up to $z \sim 1$. With the inclusion of our measurements, along with the $z \sim 1.5$ measurements of Sobral et al. (2015a), we find that $\phi^\star$ strong decreases after $z > 1$.

2.3.4.1 Predicting the [OIII] LF and AGN contribution

The results highlighted above are for the Hβ and [OIII] emitters combined as one sample since we can not separate the two types of emitters based on photometry. For this, we need to conduct spectroscopic follow-ups to properly segregate the emitters. We attempted to separate the sample by using the Hα LF of Sobral et al. (2013a). The advantage of using the LFs of Sobral et al. (2013a) is that it is fully compatible since we are both using the same data set and methodology. We start by first removing $A_{H\alpha} = 1.0$ mag dust correction, then apply an Hβ/H$\alpha = 0.35$ line ratio from Osterbrock & Ferland (2006) to get the observed Hβ LF. We then applied $A_{H\beta} = 1.38$ mag (based on Calzetti et al. (2000); assuming $A_{H\alpha} = 1.0$ mag) to the LFs and dust-corrected our Hβ+[OIII] LFs using $A_{H\beta+[OIII]} = 1.35$ (see section 2.4.3.2 for details). The next step was subtracting our Hβ+[OIII] LFs from the predicted Hβ LFs to get the predicted luminosity function for [OIII] 5007 emitters. The results are shown in figure 2.5.

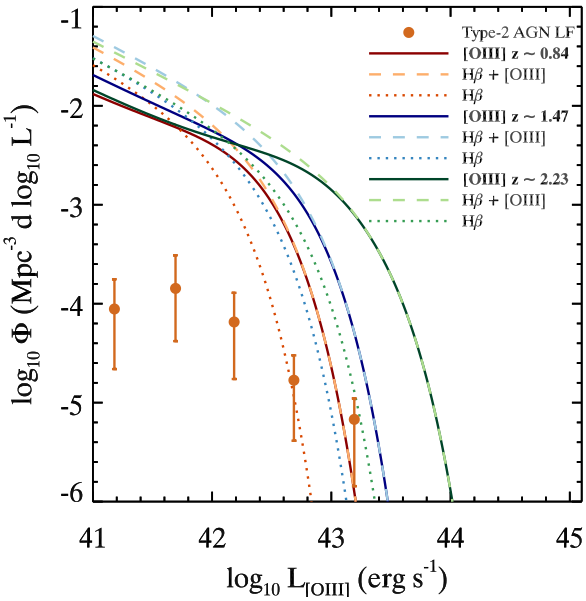

Figure 2.5: Shown is the predicted [OIII] LFs from $z \sim 0.8$ to 2.2 and compared to the $z \sim 0.71$ zCOSMOS Type-2 AGN LF of Bongiorno et al. (2010). The Hβ LFs are made by simply taking the Hα LFs of Sobral et al. (2013a) and assuming a fixed Hβ/Hα ratio to convert them. We find that our $z \sim 0.84$ LF is [OIII]-dominated at the bright-end. Also, the level of AGN contribution is very little, except for $\log_{10} L_{[OIII]} > 43.0$ erg s^{-1}.

We find that the [OIII] emitters in our sample completely dominate the Hβ+[OIII] LFs while towards the faint-end the Hβ emitters dominate. This is expected as the theoretical [OIII]/Hβ line ratio is ~ 3 (for $Z = 0.0004$; Osterbrock & Ferland 2006), which would segregate our sample such that the bright-end will be populated by [OIII] emitters and the faint-end with Hβ emitters. We also find an interesting feature where the normalization in the [OIII] LFs are the same, with

the exemption of the $z \sim 1.42$ [OIII] LF which is slightly higher. This can imply that the relative contribution of Hβ is the same for all three LFs. We note that this is a qualitative assessment and subtracting a Schechter function by another Schechter function doesn't result in the same functional form.

We also attempted to compare the $z \sim 0.8$ [OIII] LF with the zCOSMOS AGN Type-2 LF of Bongiorno et al. (2010) to qualitatively assess the contribution of AGNs. The Type-2 AGN is the best candidate that could contaminate our sample as they have a continuum that is similar to normal star-forming galaxies and they photo-ionize the same cold gas that is photo-ionized by hot massive stars. We find that we are in agreement *only* for the brightest luminosity bin of Bongiorno et al. (2010) ($\log_{10}$ L$_{[\mathrm{OIII}]} \sim 43$ erg s^{-1}), but in disagreement for the lower luminosity bins. This implies that our brightest [OIII] emitters are primarily AGNs, but the fainter emitters are a combination of star-forming galaxies and AGNs, with the star-forming galaxies being the most dominant. Future spectroscopic follow-ups of our sample would allow us to properly study the evolution of AGNs in the Universe.

2.3.5 [OII] Luminosity Function $z = 1.47$. 2.23, 3.3, and 4.7

We present here the results of the [OII] luminosity function and the Schechter fit out to $z \sim 5$. The results are highlighted in figure 2.6. We see a clear evolution of the LF with redshift, with a large increase in the characteristic luminosity with redshift. The right-hand panels of figure 2.6 show the evolution of the fitted $\phi^\star$ and $L^\star$ parameters, and figure 2.7 shows the degeneracy between the fitted values.

Included on figure 2.6 are data from the literature that range from $z = 0 - 2.2$ (Bayliss et al., 2011; Ciardullo et al., 2013; Ly et al., 2007; Takahashi et al., 2007; Sobral et al., 2012, 2015a). We find that our $z = 2.23$ binned LF data is in agreement with the CF-HiZELS result of Sobral et al. (2015a). Because their sample size is ~ 4 times larger than our measurement, we have combined their LF data points with ours. The main effect is our measurement extends

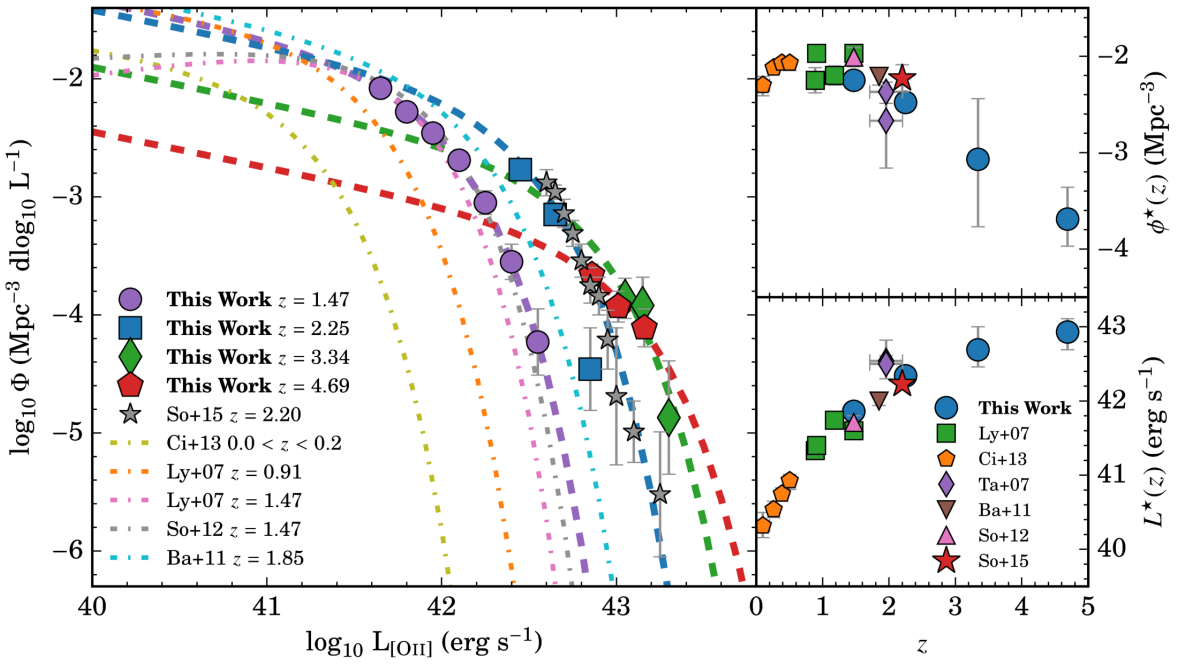

Figure 2.6: *Left:* Presented are the [OII] Luminosity Functions along with those from the literature. The SFR calibration used to create the top horizontal axis is from Kennicutt (1998) (see section 2.4.2). The darker data points are color coded to match the lighter LF fit (*dashed lines*). We find that the evolution from the low-z studies of Gallego et al. (2002) and Ciardullo et al. (2013) to our $z = 4.7$ LFs is quite strong and clear. We find that our $z = 1.47$ LF is in agreement with the HiZELS [OII] study of Sobral et al. (2012) and the Subaru Deep Survey study of Ly et al. (2007). Our $z = 2.23$ is also in agreement with the CF-HiZELS study of Sobral et al. (2015a). *Top Right:* The evolution in the normalization of the LF. We find that $\phi^\star$ has been decreasing from $z \sim 1.47$ to $z \sim 5$. *Bottom Right:* The evolution of $L^\star$. We find a clear, strong evolution in $L^\star$ all the way to $z \sim 5$.

the combined LF 0.15 dex fainter. We note that the LFs of Sobral et al. (2015a) are directly compatible with our LFs as our study follows the same methodology. In fact, the Sobral et al. (2015a) is specific to the NBJ determined LFs and the effects of cosmic variance while this study focuses on the evolution and extension of the LFs out to $z \sim 5$.

Our $z = 1.47$ measurements are in perfect agreement with Sobral et al. (2012) and close to agreement with Ly et al. (2007). We note that for Ly et al. (2007) the faint-end was measured to be $\alpha = -0.78 \pm 0.13$ and -0.9 ± 0.2 for Sobral et al. (2012) while we keep our faint-end slope fixed to -1.3 for all LFs. As seen in figure 2.6, we find that we are not probing deep enough to

Table 2.3: The Luminosity Function parameters and derived properties for all Hβ+[OIII] and [OII] emitters. Errors in $\phi^\star$ and $L^\star$ are computed by running a Monte Carlo Simulation, displacing all the measurements of $\Phi_{\rm final}$ by 1σ. The faint-end slope, α, was fixed as our data don't go faint enough to constrain the faint-end properly. The luminosity density, ρ_L, was calculated by taking the infinite integral of the LF. The SFRDs were calculated based on the Kennicutt (1998) calibration ([OII]) and Osterbrock & Ferland (2006) (Hβ+[OIII]) with $\dot{\rho}_{\star,\rm comp}$ being the completeness and filter profile corrected SFRD measurement. $\dot{\rho}_{\star,\rm corr}$ is the completeness + filter profile + dust corrected SFRD measurement. $\dot{\rho}_{\star,\rm AGN\text{-}corr}$ is the completeness + filter profile + dust corrected + AGN corrected SFRD measurement. We show every measurement as $\dot{\rho}_{\star,\rm comp}$ is the most robust measurement, while the dust and dust + AGN corrected measurements are based on assumptions regarding line ratios, dust extinction laws, and AGN selection methods.

z	$\log_{10}\phi^\star$ (Mpc^{-3})	$\log_{10}L^\star$ (ergs s^{-1})	α	$\log_{10}\rho_L$ (ergs s^{-1} Mpc^{-3})	$\log_{10}\dot{\rho}_{\star,\rm comp}$ ($M_\odot$ yr^{-1} Mpc^{-3})	$\log_{10}\dot{\rho}_{\star,\rm corr}$ ($M_\odot$ yr^{-1} Mpc^{-3})	$\log_{10}\dot{\rho}_{\star,\rm AGN\text{-}corr}$ ($M_\odot$ yr^{-1} Mpc^{-3})
Hβ+[OIII] Luminosity Function Properties							
0.84	$-2.55^{+0.04}_{-0.03}$	$41.79^{+0.03}_{-0.05}$	-1.60	39.58	$-1.549^{+0.01}_{-0.02}$	$-1.009^{+0.01}_{-0.02}$	$-1.062^{+0.03}_{-0.03}$
1.42	$-2.61^{+0.10}_{-0.09}$	$42.06^{+0.06}_{-0.05}$	-1.60	39.80	$-1.333^{+0.05}_{-0.04}$	$-0.793^{+0.05}_{-0.04}$	$-0.882^{+0.06}_{-0.05}$
2.23	$-3.03^{+0.21}_{-0.26}$	$42.66^{+0.13}_{-0.13}$	-1.60	39.98	$-1.159^{+0.10}_{-0.11}$	$-0.619^{+0.10}_{-0.11}$	$-0.766^{+0.11}_{-0.12}$
3.24	$-3.31^{+0.09}_{-0.26}$	$42.83^{+0.19}_{-0.17}$	-1.60	39.87	$-1.265^{+0.10}_{-0.09}$	$-0.725^{+0.10}_{-0.09}$	$-0.873^{+0.11}_{-0.10}$
[OII] Luminosity Function Properties							
1.47	$-2.25^{+0.04}_{-0.04}$	$41.86^{+0.03}_{-0.03}$	-1.30	39.72	$-1.132^{+0.02}_{-0.02}$	$-0.884^{+0.02}_{-0.02}$	$-0.973^{+0.04}_{-0.04}$
2.25	$-2.48^{+0.08}_{-0.09}$	$42.34^{+0.04}_{-0.03}$	-1.30	39.98	$-0.878^{+0.05}_{-0.06}$	$-0.630^{+0.05}_{-0.06}$	$-0.723^{+0.06}_{-0.07}$
3.34	$-3.07^{+0.63}_{-0.70}$	$42.69^{+0.31}_{-0.23}$	-1.30	39.74	$-1.118^{+0.43}_{-0.20}$	$-0.870^{+0.43}_{-0.20}$	$-0.964^{+0.43}_{-0.20}$
4.69	$-3.69^{+0.33}_{-0.28}$	$42.93^{+0.18}_{-0.24}$	-1.30	39.35	$-1.502^{+0.10}_{-0.10}$	$-1.255^{+0.10}_{-0.10}$	$-1.348^{+0.11}_{-0.11}$

fully see the turn in the LF for $L_{\rm [OII]} < 41$ erg s^{-1} as found by Ly et al. (2007) and Sobral et al. (2012). This is probably due to the fact that both studies used $2''$ apertures, while our study uses $3''$ apertures (provided in the Sobral et al. (2013a) catalog) to select $z = 1.47$ [OII] emitters, which means that their studies are better at recovering faint emitters.

We find a strong evolution in $L^\star$, as shown in figure 2.6 for which a strong, rising trend is seen up to $z \sim 5$. We also see the same evolution in Hα studies (e.g., Sobral et al. (2012)), where $L^\star$ is strongly increasing from $z = 0$ to 2. The same evolution of $L^\star$ is seen in UV studies (Oesch et al., 2010) up to the same redshift range. We notice some scatter for the low-z studies (Ly et al. 2007; Takahashi et al. 2007; Bayliss et al. 2011; Sobral et al. 2012; Ciardullo et al. 2013). This is primarily due to limitations in survey area and/or shallowness of the surveys.

The evolution in $\phi^\star$ is shown in figure 2.6 along with measurements from the literature.

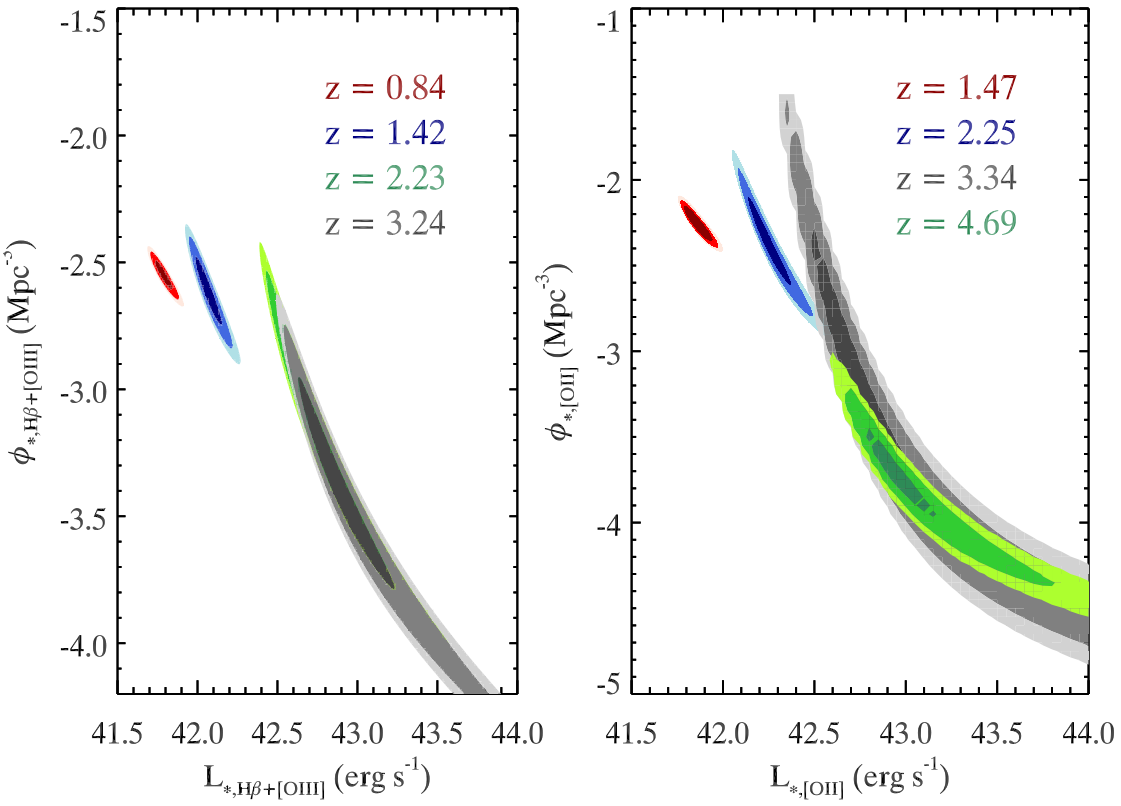

Figure 2.7: Shown is the interdependent evolution of $L^\star$ and $\phi^\star$ for Hβ+[OIII] (*left*) and [OII] (*right*). The contours are color-coded to match the text color in the legend. The confidence levels are organized such that the *darkest shade* is the 1σ level and the *lightest shade* being the 3σ level. There is a clear evolution that as redshift increases, $\phi^\star$ drops and $L^\star$ increases up to $z \sim 3$ and $z \sim 5$ for Hβ+[OIII]and [OII], respectively.

Our measurements show a decreasing trend since $z \sim 1.5$ while for redshifts less than 1.5 shows a flat evolution in $\phi^\star$.The same evolution in $\phi^\star$ is also seen in Hα studies (e.g., Sobral et al. (2013a)) where after $z \sim 1$ and up to $z \sim 2$, $\phi^\star$ is shown to be decreasing. UV measurements (Oesch et al., 2010) also see a similar trend.

Future wide surveys, such as *Euclid* and WFIRST, will be able to observe larger samples of emission-line galaxies such that our results can be used as predictions for such upcoming projects. By taking our LFs and integrating them to some flux/luminosity limit, these future surveys can estimate the number of [OII] emitters that can be detectable. Our LFs would then be quite useful as a tool to plan surveys studying [OII] emitters out to $z \sim 5$. Furthermore, our

luminosity functions can be used as a tool to gauge the level of low-z interlopers in various studies, such as Lyα studies at high-z.

2.4 Evolution of the Star-Formation History of the Universe

In this section, we present the star-formation history evolution of our [OII] sample out to $z \sim 5$. We begin by measuring the level of AGN contamination and then present the calibrations used to get the star-formation rate densities (SFRDs). We conclude with a discussion of the evolution of the SFRD based on [OII] emitters, the correction for dust, and our estimates of the stellar mass density evolution of the universe based on our SFRD fit.

2.4.1 Contribution from AGN

Active Galactic Nuclei (AGN) play an important role in the evolution of galaxies. Because AGN heat the cold gas that is photo-ionized by O & B-type stars in star-forming regions, the same emission-lines become present by both sources. It is then imperative that the SFRDs are properly corrected for AGN contamination to ensure that the sample is, by majority, a star-forming sample. Due to the low number-density of AGNs, it is difficult to use the current catalogs in the literature (e.g., *Chandra-COSMOS*) as a direct indicator on the level of AGN contribution/contamination to our sample. When comparing to *Chandra-COSMOS* (Elvis et al., 2009), we find 1, 0, 4, 0 for $z \sim 0.84$, 1.42, 2.23, and 3.24 for our Hβ+[OIII] sample and 5, 2, 1, 0 for $z \sim 1.47$, 2.25, 3.34, and 4.69 for our [OII] sample. We also compared our catalogs to the *XMM-COSMOS* catalog (Cappelluti et al., 2009) and found no matches.

These matches themselves can not give us a complete indication of the level of our AGN contamination as they are X-ray flux-limited. We instead take advantage of the rest-frame 1.6μm bump in the SEDs of star-forming galaxies. This bump arises from the minimum opacity of H^- ions in the stellar atmospheres of cool stars. For AGNs, the bump is meshed in with

various other emission (e.g., PAHs, silicate grains) resulting in a rising power-law SED after 1.6μm in the rest-frame. We use the deep IRAC data in COSMOS and UDS and with the condition that redder colors are AGNs, signifying the rising SED after 1.6μm, and anything with bluer colors are star-forming galaxies resulting in the 1.6μm bump. We measure the colors by taking the $[3.6-4.5] > 0.1$ ($z \sim 0.8$), $[4.5-5.6] > 0.1$ ($z \sim 1.5$), and $[5.6-8.0] > 0.1$ ($z \sim 2.2$) for Hβ+[OIII] emitters and $[4.5-5.6] > 0.1$ ($z \sim 1.47$) and $[5.6-8.0] > 0.1$ ($z \sim 2.23$) for [OII] emitters. We find AGN contamination for Hβ+[OIII] is $\sim 11.4\%$, $\sim 18.5\%$, and $\sim 28.8\%$ for $z \sim 0.8$, 1.5, and 2.2, respectively. The amount of AGN contamination for [OII] is $\sim 18.5\%$ and $\sim 19.4\%$ for $z \sim 1.47$ and 2.23, respectively. For $z > 2.2$ in [OII] emitters, we set the AGN contamination constant to that at $z = 2.2$ as this would require going beyond the last IRAC band. Note that these are upper limits for the level of AGN contamination such that our SFRDs are corrected for the highest contamination possible via the 1.6μm bump technique. By comparing our SFRD measurements to other star-formation tracers, we can determine if the AGN correction was too high or not. But to reliably measure the correction will require follow-up spectroscopy of our sample to properly separate the AGN from the star-forming sample. We therefore apply our determined AGN correction to the luminosity densities measured from the fully integrated LFs (decreases the SFRDs) and include 20% of the correction factor in quadrature with the luminosity density errors.

2.4.2 Calibrations

The star-formation rate density is calculated via the luminosity density from the LF at each redshift. The luminosity density is defined as:

$$L = \int_0^\infty \Phi(L) L \mathrm{d}L = \phi^\star L^\star \Gamma(\alpha + 2) \tag{2.5}$$

where L is the luminosity density, $\phi^\star$ is the normalization, $L^\star$ is the characteristic luminosity, and α is the faint-end slope. Our determined luminosity densities are highlighted in table 2.3

and consider the full range of luminosities. The star-formation rate density (SFRD) is then calculated by using the Kennicutt (1998) diagnostics:

$$\dot{\rho}_{\mathrm{SFR,[OII]}} = 1.4 \times 10^{-41} L_{\mathrm{[OII]}} M_{\odot} \mathrm{yr}^{-1} \mathrm{Mpc}^{-3} \tag{2.6}$$

where a $L_{\mathrm{[OII]}}/L_{\mathrm{H}\alpha} = 1.77$ is assumed. We note that using the [OII] SFR calibration comes with several drawbacks, such as metallicity, reddening, and line ratio assumptions, but the [OII] line is the brightest emission-line detectable at $z > 1.5$ where Hα falls in the infrared. We will present the effects of these drawbacks in a future study (Khostovan et al. in prep). Furthermore, we present the uncorrected for dust SFRD measurements to see, qualitatively, the evolution of the SFRD. This means that the results shown in figure 2.8 are lower-limits since any dust correction will just increase the SFRD measurements.

We also use the derived relation of Osterbrock & Ferland (2006):

$$\dot{\rho}_{\mathrm{SFR,H}\beta\mathrm{+[OIII]}} = 7.35 \times 10^{-42} L_{\mathrm{H}\beta\mathrm{+[OIII]}} M_{\odot} \mathrm{yr}^{-1} \mathrm{Mpc}^{-3} \tag{2.7}$$

to measure the Hβ+[OIII] SFRD[4] although this can not be taken as a purely star-forming indicator as there are several caveats behind it. We want to make this point specifically clear; we do not use the Hβ+[OIII] SFRDs in fitting the star-formation and stellar mass assembly history of the Universe. We instead use it to compare the measurements to those of the [OII] SFRDs and other tracers in the literature to show if our sample is tracing a star-forming sample and whether or not if the Hβ+[OIII] calibration is more of a "reliable" tracer of star-formation activity than previously thought.

[4]We used the dust extinction curve of Calzetti et al. (2000) for the Hβ+[OIII] emitters and applied for all redshifts, such that $A_{\mathrm{H}\beta\mathrm{+[OIII]}} = 1.35$ mag (assuming $A_{\mathrm{H}\alpha} = 1.0$ mag).

2.4.3 Star-Formation Rate Density Evolution of [OII] Emitters

2.4.3.1 Uncorrected-for-Dust

Figure 2.8 shows the evolution of the uncorrected-for-dust [OII] SFR density for the first time and determined in a self-consistent way from $z = 0-5$. The evolution is clear and signifies that a peak that occurs at $z \sim 2-3$ and then there is a fall for higher redshifts. We include [OII] measurements from the literature after uncorrecting them for dust and correcting the cosmology (the pre-2000 papers used non-ΛCDM cosmological parameters). These results plus ours can then be taken as a lower limit as any dust extinction correction would increase the SFR densities. We include a compilation of SFR densities and LF parameters from various studies, using various diagnostics, all normalized to the same cosmology as that of this paper, same Kennicutt (1998) calibration with the same line ratio, and all with $A_{[OII]} = 0$ to make it easier for future studies to utilize. This compilation is found in appendix 2.6.3. We find that our $z = 1.47$ [OII] SFRD measurement is in perfect agreement with Sobral et al. (2012) and Ly et al. (2007). We are also in perfect agreement with the measurement of Sobral et al. (2015a) and our $z = 2.23$ measurement.

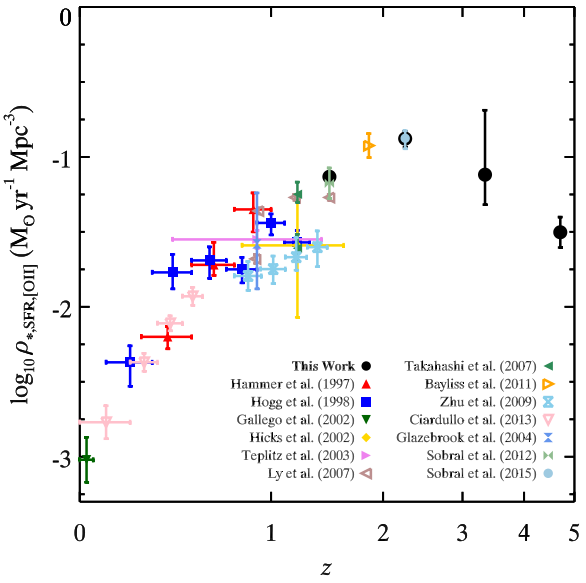

Figure 2.8: The uncorrected for dust SFRD evolution based only on [OII] emission studies. We find that our $z = 1.47$ and 2.25 LF continues the inverse power-law slope that is found from $z = 0-2$ in the majority of SFRD studies, and a continuous drop for $z > 2$. This is the first time that [OII] studies have gone beyond $z \sim 1.5$ in a reasonably, statistically constrained fashion. We find perfect agreement with Sobral et al. (2012) and are 0.15 dex off from Ly et al. (2007). Also, we find perfect agreement with the $z = 2.25$ SFRD of Sobral et al. (2015a).

We note that Bayliss et al. (2012) made a measurement at $z = 4.6$ by observing the GOODS-S

field using the NB2090 and Ks filters of the ESO HAWK-I instrument. The results of this study are restricted to a sample of only 3 genuine emitters. Although ground-breaking at the time, their SFRD estimate is severely limited by issues of sample size and cosmic variance.

2.4.3.2 Dust & AGN Corrected SFRD

To compare with other studies using different SFRD diagnostics, we adopt a dust correction using the HiZELS $z = 1.47$ measurement of Hayashi et al. (2013), $A_{H\alpha} \sim 0.35$ mag. Hayashi et al. (2013) studied Hα and [OII] emitters using HiZELS data to conclude that the traditional $A_{H\alpha} = 1.0$ mag that has been used in the literature is overestimating the dust correction for [OII] emitters at $z = 1.47$, such that these emitters are observed to have $A_{H\alpha} \sim 0.35$ mag and are less dusty than previously thought.

To test the dust extinction coefficient of Hayashi et al. (2013), we apply the traditional $A_{H\alpha} \sim 1.0$ mag to all four [OII] SFRD measurements. We find that based on this dust correction, our measurements overestimate the Hα-based SFRD measurements of Sobral et al. (2013a) and the radio-stacked measurements of Karim et al. (2011), which is impervious to dust extinction. The level of overestimation is such that our $z = 1.47$ SFRD measurement and $z = 2.23$ SFRD measurement was ~ 0.4 dex above the SFRD measurements of Sobral et al. (2013a) and Karim et al. (2011). When using the Hayashi et al. (2013) dust extinction coefficient, we find that our SFRD measurements are perfectly matched with Sobral et al. (2013a) and Karim et al. (2011), as seen in figure 2.9.

We apply the Calzetti correction (Calzetti et al., 2000) with the Hayashi et al. (2013) measurement of $A_{\mathrm{H}\alpha} \sim 0.35$ mag such that:

$$\frac{A_{[\mathrm{OII}]}}{A_{\mathrm{H}\alpha}} = \frac{k([\mathrm{OII}])}{k(\mathrm{H}\alpha)} \tag{2.8}$$

where $k([\mathrm{OII}]) = 5.86$ and $k(\mathrm{H}\alpha) = 3.31$, resulting in $A_{[\mathrm{OII}]} = 0.62$ mag. We calibrate all the measurements to the same [OII] SFR calibration of Kennicutt (1998). All measurements

hereinafter include AGN corrections as discussed in section 2.4.1.

Figure 2.9 shows our dust-corrected and AGN-corrected [OII] SFRD measurements. We also include a large compilation of studies from the literature which is a combination of the compilations of Hopkins & Beacom (2006), Madau & Dickinson (2014), Gunawardhana et al. (2013), Ly et al. (2007), and our own compilation as a comparison (appendix 2.6.3). We find that our measurements accurately reproduce the star-formation history of the universe up to $z \sim 5$. This is the first time that an [OII] study has ever accomplished such a measurement in a self-consistent manner. We find that the $z = 1.47$ and 2.23 perfectly agree with the HiZELS Hα measurements of Sobral et al. (2013a) on figure 2.9. The AGN contamination in Sobral et al. (2013a) assumed a simple $\sim 10\%$, which is backed by a detailed search of potential AGNs by Garn et al. (2010). Based on the similarities between our [OII] measurement and the independently AGN-corrected SFRD measurement of Sobral et al. (2013a), we can conclude that the level of AGN contamination measured is reasonable and the methodology sound.

Another key point is the stacked radio measurements of Karim et al. (2011) (*pink squares* on figure 2.9). The benefit of radio measurements are that they are impervious to dust, but have the downside of poor resolution and blending. We find that our $z = 1.47$ and $z = 2.25$ [OII] measurements are in agreement with Karim et al. (2011), such that the Hayashi et al. (2013) dust extinction coefficient does reliably correct our measurements to represent the dust-corrected SFRD of star-forming galaxies.

We also find an interesting result when comparing the Hβ+[OIII] SFRD measurements to our [OII] SFRDs and other measurements in the literature. As discussed above, the Hβ+[OIII] calibration is considered in the literature as a "mixed" tracer of star-formation activity. Here we find that using the calibration of Osterbrock & Ferland (2006) with a $A_{\mathrm{H}\beta+[\mathrm{OIII}]} = 1.35$ mag (based on the traditional $A_{\mathrm{H}\alpha} = 1$ mag), our Hβ+[OIII] measurement for $z = 0.84$ matches perfectly with the Hα SFRD of Sobral et al. (2013a) and the radio measurement of Karim et al. (2011). The implications of this agreement shows that not only is the dust correction technique

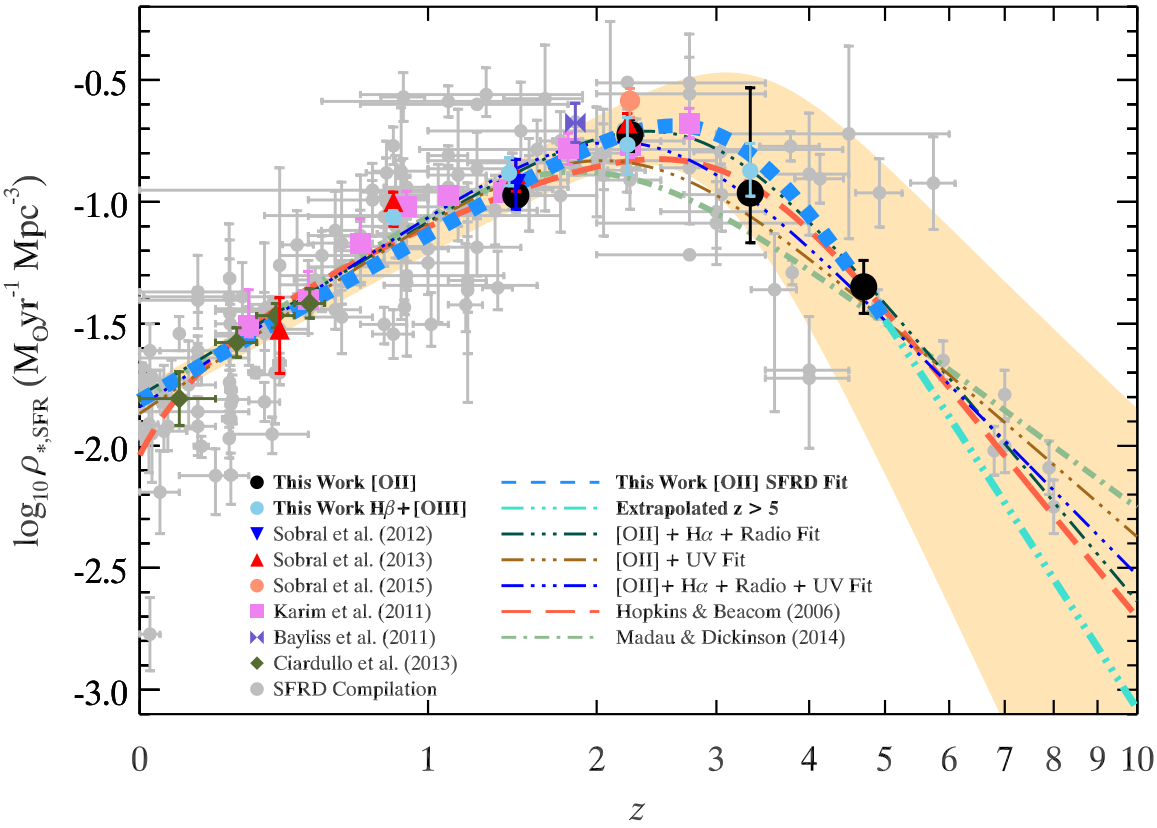

Figure 2.9: Our [OII] dust & AGN corrected SFRD evolution with the [OII] studies of Bayliss et al. (2011); Ciardullo et al. (2013); Sobral et al. (2013a) and Sobral et al. (2015a), along with the results of this paper, that are used to fit the parametrization of Madau & Dickinson (2014). The best fit is shown as the dashed line (*dodger blue*) and is only based on [OII] measurements. We also include an extrapolation to higher-z (*dashed-dotted turquoise* line), as we don't constrain this part of redshift space but can extrapolate based on our fit. The 1-σ region is highlighted in *gold* filled regions around the fit. The stacked radio study of Karim et al. (2011) and the Hα study of Sobral et al. (2013a) are also shown as a comparison and are in agreement with our measurements. Our compilation of SFRD measurements (in *gray*) are a combination of our compilation and that of Hopkins & Beacom (2006), Madau & Dickinson (2014), Ly et al. (2007), and Gunawardhana et al. (2013). We reproduce the SFRD evolution history of the universe based primarily on [OII] studies with the peak of star-formation history occurring at $z \sim 3$. We also include the fits of Hopkins & Beacom (2006) (IMF corrected to Salpeter) and that of Madau & Dickinson (2014). We find that the Hopkins & Beacom (2006) fit reasonably matches our SFRD fit, while the Madau & Dickinson (2014) fits well until $z > 2$. This is mostly because the Madau & Dickinson (2014) fit is driven by the $z > 5$ UV measurements (which are not backed by spectroscopy), for which we do not include in our [OII] fit.

applied correctly, but also that the AGN correction is accurate such that it is matching with the AGN-corrected Hα SFRD of Sobral et al. (2013a). For our $z = 1.43$ Hβ+[OIII] SFRD, we find a perfect match with Karim et al. (2011), Sobral et al. (2012), Sobral et al. (2013a), and our [OII] SFRD. The $z = 2.23$ Hβ+[OIII] SFRD matches well with Karim et al. (2011), Sobral et al. (2012), and our [OII] SFRD measurement. Lastly, we find perfect agreement between our [OII] SFRD and the Hβ+[OIII] SFRD at $z \sim 3.3$. All these perfect agreements hint to the notion that the Hβ+[OIII] SFR calibrations could in fact be more of a reliable tracer of star-formation activity than previously thought. Furthermore, this is also strong evidence to show that our Hβ+[OIII] sample is dominated by star-forming galaxies and is a reliable sample. Also, our survey seems to be detecting Hβ+[OIII] emitters that have more dust in comparison to [OII] emitters such that the traditional $A_{\mathrm{H}\alpha} = 1$ mag applies to the Hβ+[OIII] sample and a lower dust correction applies to the [OII]emitters. This notion was proposed by Hayashi et al. (2013) for their [OII] sample. Their conclusion was that dustier [OII] emitters fall to lower luminosities that are below the detection limit, while the less dusty emitters, which will be apparently brighter, are detected.

We fit the SFRD using our [OII] SFRD measurements along with the [OII] measurements of Bayliss et al. (2011); Ciardullo et al. (2013) and Sobral et al. (2012) to the parametrization of Madau & Dickinson (2014):

$$\log_{10} \dot{\rho}_\star = a \frac{(1+z)^b}{1+[(1+z)/c]^d} \ \mathrm{M}_\odot \ \mathrm{yr}^{-1} \ \mathrm{Mpc}^{-3} \tag{2.9}$$

where our fit results with $a = 0.015 \pm 0.002$, $b = 2.26 \pm 0.20$, $c = 4.07 \pm 0.51$, and $d = 8.39 \pm 2.60$. The fit is purely based on [OII] emitters, but we have also fitted for the cases of [OII]+Hα+Radio, [OII]+UV, and [OII]+Hα+Radio+UV (see figure 2.9) to show how our fit will vary based on the data that we use. Based on the [OII] fit, we see a drop at $z > 3$ that is slightly steeper than those determined by UV dropout studies (i.e., Bouwens et al. 2011, 2014; Oesch et al. 2010; Schenker et al. 2013a). Despite this drop in our [OII] SFRD compared to the UV studies, we do

find that the UV measurements are still within 1σ.

An important note to make though is that prior to this paper, there does not exist a study besides UV/Lyα studies that have measured the SFRD up to $z \sim 5$ since $z \sim 3$. This is a crucial point since there has been no other study so far that could confirm the drop-out measurements, which are severely affected by dust extinction. Furthermore, this is the first time that the cosmic star-formation history has been constrained based on a single tracer for larger volumes and up to $z \sim 5$. Our current measurements are the farthest that we can measure the [OII] SFRD due to the fact that the emission line would go past K-band and into the infrared. Future space-based narrow-band surveys, such as *JWST* and the Wide-field Imaging Surveyor for High-redshift (*WISH*), will be able to probe [OII] emitters up to $z \sim 12$, which would allow us to compare and confirm the UV SFRD measurements at $z > 5$.

We also compare our fit to those of Hopkins & Beacom (2006) and Madau & Dickinson (2014) in figure 2.9. For the $z < 2$ regime, we find that our [OII] SFRD fit agrees well with all the other fits. For the $z > 2$ regime, we do see divergences based on the fit. In terms of the actual data points, we find that the Hopkins & Beacom (2006) is closest in agreement as it has a continuing SFRD up to a peak at $z \sim 2.5$ and a drop that continues through the high-z [OII] measurements. The Madau & Dickinson (2014) is also in agreement for the high-z measurements, but fails to match with the $z \sim 2-3$ peak. This is mostly due to the fact that their measurements are driven by the $z > 5$ UV dropout SFRDs (e.g., Bouwens et al. 2011, 2014; Oesch et al. 2010; Schenker et al. 2013a).

As with all SFR measurements, there are systematic uncertainties that must be taken into account. In the case of [OII] emitters, our main systematic uncertainties come from metallicity and dust extinction. To study the metallicities and its effects on the star-formation rate calibration, we will need to conduct follow-up spectroscopy. Furthermore, studying the metallicity of our sample will give us also an understanding of the dynamics (inflow/outflow) that can affect star-formation activity. We also plan to study in a future paper the dust extinction

properties of our sample and how it relates to and affects the star-formation activity of galaxies in our sample (Khostovan et al., in prep).

2.4.4 Evolution of the Stellar Mass Density

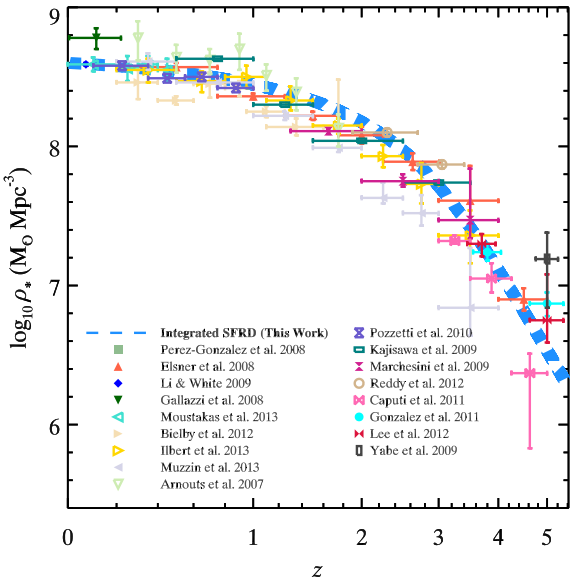

Figure 2.10: The evolution of the stellar mass density of the Universe based on the integrated [OII] SFRD. Overlaid are the SMD measurements from the literature that were compiled in the recent review of Madau & Dickinson (2014). We find that our integration of the purely [OII] determined SFRD reasonably traces the stellar mass assembly of the Universe.

We use the [OII] SFRD results presented in this paper to provide an estimate of the stellar mass density (SMD) evolution by doing a time-integral of equation 2.9. The SMD evolution gives us an understanding of how the universe has assembled its mass throughout cosmic time. This estimate is quantitatively sensitive to the choice of the IMF in terms of the normalization of the SFRD and SMD evolution, but it does not qualitatively affect the final results.

Our estimate assumes a Salpeter IMF, which has been used throughout this entire paper, and a recycling fraction of $R = 0.27$. For a review of the derivation of this factor, we refer the reader to the recent review of Madau & Dickinson (2014). We calculate the SMD by:

$$\rho_\star(z) = (1-R)\int_z^\infty \frac{\dot{\rho}_\star(z)}{H_0(1+z)\sqrt{\Omega_M(1+z)^3+\Omega_\Lambda}}dz \tag{2.10}$$

where $\dot{\rho}_\star(z)$ is the SFRD fit using the parametrization defined in equation 2.9 and R is the recycling fraction, or the fraction of stars that is returned back into the ISM and IGM. Because the equation above is using $z = \infty$ as a reference for which we do not know the SMD for, we

instead constrain the integral such that at $z = 0$ the SMD will be $\log_{10}\rho_\star \sim 8.6\ M_\odot\ Mpc^{-3}$, in agreement with measurements made at that redshift.

Our results are shown in figure 3.5. We find an evolution where the stellar mass assembly rapidly increases from $10^{6.2}$ to $10^8\ M_\odot\ Mpc^{-3}$ from $z \sim 5$ to 2, a time frame of only 2 Gyr. The evolution then tapers and flattens out by $z = 0$ which is related to the decrease in the SFRD that we have observed since $z \sim 2$. This is also the same conclusion found by observational studies of the SMD. We include measurements from Arnouts et al. (2007), Elsner et al. (2008), Gallazzi et al. (2008), Pérez-González et al. (2008), Kajisawa et al. (2009), Li & White (2009), Marchesini et al. (2009), Yabe et al. (2009), Pozzetti et al. (2010), Caputi et al. (2011), González et al. (2011), Bielby et al. (2012), Lee et al. (2012), Reddy et al. (2012), Ilbert et al. (2013), Moustakas et al. (2013), and Muzzin et al. (2013) in figure 3.5 and we find that our integrated SFRD reproduces the same evolution seen by these studies. We have found that the [OII] based SFRD and SMD accurately reproduce the evolution of mass assembly in the Universe. This match can also be seen as yet another verification that our sample of [OII] emitters are primarily star-forming galaxies as the conclusions from our SMD estimate are the same seen in the literature.

2.5 Conclusions

We have presented the largest sample of Hβ+[OIII] and [OII] emitters between $z \sim 0.8 - 5$ that have been selected based on a robust and self-consistent technique, backed up by a wide array of spectroscopic emitters. We have used the HiZELS UKIRT and Subaru narrow-band catalogs, along with multi-wavelength data from the COSMOS and UDS fields, to create a clean and well-defined sample of star-forming galaxies. The main results of this paper are as follows:

1. We have robustly selected a total of 2477, 371 , 270, 179 Hβ+[OIII] emitters at $z = 0.84$,

1.42, 2.23, and 3.24 and 3285, 137, 35, 18 [OII] emitters at $z = 1.47$, 2.25, 3.34, and 4.69 in the combined COSMOS and UDS fields. These are the largest samples of Hβ+[OIII] and [OII] emitters to have been detected in this redshift range.

2. We have extended the luminosity function in the literature to higher-z, as well as refined the lower-z measurements for both types of emitters. For the Hβ+[OIII] emitters, we find that the bright-end of our $z = 1.42$ and $z = 2.23$ LFs are in agreement with the grism spectroscopy-based luminosity functions of Colbert et al. (2013); hence, this increases the reliability of our sample being dominantly [OIII] emitters in the bright-end. We also find from our predictions of the [OIII] LFs that our sample is dominated by [OIII] emitters at the bright-end. The faint-end is dominated by Hβ emitters. We also find that the normalization of the [OIII] LFs are the same such that the relative contribution of Hβ emitters is the same between $z \sim 0.8 - 2.2$.

3. The evolution of $L^\star$ and $\phi^\star$ for Hβ+[OIII] is found to have a strong increasing/decreasing evolution, respectively, up to $z \sim 3$. For our [OII] sample, we find that $L^\star$ increases strongly up to $z \sim 5$ and $\phi^\star$ is strongly dropping up to the same redshift.

4. We have discussed that our luminosity functions are reliable to be used in making predictions of the number of emitters to be detected by future wide-surveys, such as *Euclid* and WFIRST. Furthermore, our luminosity functions can also determine the number of low-z interlopers in Lyα studies, such that the level of contamination by low-z sources can be reduced in such studies.

5. The SFRD has been constrained using [OII] measurements up to $z \sim 5$ for the first time. We find that the peak of the cosmic SFRD is located around $z \sim 3$ and is in agreement with our large compilation of UV, IR, radio, and nebular emission studies. We find that for $z > 2$, our SFRD fit drops slightly faster in comparison to the UV dropout studies in this redshift

regime. However, we find that the UV measurements are within the 1-σ error bar range of our SFRD fit. Future space-based narrow-band surveys, such as *JWST* and *WISH*, will be able to extend the range of [OII] detection out to $z \sim 12$ so that we can compare and confirm or invalidate the UV dropout measurements.

6. We also find that the Hβ+[OIII] SFRD measurements are nicely in line with our [OII] sample and other star-formation tracers. This then brings to question of whether the Hβ+[OIII] calibration is more "reliable" as a tracer of star-formation than previously thought. With our large sample of these emitters, we will have the ability to explore this issue in detail.

7. By integrating the SFRD, we have made estimates of the stellar mass density evolution and find that it steeply rose up to $z \sim 2$ and flattened out up to the present-day. This is also confirmed by the wealth of measurements in the literature.

The results in the paper have implications in the evolution of galaxies and the star-formation activity occurring in said galaxies. Despite the robustness of our sample, there is still room for improvement. Our measurements have done well to constrain the bright-end, while keeping the faint-end fixed based on measurements from the literature. We will require deeper narrow-band and broad-band measurements in order to constrain the faint-end slope of the LF. Spectroscopic follow-up will also be necessary to accurately measure the extent of AGN contamination in our sample. Although, our color-color selections have shown (see figure 2.11) that they are quite reliable due to the large set of spectroscopic measurements confirming this reliability. That being said, spectroscopic measurements of our sample will help in separating the Hβ and [OIII] samples to measure separate luminosity functions. Lastly, future narrow-band surveys, such as the proposed *WISH* telescope, will be able to extend the redshift window of Hβ+[OIII] and [OII] studies up to $z \sim 12$, which can be used to confirm the UV dropout studies at higher-z. Despite all these improvements and potential future progresses, our sample has reliably (given all the limitations) and robustly traced the evolution of star-forming activity in the universe.

Table 2.4: Definitions of the Color-Color Selection

Filter	Color-Color	Emitter	Redshift	Selection Criteria
NB921	$BRiK$	Hβ+[OIII]	0.84	$-0.3 < (B-R) < 0.08$ & $(i-K) < 2.04(B-R)+0.81$
				$0.08 < (B-R) < 1$ & $1.6(B-R) < (i-K) < 2.04(B-R)+0.81$
				$1 < (B-R) < 1.24$ & $1.6(B-R) < (i-K) < 3.21$
				$1.24 < (B-R)$ & $2.01 < (i-K) < 3.21$
		[OII]	1.47	$(B-R) < -0.3$
				$-0.3 < (B-R) < 1.17$ & $(i-K) > 2.04(B-R)+0.81$
				$(B-R) > 1.17$ & $(i-K) > 3.21$
NBJ	BzK	Hβ+[OIII] & [OII]		$(B-z) < 0.4$
				$0.4 < (B-z) < 2.41$ & $(z-K) > (B-z)-0.4$
				$2.41 < (B-z)$ & $(z-K) > 2.0$
	izK	Hβ+[OIII]	1.42	$(z-K) < 5(i-z)-0.4$
		[OII]	2.25	$(z-K) > 5(i-z)-0.4$
NBH	BzK	Hβ+[OIII]	2.23	$(B-z) < 0.4$
				$0.4 < (B-z) < 2.41$ & $(z-K) > (B-z)-0.4$
				$2.41 < (B-z)$ & $(z-K) > 2.0$
	izK	Hβ+[OIII]	2.23	$(z-K) > 5(i-z)-0.4$
	UVz	[OII]	3.34	$(U-V) > 1.2$ & $(U-V) > 0.5(V-z)+1.2$ & $(V-z) < 1.6$
NBK	UVz	Hβ+[OIII]	3.24	$(U-V) > 1.2$ & $(U-V) > 0.5(V-z)+1.2$ & $(V-z) < 1.6$
	Viz	[OII]	4.69	$(V-i) > 1.2$ & $(V-i) > 0.89(i-z)+1.2$ & $(i-z) < 1.3$

2.6 Appendix

2.6.1 Selection Technique

Here, we present, in detail, the selection of emitters that made it in to our sample. We also present the exact color-color selections that were applied in our work in table 2.4.

2.6.1.1 Hβ+[OIII] Emitters at $z \sim 0.8$

Hβ+[OIII] sources in the NB921 data at $z \sim 0.8$ are selected by their photometric redshifts within the range of $0.75 < z_{phot} < 0.95$. The color-color selection criterion reduces the number of

contaminants by separating the Hβ+[OIII] emitters from lower-z Hα and higher-z [OII] emitters. This is done by using the $BRiK$ selection (Sobral et al., 2009) in figure 2.11. Spectroscopic redshifts were used to assess the robustness and effectiveness of the selection criteria. 213 sources were spectroscopically confirmed. 169 were selected by the color-color selection. From the 213 sources (for which all were selected by their photo-z), only 11 were confirmed Hβ4861, 76 were [OIII]4959, and 126 were [OIII]5007 emitters. Removed from the sample where 9 low-z and 13 high-z spectroscopically confirmed emitters. The lower-z emitters were primarily Hα and [NII]. The higher-z emitters were primarily [OII] emitters. All these misidentified emitters were removed from the sample. Based on the spectroscopic data, we find that $\sim$91% of all spectroscopic measurements for photo-z selected objects were either Hβ or [OIII] emitters and that the $BRiK$ color-color selection does select $\sim$91% of all the Hβ+[OIII] spectroscopically confirmed emitters. In total, we have 2477 $z = 0.84$ Hβ+[OIII] emitters in our sample. Based on the spectroscopic data, we find that the color-color selection effectively selects Hβ+[OIII] emitters with a completeness of $\sim$91%, making our sample not just the largest, but the most complete sample of Hβ+[OIII] emitters to date.

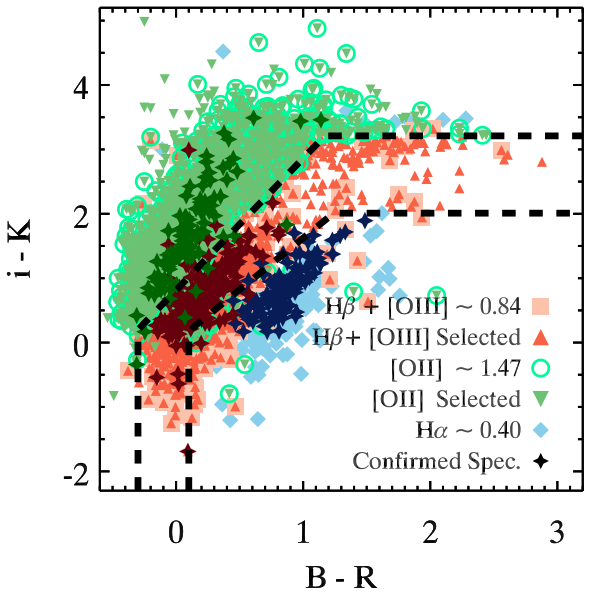

Figure 2.11: The $i-K$ versus $B-R$ color-color distribution of NB921 emitters using the color-color selection of Sobral et al. (2013a). Overall, the level of completeness is >90% as the large majority of spectroscopically confirmed emitters are within the selection area; hence, we confirm the the $BRiK$ selection of Sobral et al. (2009) is very efficient in selecting Hα, Hβ+[OIII], and [OII] samples from narrow-band surveys.

2.6.1.2 Hβ+[OIII] & [OII] Emitters at $z \sim 1.5$

[OII] emitters in NB921 are selected with photometric redshifts between $1.2 < z_{phot} < 1.7$. We use the $BRiK$ color-color selection and include any sources with spectroscopic redshifts. Included in our sample are 97 spectroscopically confirmed sources, with 90 of them being color-color selected as well. Removed from the sample were 48 low-z spectroscopically confirmed emitters, for which the majority were [OIII]. We also removed a few Hesc i emitters at $z \sim 1.28$ and Hα, and [NII] emitters ($z \sim 0.4$). The contamination from high-z emitters was significantly less (8 emitters) as there are no major emission lines beyond [OII]. The majority of this contamination came from [MgII] emitters at $z = 2.25$. The issue of contamination arises here as we may "naively" state that our level of contamination is $\sim 33\%$, but it is noted that spectroscopic measurements to date have an inherent bias to the low-z regime, such that there are more low-z than high-z measurements. This makes accurately measuring the level of contamination difficult. We note though that our color-color selection did select $\sim 93\%$ of the spectroscopically confirmed emitters. In total, we have selected 3285 $z = 1.47$ [OII] emitters. This is by far the largest sample of [OII] emitters at $z \sim 1.5$ to date and, based on the spectroscopically confirmed sources, is $\sim 93\%$ complete.

Hβ+[OIII] emitters in NBJ are selected based on a photometric redshift range of $1.20 < z_{phot} < 1.70$. The color-color selection criteria consists of a BzK and izK selection, as shown in figure 2.12. We use the BzK selection to get our initial sample of emitters and remove the lower-z contaminants, which are mostly Hα emitters. To remove the higher-z contaminants ([OII]), we use the izK selection. There were also 15 spectroscopically confirmed sources, all of which were within our color-color selection. Of these 15 emitters, 4 were Hβ, 5 [OIII]4959, and 6 [OIII]5007 emitters. We removed 5 emitters that were spectroscopically confirmed. These emitters were primarily Hα and [NII], all of which were removed from the sample. Our final sample consists of 371 Hβ+[OIII] emitters at $z = 1.47$ that were selected.

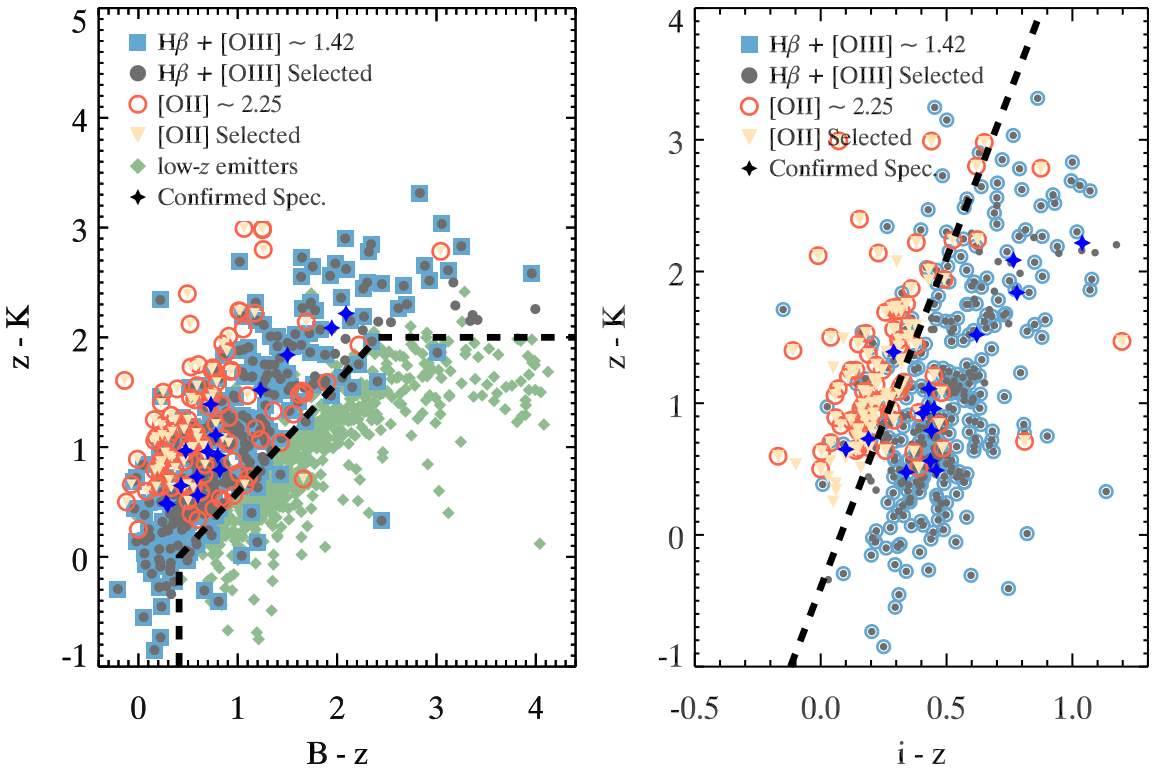

Figure 2.12: Color-color magnitude distributions for all NBJ emitters. *Left:* The $z-K$ versus $B-z$ selection used to separate the Hβ+[OIII] emitters at $z\sim1.47$ and [OII] emitters at $z\sim2.23$ from the low-z emitters that are primarily Hα. *Right:* The $z-K$ versus $i-z$ selection is used to select [OII] and Hβ+[OIII] emitters. For both selections, the spectroscopically confirmed emitters lie within the selection region adding to completeness of the sample. Both color-color selections nicely distinguish between the two samples. We note that for the izK selection, about $\sim15\%$ of selected [OII] emitters are within the selection region of Hβ+[OIII] emitters. These are photo-z selected and shows that relying on purely the color-color selection would show a $\sim15\%$ drop in the completeness of the [OII] sample, and a $\sim15\%$ increase in the contamination of the Hβ+[OIII] sample.

2.6.1.3 Hβ+[OIII] & [OII] Emitters at $z\sim2.2$

[OII] emitters in NBJ are selected if their photometric redshifts are between $1.7<z_{phot}<2.8$. We apply the BzK color-color selection to remove the lower-z contaminants, which are primarily Hα emitters, as shown in figure 2.12. We then use the izK color-color selection to separate the sample from Hβ+[OIII] emitters. There were no spectroscopically confirmed sources included in the sample. Removed from the sample were 3 contaminants, which were all low-z emitters (1 [NII], 1 [OIII], and 1 HeI). In total, there are 137 [OII] emitters selected at $z=2.25$.

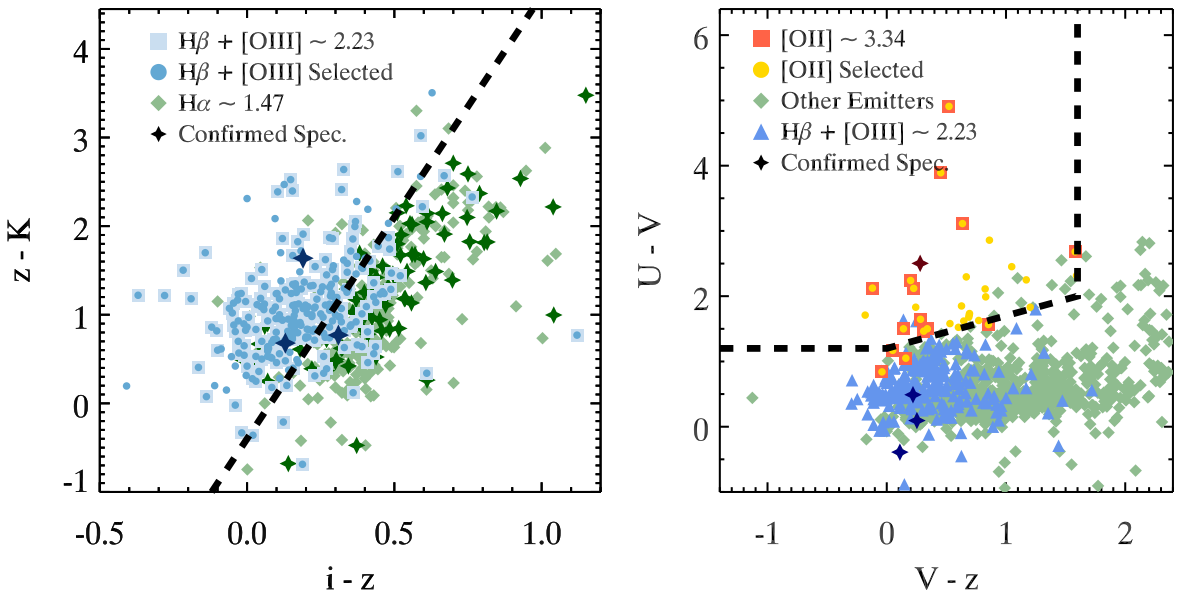

Figure 2.13: Color-color magnitude distributions of all NBH emitters. *Left:* The $z-K$ versus $i-z$ color-color selection used to separate the Hβ+[OIII] $z\sim2.23$ emitters from the Hα $z\sim1.47$ emitters (selected based on the methodology of Sobral et al. 2013a). We have highlighted the spectroscopically confirmed emitters. The color-color selection shows a clear separation between Hβ and Hα measurements based on spectroscopic measurements alone. We find that 21% of our photo-z selected Hβ+[OIII] emitters are within the selection area for Hα emitter, showing that relying on just color-color selection would result in the loss of $\sim$56 emitters from the sample and an increase in contamination of the Hα sample. *Right:* The $U-V$ versus $V-z$ color-color selection that is based on the Lyman break drop-out technique and is used to find $z\sim3.3$ [OII] emitters. We also include the Hβ+[OIII] sample and show that the vast majority of these emitters are outside the [OII] color-color selection region.

Hβ+[OIII] emitters at $z\sim2.2$ in NBH are selected with photometric redshifts between $1.7<z_{phot}<2.8$ along with BzK and izK color-color selections. We apply the BzK color-color selection to remove emitters with $z\lesssim1.5$ (primarily the $z=1.47$ Hα emitters) and then apply the izK color-color selection (shown in figure 2.13) to separate our Hβ+[OIII] sample from the $z=1.47$ Hα emitters. We find that 21% of our sample is outside the color-color region in figure 2.13 but is still selected via the photo-z selection. This would raise concerns about the reliability of the color-color selection, but we must point out that it is reliable in terms of the separation between the Hβ+[OIII] and Hα spectroscopically confirmed emitters. This also raises the point that we are more concerned with consistency in the use of selection techniques to

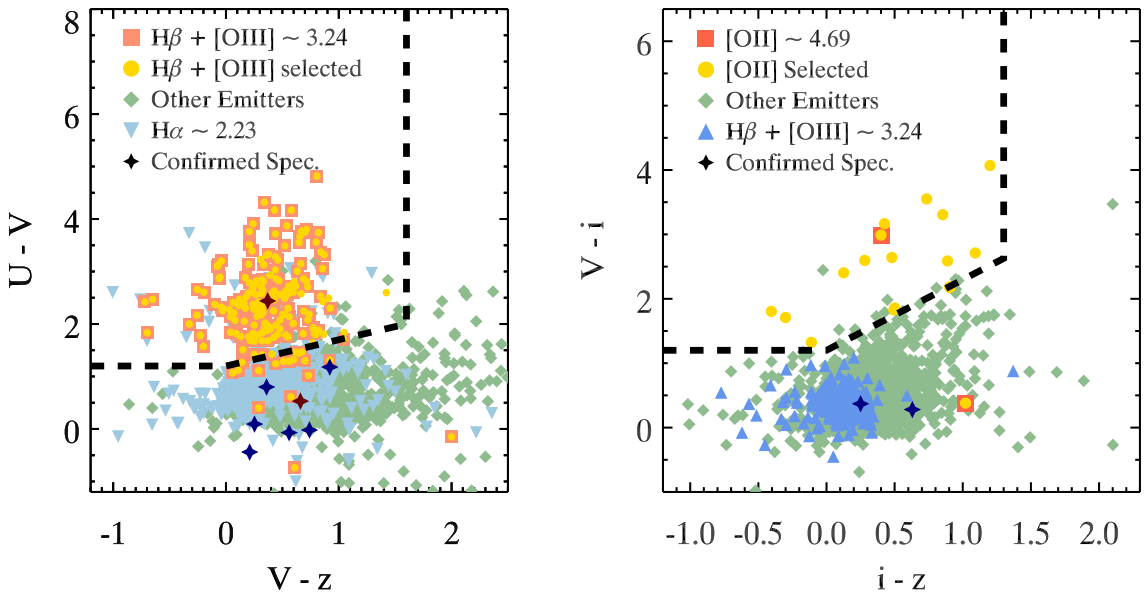

Figure 2.14: Color-color magnitude distributions of all NBK emitters. *Left:* shows the $U-V$ versus $V-z$ color-color selection used to find $z\sim3.3$ Hβ+[OIII] emitters based on the Lyman break drop-out technique. We also include the Hα emitters ($z\sim2.23$) and find that this selection reliably separates the two samples. *Right:* shows the $V-i$ versus $i-z$ color-color selection used to find $z\sim4.7$ [OII] emitters based also on the Lyman break drop-out technique. We include the Hβ+[OIII] sample to show that this selection criteria is reliable to separate the two samples. We find no Hβ+[OIII] emitter falling within the [OII] color-color region.

reduce the effects of assumptions in our sample. Furthermore, this also shows that we can not rely on the color-color selection technique alone to select emitters since this would result in a 21% drop in Hβ+[OIII] emitters and a 21% increase in the contamination of the Hα sample in Sobral et al. (2013a). By including the photo-z in our selection methodology, we reduce the level of contaminants and also increase the reliability of the sample. We also included three spectroscopically confirmed sources in the sample that were selected by their color-color selection. Of these 3, we have two [OIII]4959 and one [OIII]5007 emitter. Removed from the sample were 3 low-z spectroscopically confirmed emitters (Hα at $z\sim1.47$). There were no high-z spectroscopic measurements that contaminated the sample. A total of 271 Hβ+[OIII] emitters at $z=2.23$ were selected.

2.6.1.4 Hβ+[OIII] & [OII] Emitters at $z \sim 3.3$

[OII] emitters at $z = 3.3$ in NBH are selected if $2.8 < z_{phot} < 4$. We also select sources if they satisfy the UVz color-color criteria. This separates the lower-z contaminants from our sample. We include our Hβ+[OIII] sample in figure 2.13 to show the separation between the [OII] and Hβ+[OIII] sample and find that the UVz selection is reliable in selecting our [OII] sample. Furthermore, as there are no major emission lines that are detected at higher-z, there is no need to include another color-color criteria to account for this contamination. As shown in fig. 2.2, the number of sources greatly drops at higher-z for the redshift of interest, making the number of contaminants very small. There was only one spectroscopically confirmed source that was included in the sample and only found in COSMOS. The UVz color of this emitter places it well within the selection area, adding to the reliability of our color-color selection. No spectroscopic confirmed emitters were misidentified in the selection. In total, there are 35 of [OII] emitters at $z = 3.3$ selected.

Our Hβ+[OIII] emitters at $z = 3.3$ in NBK are selected if their photometric redshifts lie between $2.8 < z_{phot} < 4$. We use a UVz selection criteria, as shown in figure 2.13, to select Hβ+[OIII] emitters based on the Lyman break dropout technique. Sources with no detection bluer than the U-band and detection in the V and z bands greater than the 5σ magnitude detection limits were included. We also include all Hα emitters with photo-z around $z = 2.23$ in figure 2.14 to show the separation between them and our Hβ+[OIII] selected emitters. One spectroscopically confirmed source was also included in the sample from UDS. We find that this spectroscopically confirmed emitter is well within the color-color region. No spectroscopic confirmed emitters were misidentified in the selection. A total of 179 Hβ+[OIII] emitters at $z = 3.3$ were selected.

2.6.1.5 [OII] emitters at $z \sim 4.7$

We select our [OII] emitters in NBK if they have a photometric redshift between $4.0 < z_{phot} < 6.0$. Emitters are also selected by using the Viz criteria of Stark et al. (2009) for V-band dropouts. The color-color selection is shown in figure 2.14 and includes our Hβ+[OIII] sample. We find that there are no Hβ+[OIII] emitters within the [OII] selection area, which adds to the reliability of our sample. We find only one emitter was selected by its photo-z within the selection range and it is well within the color-color selection region. The majority of emitters were selected by the color-color selection. All sources selected were also under the condition that anything bluer than V-band must have no detection. A study of [OII] emitters by Bayliss et al. (2012) also used a similar technique using the BVz criteria of Stark et al. (2009) for their $z \sim 4.6$ sample. It must be noted though that the results of this study should not be taken as reliable due to the fact that they were limited to a sample size of only 3 [OII] emitters (about 3 times smaller than our sample) and the volume probed by this study is a factor of 100 times smaller than our study making it severely susceptible to cosmic variance. Our sample is statistically larger and robust in comparison to Bayliss et al. (2012). There were no spectroscopically confirmed sources in our sample and no spectroscopic confirmed emitters were misidentified in the selection, thus, giving a total of 18 [OII] emitters at $z = 4.5$ that were selected.

2.6.1.6 Notes on Contamination

We advise the reader that the measurements of contamination are *not* strictly reliable for the Hβ+[OIII] $z \sim 1.5$ emitters due to the bias in the spectroscopic redshift distribution. Two issues arise are: (1) lack of spectroscopic measurements at higher redshifts to properly quantify the level of contamination, and (2) the inherent bias of spectroscopic measurements to the lower-z regime. The first point really just requires more spectroscopic measurements to increase the population of spectroscopically confirmed sources. The second point has to do with the distribution of spec-z measurements. There exists more spec-z measurements for $z < 1$, which results in a skewed

histogram that favors the lower-z regime. When measuring the level of contamination, there are more low-z measurements than spectroscopically confirmed measurements (for example, $z = 1.47$ [OII]) which causes a "naive" and biased estimation of the level of contamination. Instead, we considered where the spectroscopically confirmed Hβ+[OIII] and [OII] measurements were on the color-color diagrams as a way to assess the reliability of our selection technique.

Based on the points described above, we can measure the level of contamination for the Hβ+[OIII] $z \sim 0.84$ sample ($\sim 10\%$). To robustly measure the contamination for the higher-z samples, we will need to conduct spectroscopic follow-up which is currently underway with Keck/MOSFIRE and ESO/VLT (Khostovan et al., in prep).

2.6.2 Binned Luminosity Function

Here we include two tables that show the binned data points of the LF that are plotted in figures 2.4 and 2.6. We include these plots as a convenience for future studies who wish to compare their LFs to ours.

2.6.3 Star-Formation Rate Density Compilation

In this section, we have compiled a table of the star-formation rate densities from different diagnostics spread over a wide redshift range. Because each study has its own set of assumptions, diagnostics, calibrations, dust corrections,etc. it is quite confusing in keeping track of which study has used which set of assumptions. Let alone, for the earliest papers, we have to even take into account the different cosmologies. To make life much easier for you as the reader who may be interested in studying the evolution of the cosmic SFR density, we have included in the appendix a long table which is our compilation of the SFR densities and luminosity function parameters from a range of different studies. Parts of this table are from Ly et al. (2007), but updated with the latest measurements.

Table 2.5: Hβ+[OIII] Luminosity Function. Φ_{obs} shows the observed LF data points per bin; simply, it is the log of the number of emitters divided by the volume. Φ_{final} is the completeness and filter profile corrected luminosity data points per bin. The errors here are Poissonian but with 20% of the corrections added in quadrature.

$\log_{10} L_{\mathrm{H}\beta+[\mathrm{OIII}]}$ (erg s^{-1})	#	Φ_{obs} (Mpc^{-3} d$\log_{10}$L)	Φ_{final} (Mpc^{-3} d$\log_{10}$L)	Volume (10^5 Mpc^3)
$z = 0.84$				
41.10 ± 0.10	703	-1.97	-1.82 ± 0.02	3.25
41.30 ± 0.10	465	-2.15	-2.04 ± 0.03	3.25
41.50 ± 0.10	262	-2.39	-2.35 ± 0.04	3.25
41.70 ± 0.10	128	-2.71	-2.61 ± 0.06	3.25
41.90 ± 0.10	68	-2.98	-2.94 ± 0.08	3.25
42.10 ± 0.10	28	-3.37	-3.17 ± 0.13	3.25
42.30 ± 0.10	12	-3.73	-3.52 ± 0.20	3.25
42.50 ± 0.10	3	-4.34	-4.12 ± 0.39	3.25
$z = 1.42$				
41.95 ± 0.15	284	-2.63	-2.49 ± 0.03	4.06
42.25 ± 0.15	73	-3.22	-3.14 ± 0.07	4.06
42.55 ± 0.15	12	-4.01	-3.89 ± 0.19	4.06
42.85 ± 0.15	2	-4.78	-4.64 ± 0.48	4.06
$z = 2.23$				
42.60 ± 0.075	84	-3.27	-3.08 ± 0.06	10.46
42.75 ± 0.075	70	-3.36	-3.14 ± 0.07	10.69
42.90 ± 0.075	22	-3.86	-3.65 ± 0.13	10.69
43.05 ± 0.075	5	-4.51	-4.26 ± 0.29	10.69
$z = 3.24$				
42.65 ± 0.075	70	-3.33	-3.17 ± 0.07	9.99
42.80 ± 0.075	52	-3.48	-3.26 ± 0.09	10.48
42.95 ± 0.075	25	-3.80	-3.55 ± 0.13	10.48
43.10 ± 0.075	6	-4.42	-4.17 ± 0.27	10.48

Table 2.6: [OII] Luminosity Function. Φ_{obs} shows the observed LF data points per bin; simply, it is the log of the number of emitters divided by the volume. Φ_{final} is the completeness and filter profile corrected luminosity data points per bin. The errors here are Poissonian but with 20% of the corrections added in quadrature.

$\log_{10} L_{[\mathrm{OII}]}$ (erg s^{-1})	#	Φ_{obs} (Mpc^{-3} d$\log_{10}$L)	Φ_{final} (Mpc^{-3} d$\log_{10}$L)	Volume (10^5 Mpc^3)
***z* = 1.47**				
41.65 ± 0.075	590	-2.24	-2.08 ± 0.02	6.80
41.80 ± 0.075	425	-2.38	-2.28 ± 0.03	6.80
41.95 ± 0.075	257	-2.60	-2.46 ± 0.04	6.80
42.10 ± 0.075	127	-2.90	-2.69 ± 0.06	6.80
42.25 ± 0.075	42	-3.39	-3.05 ± 0.10	6.80
42.40 ± 0.075	19	-3.73	-3.55 ± 0.15	6.80
42.55 ± 0.075	6	-4.23	-4.23 ± 0.28	6.80
***z* = 2.25**				
42.45 ± 0.10	92	-3.14	-2.77 ± 0.05	6.29
42.65 ± 0.10	37	-3.53	-3.15 ± 0.08	6.29
42.85 ± 0.10	3	-4.62	-4.46 ± 0.35	6.29
***z* = 3.34**				
43.05 ± 0.050	12	-4.12	-3.86 ± 0.17	15.88
43.15 ± 0.075	7	-4.37	-3.92 ± 0.24	16.52
43.30 ± 0.075	2	-5.22	-4.87 ± 0.48	16.52
***z* = 4.69**				
42.86 ± 0.075	10	-4.26	-3.66 ± 0.09	12.22
43.01 ± 0.075	5	-4.56	-3.93 ± 0.13	12.22
43.16 ± 0.075	2	-4.96	-4.11 ± 0.16	12.22

Table 2.7: SFRD Compilation

Study	z	Diagnostic	Observed			$\log_{10}\dot{\rho}_\star$
			$\log_{10}\phi_\star$	$\log_{10}L_\star$	α	
			Mpc^{-3}	erg s^{-1}		$\mathrm{M}_\odot\ \mathrm{yr}^{-1}\ \mathrm{Mpc}^{-3}$
Ciardullo et al. 2013	$0.0-0.2$	[OII]	$-2.30^{+0.09}_{-0.11}$	$40.32^{+0.18}_{-0.16}$	-1.2	-2.05 ± 0.11
	$0.2-0.325$	[OII]	$-2.12^{+0.05}_{-0.06}$	40.54 ± 0.11	-1.2	-1.82 ± 0.06
	$0.325-0.45$	[OII]	$-2.07^{+0.04}_{-0.05}$	$40.75^{+0.08}_{-0.10}$	-1.2	-1.71 ± 0.05
	$0.45-0.56$	[OII]	$-2.07^{+0.03}_{-0.08}$	$40.93^{+0.08}_{-0.12}$	-1.2	-1.66 ± 0.06
Sobral et al. 2012	1.47	[OII]	-2.01 ± 0.10	41.71 ± 0.09	-0.9 ± 0.2	-1.48 ± 0.10
Bayliss et al. 2011	1.85	[OII]	-2.23 ± 0.09	41.31 ± 0.06	-1.3 ± 0.2	-0.92 ± 0.08
Ly et al. 2007	0.89	[OII]	-2.25 ± 0.13	41.33 ± 0.09	-1.27 ± 0.14	-1.68 ± 0.03
	0.91	[OII]	-1.97 ± 0.09	41.40 ± 0.07	-1.20 ± 0.10	-1.36 ± 0.02
	1.18	[OII]	-2.20 ± 0.10	41.74 ± 0.07	-1.15 ± 0.11	-1.27 ± 0.02
	1.47	[OII]	-1.97 ± 0.06	41.60 ± 0.05	-0.78 ± 0.13	-1.27 ± 0.02
Zhu et al. 2009	0.84	[OII]	...	...	...	$-1.79^{+0.10}_{-0.10}$
	1.02	[OII]	...	...	...	$-1.75^{+0.13}_{-0.08}$
	1.19	[OII]	...	...	...	$-1.67^{+0.25}_{-0.11}$
	1.37	[OII]	...	...	...	$-1.60^{+0.16}_{-0.09}$
Takahashi et al. 2007	$1.71-1.203$	[OII]	$-2.37^{+0.10}_{-0.12}$	$41.79^{+0.07}_{-0.06}$	$-1.41^{+0.16}_{-0.15}$	$-1.25^{+0.05}_{-0.08}$
	$1.71-1.203$	[OII]	$-2.67^{+0.28}_{-0.49}$	$41.75^{+0.32}_{-0.20}$	$-1.38^{+0.40}_{-0.37}$	$-1.61^{+0.09}_{-0.28}$
Glazebrook et al. 2004	0.90	[OII]	-2.91	42.30	-1.3	$-1.35^{+0.34}_{-0.30}$
Teplitz et al. 2003	0.90 ± 0.50	[OII]	-3.06 ± 0.12	42.15 ± 0.08	-1.35	-1.55 ± 0.06
Gallego et al. 2002	0.025 ± 0.025	[OII]	-3.48 ± 0.19	41.24 ± 0.13	-1.21 ± 0.21	-3.02 ± 0.15
Hicks et al. 2002	1.20 ± 0.40	[OII]	...	...	...	$-1.59^{+0.30}_{-0.48}$
Hogg et al. 1998	0.20 ± 0.10	[OII]	...	...	...	$-2.37^{+0.11}_{-0.16}$
	0.40 ± 0.10	[OII]	...	...	...	$-1.77^{+0.09}_{-0.12}$
	0.60 ± 0.10	[OII]	...	...	...	$-1.69^{+0.06}_{-0.08}$
	0.80 ± 0.10	[OII]	...	...	...	$-1.75^{+0.07}_{-0.08}$
	1.00 ± 0.10	[OII]	...	...	...	$-1.44^{+0.09}_{-0.11}$
	1.20 ± 0.10	[OII]	...	...	...	$-1.57^{+0.18}_{-0.30}$
Hammer et al. 1997	0.375 ± 0.125	[OII]	...	...	...	$-2.20^{+0.07}_{-0.08}$
	0.625 ± 0.125	[OII]	...	...	...	$-1.72^{+0.11}_{-0.15}$
	0.875 ± 0.125	[OII]	...	...	...	$-1.35^{+0.20}_{-0.38}$
Colbert et al. 2013	$0.7-1.5$	[OIII]	-3.19 ± 0.09	42.34 ± 0.06	-1.40 ± 0.15	...
	$1.5-2.3$	[OIII]	-3.74 ± 0.43	42.91 ± 0.37	-1.67 ± 0.78	...
	$0.7-1.5$	[OIII]	-3.28 ± 0.09	42.39 ± 0.08	-1.50	...
	$1.5-2.3$	[OIII]	-3.60 ± 0.14	42.83 ± 0.11	-1.50	...
Pirzkal et al. 2013	0.5 ± 0.4	[OIII]	$-2.58^{+0.09}_{-0.09}$	$41.3^{+0.09}_{-0.09}$	$-1.21^{+0.08}_{-0.07}$	...
Ly et al. 2007	0.41	[OIII]	-2.55 ± 0.25	41.17 ± 0.22	-1.49 ± 0.11	-2.17 ± 0.06
	0.42	[OIII]	-2.38 ± 0.22	41.11 ± 0.24	-1.25 ± 0.13	-2.31 ± 0.09
	0.62	[OIII]	-2.58 ± 0.17	41.51 ± 0.15	-1.22 ± 0.13	-2.06 ± 0.05
	0.83	[OIII]	-2.54 ± 0.15	41.53 ± 0.11	-1.44 ± 0.09	-1.73 ± 0.03

CHAPTER 3

The Nature of Hβ+[OIII] and [OII] emitters to $z \sim 5$ with HiZELS: stellar mass functions and the evolution of EWs

Abstract

We investigate the properties of ~ 7000 narrow-band selected galaxies with strong Hβ+[OIII] and [OII] nebular emission lines from the High-z Emission Line Survey (HiZELS) between $z \sim 0.8-5.0$. Our sample covers a wide range in stellar mass ($M_{\rm stellar} \sim 10^{7.5-12.0}$ M$_\odot$), rest-frame equivalent widths (EW$_{\rm rest} \sim 10-10^5$ Å), and line luminosities ($L_{\rm line} \sim 10^{40.5-43.2}$ erg s^{-1}). We measure the Hβ+[OIII]-selected stellar mass functions out to $z \sim 3.5$ and find that both $M_\star$ and $\phi_\star$ increases with cosmic time. The [OII]-selected stellar mass functions show a constant $M_\star \approx 10^{11.6}$ M$_\odot$ and a strong, increasing evolution with cosmic time in $\phi_\star$ in line with Hα studies. We also investigate the evolution of the EW$_{\rm rest}$ as a function of redshift with a fixed mass range ($10^{9.5-10.0}$ M$_\odot$) and find an increasing trend best represented by $(1+z)^{3.81\pm0.14}$ and $(1+z)^{2.72\pm0.19}$ up to $z \sim 2$ and $z \sim 3$ for Hβ+[OIII] and [OII] emitters, respectively. This is the first time that the EW$_{\rm rest}$ evolution has been directly measured for Hβ+[OIII] and [OII] emitters up to these

redshifts. There is evidence for a slower evolution for $z > 2$ in the Hβ+[OIII] EW_{rest} and a decreasing trend for $z > 3$ in the [OII] EW_{rest} evolution, which would imply low [OII] EW at the highest redshifts and higher [OIII]/[OII] line ratios. This suggests that the ionization parameter at higher redshift may be significantly higher than the local Universe. Our results set the stage for future near-IR space-based spectroscopic surveys to test our extrapolated predictions and also produce $z > 5$ measurements to constrain the high-z end of the EW_{rest} and [OIII]/[OII] evolution.

3.1 Introduction

In the past two decades, great strides have been made in understanding the evolution of observed properties of star-forming galaxies across cosmic time. We now know that the peak of star formation activity occurred somewhere between $z \sim 2$ and 3 (e.g., Karim et al. 2011; Bouwens et al. 2012a,b; Cucciati et al. 2012; Gruppioni et al. 2013; Sobral et al. 2013a; Bouwens et al. 2015; Khostovan et al. 2015) and that the majority of the stellar mass assembly occurred by $z \sim 1$ (e.g., Pérez-González et al. 2008; Marchesini et al. 2009; Ilbert et al. 2013; Muzzin et al. 2013; Madau & Dickinson 2014; Sobral et al. 2014; Tomczak et al. 2014; Grazian et al. 2015). Furthermore, recent spectroscopic surveys are giving us valuable insight on the physical properties of star-forming regions in the high-z Universe (e.g., Liu et al. 2008; Swinbank et al. 2012b; Nakajima et al. 2013; Sobral et al. 2013b; Nakajima & Ouchi 2014; Newman et al. 2014; Shirazi et al. 2014; Steidel et al. 2014; Stott et al. 2014; Hayashi et al. 2015; Sanders et al. 2016; Stott et al. 2016).

As galaxies age and undergo star-formation, the byproduct of their star-formation activity is their stellar mass build up. Therefore, determining and understanding the evolution of the stellar mass function (SMF) in galaxies is crucial as measuring the distribution of stellar mass within a given comoving volume provides important observational evidence on how galaxies

may grow due to star formation (e.g., van Dokkum et al. 2010; Bauer et al. 2013), mergers (e.g., Drory & Alvarez 2008; Vulcani et al. 2015), and environmental influences (e.g., Baldry et al. 2006; Bundy et al. 2006; Bolzonella et al. 2010; Peng et al. 2010; Sobral et al. 2011; Giodini et al. 2012; Darvish et al. 2015a; Mortlock et al. 2015; Davidzon et al. 2015; Sobral et al. 2016a; Darvish et al. 2016). Measurements of the SMFs also provide valuable constraints for theoretical models of the hierarchical assembly of dark matter halos (e.g., SMF-DM Halo Mass relationship; Conroy & Wechsler 2009; Behroozi et al. 2013b; Furlong et al. 2015; Henriques et al. 2015; Rodriguez-Gomez et al. 2015; for a recent review article see Somerville & Davé 2015).

Another observational tracer of galaxy formation and evolution is the stellar mass density (SMD), which measures the total stellar mass within a specific range of masses (e.g., $> 10^9$ $M_\odot$) or full range (e.g., integrating the SMF from zero to infinity) per unit of comoving volume. By combining with other SMD measurements over a wide redshift range, the evolution of the SMD can be measured and reveal how galaxies assembled their stellar mass over cosmic time. In a compilation of the latest SMD measurements (e.g., Arnouts et al. 2007; Gallazzi et al. 2008; Pérez-González et al. 2008; Kajisawa et al. 2009; Li & White 2009; Marchesini et al. 2009; Yabe et al. 2009; Pozzetti et al. 2010; Caputi et al. 2011; González et al. 2011; Bielby et al. 2012; Lee et al. 2012; Reddy et al. 2012; Ilbert et al. 2013; Moustakas et al. 2013; Muzzin et al. 2013; Labbé et al. 2013), Madau & Dickinson (2014) showed a strong, increasing trend from $z \sim 8$ to $z \sim 1$, followed by a shallower, increasing trend from $z \sim 1$ to the present. This evolution is correlated with the cosmic star-formation rate density (SFRD) evolution, such that it is possible to model the SMD evolution based on the average SFRD evolution by taking its time integral (e.g., Sobral et al. 2013a; Madau & Dickinson 2014; Khostovan et al. 2015) and vice versa via the time derivative (e.g., Pérez-González et al. 2008).

Despite the various measurements that have provided a general indication of the SMF and SMD evolution, there are several caveats. For example, spectral energy distribution (SED) models and templates used to measure stellar masses can introduce systematic biases based on

assumptions made in the fitting process and differing methodologies (Mobasher et al., 2015). Also, the separation based on galaxy types typically is based on empirically-derived colour-colour selection diagnostics (e.g., ***BzK***, Daddi et al. 2004; ***UVJ***, Williams et al. 2009), which can vary based on the data-set used (e.g., selection effects arising from sample and/or survey size and depth). Therefore, to make further progress we need a reliable, clean sample of a specific type of galaxies over a large comoving volume that can trace the SMF and SMD evolution from low-z to high-z using a single methodology.

Recently, there has been a great deal of focus on the evolution of the specific star-formation rate (sSFR), which is defined as the star-formation rate divided by the stellar mass (e.g., Stark et al. 2013; González et al. 2014; Marmol-Queralto et al. 2015; Faisst et al. 2016). Since the sSFR is in inverse units of time, it can be interpreted as a direct measurement of the timescale of stellar growth in individual galaxies and also as the ratio between the current and past star-formation activity. Recent studies have constrained the evolution within the $z < 2$ regime, finding that the sSFR increases from $z = 0$ to $z \sim 2$ (Noeske et al., 2007; Damen et al., 2009; Sobral et al., 2014).

However, the sSFR evolution is less constrained for $z > 2$. Reddy et al. (2012) measured the sSFR evolution between $z \sim 2-3$ and Stark et al. (2009) and González et al. (2010) extended the measurements to $z > 4$. In comparison with the $z < 2$ data, the observational data show the sSFR increasing from 0.3 to 2 Gyr^{-1} between $z = 0$ and $z \sim 2$. For $z > 2$, some early studies found that sSFR showed no significant evolution and is claimed to stay flat around ~ 2 Gyr^{-1} up to $z \sim 7$ (Stark et al., 2009; González et al., 2010). In contrast, theoretical studies predict that, for the case of cold gas accretion growth, the sSFR increases as $(1+z)^{2.25}$ (Davé et al., 2011, 2012). Latest measurements from the high-resolution EAGLE simulation also predict an increasing sSFR with redshift (Furlong et al., 2015). An issue that can arise for the observational studies at $z > 4$ is that they do not take into account the effects of nebular emission lines in the SED fitting process. Strong lines can contaminate the *Spitzer* IRAC bands at these redshifts

resulting in overestimating stellar masses (e.g., Schaerer & de Barros 2009, 2010; Nayyeri et al. 2014; Smit et al. 2014). Looking at ~ 1700 $z \sim 3-6$ Lyman break galaxies (LBGs), de Barros et al. (2014) found that about two thirds of their sample had detectable emission lines and, by taking them into account when fitting the SED, resulted in significantly different physical parameters. Recently, González et al. (2014) presented newer measurements of the sSFR with the nebular contamination accounted for and found an increase of a factor of ~ 2 in comparison to the Stark et al. (2009) and González et al. (2010) measurements, but still in conflict with theoretical predictions.

To correct the overestimation of stellar masses and sSFRs requires that the contamination of nebular emission lines is taken into account. One way of doing this is by measuring the trends in the rest-frame equivalent widths ($\mathrm{EW_{rest}}$) of lines, which is defined as the ratio of the emission-line and stellar continuum flux. Studies have mapped out the $\mathrm{EW_{rest}}(\mathrm{H}\alpha)$ evolution up to $z \sim 2$ (e.g., Erb et al. 2006; Fumagalli et al. 2012; Sobral et al. 2014); however, the $z > 2$ trend is still uncertain since $\mathrm{H}\alpha$ falls into the infrared at these redshifts. Recent measurements, using colour excess in the *Spitzer* IRAC bands at $> 3\mu$m that are claimed to only be attributed to nebular emission line contribution, have attempted to extend the measurements of the evolution out to $z \sim 6$ (e.g., Shim et al. 2011; Rasappu et al. 2016). Other studies measured $\mathrm{EW_{rest}}(\mathrm{H}\beta{+}[\mathrm{OIII}])$ between $z \sim 6-8$ and, using known line ratios, converted to $\mathrm{H}\alpha$ to extend the mapping of the $\mathrm{EW_{rest}}(\mathrm{H}\alpha)$ evolution (e.g., Labbé et al. 2013; Smit et al. 2014, 2015). It should be noted that current studies are UV selected and are only sensitive to the most extreme line-emitters which can be detected in the broad-band photometry. Therefore, these measurements can be only treated as upper-limits. What we require are complete samples of emission-line selected sources (e.g., cover a wide-range in $\mathrm{EW_{rest}}$ that represents a typical emission-line galaxy) to properly measure the $\mathrm{EW_{rest}}$ evolution at $z > 2$. The lines that can be used are $\mathrm{H}\beta{+}[\mathrm{OIII}]$[1] up to $z \sim 3$ and [OII] up to $z \sim 5$ (e.g., Khostovan et al. 2015).

[1]The narrow-band filters used all have FWHMs of $\sim 130-210$Å and can differentiate between $\mathrm{H}\beta$ and

Tracing the evolution of the equivalent width of nebular emission lines also provides valuable insight to the physical conditions of the HII regions and how those physical conditions evolve over cosmic time (e.g., Liu et al. 2008; Nakajima et al. 2013; Nakajima & Ouchi 2014; Hayashi et al. 2015; Kewley et al. 2015). For example, the [OIII]/[OII] ratio as measured by $EW_{rest}([OIII])/EW_{rest}([OII])$ can, in principle, tell us about the ionization parameter and the ionization state of the gas forming stars.

In this paper, we present our investigation of the evolution in SMF, SMD, and EW_{rest} using a large sample of Hβ+[OIII] and [OII] emission-line galaxies at $z \sim 1-5$ from the High-Redshift Emission-Line Survey (HiZELS) presented by Khostovan et al. (2015). Our results have implications in terms of the evolution in the EW_{rest} and sSFR, as well as the physical conditions of the gas in the HII regions that produces the nebular emission-lines. Our results also present an empirical evolution of the EW_{rest} that can be used to estimate the nebular emission line contamination in broad-band photometry when such photometry are used in determining key physical properties (e.g., stellar masses).

The paper is structured as follows: Section 5.2 describes the HiZELS sample used in this paper; Section 4.3 presents the stellar mass, SMF, and SMD determinations; Section 5.5 highlights the results of this paper with interpretations of the SMF, SMD, EW_{rest}, and [OIII]/[OII] evolutions; Section 6.4 summarizes the main results of our study.

Throughout this paper, we assume ΛCDM cosmology, with $H_0 = 70$ km s^{-1} Mpc^{-1}, $\Omega_\Lambda = 0.3$, and $\Omega_m = 0.7$. We assume a Chabrier (2003) IMF and correct the literature measurements when needed. All magnitudes are presented as AB magnitudes (Oke & Gunn, 1983).

[OIII] emitters, but the broad-band filters used in selecting sources have FWHMs too large to separate the sample. Therefore, our Hβ+[OIII] samples are comprised of a combination of Hβ and [OIII], although Khostovan et al. (2015) and Sobral et al. (2015a) showed that the samples are dominated by [OIII] emitters.

3.2 HiZELS Sample

Our sample consists of Hβ+[OIII] and [OII] emitters selected based on narrow-band photometry from HiZELS (Geach et al., 2008; Sobral et al., 2009, 2012; Best et al., 2013; Sobral et al., 2013a) found in the COSMOS (Scoville et al., 2007) and UDS (Lawrence et al., 2007) fields. We refer the reader to Sobral et al. (2013a) for details on the initial selection of sources with narrow-band excess.

The sample consists of 3475 Hβ+[OIII] emitters between $z = 0.84$ and 3.24 and 3298 [OII] emitters between $z = 1.47$ and 4.69 in discrete redshift slices (see Table 3.1) with the redshifts corresponding to the narrow-band filters used by Sobral et al. (2013a)[2]. Our sample is backed by 233 and 219 spectroscopic measurements for Hβ+[OIII] and [OII], respectively, that are from zCOSMOS (Lilly et al., 2007), the UDSz Survey (Bradshaw et al. 2013; McLure et al. 2013), Subaru-FMOS (Stott et al., 2013b), Keck-DEIMOS/MOSFIRE (Nayyeri et al., in prep), PRIsm MUlti-object Survey (PRIMUS; Coil et al. 2011), and VIMOS Public Extragalactic Redshift Survey (VIPERS; Garilli et al. 2014). This sample is based on a large areal coverage of ~ 2 deg^2 equating to a comoving volume coverage of $\sim 10^6$ Mpc^3, which greatly reduces the effects of cosmic variance (see Sobral et al. 2015a; Stroe & Sobral 2015).

The selection of Hβ+[OIII] and [OII] emitters is discussed in Khostovan et al. (2015). In brief, we used the emission-line source catalog of Sobral et al. (2013a) to select galaxies with Hβ+[OIII] or [OII] emission lines by using a combination of selection criteria: spectroscopic redshifts, photometric redshifts, and colour-colour diagnostics (with priority given in that order). Sources that had detections in more than one narrow-band filter were also selected on the basis that their confirmation is equivalent to spectroscopic confirmation (e.g., finding [OII] in NB921 and Hα in NBH at $z = 1.47$; see Sobral et al. 2012).

Note that we define the Hβ+[OIII] sample as a combination of Hβ, [OIII]4959, and [OIII]5007.

[2]We refer the reader to Sobral et al. (2013a) for information regarding the filter profiles, FWHMs, effective wavelengths, and all other inquiries regarding the properties of the narrow-band and broad-band filters used.

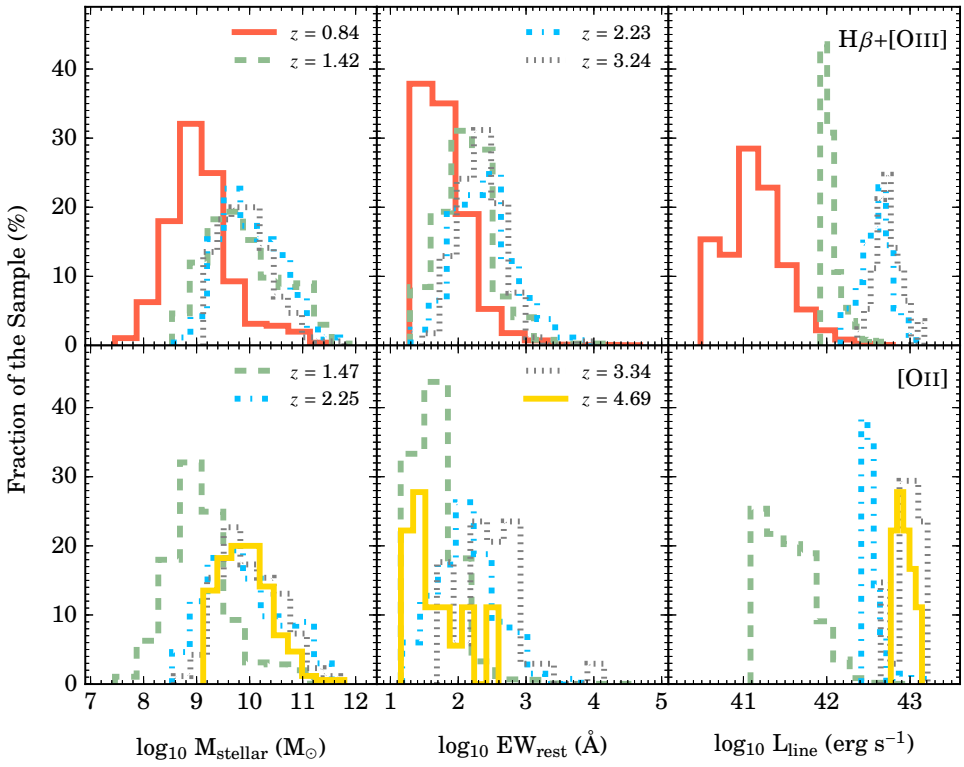

Figure 3.1: The stellar mass, EW_{rest}, and luminosity distributions for all of our samples. Based on the luminosity distributions, it is clear that our high-z sample is limited to high line luminosities ($L > 10^{42}$ erg s^{-1}). Our lowest redshift sample is the deepest and covers a wider luminosity, stellar mass, and EW_{rest} range which allows us to utilize the sample for tests of selection effects that can bias results at higher redshift.

Although the narrow-band filters can differentiate between Hβ+[OIII] and [OIII], the broad-band filters can not distinguish them. We discuss this issue in more detail in §3.3.4 and show that our sample is primarily [OIII]5007, although at lower line luminosities the fraction of Hβ and [OIII]4959 lines increases.

The rest-frame equivalent widths of emission lines are calculated using the following relation:

$$EW_{rest} \approx \frac{F_L}{f_C} = \frac{\Delta\lambda_{NB}}{1+z} \frac{f_{NB} - f_{BB}}{f_{BB} - f_{NB}(\Delta\lambda_{NB}/\Delta\lambda_{BB})} \tag{3.1}$$

where NB and BB are the narrow-band and broad-band filters, respectively, $\Delta\lambda$ is the corre-

sponding width of the filter, f is the corresponding flux measured in the filter, F_L is the flux of the nebular emission line, and f_C is the continuum flux. Figure 3.1 shows the distribution of rest-frame EWs and line luminosities of the Hβ+[OIII] and [OII] emitters. Our sample consists of rest-frame equivalent widths that are as low as ~ 10 Å and as high as 10^5 Å and a luminosity range between $10^{40.5}$ and $10^{43.2}$ erg s^{-1}. We refer the reader to Khostovan et al. (2015) for details on how the line luminosities were computed.

3.3 Methodology

3.3.1 SED Fitting

We use the Multi-wavelength Analysis of Galaxy PHYSical properties (MAGPHYS) code of da Cunha et al. (2008) to fit the SEDs of our sources and determine physical properties, such as stellar masses, star-formation rates, and $E(B-V)$. da Cunha et al. (2008) designed the code to treat the infrared as two sub-components (birth clouds and diffuse ISM) using empirical relations from Charlot & Fall (2000) and assuming a balance between the stellar and dust/infrared components (e.g., the amount of attenuation in the stellar component is accounted for in the dust/infrared component).

MAGPHYS uses different model templates for the stellar and infrared components. The stellar component is generated by the Bruzual & Charlot (2003) code, while the infrared component templates are formed based on the prescription of Charlot & Fall (2000). We note that MAGPHYS assumes a Chabrier (2003) IMF[3]. The stellar templates include (1) exponentially declining star-formation histories $e^{-t/\tau}$ with τ in the range between 0.1 to 13.5 Gyr; (2) metallicities between 0.02 and 2 $Z_\odot$; and (3) dust attenuation based on Charlot & Fall (2000). MAGPHYS then fits the observed SEDs and creates marginalized likelihood

distributions of physical parameters.

We fit the SEDs using *GALEX* FUV and NUV, CFHT Megaprime u^*, Subaru SuprimeCam $Bg'Vr'i'z'$, UKIRT WFCAM J and K, and *Spitzer* IRAC 3.6 - 8.0 μm photometry for our COSMOS sources. The SEDs of our UDS sources are fitted using CFHT MegaCam u, Subaru SuprimeCam $BVr'i'z'$, UKIRT WFCAM $YJHK$, and *Spitzer* IRAC 3.6 - 8.0 μm photometry. The outputs used in this study are the stellar masses. We use the COSMOS-30 i-band selected catalog (Capak et al., 2007; Ilbert et al., 2009) and the DR8 release of the Subaru-XMM-UKIDSS UDS K-band selected catalog (e.g., Cirasuolo et al. 2007; Lawrence et al. 2007). We refer the reader to the cited catalog papers for detailed descriptions of the multi-wavelength photometry.

We note that MAGPHYS was created to incorporate the 912 Å $< \lambda < 1$ mm rest-frame range for which we have no mid- and far-infrared constraints. The unique part about MAGPHYS is that it fits the stellar and infrared/dust templates separately, such that in the case where there are no infrared constraints, the measurements will be based on the fits using only the stellar templates. Furthermore, MAGPHYS does not have a prescription to incorporate the effects of nebular emission in the fitting process. Past studies have shown that nebular emission contamination can affect the stellar mass measurements from SED fitting (e.g., Schaerer & de Barros 2009; de Barros et al. 2014; Mobasher et al. 2015). As shown in Figure 3.1, we find that for the vast majority of our sources, the $\mathrm{EW_{rest}}$ are low enough ($< 10^3$ Å; e.g., Smit et al. 2014) and have $\sim 10-15$ individual photometric (broad-band) detections for which the effects of nebular emission line contamination are negligible (see Appendix 3.6.2.1).

3.3.2 Stellar Masses

Figure 3.1 shows the range in stellar mass that were measured from MAGPHYS for all our samples. We find that our $z > 1$ Hβ+[OIII] emitters and $z > 1.5$ [OII] emitters have typical

[3]To make our results comparable with other studies in the literature that utilize different IMFs, we state the conversions to the Salpeter IMF (+0.215 dex) and the Kroupa IMF (−0.04 dex).

stellar masses $M_{\rm stellar} \sim 10^{9.5} - 10^{10}$ $M_\odot$. The $z = 0.84$ Hβ+[OIII] and $z = 1.47$ [OII] samples have distributions that peak at lower masses ($M_{\rm stellar} \sim 10^{8.5} - 10^{9}$ $M_\odot$) and cover a wider range ($M_{\rm stellar} \sim 10^{7.5} - 10^{12.0} M_\odot$). Both samples come from NB921 observations, which, as seen in the luminosity distributions shown on Figure 3.1, probe deeper than all the other samples, but also covers a much smaller volume ($\sim 3 - 7 \times 10^5$ Mpc^{-3}, Khostovan et al. 2015). Since the COSMOS field has a wealth of multi-wavelength with measurements of stellar masses, we make a comparison between our measurements and those of Ilbert et al. (2010) and Muzzin et al. (2013) as shown in Appendix 3.6.2. We find that our measurements are consistent with those of the literature.

3.3.3 Creating Stellar Mass Functions

We create stellar mass functions by using a similar approach as in Khostovan et al. (2015) by applying the $V_{\rm max}$ estimator where the data is binned as such:

$$\phi(M_j) = \frac{1}{\Delta M_j} \sum_{i=0}^{N} \frac{1}{C(M_i) V_{{\rm max},i}} \tag{3.2}$$

where M_j is the $j^{\rm th}$ mass bin, ΔM_j is the bin-size, and $C(M_i)$ is the completeness and $V_{\rm max,i}$ is the volume for the $i^{\rm th}$ source in the $j^{\rm th}$ bin. The masses, M, used in this equation are all in log-scale.

3.3.3.1 Completeness Correction

All the stellar mass functions are corrected for completeness based on the completeness corrections determined by Khostovan et al. (2015) using the approach of Sobral et al. (2013a, 2014). We adopt this approach for correcting our SMFs because our samples are flux- and EW-limited and not mass-limited. Therefore, we need to correct based on the line flux and EWs as this is where the incompleteness arises. In brief, the completeness correction takes into account the full selection function (including the $EW_{\rm rest}$ cut and the difference in luminosity limits/depths

Table 3.1: To ensure compatibility between different redshift samples, we apply a common $L/L^\star(z)$ cut (Hβ+[OIII]: $L > 0.4L^\star(z)$ and [OII]: $L > 0.85L^\star(z)$ where the $L^\star(z)$ measurements are from Khostovan et al. (2015). For each redshift sample, we highlight the total number of emitters in the sample ($N_{\rm total}$), the total number of emitters selected after the $L/L^\star(z)$ cut ($N_{\rm sel}$), and the corresponding fraction of emitters selected.

z	$\log_{10}L^\star$ (erg s^{-1})	$N_{\rm total}$	$N_{\rm sel}$	Fraction
		Hβ+[OIII] ($L > 0.4\ L^\star(z)$)		
0.84	41.79	2477	524	21%
1.42	42.06	371	371	100%
2.23	42.66	271	256	95%
3.24	42.83	179	175	98%
		[OII] ($L > 0.85\ L^\star(z)$)		
1.47	41.86	3285	676	21%
2.25	42.34	137	137	100%
3.34	42.69	35	35	100%

between one sub-field and another) in terms of line luminosity. Furthermore, we applied a volume/filter profile correction (see Khostovan et al. 2015), which takes into account the loss of flux at the wings of the narrow-band filters. We also applied an $\rm EW_{rest}$ completeness correction to take into account the missing number of high mass galaxies in our $z = 0.84$ SMF. This is described in detail in Appendix 3.6.3.

3.3.3.2 Common Relative Luminosity Cut

As seen in Figure 3.1, each sample covers different line luminosities making it difficult to directly compare samples. Furthermore, the volumes probed per each sample are different where the lowest redshift samples have comoving volumes of $\sim 3-6\times10^5$ Mpc^3 and the highest redshift samples with $\sim 10-16\times10^5$ Mpc^3 (Khostovan et al., 2015). This raises problems in terms of compatibility for comparison as the line luminosity and volume differences can capture different populations of galaxies. In order to solve this issue, we use a similar approach to Sobral et al.

(2014) by placing a common $L/L^\star(z)$ limit to make the samples directly comparable using the $L^\star(z)$ measurements of Khostovan et al. (2015). This is accomplished by comparing the distribution of sources per redshift in terms of their $L/L^\star(z)$ ratio where we find that the common limit for Hβ+[OIII] is $\sim 0.4L^\star(z)$ and for [OII] it is $\sim 0.85L^\star(z)$ (see Table 3 of Khostovan et al. 2015 for the $L^\star(z)$ measurements). Disregarding this common limit will result in stellar mass functions and densities that trace different types of emitters.

This consequentially reduces the sample size, especially for the lowest z samples ($z \sim 0.84$ for Hβ+[OIII] and $z \sim 1.47$ for [OII]) as they are the deepest and have the largest sample size. Table 3.1 shows the change in sample size when applying the common relative luminosity cut. Percentages shown correspond to the fraction of sources that were selected in comparison to the full sample. The NB921 samples (Hβ+[OIII] $z = 0.84$ and [OII] $z = 1.47$) saw the largest reductions in sample size due to their line luminosity distributions peaking at lower luminosities (see Figure 3.1 for the line luminosity distributions of all the samples). The higher-z samples retain the vast majority of their original sample sizes due to the fact that the lower $L/L^\star(z)$ limit chosen was based on their line luminosity distributions.

3.3.4 Which one dominates: Hβ or [OIII]?

As mentioned in §5.2 and discussed in Khostovan et al. (2015), our Hβ+[OIII] sample is a combination of Hβ and [OIII] emitters. The narrow-band filters can differentiate between the two emission lines. The problem arises in the selection techniques used by Khostovan et al. (2015), which, as briefly described in §5.2, rely on a combination of spectroscopic confirmation, photometric redshifts, and colour-colour criteria. The photometric redshifts and colour-colour criteria both depend on using the multi-wavelength broad-band filters data sets, which results in the Hβ and [OIII] emitters to be blended with each other.

The important question that arises from this is which one dominates the Hβ+[OIII] sample: Hβ or [OIII] emitters? Khostovan et al. (2015) showed that the [OIII] line dominates the

population of emitters with the fraction of Hβ emitters increasing with decreasing Hβ+[OIII] line luminosities. In a similar study, Sobral et al. (2015a) used their CF-HiZELS $z \sim 1.4$ sample from the ≈ 10 deg^2 SA22 field and found that $\sim 16\%$ of their spectroscopically confirmed Hβ+[OIII] emitters were Hβ emitters.

Figure 3.2 shows the dependency of the contributing fraction of the three emission lines per luminosity bin only for the $z = 0.84$ sample, which has the most number of spectroscopic measurements (~ 200). All spectroscopic measurements are described in §5.2 and in Khostovan et al. (2015). The trend is clear such that above $L_{line} > 10^{42.5}$ erg s^{-1}, the fraction of [OIII]5007 emitters is $\sim 100\%$ and at fainter line luminosities, the fraction of [OIII]5007 emitters decreases to $\sim 65\%$ and the [OIII]4959 fraction increases to $\sim 25\%$ and the Hβ fraction up to $\sim 10\%$. Even at these faint line luminosities, the contribution of [OIII]5007 is still well above $\sim 50\%$. Therefore, we can safely assume that the [OIII] emitters dominate our Hβ+[OIII] sample.

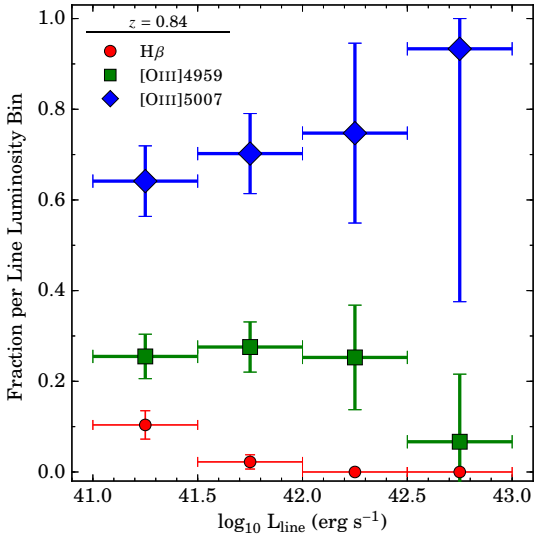

Figure 3.2: The dependency of the fraction of emitters versus the observed line luminosity for the $z = 0.84$ Hβ+[OIII] sample. All spectroscopic measurements used are described in Khostovan et al. (2015) and in §5.2. Errors shown here are Poisson and normalized to the total number of emitters per line luminosity bin. There is a clear trend that at fainter line luminosities, the fraction of [OIII]5007 emitters decreases, while the [OIII]4959 and Hβ fraction increases. Despite this change in the demographics of the sample at these line luminosities, we can still safely say that the sample is dominated by [OIII] emitters rather than Hβ emitters.

We note that for certain redshift slices (e.g., $0.8413 < z_{spec} < 0.8496$ for the NB921 sample), the narrow-band filters can capture both [OIII]4959 and [OIII]5007 within the FWHM of the filter. We incorporate this double detection in Figure 3.2 by weighting the contribution of the two lines based on the typical line ratio ([OIII]5007 = 3 - 4 × [OIII]4959). Despite this effect, we can still safely assume that the majority of the emission is coming from [OIII]5007. We later

take this into account when studying the ionization parameter using [OIII]/[OII] (see §3.4.4.3).

3.3.5 Contamination from AGN

AGN will also be selected with narrow-band surveys as the energetic UV photons they release can produce the emission lines that are also produced by the UV photons from bright, massive stars in star-forming, HII regions. Khostovan et al. (2015) and Sobral et al. (2015a) both studied the AGN contamination in their samples by using the 1.6μmbump as an observational proxy. Both found, on average, that the AGN contamination is $\sim 10-20\%$ of the total population. Khostovan et al. (2015) also compared the Hβ+[OIII] luminosity functions to the $z \sim 0.7$ zCOSMOS [OIII] type-2 AGN luminosity function of Bongiorno et al. (2010) and found that the brightest emitters in the Hβ+[OIII] sample are probable AGNs and as the Hβ+[OIII] line luminosity decreases, so does the fraction of AGN contribution.

Recently, Sobral et al. (2016b) studied the spectroscopic properties of 59 CF-HiZELS and HiZELS $L > L^\star$ Hα emitters split between $z \sim 0.8$, 1.47, and 2.23 and find a strong dependency between the AGN fraction and Hα line luminosity for $L > L^\star$ and a constant fraction for $L \leq L^\star$. Since we apply a common relative luminosity cut (see §3.3.3.2), an issue that can arise is that the AGN fraction may increase. The samples most affected by the cut are the Hβ+[OIII] $z = 0.84$ and [OII] $z = 1.47$ samples. We find that after implementing the cut, the median line luminosities are $0.62 \pm 0.19 L^\star$ and $1.17 \pm 0.24 L^\star$ for Hβ+[OIII] and [OII], respectively. Based on the results of Sobral et al. (2016b), the amount of increase in the AGN contamination will still be close to that measured for the full sample as the majority of the sample still reside at $L \approx L^\star$. We note that a complete spectroscopic study of the AGN contamination in the Hβ+[OIII] and [OII] samples is needed and is currently a work in progress.

We have removed individual sources that could be potentially AGN via the χ^2 of the SED fits. We note that any type 1 (broad line) AGN in our sample may result in a poor χ^2 SED fits making them easier to remove from the sample. The type 2 (narrow line) AGNs are harder

to remove but can still result in poor χ^2 fits. To remove this contamination, we incorporate a $\chi^2_{\rm reduced} < 100$.

3.4 Results

3.4.1 Quiescent Population?

In the past, many studies used the rest-frame UVJ colour-colour selection to separate quiescent/passive and star-forming galaxies (eg., Williams et al. 2009; Brammer et al. 2011; Muzzin et al. 2013). Unobscured star-forming galaxies will have bluer rest-frame $U-V$ colours, corresponding to younger stellar populations and a lower or no 4000Å break, and also have bluer $V-J$ colours forming a locus within the UVJ plane. Dust-free quiescent galaxies are dominated by a more evolved stellar population resulting in a more pronounced 4000Å break, resulting in redder $U-V$ colours, although dust-obscured star-forming galaxies can occupy the same regime due to attenuation. This degeneracy is broken by $V-J$, where dust-free quiescent galaxies have bluer colours than the dust-obscured star-forming galaxies. The UVJ classification scheme does not take into account possibility of AGN contamination, such that galaxies that fall under both classifications can also be potential AGNs. Both classifications can also include sources with more complex spikes of obscured/unobscured star formation. We therefore refer to the quiescent classification as "passive" and the star-forming classification as "active" to take into account AGNs.

It must be noted that the UVJ selection is empirically driven and varies based on the data-set used, as well as the filters used in determining the rest-frame AB magnitudes. We apply the Muzzin et al. (2013) UVJ selection and use the same filters (Johnson U and V and 2MASS J) to study the nature of our sample. Figure 3.3 shows our full sample of emitters and the Muzzin et al. (2013) colour-colour selection, with the rest-frame UVJ colours measured using the best-fit SEDs and the corresponding bandpasses. We include the 1σ range for all

sources per emission line that is calculated from the observed error bars of the corresponding UVJ observer-frame filters.

We find that, for all our Hβ+[OIII] and [OII] samples, $>98.5\%$ are classified as active based on this selection criteria. We also find a small population of emitters that fall under the passive classification area. For the Hβ+[OIII] sample, only 0.8% (26 emitters) fall within this selection area with the majority ($\sim 38\%$ of the 26 emitters) being from the $z \sim 1.42$ sample. The [OII] sample has a total of 2.4% (79 emitters) of the full sample within the passive selection region with the vast majority ($\sim 96\%$; 76 of the 79 emitters) coming from the $z \sim 1.47$ sample. These are mostly faint sources that fall into the passive selection region and are consistent with photometric scatter. Overall, the sources discussed above make a small fraction of our full sample.

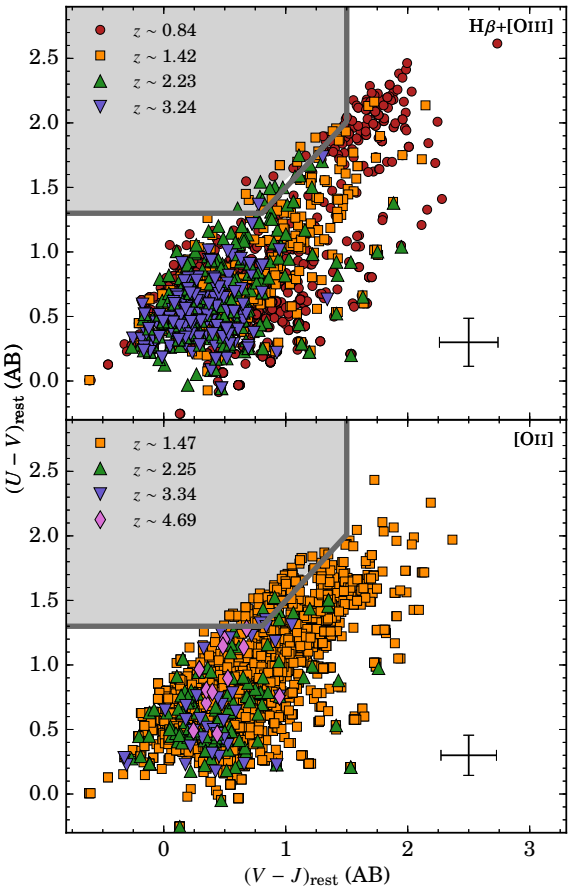

Figure 3.3: The rest-frame UVJ colour-colour diagnostic used to separate star-forming galaxies from quiescent galaxies. The highlighted region and *grey* boundaries are the Muzzin et al. (2013) quiescent selection region. Included is the typical 1σ range for all sources per emission line. We find that the majority of our sources reside within the star-forming classification region. Sources that are within the quiescent region are consistent with photometric scatter. We find a general trend in the UVJ plane where high-z sources tend to have bluer rest-frame UVJ colours that could be caused by changes in dust and/or the star-formation efficiency (e.g., Papovich et al. 2015).

The UVJ selection criteria also confirms that the great majority ($>98\%$) of our sample can be classified as active. There is also a general trend where rest-frame colours become bluer with increasing redshift implying that our high-z samples are likely comprised of less dusty systems. This could be attributed to sample bias as dusty systems would result in fainter emission-line fluxes leaving behind the less dusty

and observationally bright systems (e.g., Hayashi et al. 2013). This leads to the caveat that the samples are not fully comparable across redshift as we will be missing the dustier systems. On the other hand, this could also indicate that there is a redshift evolution in the UVJ plane for which galaxies at high-z tend to have bluer rest-frame colours. As these galaxies evolve and their star-formation efficiency decreases and the amount of dust increases, their UVJ colours become redder. This is consistent with the Milky Way progenitor evolution study of Papovich et al. (2015).

3.4.2 Stellar Mass Functions

In this section, we present the stellar mass function (SMF) of line emitters up to $z \sim 3$ (we exclude the $z = 4.69$ [OII] emitters since we could not constrain the SMF due to the small sample size). All samples used to measure the SMF have a common $L/L^{\star}(z)$ cut ($0.4L^{\star}(z)$ and $0.85L^{\star}(z)$ for Hβ+[OIII] and [OII], respectively) in order to make them comparable (tracing a similar galaxy population). The observed measurements are shown in Figures 3.4. All the measurements have been completeness and filter profile corrected as described in §3.3.3. We fit the observed binned data to the Schechter function in log-form:

$$\Phi(M)\mathrm{d}M = \phi_{\star}\ \ln 10 \left(\frac{M}{M_{\star}}\right)^{1+\alpha} e^{-(M/M_{\star})} \mathrm{d}\log_{10} M \tag{3.3}$$

where $\phi_{\star}$ is the normalization, $M_{\star}$ is the characteristic mass, and α is the faint-end slope. The fits are plotted in Figures 3.4 with the fitted parameters shown in Table 3.2. Note that we also placed a $L/L^{\star}(z)$ limit as discussed at the end of §3.3.3 to make all our samples comparable to one another (tracing the same type of emitters).

We initially measure the faint-end slope for our deepest samples and compare them to those measured in the literature (Pérez-González et al., 2008; Marchesini et al., 2009; Muzzin et al., 2013). Based on these three studies that trace the SMF evolution up to $z \sim 5$, the faint-end slope does not evolve strongly. Therefore, to be comparable from sample to sample and also to

Table 3.2: Our fitted Schechter parameters of our stellar mass functions. Shown are the parameters when α is free and also in the case when we fix α to -1.3 in order to make our measurements comparable with the literature. Note that only the $z = 0.84$ and 1.42 Hβ+[OIII] measurements and $z = 1.47$ [OII] measurements are used for the case of α being free. This is because the sample size was large enough to probe the faint-end slope, which is then used in comparison to the literature to set a fixed α for all redshift samples. We show the Schechter parameters for where α is free only for our most populated samples. Stellar mass densities are calculated by fully integrating the stellar mass functions. Also included is the $L/L^\star(z)$ limit used to make all the samples compatible for comparison.

Hβ+[OIII]-selected Stellar Mass Function Properties ($L/L^\star(z) > 0.4$)						
z	$\log_{10}\phi_\star$ (Mpc^{-3})	$\log_{10} M_\star$ ($\mathrm{M}_\odot$)	α	$\log_{10}\phi_{\star,\alpha=-1.3}$ (Mpc^{-3})	$\log_{10} M_{\star,\alpha=-1.3}$ ($\mathrm{M}_\odot$)	$\log_{10}\rho_{\star,\alpha=-1.3}$ ($\mathrm{M}_\odot\ \mathrm{Mpc}^{-3}$)
0.84	$-3.77^{+0.16}_{-0.20}$	$11.49^{+0.30}_{-0.17}$	$-1.27^{+0.06}_{-0.07}$	$-3.87^{+0.06}_{-0.11}$	$11.60^{+0.29}_{-0.13}$	$7.62^{+0.20}_{-0.08}$
1.42	$-3.88^{+0.12}_{-0.16}$	$11.53^{+0.17}_{-0.09}$	$-1.28^{+0.07}_{-0.08}$	$-3.90^{+0.05}_{-0.07}$	$11.55^{+0.12}_{-0.08}$	$7.76^{+0.07}_{-0.06}$
2.23	—	—	—	$-4.16^{+0.05}_{-0.07}$	$11.22^{+0.11}_{-0.07}$	$7.18^{+0.06}_{-0.05}$
3.24	—	—	—	$-4.16^{+0.08}_{-0.08}$	$10.96^{+0.15}_{-0.08}$	$6.90^{+0.07}_{-0.06}$
[OII]-selected Stellar Mass Function Properties ($L/L^\star(z) > 0.85$)						
1.47	$-3.88^{+0.13}_{-0.13}$	$11.59^{+0.16}_{-0.09}$	$-1.29^{+0.06}_{-0.07}$	$-3.92^{+0.05}_{-0.05}$	$11.62^{+0.10}_{-0.09}$	$7.74^{+0.06}_{-0.06}$
2.25	—	—	—	$-4.48^{+0.07}_{-0.09}$	$11.58^{+0.20}_{-0.08}$	$7.21^{+0.10}_{-0.08}$
3.34	—	—	—	$-5.18^{+0.09}_{-0.13}$	$11.58^{+0.26}_{-0.11}$	$6.51^{+0.16}_{-0.09}$

the literature when making our comparisons, we fix $\alpha = -1.3$ and refit for $\phi_\star$ and $M_\star$ (shown in Table 3.2). Note that our measured α for the Hβ+[OIII] $z = 0.84$ and $z = 1.42$ SMFs and the [OII] $z = 1.47$ SMF are in agreement with the fixed α constraint as shown in Table 3.2.

3.4.2.1 Hβ+[OIII] SMFs: z = 0.84 - 3.24

We show on the left panel of Figure 3.4 the Hβ+[OIII] SMFs from $z = 0.84$ to 3.24 with the corresponding binned measurements and the 1σ confidence area. The tabulated measurements are shown in Table 3.5. We find a strong evolution in $M_\star$ where the characteristic mass increases from $z = 3.24$ to 1.42 and then varies slowly by $z = 0.84$. This is also accompanied by an evolution in $\phi_\star$ where the normalization increases from $z = 3.24$ to 1.42 and, just like $M_\star$, changes very

little to $z = 0.84$. From the viewpoint of the cosmic SFR evolution, we are most likely seeing the rapid build-up of stellar mass between $z = 3.24$ and $z = 1.42$, followed by the decrease in stellar mass growth by $z = 0.84$ as star-formation activity in galaxies declines. We note that this could also be caused by the Hβ+[OIII] selection picking up different populations across cosmic time, particularly due to the change in the typical ionization parameter (see §3.4.4.3).

We compare our results with the UVJ-selected SF SMFs of Muzzin et al. (2013), $NUVrJ$-selected SF SMFs of Ilbert et al. (2013), and *Spitzer* IRAC selected SF SMFs of Pérez-González et al. (2008). Not surprisingly (due to different selection), we find that our measurements, in terms of $\phi_\star$ and $M_\star$, are in disagreement with those from the literature. The only exception is the $z = 1.45$ measurement of Pérez-González et al. (2008), which is in agreement within 1σ of our $z = 1.42$ measurement. As stated above, we fixed $\alpha = -1.3$ based on the faint-end slope measurements from the studies mentioned above. The discrepancy is most likely based on sample selection as our sample is narrow-band selected and will select different population types in comparison to attempts at mass-selected samples such as Pérez-González et al. (2008), Ilbert et al. (2013), or Muzzin et al. (2013).

We also compared our measurements to the HiZELS Hα SMFs of Sobral et al. (2014). We find that there is still discrepancies between our $\phi_\star$ and $M_\star$ and those of Sobral et al. (2014). For the overlapping $z = 0.84$, 1.42, and 2.23 samples, we find disagreements in both $\phi_\star$ and $M_\star$. They find $\log_{10}\phi_\star = -3.55$, -3.71, and -3.82 Mpc^{-3}, $\log_{10} M_\star = 11.17$, 11.11, and 11.37 M$_\odot$, and with a fixed $\alpha = -1.37$ for the overlapping redshifts, respectively. This discrepancy can be attributed to population differences since the Hα samples of Sobral et al. (2014) cover the full range of star-forming galaxies (see Oteo et al. 2015). The issue could be that our Hβ+[OIII] samples (especially at higher redshifts) are missing the dustier, starburst galaxies as shown in Figure 3.3 where we find that the rest-frame UVJ colours are bluer with increasing redshift.

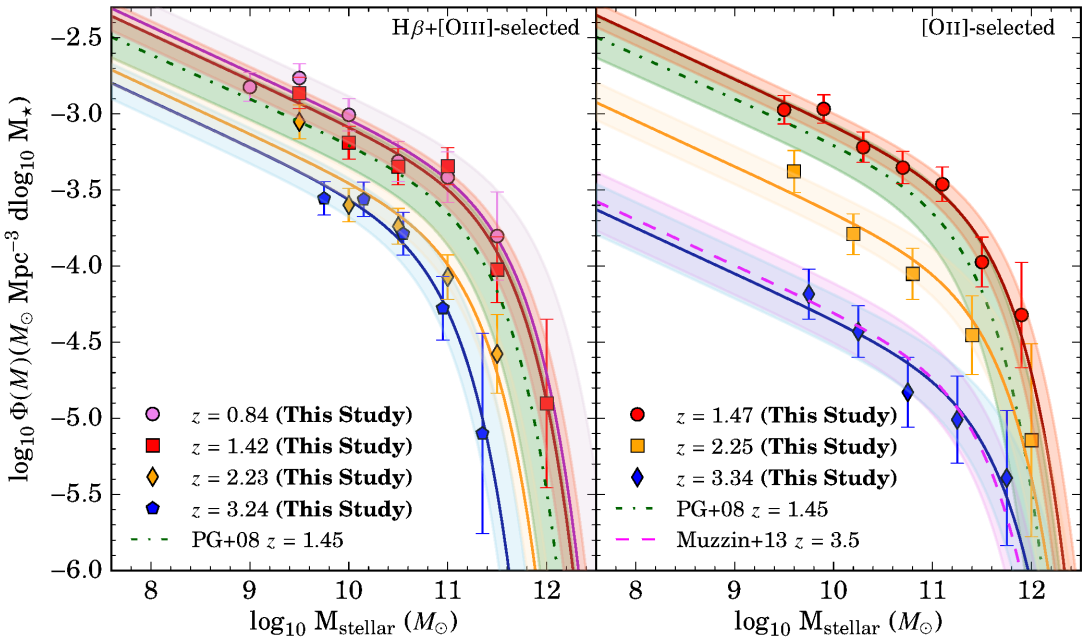

Figure 3.4: *Left:* Hβ+[OIII] stellar mass functions and its evolution from $z \sim 0.84$ to $z \sim 3.24$ for emission-line selected sources. We find that around the $z \sim 2-3$, there is no significant evolution until $z < 2$. *Right:* [OII] stellar mass functions between $z = 1.47$ and 3.34. For [OII], we find a strong, increasing evolution with increasing redshift in $\phi_\star$ while Hβ+[OIII] varies little. We also find that $M_\star$ is strongly decreasing with increasing redshift for Hβ+[OIII] and is relatively constant between $z \sim 1.47$ to 3.34 for [OII].

3.4.2.2 [OII] SMFs: $z = 1.47$ - 3.34

Figure 3.4 presents the [OII] SMFs from $z = 1.47$ to 3.34 with the highlighted regions showing the 1σ confidence area. The tabulated measurements are shown in Table 3.6. We find that there is a strong evolution in $\phi_\star$ and a constant $M_\star$ for all three redshifts sampled. The quick increase in the SMFs as shown in Figure 3.4 could be evidence of the build-up of stellar masses due to an increase in star-forming activity towards the peak of cosmic star-formation.

In comparison to the measurements from the literature, we find that we are in agreement with the UltraVISTA/COSMOS measurements of Muzzin et al. (2013) where they measure a $z = 3.5$ SMF with $\phi_\star = 10^{-5.10\pm0.11}$ Mpc^{-3} and $M_\star = 10^{11.47\pm0.07}$ M$_\odot$ in comparison to our $z = 3.34$ SMF with $\phi_\star = 10^{-5.19^{+0.09}_{-0.13}}$ Mpc^{-3} and $M_\star = 10^{11.58^{+0.26}_{-0.11}}$ M$_\odot$ (within 1σ agreement).

Note that Muzzin et al. (2013) fixed $\alpha = -1.3$ (the same that we used in fitting the SMFs). We also find agreement with the *Spitzer* IRAC-selected, star-forming $z = 1.45$ SMF of Pérez-González et al. (2008) where they find a $\phi_\star = 10^{-3.96\pm0.09}$ Mpc^{-3} and $M_\star = 10^{11.40\pm0.10}$ M$_\odot$ with $\alpha = -1.29 \pm 0.08$ (corrected from Salpeter to Chabrier IMF) in comparison to our $z = 1.47$ SMF with $\phi_\star = 10^{-3.92\pm0.05}$ Mpc^{-3} and $M_\star = 10^{11.62^{+0.10}_{-0.09}}$ M$_\odot$.

We also compare to the HiZELS Hα SMF of Sobral et al. (2014) to the overlapping $z = 1.47$ and $z = 2.25$ measurements. As in the Hβ+[OIII]-Hα comparison, we find discrepancies when comparing $\phi_\star$ and $M_\star$ where they find $\log_{10}\phi_\star = -3.71$ and -3.82 Mpc^{-3}, $\log_{10} M_\star = 11.11$ and 11.37 M$_\odot$, and with a fixed $\alpha = -1.37$, respectively. This discrepancy most likely arises from the Hα sample tracing the full star-forming population, while the [OII] sample could include potential LINERs (low [OIII]/Hβ ratios equates to higher [OII] luminosities) and bright emitters as potential AGNs. Despite this contamination, [OII] has been shown to be a reliable star-forming indicator[4](e.g., Hayashi et al. 2015) and to test whether LINERs and AGNs may be contributing to this discrepancy will require spectroscopic follow-up.

3.4.2.3 Implications of Stellar Mass Function Evolution

The measurements presented in the last two subsections constitutes the first Hβ+[OIII] and [OII] SMFs ever measured in the literature within this redshift range. As discussed above, the Hβ+[OIII] SMFs show an evolution in both Schechter parameters, while the [OII] SMFs only show an evolution in the characteristic normalization. Since we are probing emitters via their emission-lines, the observed measurements will be sensitive to the physical state of the gas that is producing these emission-lines.

One important property is the ionization parameter as measured via the [OIII]/[OII] nebular

[4]This is still a matter of debate as the [OII] line is also metallicity dependent (e.g., Kewley et al. 2004). A recent study by Darvish et al. (2015b) used a sample of 58 spectroscopically-confirmed $z \sim 0.53$ star-forming galaxies and found that the dust- and metallicity-corrected SFR([OII]) was consistent up to ~ 0.02 dex with SFR(Hβ). Future $z > 1$ spectroscopic measurements are needed to reliably ascertain the nature of [OII] as a star-formation indicator.

diagnostic, where a higher ionization parameter will signify strong [OIII] and weak [OII] emission. Recent studies have shown that at a given redshift, the [OIII]/[OII] line ratio is anti-correlated with stellar mass (e.g., Nakajima & Ouchi 2014; Hayashi et al. 2015; Kewley et al. 2015; Sanders et al. 2016). It may then not be surprising to find that the SMFs of [OII] are shifted towards higher $M_\star$, in comparison to the Hβ+[OIII] $M_\star$ measurements for all redshift slices, as those sources would be easier to detect due to lower [OIII]/[OII] ratios (e.g., stronger [OII] versus [OIII]). The evolution in the normalization of the [OII] SMFs may also be hinting to a stronger ionization parameter as the number densities drop relative to [OIII] with increasing redshifts.

In comparison with the HiZELS Hα measurements of Sobral et al. (2014), we find that the Hβ+[OIII] and [OII] SMF parameters have lower $\phi_\star$ and higher $M_\star$ values. When integrating the SMFs to calculate number densities within a finite range ($8.0 < \log_{10} M < 14.0$ $M_\odot$), we find that the number densities of Hα are higher ($\sim 0.2-0.7$ dex) for every redshift slice compared to our samples. This could be due to the Hβ+[OIII] and [OII] emitters being a subset of the total population of SF galaxies traced by Hα (e.g., Oteo et al. 2015). For example, we show in Figure 3.3 that our samples could potentially be missing the dustier, lower-mass, starburst galaxies compared to Hα samples.

3.4.3 Evolution of Stellar Mass Densities

We infer the stellar mass densities (SMDs) by integrating the stellar mass functions for the full mass range:

$$\rho_\star = \int_0^\infty M\Phi(M)\mathrm{d}M = \phi_\star M_\star \Gamma(2+\alpha) \tag{3.4}$$

where $\rho_\star$ is the stellar mass density, $\phi_\star$ is the normalization, $M_\star$ is the characteristic stellar mass, and α is the faint-end slope. We report the SMDs in Table 3.2 for all of our samples.

Our measurements are shown in Figure 3.5 for both Hβ+[OIII] and [OII] up to $z \sim 3.3$. We find that for $z \sim 3.3$ to $z \sim 1.5$, both samples of line emitters shown an increase in stellar mass build-up. This is consistent with the view that galaxies were producing stars at an increasing

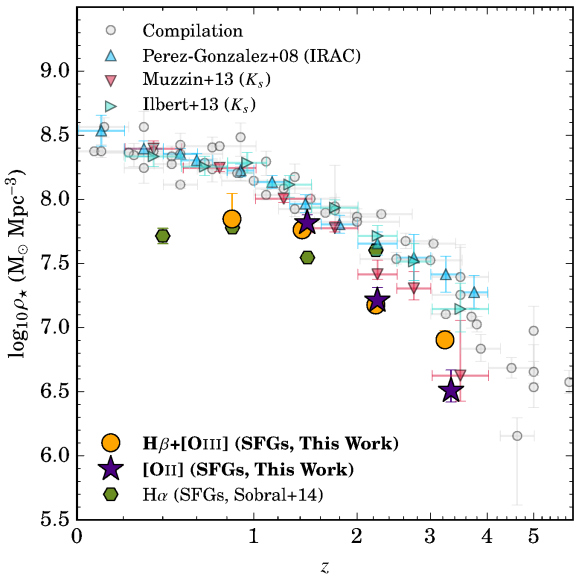

Figure 3.5: The cosmic stellar mass density evolution of our Hβ+[OIII] and [OII] sample. Overlaid are the full population (star-forming + quiescent) measurements from the Madau & Dickinson (2014) compilation. We also highlight the Pérez-González et al. (2008), Ilbert et al. (2013), and Muzzin et al. (2013) SMD measurements. We find that our measurements match the general picture of a fast stellar mass build-up from $z \sim 3.3$ to $z \sim 1$. By $z \sim 1$, we find that our measurements diverge from the full population literature measurements, implying that star-formation activity in emission-line selected galaxies is decreasing resulting in a slower stellar mass assembly growth and a population transition from star-forming/active to quiescent/passive systems.

rate up to $z \sim 2$. In the case of [OII], our assessment of the SMD ends here as we have no $z < 1.5$ [OII] measurements.

We also find that our Hβ+[OIII] and [OII] measurements at $z \sim 1.5$ and ~ 2.2, respectively, are in good agreement. For the $z \sim 3.3$ measurements, we find a discrepancy between the Hβ+[OIII] and [OII] measurements where the separation is ~ 0.4 dex. This discrepancy could be attributed to a sample bias due to the different $L^\star(z)$ cuts that were applied ($0.4L^\star(z)$ and $0.85L^\star(z)$ for Hβ+[OIII] and [OII], respectively) or even number statistics (since the [OII] $z = 3.34$ is the smallest sample being comprised of only 35 emitters, while the Hβ+[OIII] sample contains 179 emitters).

Figure 3.5 also presents a comparison to the full population (star-forming + quiescent) literature compilation of Madau & Dickinson (2014). We also highlight the IRAC-selected full sample of Pérez-González et al. (2008), and the COSMOS/UltraVISTA K_s-band measurements of Ilbert et al. (2013) and Muzzin et al. (2013). We note that these samples have measurements for the star-forming population, although these mass-selected samples are divided by using a colour-colour selection(s) (e.g., UVJ) to separate the quiescent and star-forming populations. We instead use the full population literature measurements as a way to qualitatively gauge the evolution of the star-forming fraction of galaxies.

Also shown on Figure 3.5 are the SMD measurements of the HiZELS Hα sample from Sobral et al. (2014). We find that our measurements are consistent with the literature in the sense that all our measurements are implying a stellar mass build-up all the way to $z = 0.84$. In comparison to the SMD compilation of Madau & Dickinson (2014) and the measurements of Pérez-González et al. (2008), Ilbert et al. (2013), and Muzzin et al. (2013), we find that our Hβ+[OIII] and [OII] SMDs are all below the literature, which is expected as these are for a subset ("active" galaxies) of the total population of galaxies. From $z \sim 3$ to ~ 1.5, this gap diminishes implying that the star-formation fraction increases up to $z \sim 1.5$ where it then decreases until $z \sim 0.8$ as the gap increases. In comparison to the HiZELS Hα measurements of Sobral et al. (2014), we find that we are in agreement for the $z \sim 0.84$ Hβ+[OIII] sample. At all other redshifts, we are not in agreement, but this is due to sample biases where at $z = 1.47$ our Hβ+[OIII] and [OII] samples probe ~ 0.30 and ~ 0.17 dex deeper in line luminosity, respectively, than the Hα measurements. For the $z = 2.23$ measurements, our Hβ+[OIII] and [OII] measurements are at the same line luminosity depth as the Hα measurements of Sobral et al. (2014). The inconsistency could then be attributed to the evolution of the emission lines itself.

We note that this evolution (especially at higher redshifts) could be a byproduct of the change in the physical conditions that produce these lines (see above discussion, §3.4.2.3). Therefore, it is important to keep in mind when interpreting the results shown in Figure 3.5 that other variables (e.g., electron densities, ionization parameter, gas abundances, metal absorption, etc.) can affect and/or drive the evolution (e.g., Nakajima & Ouchi 2014; Hayashi et al. 2015). With this in mind, it becomes apparent that we must study the physical conditions of the ISM for which these lines originate from. We do this in the following sections by investigating the EW_{rest} evolution for each emission line, as well as the observational proxy of the ionization parameter ([OIII]/[OII]) and its evolution over cosmic time.

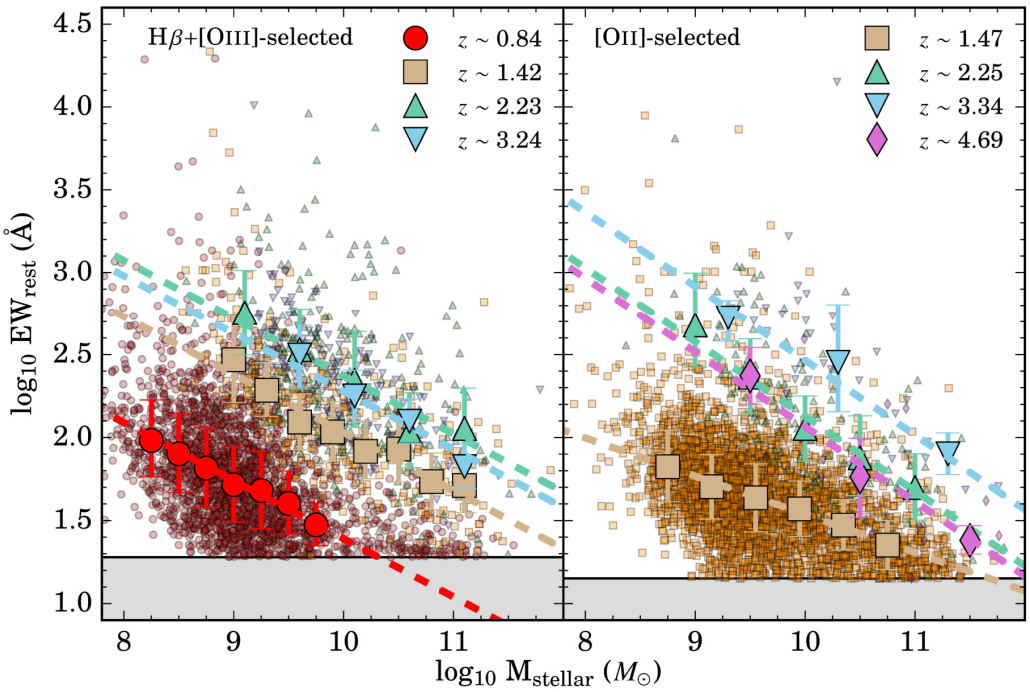

Figure 3.6: Shown is a scatter plot of the EW_{rest} versus $M_{stellar}$ for all our samples. We also include, as larger symbols, the median EW_{rest} for given stellar mass bins. Highlighted in *grey* is the EW_{rest} limit, which results in an incompleteness in our sample for the high-mass sources. This effect is only seen in the Hβ+[OIII] $z = 0.84$ sample and to some extent in the [OII] $z = 1.47$ sample. For the other high-z samples, the EW_{rest} limit does not cause any incompleteness in the high-mass end as we do not probe high enough masses (low EW_{rest}) for which it must be considered.

3.4.4 Equivalent Widths of Hβ+[OIII] and [OII] Emitters

3.4.4.1 Equivalent Width – $M_{stellar}$ Relation

Fumagalli et al. (2012) and Sobral et al. (2014) have both shown a power-law relationship between the median $EW_{rest}(H\alpha)$ and $M_{stellar}$, as well as an increasing evolution in the normalization. This signifies that for every mass bin, the median EW_{rest} for Hα increases with redshift. We extend this analysis for our Hβ+[OIII] and [OII] sample and measure the EW_{rest}-$M_{stellar}$ relationship up to $z \sim 5$.

The EW_{rest} are calculated using Equation 3.1. Note that no dust correction has been applied to the line and continuum fluxes as we assume that $E(B-V)_{nebular} \sim E(B-V)_{stellar}$. The credibility

Table 3.3: Shown are the fitted parameters of the power-law that relates EW_{rest} to $M_{stellar}$. We run two different fits: one for which both parameters are free and the other where $\beta = -0.35$ and -0.45 for Hβ+[OIII] and [OII], respectively. This is to ensure compatibility between samples and mitigation of the bias from selection effects when looking at the evolution of the normalization. The only exception is the $z = 1.47$ [OII], which is fitted for a constant $\beta = -0.23$ as this better fits the data.

Parameters of the Power-Law $EW_{rest} \propto M^{\beta}$				
z	Emitter	β	$\log_{10}$ Norm.	$\log_{10}$ Norm. (β fixed)
0.84	Hβ+[OIII]	-0.33 ± 0.02	4.72 ± 0.14	4.89 ± 0.01
1.42	Hβ+[OIII]	-0.33 ± 0.03	5.33 ± 0.32	5.53 ± 0.02
2.23	Hβ+[OIII]	-0.38 ± 0.06	6.20 ± 0.61	5.87 ± 0.04
3.24	Hβ+[OIII]	-0.43 ± 0.04	6.66 ± 0.38	5.78 ± 0.03
1.47	[OII]	-0.23 ± 0.01	3.79 ± 0.12	3.84 ± 0.01
2.25	[OII]	-0.48 ± 0.04	6.90 ± 0.44	6.63 ± 0.03
3.34	[OII]	-0.41 ± 0.04	6.58 ± 0.45	6.97 ± 0.04
4.69	[OII]	-0.49 ± 0.04	6.97 ± 0.44	6.57 ± 0.03

of assuming that the reddening of the nebular is equivalent to that of the stellar continuum is still in debate. Calzetti et al. (2000) finds $E(B-V)_{nebular} = 2.27E(B-V)_{stellar}$ for which other studies have reached the same conclusion (e.g., Förster Schreiber et al. 2009; Wild et al. 2011; Wuyts et al. 2011; Hemmati et al. 2015). Kashino et al. (2013) measured $E(B-V)_{nebular} = 1.20E(B-V)_{stellar}$ using a sample of 271 sBzK-selected, spectroscopically confirmed Hα sources as part of the FMOS-COSMOS survey. Using 3D-*HST* grism spectroscopic measurements of 79 $z \sim 1$ *Herschel*-selected main sequence star-forming galaxies, Puglisi et al. (2016) measured $E(B-V)_{nebular} = 1.07E(B-V)_{stellar}$. Recently, Shivaei et al. (2015) used a sample of 262 spectroscopically confirmed $z \sim 2$ star-forming galaxies from the MOSDEF survey and concluded that, on average, $E(B-V)_{nebular} = E(B-V)_{stellar}$, although they find it to dependent on SFR. Reddy et al. (2015) came to a similar conclusion that $E(B-V)_{nebular} - E(B-V)_{stellar} = -0.049 + 0.079/\xi$, where $\xi = 1./(\log_{10}[\mathrm{sSFR(SED)/yr^{-1}}] + 10)$. Due to the conflicting measurements in the literature, we find that a change in our initial assumption would result in our EW_{rest} measurements

systematically changing by a factor of $-0.4k(\lambda)[E(B-V)_{\rm nebular} - E(B-V)_{\rm stellar}]$ dex, where $k(\lambda)$ is the dust attenuation curve.

Figure 3.6 shows the full sample with the binned measurements. Because of the significant scatter, each of the binned data points represent the median $\rm EW_{rest}$ and the 1σ errors are measured via bootstrapping to incorporate the errors due to scattering. Based on the actual data points and the binned data, we can see a linear trend such that the $\rm EW_{rest}$ is increasing with decreasing stellar mass. This is also seen in the Hα studies of Fumagalli et al. (2012) and Sobral et al. (2014). We also highlight in Figure 3.6 the $\rm EW_{rest}$ cut which was used in the initial selection of narrow-band colour excess (Sobral et al., 2013a). For the Hβ+[OIII] $z > 1$ and [OII] $z > 2$ samples, this selection does not have an effect on the medians calculated since their $\rm EW_{rest}$ are much higher than the $\rm EW_{rest}$ selection limit. Although, the line flux-limit is more important for our high-z samples as the effect would be the lack of fainter emission-line sources which consequentially leads to sources with lower $\rm EW_{rest}$. For our Hβ+[OIII] $z = 0.84$ and [OII] $z = 1.47$ samples, the $\rm EW_{rest}$ limit affects the median $\rm EW_{rest}$ measured beyond a set mass range. We then only show median $\rm EW_{rest}$ measurements below 10^{10} $\rm M_{\odot}$ for Hβ+[OIII] and 10^{11} $\rm M_{\odot}$ for [OII].

As in Fumagalli et al. (2012) and Sobral et al. (2013a), we find that the median $\rm EW_{rest}$-$M_{\rm stellar}$ relationship is best fitted with a power-law of the form $\rm EW_{rest} \propto M^{\beta}$, where M is the stellar mass and β is the power-law slope. Table 3.3 shows the fitted parameters for each sample. We notice that for all Hβ+[OIII] samples, $\beta \sim -0.35$ which is somewhat higher than the $\beta = -0.25 \pm 0.01$ measured by Sobral et al. (2014) for their Hα samples. This is also consistent with the 3D-*HST* $1.1 < z < 1.5$ $\beta = -0.38$ of Fumagalli et al. (2012). The normalization is found to increase with increasing redshift and flatten out by $z = 3.24$. For the [OII] samples, we find that the $z = 1.47$ is consistent with $\beta = -0.23 \pm 0.01$ while the $z > 1.5$ samples have $\beta \sim -0.45$. This is consistent with the $z = 0.53$ spectroscopic [OII] measurement of Darvish et al. (2015b) where they find $\beta = -0.47 \pm 0.06$. We find the normalization increases up to $z = 3.34$ then seems

to drop by $z = 4.69$.

We note that this evolution is affected by systematic effects arising from selection biases. Since our sample is both EW_{rest}-limited and luminosity-limited, we then miss lower-mass sources ($M < 10^{8.5}$ $M_\odot$) due to the luminosity-limit, and higher-mass sources ($M > 10^{10}$ $M_\odot$; for $z = 0.84$ Hβ+[OIII]) due to the EW_{rest} cut at a fixed SFR. To test how the selection effects can affect our results, we use our most populated and deep samples (Hβ+[OIII] $z = 0.84$ and [OII] $z = 1.47$) and apply luminosity limits between $10^{40.4}$ to $10^{41.7}$ erg s^{-1} in increments of 0.1 dex and fit the same power-law to the sample. We then look at the variations in β and the normalization as a function of the luminosity limit. We find that as the luminosity limit increases, β becomes steeper while the normalization increases. This is expected since the two are not independent from each other. As the luminosity limit increases, then more sources with low-mass will be removed such that the median EW_{rest} increases more towards lower masses, resulting in β becoming steeper and the normalization increasing.

Because of this degeneracy, we then repeat the same methodology with β fixed to -0.35 and -0.45 for all Hβ+[OIII] and [OII] samples, respectively, (except for the [OII] $z = 1.47$ where $\beta = -0.23$) and fit for the normalization as a function of the luminosity limit. We find that the normalization does not change more than < 0.1 dex for Hβ+[OIII] and < 0.01 dex for [OII].

The fit is shown in Table 3.3 and Figure 3.6. We find that the normalization evolution is in fact real and implies that with increasing redshift, the median EW_{rest} for a given stellar mass increases up to $z = 2.23$ for Hβ+[OIII] and for our [OII] sample up to $z = 3.34$.

3.4.4.2 Evolution of Equivalent Widths with Redshift

Based on the normalization seen in the EW_{rest}-$M_{stellar}$ relationship, we study the evolution of the normalization and compare with measurements from the literature. Figure 3.7 shows the evolution of the median EW_{rest} for our Hβ+[OIII] and [OII] measurements. For each measurement, we make a correction for the skewness of the mass distribution per each measurement. Since we

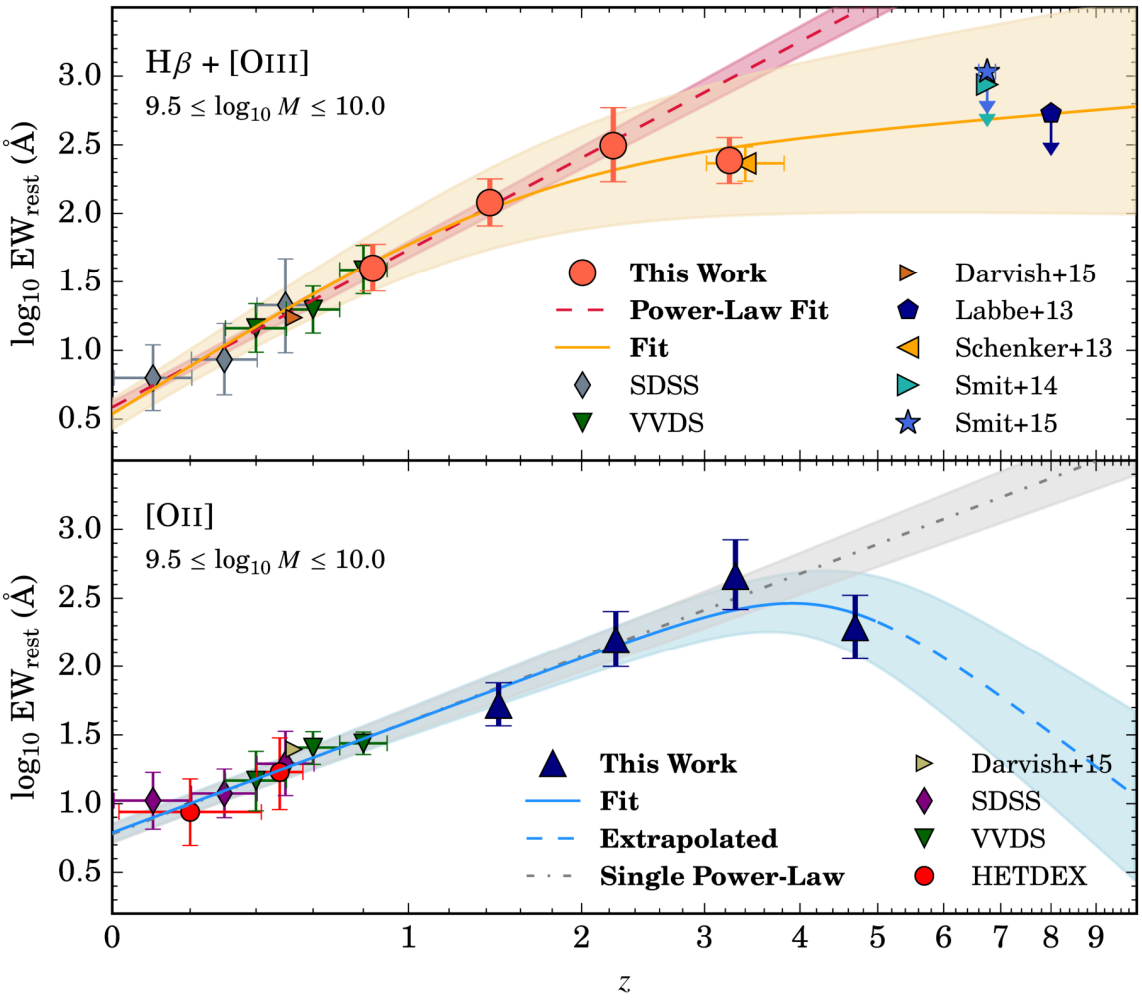

Figure 3.7: Presented is the EW_{rest} evolution for sources that have $9.5 < \log 10 M_{stellar} < 10$ $M_{\odot}$. We also include measurements from the literature to constrain the low-z end and to compare to our extrapolated fits in the high-z regime. We fit single power-law and mixed power-law functions (combination of two power-laws) to our measurements and those from the literature. Included for each fit is the shaded 1σ region. We find that the EW_{rest} evolution for Hβ+[OIII] flattens out to $z > 5$ and the [OII] drops in this regime. In terms of the ionization state of the gas, we find that the EW_{rest} evolution of both emission-lines hints to a harder ionizing source, although other factors such as metallicities and abundances can affect the evolution as well.

select a specific mass range between $10^{9.5} < \log_{10} M < 10^{10.0}$ $M_\odot$[5], we ideally would want the median stellar mass of each of our measurements to be equal to $10^{9.75}$ $M_\odot$. This is not always the case such that the stellar mass distribution is skewed from a normal distribution. Because of the dependency between EW_{rest} and $M_{stellar}$, not correcting for the skewness in the distribution would result in systematic increases/decreases in the measured median EW_{rest} (corresponding to the mean stellar mass measured). To correct for this, we measure the mean mass for each sample and compute the inferred EW_{rest} from the corresponding fit. We then compute based on the fit what the median EW_{rest} should be at the center of the mass bin ($10^{9.75}$ $M_\odot$) and then subtract both measurements to get a correction factor. The result is that the median EW_{rest} increases/decreases (~ 0.1 dex) based on whether the mean mass was above/below $10^{9.75}$ $M_\odot$.

Included in Figure 3.7 are the Hβ+[OIII] measurements from the literature (Labbé et al., 2013; Schenker et al., 2013b; Smit et al., 2014, 2015). To ensure a constrained $EW_{rest}(z = 0)$, we compute the median EW_{rest} from the SDSS-III/BOSS-DR12 spectroscopic sample Thomas et al. (2013) by selecting only emission-lines with $EW_{rest} > 3$ Å to ensure that the measured EW_{rest} is not dominated by uncertainties in the stellar continuum subtraction (Fumagalli et al., 2012) and all galaxies that were classified as star-forming based on the BPT diagram. The VVDS catalog of Lamareille et al. (2009) was also included where only galaxies identified as star-forming were selected. We also include the [OIII] $z \sim 0.53$ EW_{rest} measurements from the Keck DEIMOS spectroscopic sample of Darvish et al. (2015b).

For the [OII] sample, we also compute the median EW_{rest} from the HETDEX survey (Adams et al., 2011; Bridge et al., 2015) and remove any sources with X-ray detection found by Bridge et al. (2015) to eliminate AGN contamination. We also include the [OII] $z \sim 0.53$ EW_{rest} measurements from Darvish et al. (2015b). Figure 3.8 shows the Hα EW_{rest} evolution

[5]We select this mass range to be consistent with the $z > 5$ studies (e.g, Labbé et al. 2013; Smit et al. 2014; Rasappu et al. 2016; Smit et al. 2015) and also because it corresponds to the peaks in our stellar mass distributions as shown in Figure 3.1.

Power-Law Fit Parameters					
Sample	Model	$EW_{rest}(z=0)$ (Å)	γ	ϵ	c
Hβ+[OIII]	Single	3.85 ± 0.34	3.81 ± 0.14	...	...
Hβ+[OIII]	Mixed	3.53 ± 0.90	4.53 ± 0.63	3.93 ± 0.47	2.57 ± 0.46
[OII]	Single	6.00 ± 0.90	2.72 ± 0.19	...	...
[OII]	Mixed	6.14 ± 0.95	2.68 ± 0.25	8.09 ± 1.38	5.35 ± 0.54
Hα	Single	21.14 ± 2.54	1.82 ± 0.20	...	...

Table 3.4: Measurements of the Power-Law Parameters. Two different models were used to fit the data. Those listed as "single" refer to a single power-law of the form $(1+z)^{\gamma}$ and those listed as "mixed" refer to the model as defined in Equation 3.5.

found in the literature (Erb et al., 2006; Fumagalli et al., 2012; Sobral et al., 2014; Rasappu et al., 2016; Faisst et al., 2016) in comparison to the EW_{rest} evolution of the Hβ+[OIII] and [OII] samples. We selected a mass range of $10^{9.5} < M < 10^{10.0}$ $M_{\odot}$ for all determinations of the EW_{rest} evolution. Changing the mass range used in Figures 3.7 and 3.8 only changes the normalization because of the power law relationship shown in Figure 3.6. Furthermore, all errors presented in Figure 3.7 and 3.8 for our sample and the SDSS, VVDS, and HETDEX determined measurements are based on a bootstrapping assessment to calculate the 95% confidence intervals.

To ensure that all the literature data is consistent and comparable with our data set, we correct the literature measurements to match our IMF (convert from the literature-assumed IMF to Chabrier (2003) IMF) and also cover the same mass range ($10^{9.5} < M < 10^{10.0}$ $M_{\odot}$). We also make another correction for the $z > 5$ Hβ+[OIII] literature data points (Labbé et al., 2013; Smit et al., 2014, 2015) as described in Appendix 3.6.4 to take into account the contribution of Hβ in the total EW_{rest} measured in these studies.

We fit the evolution of the EW_{rest} (z) to a mix of power-laws of the form:

$$EW_{rest}(z) = EW_{rest}(z=0)\frac{(1+z)^{\gamma}}{1+[(1+z)/c]^{\epsilon}} \tag{3.5}$$

where γ and ϵ are the power-law slopes. This functional form is similar to that used by Madau

& Dickinson (2014) to model the cosmic SFRD evolution. For the Hβ+[OIII] sample, we only use our measurements, our SDSS and VVDS determinations, and the upper limits set by Labbé et al. (2013) and Smit et al. (2014, 2015) to constrain the fit. For the [OII] sample we use our measurements, the SDSS and VVDS determinations, and the HETDEX measurements. The fitted parameters are shown in Table 3.4 for our sample of Hβ+[OIII] and [OII] emitters, as well as the HiZELS Hα sample from Sobral et al. (2014), which was further constrained by the SDSS and VVDS data. We also overlay the fits and their 1σ error range on Figure 3.7. Note that we also fit a simple power-law of the form $(1+z)^{\gamma}$. This functional form has been shown to work for the Hα $\mathrm{EW_{rest}}$ evolution (e.g., Fumagalli et al. 2012; Sobral et al. 2014; Rasappu et al. 2016; Marmol-Queralto et al. 2015).

As shown in Figure 3.7, a single power-law would match our Hβ+[OIII] measurements and others drawn from the literature up to $z \sim 2$. For $z > 2$, a single power-law model would pass above the upper limits set by Smit et al. (2014, 2015) and Labbé et al. (2013) hinting that the slope becomes shallower and deviates from a simple power-law form. Also, our $z = 3.24$ and the $z \sim 3.5$ measurement of Schenker et al. (2013b) both provide evidence that the evolution becomes shallower. The change in the slope of the $\mathrm{EW_{rest}}$ evolution has also been recently detected by Marmol-Queralto et al. (2015) where they use grism spectroscopy of the Hα line from the 3D-*HST* survey and samples of spectroscopically confirmed and photometric-redshift selected galaxies from CANDELS within the redshift interval $1 < z < 5$. Faisst et al. (2016) also reports a change in the power-law slope with increasing redshift up to $z \sim 6$ where the power-law deviates from $(1+z)^{1.8}$ to $(1+z)^{1.3}$. We use the mixed power-law model shown in Equation 3.5 to incorporate the deviation from a single power-law and fit to our measurements, the SDSS determinations, the $z \sim 3.5$ measurements of Schenker et al. (2013b), and the upper limits set by Labbé et al. (2013) and Smit et al. (2014, 2015). We find that the model defined in Equation 3.5 better fits the observed measurements.

The lower panel of Figure 3.7 shows the [OII] $\mathrm{EW_{rest}}$ evolution up to $z \sim 5$, along with

measurements from HETDEX, VVDS, SDSS, and Darvish et al. (2015b). Our measurements are the first that cover the $z \sim 1.5$ to 5 range allowing us to compare to the $z < 1$ regime. We initially fit to a single power-law and find that the [OII] evolution increases up to $z \sim 3$. There is some evidence in our measurements for a drop from $z \sim 3$ to ~ 5, but more measurements have to be made in the $z > 3$ regime in order to confirm the decreasing evolution. To incorporate this drop seen between our $z = 3.34$ and $z = 4.69$ measurements, we fit using the model described in Equation 3.5.

Our Hβ+[OIII] and [OII] fits using the mixed power-law model described in Equation 3.5 are shown in Figure 3.7 with the measured parameters described in Table 3.4. We find an increasing evolution in the EW_{rest}(Hβ+[OIII]) and EW_{rest}([OII]) up to $z \sim 2-3$. The Hβ+[OIII] evolution trend becomes shallower from $z \sim 2$ to higher z. This is constrained by our $z \sim 2.23$ and ~ 3.34 measurements, the $z \sim 3.5$ measurement of Schenker et al. (2013b), and the recent measurements of Labbé et al. (2013) and Smit et al. (2014, 2015). The literature measurements can be interpreted as upper limits since they require a significant excess in the *Spitzer* IRAC bands to be detected. But this assumes that the UV is bright enough that the highest EW sources are detected. Based on this interpretation, we can constrain the high-z end using our $z > 2$ measurements with the condition that the fit cannot exceed the upper limits.

Beyond $z > 3$, we find some evidence that the EW_{rest}([OII]) is decreasing to higher z. Currently, there are no other measurements in the literature that cover this redshift regime. Our EW_{rest}([OII]) measurements are the first presented in the literature at these redshifts for which we can assess the cosmic evolution of the [OII] equivalent width. Future studies from the next-generation of telescopes and space observatories will better constrain the EW_{rest}([OII]) evolution. Based on our results, we can conclude that there is some evidence of a decrease in the EW_{rest}([OII]) for $z > 3$. It is not surprising then that high-z UV studies (e.g., Smit et al. 2014, 2015) do not find strong evidence for [OII] but do find [OIII] since, based on our measurements and the mixed power-law fits, the [OII] EW_{rest} is significantly lower than [OIII]. This could be

due to a combination of changes in the oxygen abundances and ionization state of the gas.

We also show in Figure 3.8 the comparison of the $EW_{rest}(H\alpha)$ evolution, measured from the HiZELS Hα sample of Sobral et al. (2014), with our $EW_{rest}(H\beta+[OIII])$ and $EW_{rest}([OII])$ measured evolution. We find that based on the fits, $EW_{rest}(H\beta+[OIII])$ drops from high to low-z the fastest, followed by [OII] and then by Hα. In terms of the required ionization potentials to form these lines, it is then not surprising that the $EW_{rest}(H\beta+[OIII])$ drops the fastest since it requires a higher ionization parameter (photons with ≈ 35.12 eV) to cause a strong [OIII] line. This is then followed by [OII] (≈ 13.62 eV) and Hα (≈ 13.60 eV) in decreasing order of required ionization potentials. The EW_{rest} evolution of Hβ+[OIII] compared to [OII] and Hα is consistent with the view that the ionization parameter is decreasing with decreasing redshift. However, the difference in the EW_{rest} evolution of [OII] and Hα is most likely attributed to the evolution in metallicities as the ionization potentials are essentially the same. It has been found that the oxygen abundance ($12+\log_{10}O/H$) increases by $0.2-0.3$ dex from $z\sim2$ to $z\sim0$ (e.g., Steidel et al. 2014; Sanders et al. 2015). This corresponds to lower electron temperatures resulting in electrons with less energy ($\sim kT_e$) to form the [OII] line. The same applies for the [OIII] line but, because of the large difference in ionization potentials between O^{++} and H^{+}, the evolution in the ionization

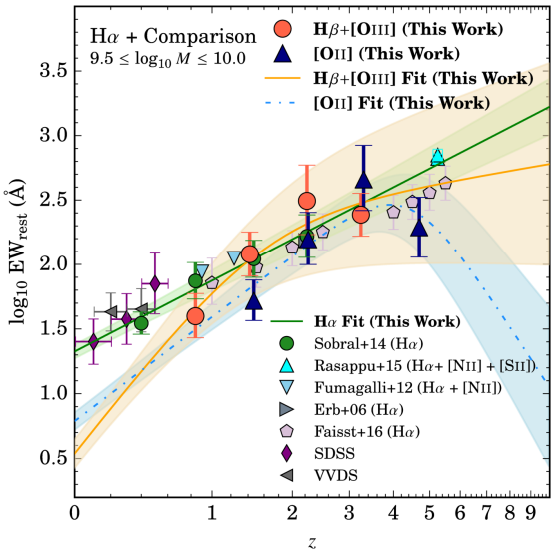

Figure 3.8: The EW_{rest} evolution of major rest-frame optical emission lines within $9.5 < \log_{10} M_{stellar} < 10$ $M_\odot$. We include our empirical fits of the Hβ+[OIII] and [OII] EW_{rest} evolution in order to study how the EW_{rest} evolves per nebular emission-line. We find that the Hβ+[OIII] EW_{rest} drops faster from high-z to low-z than the other emission-lines. This is followed by [OII] and then by Hα such that the Hβ+[OIII] EW_{rest} at $z=0$ is weaker compared to [OII], which is also weaker than Hα. The drops are in order of higher to lower ionization potentials such that in the low-z Universe, higher ionization potential lines have lower EW_{rest} relative to low ionization potential lines. We also find that the Hβ+[OIII] EW_{rest} is much higher than [OII] for $z>5$, implying a Universe with extreme ionizing sources that easily can produce the [OIII] line.

parameter could be the dominant factor. Overall, the EW_{rest} decline for all emission-lines matches the current view of cosmic star-formation activity which has been in decline for the ~ 11 Gyr. A decrease in star formation rates results in the decrease of bright, massive stars that can create UV photons to form the emission lines we observe.

3.4.4.3 Evolution of the Ionization State

We have shown in Figures 3.7 and 3.8 the evolution in the three major nebular emission-lines associated with star-formation to high-z. Based on this evolution, we investigate how the [OIII]/[OII][6] ratio changes with redshift. The [OIII]/[OII] line ratio is an important observational proxy of the ionization state of the gas since the [OIII] line has a higher ionization potential compared to the [OII] line and has been used in many studies in the literature (e.g., Nakajima et al. 2013; Nakajima & Ouchi 2014; Hayashi et al. 2015). We note that the [OIII]/[OII] line ratio is also dependent on stellar mass and metallicity (e.g., Kobulnicky & Kewley 2004; Liu et al. 2008; Hayashi et al. 2015; Kewley et al. 2015). To properly understand the dependency of [OIII]/[OII] with the ionization parameter, stellar mass, gas-phase abundances and metallicities requires spectroscopic follow-up. In this section, we present our analysis of the [OIII]/[OII] evolution in terms of the evolution in the ionization parameter but caution the reader that other factors affect this evolution as well.

If we assume that our Hβ+[OIII] samples are primarily [OIII] emitters (see discussion in §3.3.4), then we can take our observed Hβ+[OIII] and [OII] EW_{rest} and measure the ratio to determine [OIII]/[OII]. We take the ratios of the equivalent widths rather than the ratios of the emission lines as the dependency on dust correction is eliminated with the assumption that $E(B-V)_{\rm nebular} \sim E(B-V)_{\rm stellar}$ (see discussion in §3.4.4.1 on how this assumption affects the results). An issue that arises is that the continuum flux at rest-frame **3727**Å and **5007**Å may not

[6] We define [OIII]/[OII] as [OIII]4959,5007/[OII]3726,3729. This is to take into account the potential double detection of [OIII]4959 and [OIII]5007 in the NB photometry as discussed in §3.3.4. All literature measurements have the same [OIII]/[OII] definition.

be equivalent/similar. To test how this can affect our measurements of [OIII]/[OII], we compare the EW_{rest}([OIII])/EW_{rest}([OII]) and the $\boldsymbol{F}_{[OIII]}/\boldsymbol{F}_{[OII]}$ line ratios from the SDSS-III/BOSS-DR12 (Thomas et al., 2013) and VVDS (Lamareille et al., 2009) catalogs. This comparison is shown in Appendix 3.6.5. We find that using the EW_{rest} to measure [OIII]/[OII] is consistent, on average, with using the line fluxes with a negligible systematic offset arising from the differing continuum fluxes (-0.06 and -0.04 dex for SDSS and VVDS, respectively; see Figure 3.11).

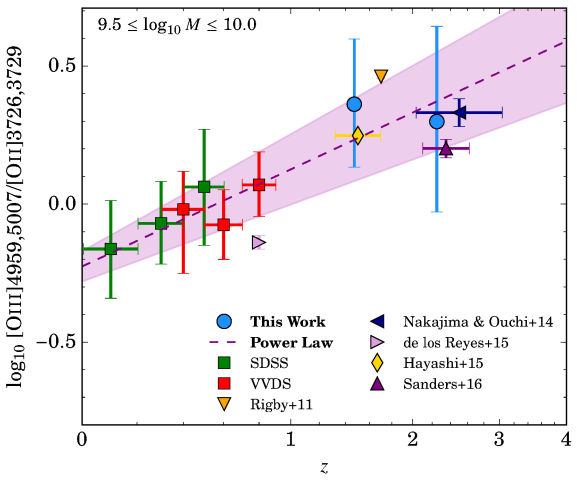

Figure 3.9: Shown is the [OIII]/[OII] evolution. Included are measurements from SSDS and VVDS, as well as other spectroscopic measurements from the literature. We find that the [OIII]/[OII] increases with redshift suggesting an increasing ionization parameter with redshift, which can be attributed to a harder ionization field and/or changes in metallicity and electron densities. Overall, the [OIII]/[OII] evolution shown here explains why recent studies have detected emission lines that require high ionization potentials at $z > 6$ (e.g., Vanzella et al. 2010; Sobral et al. 2015a; Stark et al. 2015a,b).

Figure 3.9 shows the [OIII]/[OII] evolution with our observational measurements at $z = 1.47$ and 2.25 along with measurements we computed from SDSS-III/BOSS-DR12 (3498 sources; Thomas et al. 2013) and VVDS (204 souces; Lamareille et al. 2009; Le Fèvre et al. 2013). We also include the $z \sim 2.3$ measurement of MOSDEF (41 sources; Sanders et al. 2016)[7], the $z \sim 1.5$ measurement of (68 sources; Hayashi et al. 2015), and the single lensed, star-forming galaxy $z \sim 1.7$ measurement of Rigby et al. (2011). We also compute the [OIII]/[OII] ratios of the NewHα (112 sources; de los Reyes et al. 2015) and Nakajima & Ouchi (2014, 14 sources) samples by selecting sources with stellar masses within $9.5 < \log_{10} M < 10.0$ $M_\odot$. The [OIII]/[OII] measurement for a lensed, star-forming galaxy is also included (Rigby et al., 2011). We have also measured the [OIII]/[OII] ratio for $z = 3.34$ and $z = 4.69$ (using the EW_{rest}(Hβ+[OIII]) fit at that redshift) but the error bars are ~ 1 dex. Therefore, we exclude these two measurements as they do not really provide any extra constraints, but we note that they are consistent, within 1σ, with our results

in Figure 3.9.

Overall, our measurements combined with those from the literature show that the [OIII]/[OII] ratio is increasing up to $z \sim 3$ such that at higher redshifts the ionization parameter was higher. When we compare our measurements with those within the same redshift range, we find that we are within 1σ agreement. We note that the literature measurements are for the mass range $9.5 < \log_{10} M < 10.0$ $M_\odot$.

We fit the evolution of the [OIII]/[OII] ratio to a power-law of the form:

$$[\text{OIII}]/[\text{OII}] = [\text{OIII}]/[\text{OII}](z = 0)(1 + z)^{\eta} \tag{3.6}$$

where we find $[\text{OIII}]/[\text{OII}](z = 0) = 0.59 \pm 0.07$ (normalization) and $\eta = 1.17 \pm 0.24$ (power-law slope). We only use the SDSS, VVDS, and our measurements to fit for the power-law. The fit along with the 1σ region is shown in Figure 3.9 and matches well with the observed data points not used in the fitting process. Based on our power-law model, the [OIII]/[OII] ratio is predicted to continue to increase with redshift. This matches with the fits shown on Figure 3.7 where we find that the evolution of $\text{EW}_{\text{rest}}(\text{H}\beta+[\text{OIII}])$ becomes shallower and the $\text{EW}_{\text{rest}}([\text{OII}])$ drops significantly. The situation could be that the hardness of the ionizing source increases when going back in cosmic time such that the production of an [OII] emission-line is suppressed as electrons in doubly-ionized oxygen are unable to transition to lower energy levels when bombarded by highly energetic photons and free electrons. The conclusion that a harder ionization field is driving the [OIII]/[OII] evolution has also been suggested by Hayashi et al. (2015) and Kewley et al. (2015). We note that this can also be the byproduct of changes in the metallicity of galaxies (Sanders et al., 2016), higher electron densities (Shirazi et al., 2014), geometry of the gas (Kewley et al., 2013), or a combination of global properties (Nakajima & Ouchi, 2014).

[7] The Sanders et al. (2016) measurement was recomputed to only cover the $9.5 < \log_{10} M < 10.0$ $M_\odot$ since [OIII]/[OII] is also a function of stellar mass (e.g., Hayashi et al. 2015). We recompute their [OIII]/[OII] measurement and calculate the errors via bootstrapping. The measurement cited in Sanders et al. (2016) is $\log_{10}[\text{OIII}]/[\text{OII}] = 0.10^{+0.37}_{-0.11}$. Also, the total sample size used in the [OIII]/[OII] measurement of Sanders et al. (2016) was 103 sources. Due to the stellar mass cut, the sample size was reduced to 41 sources.

Future spectroscopic studies covering a wide range of galaxy types are needed to study what is driving the changes in the ionization parameter and whether or not it is a combination of different components. Based on our results, we can safely state the ionization parameter is increasing although the origin is still a matter of debate.

Our results for the [OIII]/[OII] evolution and its extrapolation to $z > 3$ can also explain why recent spectroscopic observations are able to find emission-lines from high ionization potential transitions (e.g., CIII], CIV, NIV, HeII). Stark et al. (2014) spectroscopically observed 17 $z \sim 2$ gravitationally-lensed galaxies to find strong NIV], OIII], CIV, SiIII], and CIII] emission-lines requiring photons with energies > 47 eV, much higher than the local Universe. Their argument is using such emission-lines that require high ionization energies could be used in conjunction with Lyα to study reionization. This led to the spectroscopic detection of NIV ($z = 5.56$; Vanzella et al. 2010), CIII] ($z \sim 6-7$; Stark et al. 2015a), and CIV ($z = 7.045$; Stark et al. 2015b) emitters, such that the ionizing source is much harder with increasing redshift. An even more extreme case is the recent discovery of HeII in the COSMOS Redshift 7 (CR7) source (Sobral et al., 2015b). To produce this emission line requires ionizing photons with energy ~ 54 eV and has been attributed to the presence of PopIII stars or direct collapse black holes (e.g., Pallottini et al. 2015; Dijkstra et al. 2016; Visbal et al. 2016). The following studies comprise a handful of sources but match our extrapolation of the [OIII]/[OII] evolution to show that the ionization parameter increases with redshift. Future studies using the next-generation space-based observatories (e.g., ***JWST***) could spectroscopically observe the traditional optical emission-lines for $z > 5$ (falls in observer-frame infrared) and assess the ionization state of the gas with better accuracy. For now, we present our extrapolated $z > 3$ results as a prediction that can be tested by future high-z studies.

3.5 Conclusions

We have presented the evolution of the stellar mass functions and densities up to $z \sim 3$, the evolution of the rest-frame equivalent widths up to $z \sim 5$, and the evolution of the ionization parameter as described by the [OIII]/[OII] ratio up to $z \sim 3$. The main results of this study are the following:

1. In conjunction with the widely used UVJ colour-colour classification scheme, we find that $\sim 98\%$ of all Hβ+[OIII] and [OII] emitters are classified as "active" (star-forming or AGN) galaxies.

2. The stellar mass functions of Hβ+[OIII] emitters show a strong, increasing evolution in $M_\star$ from $10^{10.96^{+0.15}_{-0.08}}$ M$_\odot$ to $10^{11.60^{+0.29}_{-0.13}}$ M$_\odot$ and a weak, increasing evolution in $\phi_\star$ from $10^{-4.16\pm0.08}$ Mpc^{-3} to $10^{-3.87^{+0.06}_{-0.11}}$ Mpc^{-3} with decreasing redshift. Similar trends are seen for the stellar mass functions of [OII] emitters from $z = 1.47$ to $z = 3.34$ where an unchanging $M_\star \sim 10^{11.60}$ M$_\odot$ is seen for all redshifts sampled and a strong, increasing evolution in $\phi_\star$ from $10^{-5.18^{+0.09}_{-0.13}}$ Mpc^{-3} to $10^{-3.92\pm0.05}$ Mpc^{-3} with decreasing redshift.

3. The similarity between the $z = 0.84$ and 1.42 Hβ+[OIII] SMFs and the rise in the SMFs between $z = 3.24$ to $z = 1.42$ is probable evidence for the rapid stellar mass build-up followed by its decay due to the decrease of star-formation activity in the Universe. The stellar mass functions of the [OII] emitters all shows rapid build-up of stellar masses from $z = 3.34$ to $z = 1.47$ for [OII]-selected galaxies.

4. Stellar mass densities of our Hβ+[OIII] and [OII] emitters, in conjunction with the HiZELS Hα SMDs of Sobral et al. (2014), show how the evolution in the SMDs traces that of the full sample (passive + active) as found in the literature. By $z = 0.84$, we find that the SMDs deviate from the full population implying the transition of active galaxies into passive galaxies. This ties into the picture of decreasing star-formation activity in the Universe.

5. The relationship between EW_{rest} and stellar mass for Hβ+[OIII] and [OII] emitters up to $z \sim 3$ and ~ 5, respectively, is studied for the first time where we find a power-law relationship between the two physical properties as seen in Hα studies (e.g., Fumagalli et al. 2012; Sobral et al. 2014). We find that all our Hβ+[OIII] samples are best represented by $EW_{rest} \propto M^{-0.35}$ and the [OII] samples as $\propto M^{-0.45}$. The $z = 1.47$ [OII] sample has a shallower trend best fit as $\propto M^{-0.23}$.

6. We find that the Hβ+[OIII] EW_{rest} increases from $z = 0$ to $z \sim 2$ by a factor of ~ 100. From $z \sim 2$ to ~ 8, we find evidence for a shallower trend by using the *Spitzer* IRAC measurements of Labbé et al. (2013) and Smit et al. (2014, 2015) as upper limits and also the deviation from the $z = 0 - 2$ power-law seen by our $z = 3.24$ EW_{rest} and the $z \sim 3.5$ Keck/MOSFIRE EW_{rest} measurement of Schenker et al. (2013b).

7. We present the first measurement of the [OII] EW_{rest} out to $z \sim 5$. We find that the [OII] EW_{rest} increases by a factor of ~ 60, followed by a decrease in EW_{rest} to higher redshift. This could be one reason why no high-z measurements of [OII] exists in the $z > 5$ regime from UV studies that are finding ubiquitous high Hβ+[OIII] EW sources.

8. We study the evolution of the ionization state of the gas using the [OIII]/[OII] line ratio. The line ratio increases beyond $z \sim 3$ such that the higher the redshift, the higher the ionization parameter. This could explain the lack of [OII] detections at high-z. If the higher ionization parameter is due to a harder ionizing source (e.g., high energy photons coming from massive stars), then it could suppress the [OII] line while producing a stronger [OIII] line as the doubly-ionized oxygen atoms are bombarded with highly energetic photons and free electrons such that they can not make the transition to produce an [OII] line. The higher ionization parameter can also explain the recent detections of emission lines with high ionization potentials at $z \sim 5$ to ~ 7 (e.g., CIII], CIV, HeII, NIV). The physical reason for a higher

ionization parameter is still in debate and can be explained by a harder ionizing radiation field, electron densities, and metallicities.

Our results present a clearer picture of the EW_{rest} of the Hβ+[OIII] and [OII] lines, as well as an understanding of how the strengths of these lines and its dependency on the changes in the ionization state of the gas can explain the recent developments in detecting Hβ+[OIII] at $z \sim 6-8$ and other emission lines that arise from transitions involving high ionization potentials. The results highlighted in this paper prepare for the next-generation of ground-based telescopes (e.g., Thirty Meter Telescope) and state-of-the-art space-based observatories (e.g., *JWST*, *EUCLID*, *WFIRST*) by presenting an outline of the evolution of the EW_{rest} and the [OIII]/[OII] line ratio and predictions for the high-z Universe that can better our understanding of the physical conditions for which forms the observed EW_{rest} and [OIII]/[OII] line ratios.

3.6 Appendix

3.6.1 Stellar Mass Functions

3.6.2 Stellar Mass Comparisons

The COSMOS and UDS fields both have a wealth of multi-wavelength data, which is useful when measuring the physical properties (e.g., stellar masses) of galaxies via SED fitting. Stellar masses for COSMOS includes the i-band selected measurements of Ilbert et al. (2010) using *Le Phare* and the UltraVISTA/COSMOS K_s-band selected measurements of Muzzin et al. (2013) using *FAST*. Our Hβ+[OIII]- and [OII]-selected samples are from both fields but we measure the stellar masses using MAGPHYS. This is to ensure that stellar masses are measured using the same SED fitting code in both fields. Not normalizing the stellar mass determinations to the same code can introduce systematic effects arising from model dependencies.

Table 3.5: Hβ+[OIII]-selected stellar mass function. Shown are the stellar mass bins ($\log_{10} M$), the number of sources per bin (#), the observed ($\Phi_{\rm obs}$) and final ($\Phi_{\rm final}$) stellar mass distribution per stellar mass bin, and the comoving volume per bin. $\Phi_{\rm final}$ includes the completeness, EW, and filter profile corrections.

$\log_{10} M$ ($M_\odot$)	#	$\Phi_{\rm obs}$ (Mpc^{-3} d$\log_{10}$M)	$\Phi_{\rm final}$ (Mpc^{-3} d$\log_{10}$M)	Volume (10^5 Mpc^3)
$z = 0.84$				
9.00±0.25	185	−2.95	-2.82 ± 0.09	3.33
9.50±0.25	185	−2.95	-2.76 ± 0.09	3.33
10.00±0.25	64	−3.42	-3.01 ± 0.10	3.33
10.50±0.25	23	−3.86	-3.31 ± 0.13	3.33
11.00±0.25	11	−4.18	-3.42 ± 0.17	3.33
11.50±0.25	3	−4.74	-3.80 ± 0.29	3.33
$z = 1.42$				
9.50±0.25	111	−3.03	-2.86 ± 0.10	2.37
10.00±0.25	80	−3.40	-3.19 ± 0.11	4.06
10.50±0.25	54	−3.57	-3.35 ± 0.12	4.06
11.00±0.25	44	−3.66	-3.34 ± 0.12	4.06
11.50±0.25	8	−4.40	-4.02 ± 0.22	4.06
12.00±0.25	1	−5.31	-4.90 ± 0.55	4.06
$z = 2.23$				
9.50±0.25	74	−3.26	-3.05 ± 0.11	2.72
10.00±0.25	77	−3.83	-3.60 ± 0.11	10.45
10.50±0.25	53	−4.00	-3.74 ± 0.12	10.68
11.00±0.25	22	−4.39	-4.07 ± 0.15	10.68
11.50±0.25	5	−5.03	-4.58 ± 0.26	10.68
$z = 3.24$				
9.75±0.20	50	−3.88	-3.56 ± 0.11	9.38
10.15±0.20	49	−3.93	-3.56 ± 0.11	10.47
10.55±0.20	19	−4.34	-3.79 ± 0.14	10.47
10.95±0.20	6	−4.84	-4.28 ± 0.21	10.47
11.35±0.20	1	−5.62	-5.10 ± 0.66	10.47

Table 3.6: [OII]-selected stellar mass function. Same as in 3.5.

$\log_{10} M$ ($M_\odot$)	#	$\Phi_{\rm obs}$ (Mpc^{-3} d$\log_{10}$M)	$\Phi_{\rm final}$ (Mpc^{-3} d$\log_{10}$M)	Volume (10^5 Mpc^3)
$z = 1.47$				
9.50±0.20	202	−3.14	-2.97 ± 0.09	6.97
9.90±0.20	188	−3.17	-2.97 ± 0.09	6.97
10.30±0.20	94	−3.47	-3.22 ± 0.10	6.97
10.70±0.20	64	−3.64	-3.35 ± 0.11	6.97
11.10±0.20	42	−3.82	-3.46 ± 0.11	6.97
11.50±0.20	11	−4.40	-3.97 ± 0.16	6.97
11.90±0.20	2	−5.14	-4.32 ± 0.35	6.97
$z = 2.25$				
9.60±0.30	47	−3.48	-3.38 ± 0.14	2.36
10.20±0.30	43	−3.94	-3.79 ± 0.13	6.29
10.80±0.30	22	−4.23	-4.05 ± 0.17	6.29
11.40±0.30	7	−4.73	-4.45 ± 0.26	6.29
12.00±0.30	1	−5.58	-5.14 ± 0.63	6.29
$z = 3.34$				
9.75±0.25	13	−4.44	-4.18 ± 0.16	7.13
10.25±0.25	10	−4.73	-4.43 ± 0.17	10.84
10.75±0.25	5	−5.14	-4.83 ± 0.23	13.81
11.25±0.25	3	−5.36	-5.01 ± 0.29	13.81
11.75±0.25	1	−5.84	-5.39 ± 0.44	13.81

We compare our stellar mass measurements in Figure 3.10 to those of Ilbert et al. (2010) (*top panel*) and Muzzin et al. (2013) (*bottom panel*). Both studies used a Chabrier IMF but different SED fitting codes and sets of filters, which is the most probable reason for the scatter. To eliminate the scatter arising from redshift differences, we only show comparison measurements for which the difference between the redshift measurement in our catalogs (measured using EaZY, see Khostovan et al. 2015) and the comparison measurements is < 0.1. Overall, we find that our measurements are consistent with the literature.

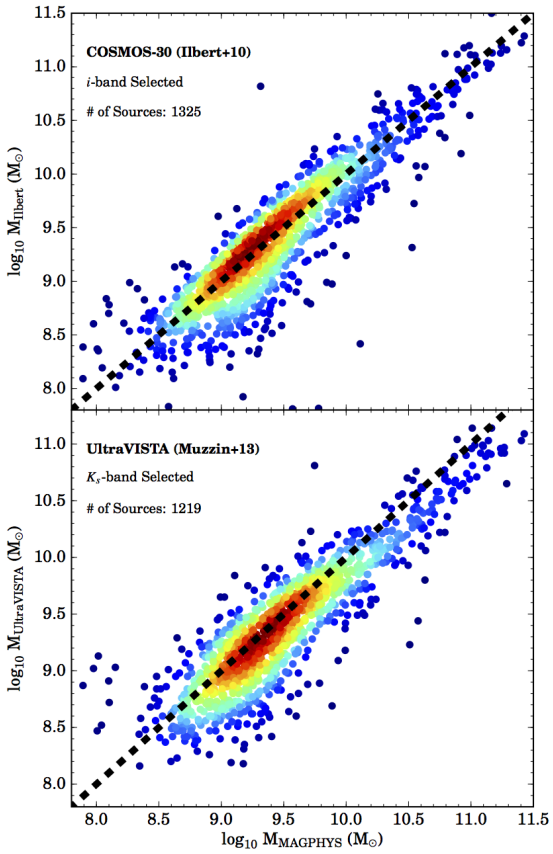

Figure 3.10: Present is the comparison between the stellar masses measured by Ilbert et al. (2010) (*top panel*) and Muzzin et al. (2013) (*bottom panel*) versus the stellar masses we measure using MAGPHYS. The *dashed black line* is the 1:1 relation. We find that, overall, our measurements are consistent with those from the comparison samples. The scatter in the measurements is most probably arising from the different sets of assumptions (e.g., SF history, metallicity range, dust prescription). We eliminate the scatter arising from differing redshifts by only comparing sources that have a $\Delta z < 0.1$, where Δz represents the difference between the photometric redshift measured by Khostovan et al. (2015) and the comparison studies.

3.6.2.1 The effects of nebular emission lines on stellar mass measurements

Recent studies have shown that SED fitting without nebular emission lines taken into account can result into overestimations of stellar masses (e.g., de Barros et al. 2014), which can be a potential problem for our emission line-selected sample. We note that for emission lines to become a problem in the SED fitting of broad-band photometry would require EWs high enough to dominate the stellar continuum of the broad-band filters.

We test the effects of nebular emission lines on the stellar mass determinations by running MAGPHYS on our highest redshift samples (Hβ+[OIII] and [OII] $z \sim 3.3$ and [OII] $z = 4.69$) with the potentially contaminated bands removed from the SED fitting process. The contaminated bands removed are the H ([OII]) and K (Hβ+[OIII]) bands for the $z \sim 3.3$ sample and the K ([OII]) and IRAC CH1 (Hα) bands for the $z = 4.69$ sample. At $z \sim 3.3$ and $z = 4.69$, Hα and Hβ+[OIII] falls between K and IRAC CH1, respectively. We find a median stellar mass difference of $\Delta \log_{10} M = 0.002 \pm 0.098$ and 0.025 ± 0.042 at $z \sim 3.3$ and $z = 4.69$, respectively. This shows that, for our samples, the nebular emission lines does not affect the stellar mass measurements implying that (a) there are enough photometric data points in the SED fitting for which nebular emission line contamination is negligible and/or (b) the equivalent widths of the lines are not high enough such that the broad-band filters are dominated by the stellar continuum used to measure stellar mass.

3.6.3 Equivalent Width Completeness

We incorporate a second completeness correction which deals with the EW_{rest} cut causing a loss in high-mass sources (e.g., §3.1 in Sobral et al. 2014; Figure 3.6). For our $z > 1$ Hβ+[OIII] and [OII], this incompleteness is not an issue since it will only affect our measurements at very high masses ($> 10^{12}$ $M_\odot$, except for [OII] $z = 1.47$ where the incompleteness arises by $> 10^{11.25}$ $M_\odot$). Our $z \sim 0.84$ Hβ+[OIII] sample is affected for masses $> 10^{10}$ $M_\odot$. The $z \sim 1.47$ [OII] sample is relatively complete up to masses for which we probe.

We correct for this incompleteness using a similar approach from Sobral et al. (2014). Since our $z > 1$ Hβ+[OIII] are complete for the full range of stellar masses (Figure 3.1), we use these samples as proxies in measuring the incompleteness. We start by binning up the full sample in stellar mass bins which corresponds to a median EW_{rest}. We then decrease the corresponding EW_{rest} to match the $z \sim 0.84$ median EW_{rest} stellar mass bins, which results in a number of high-mass sources removed from the full sample because of the $z = 0.84$ Hβ+[OIII] EW_{rest} cut.

The correction factor is then calculated as the number of sources that are recovered relative to the total number of sources in each bin. We run these correction determinations based off the $z \sim 1.47$, 2.23, and 3.24 samples and find that for all redshifts probed in the Hβ+[OIII] sample, the EW_{rest} cut completeness correction does not evolve. To apply the completeness corrections, we extrapolate for the mass range of the $z \sim 0.84$ sample and apply the corrections accordingly. These corrections are mass dependent and range from $\sim 50\%$ to 200% increase in $\Phi(M)$ between 10^{10} $M_\odot$ to 200% and $10^{11.5}$ $M_\odot$, respectively.

3.6.4 Correcting $z > 5$ Hβ+[OIII] Equivalent Widths

To ensure that the $z > 5$ Hβ+[OIII] literature data points (Labbé et al., 2013; Smit et al., 2014, 2015) are comparable to our measurements, we must take into account the Hβ contribution in the total EW_{rest} measured. These samples used nebular excess in the *Spitzer* IRAC bands to probe the combined Hβ4861, [OIII]4959, and [OIII]5007 lines. Our sample on the other hand consists of either Hβ, [OIII]4959, or [OIII]5007 because the narrow-band filter is narrow enough to separate the lines, but the broad-band and photometric redshift selections used can not. As inferred in Khostovan et al. (2015), the sample is primarily [OIII]5007 for the brightest sources, but towards fainter line fluxes we start picking up more Hβ emitters. Sobral et al. (2015a) observed $z = 1.42$ Hβ+[OIII] emitters in the ~ 10 deg^2 CF-HiZELS survey and had spectroscopic measurements to differentiate between Hβ and [OIII] to find that the sample consisted of primarily [OIII]5007 emitters. To compensate for this, we reduce the EW_{rest} measured by Labbé et al. (2013), Smit et al. (2014), and Smit et al. (2015) by 20% based on the [OIII]/Hβ ratios from the $z \sim 2.3$ studies of the MOSDEF survey (Sanders et al., 2015).

3.6.5 Ratios of EW_{rest} = Fluxes?

The [OIII]/[OII] line ratio is typically measured by taking the ratio of the dust-corrected [OIII] and [OII] fluxes. In §3.4.4.3, we use the ratio of the EW_{rest} instead of the line fluxes

to determine [OIII]/[OII], as this eliminates the dependency of dust corrections under the assumption that $E(B-V)_{\rm nebular} \sim E(B-V)_{\rm stellar}$ (e.g., Reddy et al. 2015; Shivaei et al. 2015). An issue that arises with this approach is that the $EW_{\rm rest}$ is a ratio between the line and continuum flux, where the continuum flux at 3727Å may not be equivalent/similar to the continuum flux at 5007Å. Therefore, we must assess how well does the $EW_{\rm rest}$([OIII])/$EW_{\rm rest}$([OII]) correlate with $F_{\rm [OIII]}/F_{\rm [OII]}$, where the only factor that can cause any systematic deviation is the difference between the continuum fluxes.

To assess this issue, we use the SDSS DR12 (Thomas et al., 2013) and VVDS (Lamareille et al., 2009) catalogs. Both are spectroscopic surveys and contain the $EW_{\rm rest}$ and line fluxes for both [OIII] and [OII], allowing us to directly measure the correlation between $EW_{\rm rest}$([OIII])/$EW_{\rm rest}$([OII]) and $F_{\rm [OIII]}/F_{\rm [OII]}$. Both flux measurements are dust-corrected assuming a Calzetti et al. (2000) dust attenuation curve and $E(B-V)_{\rm nebular} \sim E(B-V)_{\rm stellar}$. For both catalogs, we select only sources that are confirmed to be star-forming and within the stellar mass range of $9.5 < \log_{10} M < 10.0$ $M_\odot$.

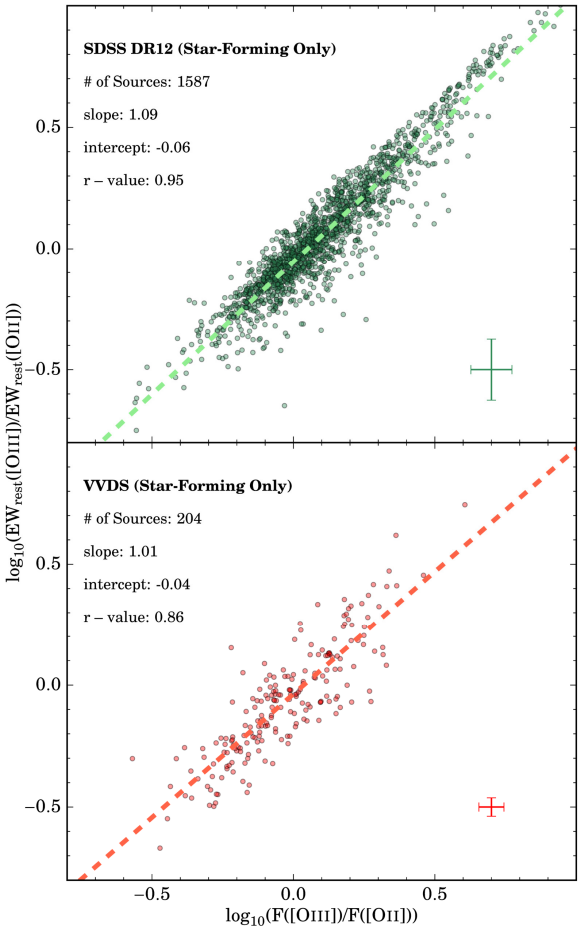

Figure 3.11: The comparison between the [OIII]/[OII] determined by the ratio of the $EW_{\rm rest}$ and the line fluxes in log-space. The intercept represents the ratio of the continuum fluxes. We find that the intercepts are ~ 0 and the slopes of the correlation are near unity, such that the ratio of the $EW_{\rm rest}$ directly traces the [OIII]/[OII] line ratio with negligible systematic offsets introduced by differing continuum fluxes.

Figure 3.11 shows the correlation between $EW_{\rm rest}$([OIII])/$EW_{\rm rest}$([OII]) and $F_{\rm [OIII]}/F_{\rm [OII]}$.

We measure the correlation in log-scale as:

$$\log_{10}\frac{\mathrm{EW_{rest}([OIII])}}{\mathrm{EW_{rest}([OII])}} = \log_{10}\frac{F_{[\mathrm{OIII}]}}{F_{[\mathrm{OII}]}} + \log_{10}\frac{f_{C,[\mathrm{OII}]}}{f_{C,[\mathrm{OIII}]}} \tag{3.7}$$

where f_C is the continuum flux at the wavelength of the emission line. Therefore, a linear correlation in log-space would have the intercept equivalent to the ratio of the continuum fluxes, which would represent the systematic offset introduced by using the $\mathrm{EW_{rest}}$ ratios to measure [OIII]/[OII]. Furthermore, because we assume $E(B-V)_{\mathrm{nebular}} \sim E(B-V)_{\mathrm{stellar}}$ the dust corrections would still cancel out. Changes in this assumption would introduce a systematic factor due to dust correction and not continuum flux differences of $0.4(k_{[\mathrm{OII}]}-k_{[\mathrm{OIII}]})(E(B-V)_{\mathrm{nebular}}-E(B-V)_{\mathrm{stellar}})$ dex.

We find that for the SDSS and VVDS samples, the slope of the correlation is close to unity such that $\mathrm{EW_{rest}([OIII])/EW_{rest}([OII])} \sim F_{[\mathrm{OIII}]}/F_{[\mathrm{OII}]}$. The r-value (correlation coefficient) is ~ 0.9 for both samples which implies that the two different ratios are strongly correlated. More importantly, we find that the intercepts measured are -0.06 and -0.04 dex for SDSS and VVDS, respectively. This suggests that, on average, the systematic offset introduced by the ratio of the continuum fluxes is negligible in the determination of [OIII]/[OII] via the ratio of the $\mathrm{EW_{rest}}$.

We note that the result of a negligible systematic offset due to variations in the continuum fluxes only applies for the full sample and not on an individual source basis. Furthermore, we selected sources based on the same selection criteria for our sample (star-forming and within $9.5 < \log_{10} M < 10.0$ $\mathrm{M_\odot}$). This would correspond to young galaxies with weaker 4000 Å breaks in comparison to more evolved systems. Therefore, in the context of our sample, a negligible systematic offset works but this is not true for samples comprised of more massive, older systems for which a greater 4000 Å break will result into an offset between the continuum fluxes at 3727 Å and 5007 Å.

CHAPTER 4

The clustering of Hβ+[OIII] and [OII] emitters since $z \sim 5$: dependencies with line luminosity and stellar mass

Abstract

We investigate the clustering properties of ~ 7000 Hβ+[OIII] and [OII] narrowband-selected emitters at $z \sim 0.8-4.7$ from the High-z Emission Line Survey. We find clustering lengths, r_0, of 1.5 – 4.0 h^{-1} Mpc and minimum dark matter halo masses of $10^{10.7-12.1}$ $M_\odot$ for our $z = 0.8-3.2$ Hβ+[OIII] emitters and $r_0 \sim$ 2.0 – 8.3 h^{-1} Mpc and halo masses of $10^{11.5-12.6}$ $M_\odot$ for our $z = 1.5-4.7$ [OII] emitters. We find r_0 to strongly increase both with increasing line luminosity and redshift. By taking into account the evolution of the characteristic line luminosity, $L^\star(z)$, and using our model predictions of halo mass given r_0, we find a strong, redshift-independent increasing trend between $L/L^\star(z)$ and minimum halo mass. The faintest Hβ+[OIII] emitters are found to reside in $10^{9.5}$ $M_\odot$ halos and the brightest emitters in $10^{13.0}$ $M_\odot$ halos. For [OII] emitters, the faintest emitters are found in $10^{10.5}$ $M_\odot$ halos and the brightest emitters in $10^{12.6}$ $M_\odot$ halos. A redshift-independent stellar mass dependency is also observed

where the halo mass increases from 10^{11} $M_\odot$ to $10^{12.5}$ $M_\odot$ for stellar masses of $10^{8.5}$ $M_\odot$ to $10^{11.5}$ $M_\odot$, respectively. We investigate the interdependencies of these trends by repeating our analysis in a $L_{\rm line}$ – $M_{\rm star}$ grid space for our most populated samples (Hβ+[OIII] $z = 0.84$ and [OII] $z = 1.47$) and find that the line luminosity dependency is stronger than the stellar mass dependency on halo mass. For $L > L^\star$ emitters at all epochs, we find a relatively flat trend with halo masses of $10^{12.5-13}$ $M_\odot$ which may be due to quenching mechanisms in massive halos which is consistent with a transitional halo mass predicted by models.

4.1 Introduction

The current consensus of galaxy formation is that galaxies formed hierarchically inside dark matter halos (see Benson 2010 for a review and references therein), suggesting that the two co-evolve. The question that arises then is how exactly are the physical properties of galaxies related to their host dark matter halos? How significant is this halo dependency on the evolution of a galaxy and at what cosmic times was this connection set in place?

Observationally, two-point correlation statistics trace the spatial clustering of galaxies and can provide us with insights of the underlying dark matter distribution. This then becomes helpful in relating the spatial clustering of galaxies as a function of their physical characteristics (e.g., star formation rate, mass, morphology) to dark matter halo properties to understand the galaxy-halo connection. It allows us to understand how the non-linear, stochastic processes that affect baryons are connected to the simple, gravitational processes that govern dark matter halo growth.

With the advent of large galaxy photometric and spectroscopic surveys, (e.g., SDSS: York et al. 2000, 2dFGRS: Colless et al. 2001, DEEP2: Davis et al. 2003, VVDS: Le Fèvre et al. 2005, PRIMUS: Coil et al. 2011, GAMA: Driver et al. 2011, BOSS: Dawson et al. 2013, VIPERS: Garilli et al. 2014, eBOSS: Dawson et al. 2016) in the last two decades, it has become possible

to perform detailed analysis of clustering of galaxies as a function of their physical properties (e.g., colors, luminosities, star formation rates, and stellar masses). At low redshifts ($z \sim 0-1$), it has been found that red, passive galaxies are more clustered than blue, active galaxies (e.g., Norberg et al. 2002; Zehavi et al. 2005; Coil et al. 2008; Zehavi et al. 2011; Guo et al. 2013, 2014). Similar luminosity trends with clustering strength/halo mass are also observed at $z \sim 1-2$ (e.g., Hartley et al. 2008; McCracken et al. 2010; Marulli et al. 2013; Ishikawa et al. 2015) and, using primarily Lyman Break galaxies (LBGs), at $z \sim 2-7$ (e.g., Adelberger et al. 2005; Barone-Nugent et al. 2014; Harikane et al. 2016). Correlations between increasing stellar mass and increasing clustering strength/dark matter halo mass have also been reported in the literature (e.g., Meneux et al. 2008, 2009; Wake et al. 2011; Lin et al. 2012; Mostek et al. 2013; McCracken et al. 2015).

The significance of the results highlighted above suggests that dark matter halos have an important role in the star formation processes that occur within galaxies. Large narrowband and spectroscopic surveys have been able to study how the clustering properties of galaxies correlates with star formation activity directly. Recent narrowband measurements using Hα (tracing the instantaneous SFR) up to $z \sim 2$ find that the clustering signal strongly increases with increasing Hα line luminosity (Sobral et al., 2010; Stroe & Sobral, 2015; Cochrane et al., 2017). Surprisingly, Sobral et al. (2010) found that the dependency is also redshift-independent in terms of $L/L^{\star}(z)$, with $L^{\star}(z)$ being the characteristic Hα luminosity at each redshift, equivalent to a characteristic SFR (SFR*, Sobral et al. 2014). Other studies find similar line luminosity/SFR trends with clustering strength/halo mass up to $z \sim 2$ (e.g., Mostek et al. 2013; Dolley et al. 2014; Coil et al. 2017). The trends observed by Sobral et al. (2010) also show a shallower/flat slope at $L > L^{\star}(z)$, which is suggested to be a signature of quenching processes within the most massive halos.

Current results are primarily based on samples of the nearby Universe and a handful of $z \sim 1-2$ studies. There are also a few Lyman Break Galaxy (LBG) selected samples up to $z \sim 7$, but such samples are severely biased against dusty systems (e.g., Oteo et al. 2015), have

photometric redshifts that are uncertain, and complex selection functions. In order to effectively study the clustering properties of galaxies and understand how and when these galaxy-halo trends formed requires samples that are: 1) well-defined in terms of selection criteria, 2) cover a range of redshifts to trace the evolving parameters over cosmic time, 3) cover multiple and large comoving volumes to reduce the effects of cosmic variance, 4) span a wide range in physical properties to properly subdivide the samples, and 5) have known redshifts.

In this study, we use a sample of Hβ+[OIII] and [OII] emission line-selected galaxies from Khostovan et al. (2015) to study the clustering properties and dependencies with line luminosity and stellar mass up to $z \sim 5$ in 4 narrow redshift slices per emission line. Since our samples are emission line-selected, this gives us the advantage of knowing the redshifts of our sources within $\sigma_z = 0.01 - 0.03$ (based on the narrowband filter used) and forms a simple selection function, which is usually not the case with previous clustering studies using either broadband filters or spectroscopic surveys. This also means that there is almost no redshift projection that can affect the measured clustering signals such that we can easily get high signal-to-noise clustering measurements using smaller samples in comparison to photometric and spectroscopic surveys, which typically span a very large redshift range and thus are subject to enormous projection effects. Lastly, our samples are also large enough (~ 7000 sources) to properly subdivide to study the dependency of galaxy properties on the clustering strength and spread over the COSMOS and UDS fields (~ 2 deg^2) to reduce the effects of cosmic variance.

This paper is structured as follows: in §5.2, we describe our emission line-selected samples used in the clustering measurements. In §4.3 we present our methodology of measuring the angular correlation function, discuss the effects of contamination, describe how we corrected for cosmic variance, present our measurements of the spatial correlation function, and describe our model to convert the clustering length to minimum dark matter halo mass. In §5.5 we analyze the results for the full sample measurements and then investigate the individual dependencies with halo mass starting with stellar mass and line luminosity. We then show the dependency

with halo mass in a line luminosity-stellar mass grid space. In §4.5 we present our interpretations of the results. We present our main conclusions in §6.3.

Throughout this paper we assume ΛCDM cosmology with $H_0 = 70$ km s^{-1}, $\Omega_m = 0.3$, and $\Omega_\Lambda = 0.7$. All stellar masses reported assume a Chabrier initial mass function.

4.2 Sample

In this study, we use the large sample of Hβ+[OIII] and [OII] selected emission-line galaxies from the narrowband High-z Emission Line Survey (HiZELS; Geach et al. 2008; Sobral et al. 2009, 2012, 2013a) presented by Khostovan et al. (2015). Our samples are distributed over the COSMOS (Scoville et al., 2007) and UDS (Lawrence et al., 2007) fields with a combined areal coverage of ~ 2 deg^2 which equates to comoving volume coverages of $\sim 10^6$ Mpc^3. The sample consists of 3475 Hβ+[OIII] emitters at narrow redshift slices of $z = 0.84$, 1.42, 2.23, and 3.24 and 3298 [OII] emitters at $z = 1.47$, 2.25, 3.34, and 4.69. There are 223 and 219 spectroscopically confirmed Hβ+[OIII] and [OII] emitters, respectively, drawn from the UDSz Survey (Bradshaw et al., 2013; McLure et al., 2013), Subaru-FMOS measurements (Stott et al., 2013b), Keck/DEIMOS and MOSFIRE measurements (Nayyeri et al., in prep), PRIsm MUlti-object Survey (PRIMUS; Coil et al. 2011), and VIMOS Public Extragalactic Redshift Survey (VIPERS; Garilli et al. 2014). Recent Keck/MOSFIRE measurements of $z = 1.47 - 3.34$ emitters are also included as well as recent VLT/VIMOS measurements for UDS sources (Khostovan et al., in prep).

The selection criteria used is explained in detail in Khostovan et al. (2015). In brief, Hβ+[OIII] and [OII] emitters are selected based on a combination of spectroscopic measurements, photometric redshifts, and color-color selections (in order of priority) from the HiZELS narrowband color excess catalog of Sobral et al. (2013a). Sources that have detections in multiple narrowband filters were also included in the final sample as the multiple emission line detections

are equivalent to spectroscopic confirmation (e.g., the detection of [OII] in NB921 and Hα in NBH, see Sobral et al. 2012; [OIII] in NBH and Hα in NBK, Suzuki et al. 2016; see also Matthee et al. 2016 and Sobral et al. 2017 for dual NB-detections of Lyα and Hα emitters at $z = 2.23$).

Stellar masses of the sample were measured by Khostovan et al. (2016) using the SED fitting code of MAGPHYS (da Cunha et al., 2008), which works by balancing the stellar and dust components (e.g., the amount of attenuated stellar radiation is accounted for in the infrared). The level of AGN contamination was assessed by Khostovan et al. (2015) to be on the order of $\sim 10-20\%$ using the 1.6μm bump as a proxy via the color excesses in the *Spitzer* IRAC bands. Individual AGNs were not excluded in the sample due to the lack of X-ray detections (see Khostovan et al. 2015; §4.1). Overall, the sample covers a wide range in physical properties with stellar masses between $10^{8-11.5}$ $M_\odot$, EW_{rest} between $10-10000$ Å, and line luminosities between $10^{40.5-43.0}$ erg s^{-1}, providing a wealth of different types of "active" galaxies (star-forming + AGN; Khostovan et al. 2016). This is important when investigating the connection between physical and clustering properties of galaxies.

A unique advantage of narrowband surveys in terms of clustering studies is knowing the redshift distribution of each line (emission line-selected) which removes any redshift projections. Figure 4.1 shows the spatial distribution of the NBJ samples (Hβ+[OIII] $z = 1.42$ and [OII] $z \sim 2.25$) where, visually, it is clear that sources in both samples have a non-random, spatial clustering.

4.3 Methodology

4.3.1 Generating the Random Sample

When looking for a clustering signal, an equivalent and consistent random catalog is required to test for a non-random spatial distribution within the sample. If all the sources within the sample are consistent with a random spatial distribution, then no spatial correlation would

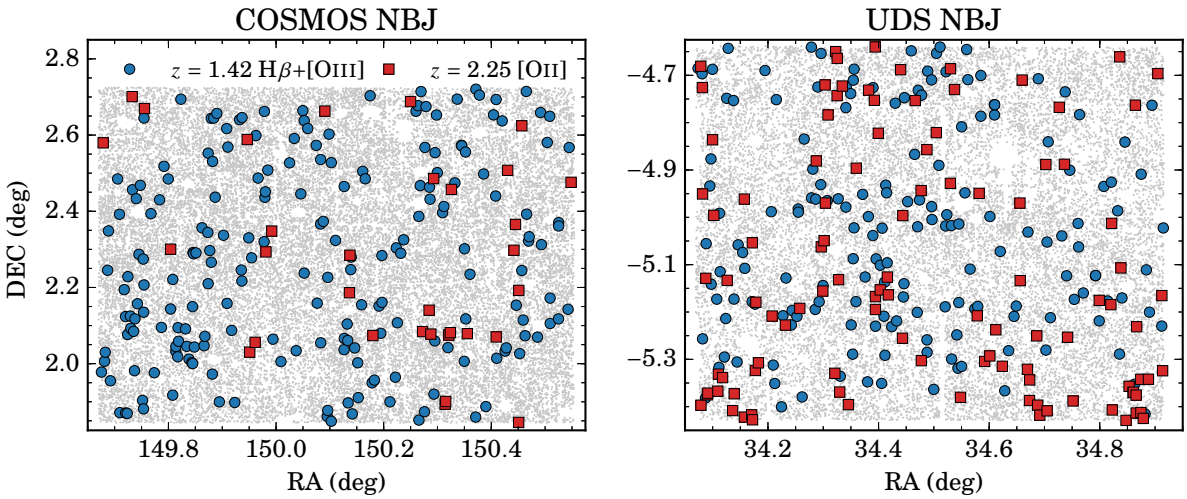

Figure 4.1: The full COSMOS and UDS on-sky coverages with the NBJ filter. Shown in *blue circles* and *red squares* are the $z = 1.42$ Hβ+[OIII] and $z = 2.25$ [OII] emitters, respectively. The *grey dots* are all sources in the raw catalog used to select emission-line galaxies and clearly outline the masked regions which are associated with bright stars and artifacts. We refer the reader to Sobral et al. (2013a) for a detailed description of how the masked regions were identified. The spatial distributions shows, visually and qualitatively, signatures of a non-random distribution. To properly quantify the clustering signal, we need to produce random samples that carefully take into account masked regions as outlined above.

exist within the errors. Therefore, the methodology of creating the random sample has to be consistent with the real dataset in terms of depth, survey geometry, and masked regions (see Figure 4.1).

We create our random samples on an image-by-image basis in order to take into account the different survey depths.[1]As we also want to investigate the dependency with line luminosity and stellar mass (see §4.4.2 - 4.4.4), we populate each image using the line luminosity functions of Khostovan et al. (2015). For each image, we calculate the total effective area which takes into account the masked areas. We then integrate the Khostovan et al. (2015) luminosity functions down to the 3σ detection limit of each image to calculate the total number of sources expected within the image area. This is then rescaled up by a factor of 10^5 such that each random sample generated has a total of $\sim 10^6$ mock sources for each field. Figure 4.1 shows the masked regions of the NBJ images for both the COSMOS and UDS fields that are taken into account when

generating the random samples.

4.3.2 Angular Correlation Function

We use the Landy & Szalay (1993, LS) estimator to measure the two-point angular correlation function (ACF) defined as:

$$w(\theta) = 1 + \left(\frac{N_R}{N_D}\right)^2 \frac{DD(\theta)}{RR(\theta)} - 2\left(\frac{N_R}{N_D}\right)\frac{DR(\theta)}{RR(\theta)} \tag{4.1}$$

where $w(\theta)$ is the angular correlation function, DD is the number of data-data pairs, RR is the number of random-random pairs, DR is the number of data-random pairs, θ is the angular separation, and N_R and N_D are the total number of random and data sources, respectively. The error associated with the LS estimator is defined as:

$$\Delta w(\theta) = \frac{1 + w(\theta)}{\sqrt{DD(\theta)}} \tag{4.2}$$

which assumes Poisson error. We refer the reader to Landy & Szalay (1993) for technical details about the estimator and Kerscher et al. (2000) for a comparison with other known two-point correlation estimators.

Due to our small sample sizes in comparison to other clustering studies, binning effects could introduce uncertainties in measuring the ACFs. This is a signal-to-noise problem where if the bins are too small, then the measured data-data (signal) are not sufficiently populated such that the random-random pairs (noise) dominates the measured ACF.

To take this into account, we adopt the approach of Sobral et al. (2010) and measure the ACF 2000 times assuming Poisson errors as described in Equation 5.3 with varying bin centers and sizes. For each ACF, we apply a random bin size ($\Delta \log\theta = 0.05 - 0.25$ dex) with $\theta_{\rm min} = 1.0''$ to $5.0''$ (randomly selected per ACF) and $\theta_{\rm max} = 3100''$. Each realization draws 10 - 100 times the number of real sources from the random sample discussed in Section 4.3.1 and the number

[1]Refer to Table 2 of Sobral et al. (2013a) for information regarding the depth of each image.

of data-data, random-random, and data-random pairs are measured. We then fit a power law of the form:

$$w(\theta) = A_w\left(\theta^{\beta} - \mathrm{IC}\right)$$
$$IC = \frac{\sum RR\theta^{\beta}}{\sum RR} \quad (4.3)$$

with A_w as the clustering amplitude and β as the power-law slope fixed at -0.8. The second equation is the integral constraint (IC; Roche et al. 2002) that takes into account the limited survey area. We note that the integral constraint has a marginal effect on our measurements of r_0 as HiZELS coverage is >1 deg^2. The final measurements and errors for A_w and the clustering length (r_0; see §4.3.4) are based on the distributions of values from the 2000 ACFs. In this way, we take into account the effects associated with binning. We find that our approach of assuming Poisson errors is consistent with measuring errors via bootstrapping assuming a fixed bin size and center and refer the reader to Appendix 4.7.3 for details. The final ACFs are shown in Figure 4.2 and discussed in §4.4.1.

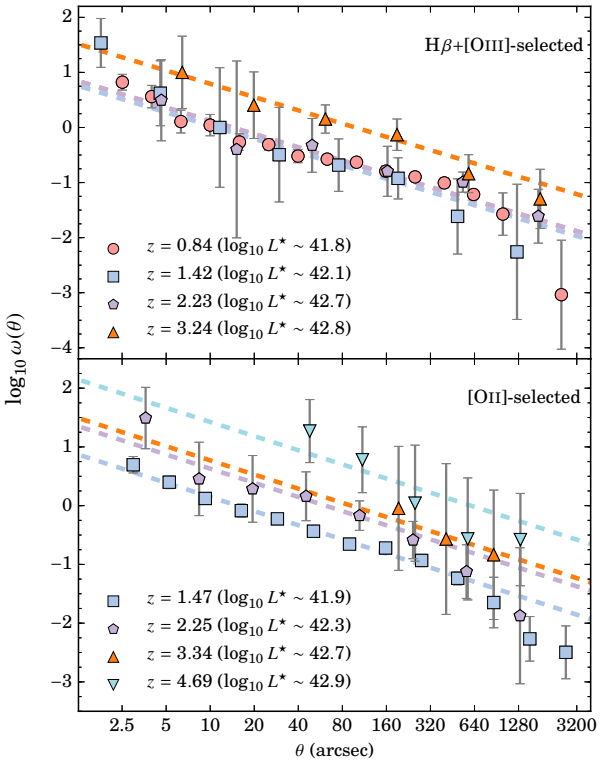

Figure 4.2: The angular correlation function based on the median of all the 2000 realizations per sample with the corresponding Limber approximation fits. All ACFs are calculated using the LS estimator. The fits shown are constrained to angular separations for which the ACF is best described by a power law with slope, $\beta = -0.8$. There is evidence for an evolution in the clustering amplitude, but we stress the point that the clustering signal is sensitive to the range of physical properties (e.g., luminosity and stellar mass), which we explore in §5.5.

Our measurements are corrected for cosmic (sample) variance by using the empirical relation measured by Sobral et al. (2010), where the uncertainty in A_w (in percentage) is related to the survey area as $20 \times \Omega^{-0.35}$, with Ω representing the area in units of deg^2. Our survey size of ~ 2 deg^2 corresponds to an uncertainty of $\sim 16\%$ due to cosmic variance in the measurement of A_w.

We incorporate this uncertainty by adding $\sim 16\%$ of A_w in quadrature to the error from the fit. For the clustering length, r_0, we propagate the error from A_w and find that the error in r_0 is increased by $\sim 11\%$.

4.3.3 Effects of Contamination

The issue of contamination within the sample can be marginal or quite significant and is based on many factors such as the sample selection. Clustering studies typically consider the contaminants in a sample to be randomly distributed, such that the clustering amplitude is underestimated by a factor of $(1-f)^2$, with f being the contamination fraction. For the clustering length, r_0, this results in an underestimation by a factor of $(1-f)^{2/|\gamma|}$.

The level of contamination was briefly investigated in Khostovan et al. (2015) and was found to be on the order of ~ 10 percent for the lowest redshift samples. This would result in a 23 percent increase in A_w and a 12 percent increase in r_0. Note that this assumes that the contaminants are randomly distributed and, hence, lowers the clustering strength, which may not be true for narrowband surveys. For our samples, contaminants could be due to galaxies with misidentified emission lines. For example, a source at $z = 1.47$ that is misidentified as [OII] in the NB921 filter could actually be a $z = 0.84$ [OIII] emitter or a $z = 0.40$ Hα emitter. Because galaxies selected by nebular emission lines are shown to be clustered as well (see below and Sobral et al. 2010 and Cochrane et al. 2017 for Hα), the effects could be negligible and not follow the typical $(1-f)^2$ correction factor. Therefore, we do not correct our measurements due to contamination.

4.3.4 Spatial Correlation Function

The two-point (spatial) correlation function is a useful tool in measuring the physical clustering of galaxies and is best described, empirically, by $\xi = (r/r_0)^{\gamma}$, with r_0 being the clustering length. Typically the Limber approximation (Limber, 1953) is used to relate the spatial and angular

Table 4.1: Properties of the Narrowband filters and their Gaussian representations.

Filter	Narrowband Filter		Gaussian Filter			
	$\lambda_{\rm obs}$ (Å)	FWHM (Å)	$r_{c,{\rm H}\beta+[{\rm OIII}]}$ (Mpc h^{-1})	$\sigma_{{\rm H}\beta+[{\rm OIII}]}$ (Mpc h^{-1})	$r_{c,[{\rm OII}]}$ (Mpc h^{-1})	$\sigma_{[{\rm OII}]}$ (Mpc h^{-1})
NB921	9196	132	2016	20	3008	19
NBJ	12110	150	2945	16	3862	14
NBH	16170	211	3846	15	4663	14
NBK	21210	210	4601	10	5323	9

correlation functions, but Simon (2007) found that this approximation breaks down at larger angular separations and when redshift distributions become more like a delta function. In such cases they find that the observed angular correlation function becomes a rescaled version of $\xi(r)$ with the slope of $w(\theta)$ changing from $\gamma+1$ to γ. This has been observed by various narrowband studies (e.g., Guaita et al. 2010; Sobral et al. 2010; Geach et al. 2012; Stroe & Sobral 2015; Bielby et al. 2016; Cochrane et al. 2017; Ouchi et al. 2018).

We adopt the exact equation presented by Simon (2007) and used by Sobral et al. (2010) to relate the real-space and angular correlation functions and calculate r_0. The relation is described as:

$$\begin{aligned} \omega(\theta) &= \frac{r_0^{-\gamma}}{1+\cos\theta}\int_0^{\infty}\int_{\bar{r}\sqrt{2(1-\cos\theta)}}^{2\bar{r}} \frac{2p(\bar{r}-\Delta)p(\bar{r}+\Delta)}{R^{-\gamma-1}\Delta}{\rm d}R{\rm d}\bar{r} \\ \Delta &= \sqrt{\frac{R^2-2\bar{r}^2(1-\cos\theta)}{2(1+\cos\theta)}} \end{aligned} \tag{4.4}$$

where p is the filter profile in radial comoving distance units, $\bar{r}=(r_1+r_2)/2$ as the mean spatial position of two sources, R as the distance between the two sources, and $\gamma=-1.8$ ($\gamma=\beta-1$) as the power law slope of the spatial correlation function. Filter profiles are best represented as single Gaussians and trace the redshift distribution of the sample. The parameters of the filters

and gaussian representations are described in Table 4.1. We use Equation 4.4 to fit r_0 to our measurements of $w(\theta)$.

Figure 4.3 shows the comparison between the Limber approximation (assuming a single power law to describe $w(\theta)$ as shown in Equation 4.3) and the exact Limber equation as described in Equation 4.4 for the $z = 1.47$ [OII] sample. We find that the Limber approximation breaks down at angular separations of $\gtrsim 500''$. Using the Limber approximation results in $r_{0,\mathrm{limber}} = 1.75 \pm 0.21\ h^{-1}$ Mpc and reduced $\chi^2 = 2.8$, while using the approach of Simon (2007) results with $r_{0,\mathrm{exact}} = 1.90 \pm 0.21\ h^{-1}$ Mpc and reduced $\chi^2 \sim 1$. Although both methods produce measurements that are consistent within 1σ (errors dominated by cosmic variance), our results shown on Figure 4.3 highlights the importance of using the exact Limber equation to measure the clustering length since it can compensate for the rescaling of the ACF and provides a better reduced χ^2. Throughout the rest of this paper, we refer to r_0 as the clustering length measured using Equation 4.4.

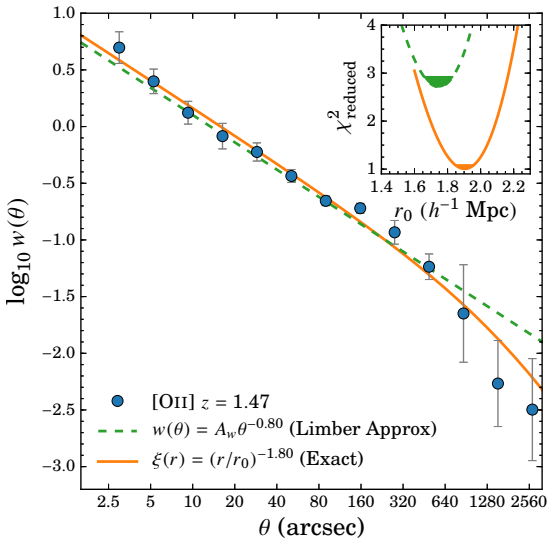

Figure 4.3: The angular correlation function for the z = 1.47 [OII] sample. Shown are the observed $w(\theta)$ measurements as in Figure 4.2 with the corresponding Limber approximation and exact equation fits. We use the full range of angular separations for both fits, even though the Limber approximation fails at $\theta \sim 500''$. The exact equation results in a reduced $\chi^2 \approx 1$ and $r_{0,\mathrm{exact}} = 1.90 \pm 0.21$, while the Limber approximation results in a reduced $\chi^2 \approx 2.8$ and $r_{0,\mathrm{exact}} = 1.75 \pm 0.21$. Errors shown in the χ^2 distribution are only based on the fits. The results shown here signify the importance of the exact Limber equation when using narrowband samples for large angular separations.

4.3.5 Dark Matter Halo Model

Our theoretical understanding of galaxy formation is that galaxies form with the assistance of the gravitational potentials of their host dark matter halos. In effect, the spatial clustering of

galaxies is then related to the clustering of dark matter. Matarrese et al. (1997) and Moscardini et al. (1998) used this link between galaxies and dark matter halos to predict the clustering length of a sample for a given minimum dark matter halo mass and redshift. In this section, we use the same methodology used to generate their predictions, but update to the latest cosmological prescriptions.

We first begin by measuring the matter-matter spatial correlation function using a suite of cosmological codes named `Colossus` (Diemer & Kravtsov, 2015). This is calculated by taking the Fourier transform of the matter power spectrum, assuming an Eisenstein & Hu (1998) transfer function. We then calculate the effective bias by using the following equation:

$$b_{eff}(z) = \frac{\int_{\mathrm{M_{min}}}^{\infty} b_h(M,z)\langle N_g(M,z)\rangle n(M,z)\mathrm{d}M}{\int_{\mathrm{M_{min}}}^{\infty} \langle N_g(M,z)\rangle n(M,z)\mathrm{d}M} \tag{4.5}$$

where $b_h(M,z)$ and $n(M,z)$ are the halo bias and mass functions, respectively, $\langle N_g(M,z)\rangle$ is the average galaxy-halo occupation, and $\mathrm{M_{min}}$ is the minimum dark matter halo mass. The effective bias is related to the spatial correlation of galaxies by:

$$b_{eff}^2 = \xi_{gg}/\xi_{mm} \tag{4.6}$$

with ξ_{gg} and ξ_{mm} being the galaxy-galaxy and matter-matter spatial correlation functions, respectively.

We use the Tinker et al. (2010) halo bias prescription and the Tinker et al. (2008) halo mass function. The previous predictions of Matarrese et al. (1997) and Moscardini et al. (1998) used the Press & Schechter (1974) halo mass function and Mo & White (1996) halo bias functions. Their assumed ΛCDM cosmology was also different ($H_0 = 65$ km s^{-1} Mpc^{-1}, $\Omega_m = 0.4$, and $\Omega_\Lambda = 0.6$) than the current measurements. We present a discussion regarding the uncertainties of assuming a bias and mass function in Appendix 4.7.1.

For the galaxy-halo occupation, we consider the simple case of $\langle N_g(M,z)\rangle = 1$ where every dark matter halo is occupied by a single central galaxy. Typical halo occupation distribution

(HOD) models consider satellite galaxy contributions, a wide range of parameter space, and detailed prescriptions for galaxy-halo occupation (e.g., Kravtsov et al. 2004; Zheng et al. 2005). For narrowband studies, such as this one, the survey depths are too shallow to capture faint, satellite galaxies. For example, Geach et al. (2012) and Cochrane et al. (2017) used the Hα HiZELS samples between $z \sim 0.8-2.2$ and found a negligible satellite fraction of ~ 5 precent. We can safely then assume that our samples are made up of primarily central galaxies (see §4.4.1).

We also note that our samples are flux-complete down to a limiting flux, but are not stellar mass-complete. Although this could potentially cause problems in terms on how we are assigning galaxies to halos, we show further in this study that halo masses are consistent with abundance matching studies when looking at the stellar-halo mass relationship (see §4.4.2). We also show a comparison between our r_0-DMH model measurements and those drawn from the literature in Appendix 4.7.2 and find that our minimum halo masses measured from our model are consistent with the effective halo masses from typical HOD models.

4.4 Results

4.4.1 Clustering Properties of Hβ+[OIII] and [OII] emitters

The angular and spatial distributions of galaxies encodes information regarding their clustering properties and, in turn, the types of dark matter halos for which they reside in. Our measured angular correlation functions for our samples are shown in Figure 4.2 with the respective best-fit model overlaid. As shown in Table 4.2, we fit the observed ACFs using Equation 4.3 with β as a free parameter and find that our measurements are within $\sim 1\sigma$ of the fiducial slope of -0.8. We therefore fix $\beta = -0.8$ throughout the rest of this paper.

Figure 4.2 shows the median $w(\theta)$ for all 2000 realizations with the best-fitted A_w defining the power law. There are weak signs of the 1-halo term (small-scale clustering/contribution of

Table 4.2: The clustering properties for our Hβ+[OIII] and [OII] samples. The power-law slope, β, in the ACF is shown and corresponds to the clustering amplitude, $A_{w,\mathrm{free}}$, which corresponds to when β is a free-parameter in the fit. All other measurements shown have β fixed to -0.8, which corresponds to $\gamma = -1.8$ in the real-space two-point correlation function. $r_{0,\mathrm{exact}}$ is the clustering length measured using the exact Limber equation as defined in Equation 4.4. Dark matter halo masses are measured using our r_0-halo mass models. The reduced chi-sq, χ^2_{red}, is based on the exact equation fits using the Levenberg-Marquardt algorithm.

Clustering Properties for Full Sample							
z	N_D	β	$A_{w,free}$ (arcsec)	$A_{w,\beta=-0.8}$ (arcsec)	$r_{0,exact}$ (Mpc h^{-1})	$\log_{10}$ M$_{\mathrm{min}}$ (M$_\odot$ h^{-1})	χ^2_{red}
Hβ+[OIII] Emitters							
0.84	2477	$-0.69^{+0.03}_{-0.03}$	$5.19^{+1.32}_{-1.22}$	$11.53^{+2.33}_{-2.33}$	$1.71^{+0.19}_{-0.19}$	$11.18^{+0.33}_{-0.33}$	3.01
1.42	371	$-0.79^{+0.07}_{-0.04}$	$7.47^{+3.58}_{-3.24}$	$8.32^{+2.18}_{-2.08}$	$1.45^{+0.20}_{-0.20}$	$10.70^{+0.40}_{-0.40}$	0.18
2.23	270	$-0.81^{+0.15}_{-0.12}$	$11.10^{+12.42}_{-6.57}$	$10.42^{+2.80}_{-2.62}$	$2.43^{+0.31}_{-0.31}$	$11.61^{+0.22}_{-0.22}$	0.37
3.24	179	$-0.78^{+0.04}_{-0.03}$	$42.28^{+13.22}_{-13.56}$	$48.70^{+10.71}_{-10.83}$	$4.01^{+0.49}_{-0.49}$	$12.08^{+0.17}_{-0.17}$	0.12
[OII] Emitters							
1.47	3285	$-0.83^{+0.02}_{-0.04}$	$10.06^{+2.66}_{-2.21}$	$11.61^{+2.34}_{-2.34}$	$1.99^{+0.22}_{-0.22}$	$11.46^{+0.23}_{-0.24}$	1.01
2.25	137	$-0.78^{+0.05}_{-0.03}$	$25.51^{+9.08}_{-9.18}$	$29.99^{+7.24}_{-7.00}$	$3.14^{+0.43}_{-0.41}$	$12.03^{+0.21}_{-0.20}$	0.16
3.34	35	$-0.79^{+0.23}_{-0.06}$	$53.67^{+41.66}_{-44.95}$	$57.49^{+22.49}_{-24.67}$	$5.06^{+1.08}_{-0.94}$	$12.37^{+0.28}_{-0.24}$	0.13
4.69	18	$-0.83^{+0.04}_{-0.04}$	$208.50^{+116.82}_{-91.58}$	$139.44^{+53.69}_{-44.63}$	$8.25^{+1.54}_{-1.44}$	$12.62^{+0.22}_{-0.20}$	0.26

satellite galaxies) at angular separations $< 20''$ (~ 150 kpc) for the $z = 0.84$ Hβ+[OIII] sample and the deviation from the power law fit (although within 1σ) is consistent with the 1-halo term. We find no significant detection of the 1$-$ halo term in the [OII] samples. This implies that the fraction of satellite galaxies within our samples is quite low, which is consistent with other emission line galaxy studies (e.g., Geach et al. 2012; Cochrane et al. 2017; Hα satellite fractions of ~ 5 percent). One possible reason for the presence of the 1-halo term for the $z = 0.84$ Hβ+[OIII] ACF could be due to the ~ 10 Mpc-scale overdense region in the COSMOS field, which contains several X-ray confirmed clusters/groups and large filaments (e.g., Sobral et al. 2011; Darvish et al. 2014), but we defer from a detailed analysis of the satellite fractions as

it is beyond the scope of this work. Overall, our samples are dominated by central galaxies which allows us to ignore the effects of a satellite population of galaxies in our dark matter halo model (see §4.3.5).

We explore the spatial correlation of our samples using our observed measurements of the angular correlation functions as described in Equation 4.4 and in §4.3.4. The spatial correlation allows us to investigate the clustering of galaxies in terms of the physical projection between two galaxies and is characterized by the clustering length (r_0). Figure 4.4 shows the evolution of r_0 for Hβ+[OIII] and [OII] emitters up to $z \sim 3$ and ~ 5, respectively. Included are the r_0 predictions for dark matter halos with minimum masses between $10^{11} - 10^{13}$ $M_\odot$ based on our model described in §4.3.5.

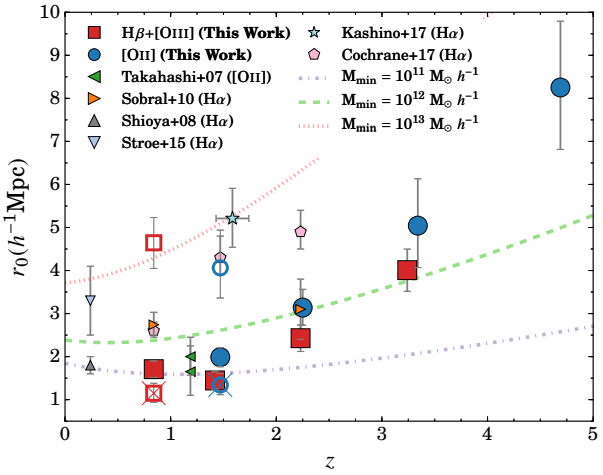

Figure 4.4: Shown is the evolution of the clustering length up to $z \sim 5$. Included are the predicted clustering lengths for minimum dark matter halo masses between 10^{11-13} $M_\odot$. Although there is a clear sign of a redshift evolution in r_0, we stress the point that this is due to selection bias such that these measurements are sensitive to the range of physical properties, such as line luminosity. As a demonstration, we overlay the brightest (*open symbol*) and faintest (*open symbol with a cross*) line luminosity bins (see Table 4.3) with the symbol type and color consistent with that used for the full sample measurement. The brightest emitters are found to have r_0 measurements $\sim 2-3$ times that of the full sample and the faintest emitters with $\sim 50\%$ lower r_0 values.

We find that Hβ+[OIII] emitters tend to reside in $\sim 10^{10.7} - 10^{12.1}$ $M_\odot$ dark matter halos while the [OII] emitters are found to vary less with $\sim 10^{11.5}$ $M_\odot$ at $z = 1.47$ to $\sim 10^{12.6}$ $M_\odot$ at $z = 4.69$, although these are primarily driven by selection effects. In comparison to each other, all overlapping samples, except for the $z \sim 1.5$ samples, have similar r_0 measurements within 1σ error bars. This then suggests that Hβ+[OIII]- and [OII]-selected galaxies reside in dark matter halos with similar masses.

Included in Figure 4.4 are the Hα measurements of Shioya et al. (2008), Sobral et al. (2010), Stroe & Sobral (2015), Cochrane et al. (2017), and Kashino et al. (2017). The Sobral et al.

(2010) measurement at $z = 2.23$ is consistent with that of the Hβ+[OIII] and [OII] samples at the same redshift, suggesting that Hβ+[OIII]- and [OII]-selected emitters reside in dark matter halos with similar masses as Hα-selected emitters and can be tracing a similar underlying population of star-forming/active galaxies. We also include the $z \sim 1.2$ [OII] measurements of Takahashi et al. (2007). Although our closest sample in terms of redshift is at $z = 1.47$, we find that our measurements are in agreement.

Despite the agreement between Hα, Hβ+[OIII], and [OII] samples, we note that such a comparison is not entirely fair. A comparison between the Hα measurements of Stroe & Sobral (2015, 26 deg^2 survey, 3σ $F_{lim} \sim 7.3 \times 10^{-16}$ ergs s^{-1} cm^{-2}) and Shioya et al. (2008, 1.5 deg^2 survey, 3σ $F_{lim} \sim 7 \times 10^{-18}$ ergs s^{-1} cm^{-2}) shows a factor of two difference in r_0 and two orders of magnitude difference in minimum dark matter halo mass. This is due to sample bias as a result of the survey parameters where the Stroe & Sobral (2015) sample is dominated by the brightest emitters relative to the Shioya et al. (2008) sample.

As a demonstration of this same feature, we show r_0 of the brightest (open symbols) and faintest (open symbols with a cross) galaxies in our Hβ+[OIII] $z = 0.84$ and [OII] $z = 1.47$ samples in Figure 4.4. We find that the most luminous (faintest) galaxies have higher (lower) clustering lengths relative to the full sample measurement. It is then not surprising that we find higher r_0 with increasing redshift as a result of Malmquist bias. This leads to the conclusion that any comparison needs to be interpreted with caution as each measurement for a full sample will be dependent on how wide a range of physical properties, such as luminosity, is covered. To properly compare samples and investigate the redshift evolution of the clustering and dark matter halo properties of galaxies, we need to then study the various dependencies between galaxies and halos.

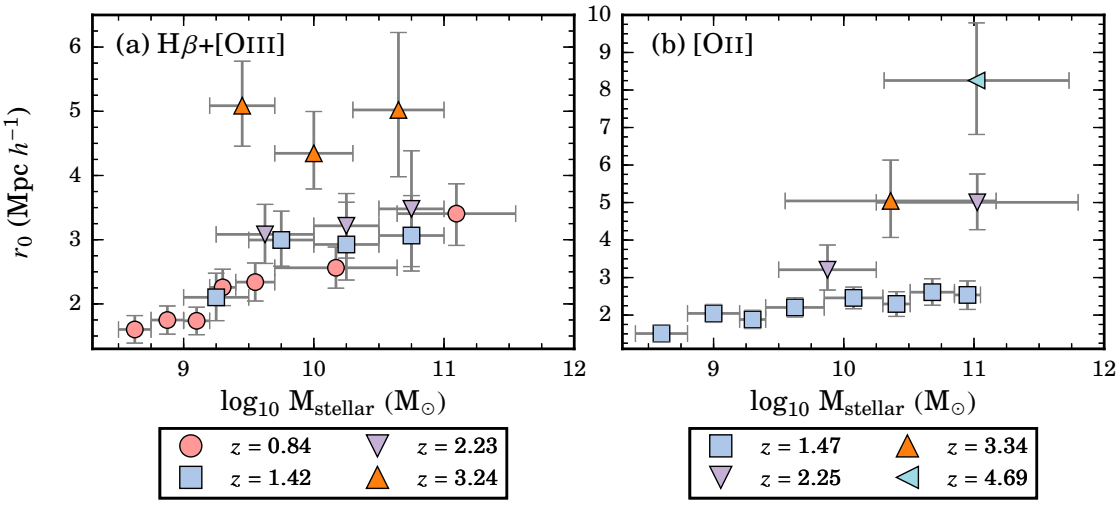

Figure 4.5: The clustering length as measured per stellar mass bins. We find that for both Hβ+[OIII] and [OII] emitters the clustering length increases with increasing stellar mass. Our results show that r_0 also increases with redshift for a fixed stellar mass. In comparison to the line luminosity dependency, we find that the increasing trend with stellar mass is weaker but we note that this could be a result of the line luminosity dependency or vice versa. This is because for each stellar mass bin there is a wide range of line luminosities. We explore this inter-dependency in §4.4.4.

4.4.2 Stellar Mass Dependency on Halo Mass

A stellar - halo mass relationship has been extensively observed in the literature and forms the main basis of the abundance matching technique (e.g., Vale & Ostriker 2004; Leauthaud et al. 2011, 2012; Behroozi et al. 2013b; Moster et al. 2013; Coupon et al. 2015; Moster et al. 2017). Since our samples are not stellar mass-complete, a comparison of the stellar-halo mass relationship between our measurements and abundance matching measurements can test the accuracy of our models. Exploring trends between stellar mass and halo mass also allows us to understand how one of the fundamental properties of galaxies is related to the fundamental property of dark matter halos with our unique sample of active, star-forming galaxies.

Figure 4.5 shows the changes in r_0 per stellar mass bin for our samples with the results tabulated in Tables 4.3 and 4.4. We find r_0 increasing by a factor of ~ 2 with increasing stellar mass for $z = 0.84$ Hβ+[OIII] emitters and a shallower increase for the $z > 1$ Hβ+[OIII] emitters.

Similar trends for the [OII] emitters are also observed, although we can only make such statements regarding the $z < 3$ samples since the higher-z [OII] samples are not sufficiently populated to subdivide them in stellar mass. We find a strong, redshift evolution in r_0 for fixed stellar mass for both Hβ+[OIII] and [OII] emitters. The results above are in agreement with the basic assumption of abundance matching that massive galaxies are more clustered than low-mass galaxies.

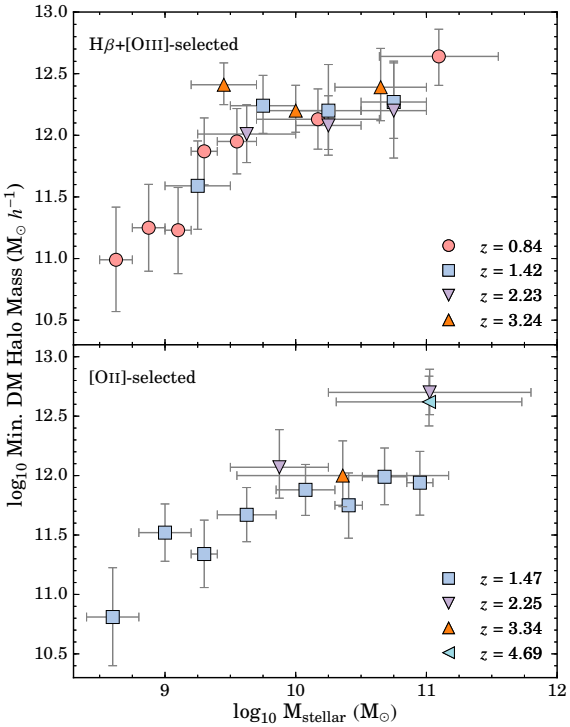

Figure 4.6: The minimum halo mass dependency with stellar mass. We find a strong relationship at all redshift slices for our Hβ+[OIII] samples and for the $z = 1.47$ [OII] sample. The $z = 2.25$ [OII] sample also shows an increasing trend, but is limited only to two stellar mass bins. The other [OII] samples are limited due to sample size and could not be separated in stellar mass bins. We find no redshift evolution in the relationship. Interestingly at stellar masses $> 10^{9.75}$ M$_\odot$ the halo mass is found to be constant at $\sim 10^{12.3}$ M$_\odot$ for Hβ+[OIII] emitters and $\sim 10^{12}$ M$_\odot$ for [OII] emitters.

Figure 4.6 shows the dependency between stellar and minimum halo mass for all redshift slices. We find a strong, redshift-independent trend between stellar and halo mass for both the Hβ+[OIII] and [OII] emitters where galaxies with higher stellar masses reside in higher mass halos. For the Hβ+[OIII] sample, we notice that although the measurements are consistent with each other at a given stellar mass for all redshifts, the slope of the trend decreases such that by $z \gtrsim 2.2$ the trend is flat. Interestingly, these measurements occur in the same mass range ($9.2 < \log_{10}$ M$_{\rm stellar}$/M$_\odot < 11.0$) where for all redshifts the trend is flat and then increases for higher stellar masses. A similar flat, redshift-independent trend is seen for [OII] emitters within the stellar mass range of $10^{9.75-11.0}$ M$_\odot$.

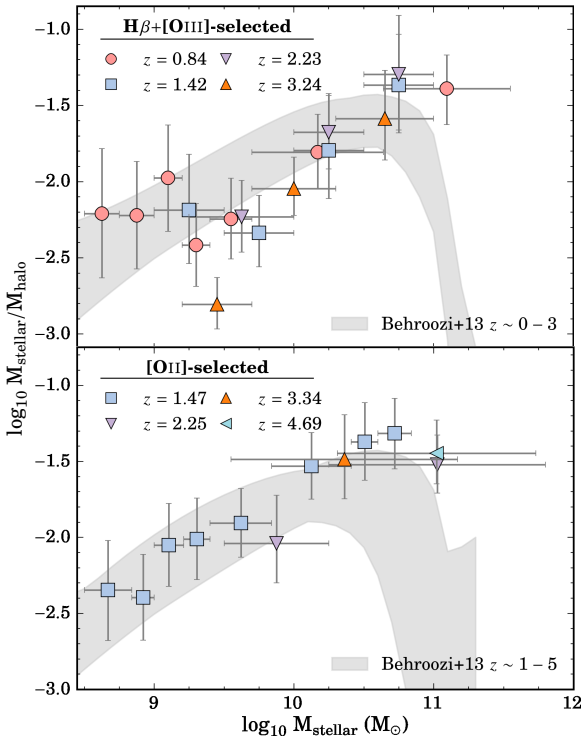

Figure 4.7: The stellar-halo mass (SHM) ratio as a function of stellar mass. We find our [OII] measurements show a continuous, redshift-independent increase in the SHM ratio for the full stellar mass range. The Hβ+[OIII] measurements show a constant ratio up to $\sim 10^{9.75}$ $M_\odot$ followed by a continuous, redshift-independent increase in the ratio. We compare our measurements with the abundance matching measurements of Behroozi et al. (2013b) overlaid in grey. We find that our [OII] and Hβ+[OIII] measurements are in agreement within 1σ except for our Hβ+[OIII] $10^{9.75-10.00}$ $M_\odot$ measurements.

Figure 4.7 shows the stellar-halo mass (SHM) ratio as a function of stellar mass, where we find it to be redshift-independent for all stellar masses. We find the SHM ratio for $z = 0.84$ and 1.42 Hβ+[OIII] emitters to be constant between $8.5 < \log_{10} M_{stellar}/M_\odot < 9.75$ and increasing for all redshift slices at $M_{stellar} > 10^{9.75}$ $M_\odot$. The [OII] emitters shows a continuous increase in the SHM ratio from the lowest masses to the highest masses probed.

Overlaid in Figure 4.7 are the measurements of Behroozi et al. (2013b), which used abundance matching along with constraints from observational measurements of global stellar mass functions to calculate the SHM ratio up to $z \sim 8$. Behroozi et al. (2013b) found that the ratio is redshift-independent and we therefore only highlight in Figure 4.7 the 1σ confidence region of their measurements that correspond to the redshifts of our sample. We find all four redshift slices for the [OII] samples are in agreement with the Behroozi et al. (2013b) measurements. Our Hβ+[OIII] measurements are also in agreement for $M_{stellar} < 10^{9.5}$ $M_\odot$ and $> 10^{10}$ $M_\odot$. Note that the Behroozi et al. (2013b) measurements are based on 'global' (passive+active galaxy) stellar mass functions, while our samples are comprised of 'active' galaxies (see Figure 3 of Khostovan et al. (2016) for the UVJ diagram) which could explain the discrepancy at $\sim 10^{9.75}$ $M_\odot$ shown in Figure 4.7 for

the Hβ+[OIII] samples. The results suggest that our halo mass measurements derived from our dark matter halo models are able to reproduce the SHM ratio, although we discuss the caveats in the section below.

The comparison with Behroozi et al. (2013b) is not exactly a like-to-like comparison as their measurements are constrained using global stellar mass functions. Our samples are emission line-selected, such that they are selecting the active population of galaxies and are not stellar mass complete. Furthermore, the halo masses reported in Behroozi et al. (2013b) are defined as the mass of a host halo similar to an effective halo mass. Their models also take into account satellite galaxies, while our model assumes one central galaxy per host dark matter halo. We note that, as shown in Appendix 4.7.2, our minimum halo masses are consistent with effective halo masses reported in the literature due to our halo model assumptions. Our measurements shown in Figure 4.7 then have the main caveat of stellar mass incompleteness.

Despite this caveat, it is interesting that our measurements of the SHM ratio are consistent with those of Behroozi et al. (2013b). The strong agreement with our [OII] SHM ratio measurements shown in Figure 4.7 also suggests that our [OII] samples are more representative of a stellar mass-complete sample in comparison to our Hβ+[OIII] samples. Also, the agreement provides more evidence on top of what is shown in Appendix 4.7.2 that the minimum halo masses measuring using our halo models is consistent with effective halo masses.

4.4.3 Observed Line Luminosity Dependency on Halo Mass

As discussed in §4.4.1, the clustering properties of galaxies are tied to their physical properties such that an investigation of their dependencies is required to properly map out the clustering evolution and study the connection between dark matter halos and galaxies. In this section, we study how the clustering length and halo properties are dependent on the observed line luminosities.

Figure 4.8 shows the r_0 dependency with line luminosity normalized by the characteristic

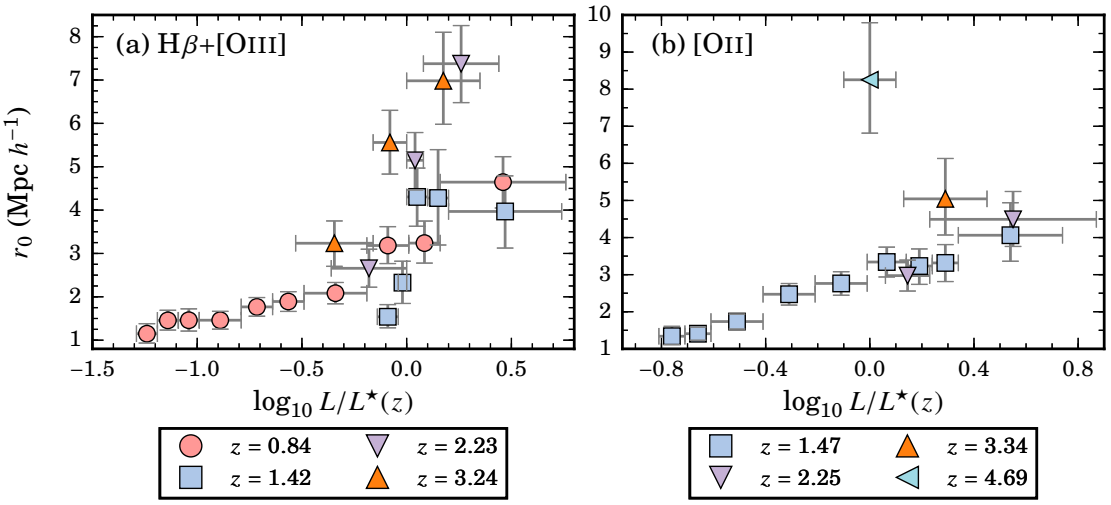

Figure 4.8: The clustering length measured in terms of $L/L^\star(z)$. Studying the dependency of the clustering length with luminosity as a function of the ratio between line and characteristic luminosity removes the effects caused by the cosmic evolution in the luminosity functions. For each redshift slice we find that there is a strong correlation between the clustering length and $L/L^\star(z)$. There is an evolution in the clustering length such that r_0 increases with redshift at any given $L/L^\star(z)$. For example, the clustering lengths at $L \sim L^\star(z)$ are 3.2, 4.3, 5.2, and 7.0 h^{-1} Mpc for our Hβ+[OIII] samples at $z = 0.84$, 1.42, 2.23, and 3.24. The same strong, increasing trend between r_0 and $L/L^\star(z)$ is also seen for the [OII] sample.

line luminosity at the corresponding redshift, $L/L^\star(z)$, with the tabulated measurements shown in Tables 4.3 and 4.4. We show our measurements in terms of $L/L^\star(z)$ so that we may investigate the clustering evolution of our samples independent of the cosmic evolution of the line luminosity functions. This was motivated by the results of Sobral et al. (2010) and Cochrane et al. (2017) for their Hα samples. Khostovan et al. (2015) showed that $L^\star(z)$ can evolve by a factor of $\sim 11-12$ from $z \sim 0.8-5$ for both Hβ+[OIII]- and [OII]-selected samples.

For each redshift slice, we find that r_0 strongly increases with increasing line luminosity for both Hβ+[OIII] and [OII] emitters. A redshift evolution is also seen at fixed $L/L^\star(z)$ for both emission line samples such that galaxies with increasing line luminosity and redshift are more clustered. Although our results suggest some redshift evolution in the clustering of galaxies as a function of line luminosity, we must also take into account the intrinsic clustering evolution due to halos as shown in Figure 4.4. A reasonable way to assess if there is an evolution in the

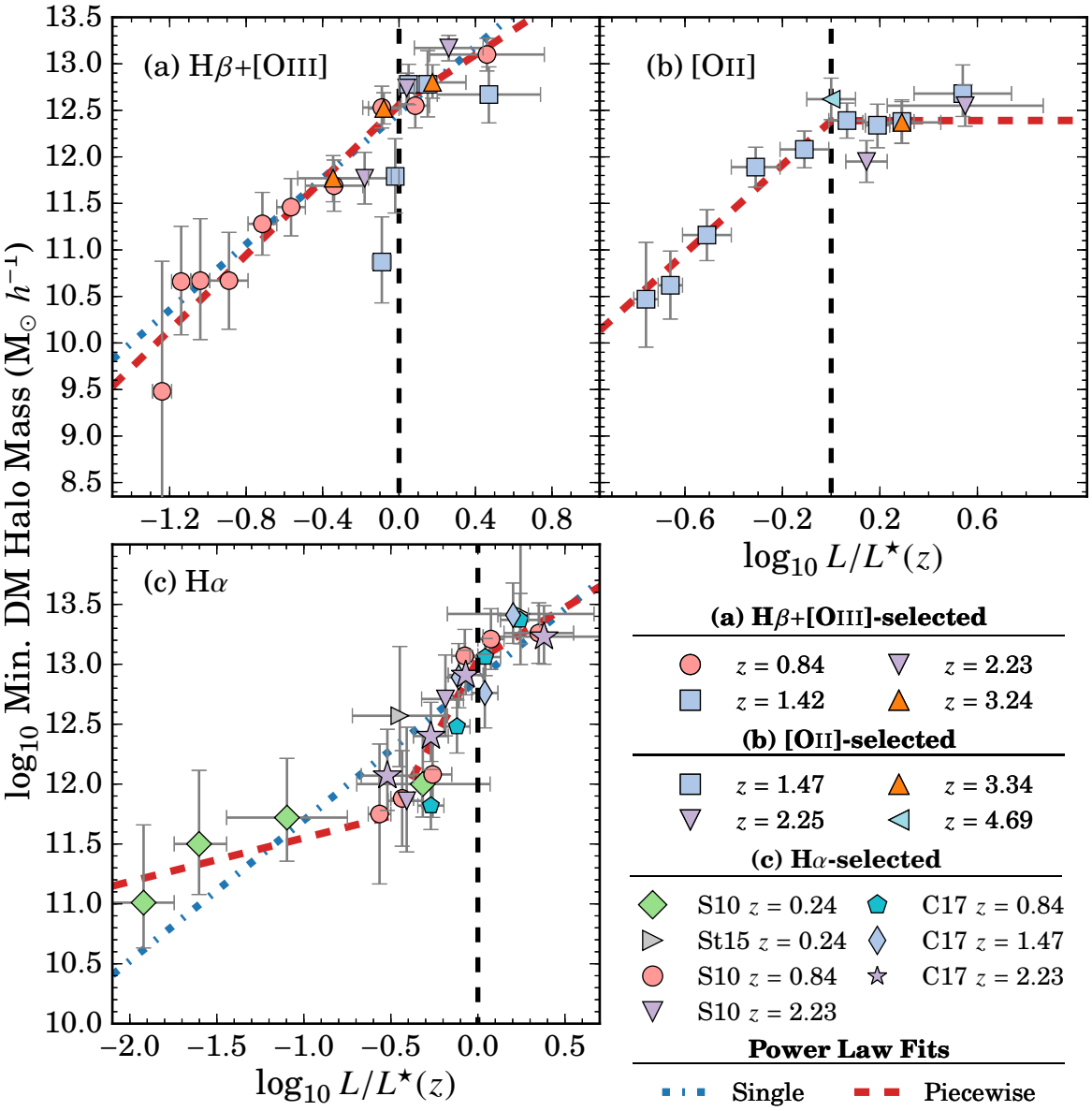

Figure 4.9: The dependency between $L/L^\star(z)$ versus minimum halo mass for our Hβ+[OIII] and [OII] samples. We find a strong correlation between line luminosity and dark matter halo mass and find no redshift evolution in $L/L^\star(z)$ such that galaxies at redshifts as high as $z \sim 5$ for a given $L/L^\star(z)$ reside in halos of similar mass as galaxies at $z \sim 1$. As a comparison, we also include the Hα measurements at $z = 0.24$ from Shioya et al. (2008) (recomputed by Sobral et al. (2010, S10)) and Stroe & Sobral (2015, St15), $z = 0.84$ from Sobral et al. (2010), and $z = 2.23$ from Geach et al. (2008) (recomputed by Sobral et al. (2010)). The latest Hα results of Cochrane et al. (2017, C17) are also included at $z = 0.84$, 1.47, and 2.23. The consensus from Hα studies is a strong dependency between line luminosity and halo mass. For $L > L^\star$ emitters, we find a flat trend with halo mass consistent with $10^{12.5}$ $M_\odot$ for [OII] emitters and a shallower increasing trend for Hα and Hβ+[OIII] emitters, although the scatter in the measurements are ~ 0.5 dex which can also be consistent with a flat trend.

clustering properties is by investigating it in terms of halo masses and $L/L^{\star}(z)$. This relation was first studied by Sobral et al. (2010) for Hα emitters up to $z = 2.23$ where they reported a strong, redshift-independent trend between halo mass and $L/L^{\star}(z)$. Here we investigate if such a relation exists for our Hβ+[OIII] and [OII] emitters to even higher redshifts.

Figure 4.9 shows the line luminosity dependence on minimum dark matter halo masses. We find that there is a strong relationship between line luminosity and halo mass for all redshift samples. More interestingly, we find no significant redshift evolution in the minimum dark matter halo mass such that galaxies reside in halos with similar masses independent of redshift at fixed $L/L^{\star}(z)$. This is found for both Hβ+[OIII] and [OII], as well as Hα studies (Geach et al., 2008; Shioya et al., 2008; Sobral et al., 2010; Cochrane et al., 2017) as shown in the bottom panel of Figure 4.9.

We quantify the observed trends by fitting both single and piecewise power laws to all measurements at all redshifts. The piecewise power laws are used in order to test the significance of a possible flattening of the observed, increasing trends for $L > L^{\star}(z)$. Our single power law fits are:

$$\frac{\mathrm{M_{min}}}{\mathrm{M_{\odot}}/h} = \begin{cases} 10^{12.48\pm0.07}\left(\dfrac{L}{L^{\star}(z)}\right)^{1.77\pm0.21} & \mathrm{H}\beta\text{+[OIII]} \\ 10^{12.87\pm0.06}\left(\dfrac{L}{L^{\star}(z)}\right)^{1.17\pm0.14} & \mathrm{H}\alpha \end{cases} \tag{4.7}$$

where we only show the measurements for Hβ+[OIII] and Hα as the [OII] measurements show a clear deviation for $L > L^{\star}(z)$. We find that the Hβ+[OIII] emitters show a steeper increasing trend in comparison to Hα but with a lower halo mass at $L \sim L^{\star}(z)$. This could be due to a higher population of [OIII]-selected AGNs that reside in massive halos compared to Hα, which we discuss in §4.5.

Figure 4.9 shows a clear deviation from a single power law trend at $L \sim L^{\star}(z)$ for the [OII] samples. There is some signature of such a deviation in our Hβ+[OIII] and also the Hα samples from the literature where the slope of the trends becomes shallower. We fit piecewise power

laws split at $L \sim L^{\star}(z)$ and find:

Hβ+[OIII]:

$$\frac{\mathrm{M_{min}}}{\mathrm{M_{\odot}}/h} = 10^{12.56\pm0.11} \begin{cases} \left(\frac{L}{L^{\star}(z)}\right)^{2.02\pm0.32} & L < L^{\star} \\ \left(\frac{L}{L^{\star}(z)}\right)^{1.35\pm0.47} & L > L^{\star} \end{cases} \tag{4.8}$$

[OII]:

$$\frac{\mathrm{M_{min}}}{\mathrm{M_{\odot}}/h} = 10^{12.39\pm0.08} \begin{cases} \left(\frac{L}{L^{\star}(z)}\right)^{2.37\pm0.31} L < L^{\star} \\ \left(\frac{L}{L^{\star}(z)}\right)^{0.003\pm0.003} L > L^{\star} \end{cases} \tag{4.9}$$

Hα:

$$\frac{\mathrm{M_{min}}}{\mathrm{M_{\odot}}/h} = 10^{13.04\pm0.08} \begin{cases} \left(\frac{L}{L^{\star}(z)}\right)^{0.36\pm0.20} L < 0.3L^{\star} \\ \left(\frac{L}{L^{\star}(z)}\right)^{2.61\pm0.36} 0.3L^{\star} < L < L^{\star} \\ \left(\frac{L}{L^{\star}(z)}\right)^{0.87\pm0.43} L > L^{\star} \end{cases} \tag{4.10}$$

where only the Hα measurements includes a second split at $L \sim 0.3L^{\star}$ which is only constrained by the $z \sim 0.24$ Hα measurements of Shioya et al. (2008). Therefore, we cannot state that the trend is redshift-independent below $0.3L^{\star}$ for Hα-selected emitters due to lack of measurements at different redshifts.

Equations 4.8 – 4.10 show a steep, increasing trend up to $L \sim L^{\star}$ followed by significantly shallower slopes beyond L^{*}. The Hβ+[OIII] fit shows the steepest slope of 1.35 ± 0.47 beyond $L^{\star}$, which could be due to a higher AGN fraction compared to Hα and [OII] since the [OIII] line is a high ionization potential line that can be very bright due to intense star formation and/or AGN activity. The fits confirm a near constant halo mass for $L > L^{\star}(z)$ such that emission line-selected galaxies (Hα, Hβ+[OIII], and [OII]) with different line luminosities $> L^{\star}$ reside in halos with similar masses independent of redshift. This suggests that the mechanisms and

processes causing this flattening of the line luminosity-halo mass relation is possibly the same in Hα, Hβ+[OIII], and [OII] emitters for all redshift slices probed. We discuss the physical causes of the shallower/flat trend in §4.5. The flat/shallower slope could also be due to the lower number density of $\mathbf{10^{12.5-13.0}}$ $M_\odot$ halos given the comoving volume of our survey.

Our results also imply that there is a simple, redshift-independent relationship between the emission line luminosities of galaxies and their host halos once accounting for the evolution in $\boldsymbol{L^\star}$ (Sobral et al., 2010). This has implications for theoretical studies that use photoionization codes along with semi-analytical modeling to study the connection between nebular emission lines and dark matter halo properties (e.g., Orsi et al. 2014).

The results reported in Equations 4.7 – 4.10 and shown in Figure 4.9 do not take into account the errors in $\boldsymbol{L^\star(z)}$. The errors for each sample are listed in Tables 4.3 and 4.4. We find that the errors are on the order of $\mathbf{0.05}$ dex for the lowest redshift samples and $\mathbf{\sim 0.20}$ dex for the highest redshift samples. Taking into account this error does not significantly remove the redshift independency seen in Figure 4.9, but may change the measurements shown in Equations 4.7 - 4.10.

4.4.4 Observed Line Luminosity – Stellar Mass Dependency on Halo Mass

Observations have found a correlation between the star-formation rate and stellar mass in the local Universe (e.g., Salim et al. 2007; Lee et al. 2011), around cosmic noon (e.g., Daddi et al. 2007; Noeske et al. 2007; Rodighiero et al. 2011; Whitaker et al. 2014; Shivaei et al. 2015), and at higher redshifts (e.g., Schreiber et al. 2015; Tasca et al. 2015; Tomczak et al. 2016). Line luminosities trace star-formation activity (e.g., [OIII]: Suzuki et al. 2016; [OII]: Kennicutt 1998; Kewley et al. 2004) and we find a dependence between halo mass, line luminosity, and stellar mass. The question that arises is how much does the dependency of line luminosity affect the dependency measured with stellar mass or vice versa?

We test this by redoing our clustering analysis in 10000 randomly selected parts of the

Table 4.3: Clustering Properties of the Hβ+[OIII] samples as a function of line luminosities and stellar masses. We include $L^\star(z)$ for each sample as measured by Khostovan et al. (2015). All measurements assume a fixed $\gamma = -1.8$. The minimum dark matter halo masses are measured from the r_0 measurements in conjunction with our r_0-halo mass models. All measurements are corrected for cosmic variance by adding in quadrature 11% of r_0 in the total error cited.

Subsample	N_D	$r_{0,\mathrm{exact}}$ (Mpc h^{-1})	$\log_{10}$ $\mathrm{M_{min}}$ ($\mathrm{M_\odot}$ h^{-1})
Hβ+[OIII] $z = 0.84$ ($\log_{10}L^\star = 41.79^{+0.03}_{-0.05}$)			
$40.50 < \log_{10}L_{\mathrm{line}} < 40.60$	188	$1.15^{+0.23}_{-0.22}$	$9.48^{+1.40}_{-1.30}$
$40.60 < \log_{10}L_{\mathrm{line}} < 40.70$	175	$1.46^{+0.23}_{-0.22}$	$10.66^{+0.59}_{-0.57}$
$40.70 < \log_{10}L_{\mathrm{line}} < 40.80$	150	$1.46^{+0.26}_{-0.25}$	$10.67^{+0.67}_{-0.63}$
$40.80 < \log_{10}L_{\mathrm{line}} < 41.00$	279	$1.46^{+0.20}_{-0.21}$	$10.67^{+0.52}_{-0.52}$
$41.00 < \log_{10}L_{\mathrm{line}} < 41.15$	538	$1.77^{+0.22}_{-0.21}$	$11.28^{+0.34}_{-0.34}$
$41.15 < \log_{10}L_{\mathrm{line}} < 41.30$	404	$1.89^{+0.23}_{-0.23}$	$11.46^{+0.31}_{-0.31}$
$41.30 < \log_{10}L_{\mathrm{line}} < 41.60$	492	$2.08^{+0.25}_{-0.24}$	$11.69^{+0.28}_{-0.27}$
$41.60 < \log_{10}L_{\mathrm{line}} < 41.80$	131	$3.18^{+0.44}_{-0.42}$	$12.53^{+0.23}_{-0.22}$
$41.80 < \log_{10}L_{\mathrm{line}} < 41.95$	51	$3.24^{+0.51}_{-0.46}$	$12.55^{+0.26}_{-0.24}$
$41.95 < \log_{10}L_{\mathrm{line}} < 42.55$	61	$4.64^{+0.59}_{-0.60}$	$13.10^{+0.17}_{-0.18}$
$8.50 < \log_{10}M < 8.75$	368	$1.60^{+0.22}_{-0.21}$	$11.15^{+0.32}_{-0.32}$
$8.75 < \log_{10}M < 9.00$	483	$1.75^{+0.22}_{-0.22}$	$11.35^{+0.28}_{-0.28}$
$9.00 < \log_{10}M < 9.20$	391	$1.74^{+0.21}_{-0.22}$	$11.33^{+0.27}_{-0.28}$
$9.20 < \log_{10}M < 9.40$	294	$2.26^{+0.28}_{-0.28}$	$11.89^{+0.26}_{-0.26}$
$9.40 < \log_{10}M < 9.70$	271	$2.34^{+0.30}_{-0.29}$	$11.96^{+0.26}_{-0.26}$
$9.70 < \log_{10}M < 10.64$	213	$2.56^{+0.32}_{-0.32}$	$12.11^{+0.20}_{-0.19}$
$10.64 < \log_{10}M < 11.55$	74	$3.41^{+0.46}_{-0.49}$	$12.55^{+0.21}_{-0.22}$
Hβ+[OIII] $z = 1.42$ ($\log_{10}L^\star = 42.06^{+0.06}_{-0.05}$)			
$41.92 < \log_{10}L_{\mathrm{line}} < 42.02$	191	$1.54^{+0.28}_{-0.25}$	$10.87^{+0.49}_{-0.44}$
$42.02 < \log_{10}L_{\mathrm{line}} < 42.06$	63	$2.33^{+0.49}_{-0.48}$	$11.79^{+0.40}_{-0.39}$
$42.06 < \log_{10}L_{\mathrm{line}} < 42.16$	58	$4.30^{+0.67}_{-0.68}$	$12.78^{+0.22}_{-0.22}$
$42.16 < \log_{10}L_{\mathrm{line}} < 42.26$	25	$4.28^{+1.12}_{-1.08}$	$12.78^{+0.36}_{-0.35}$
$42.26 < \log_{10}L_{\mathrm{line}} < 42.80$	34	$3.97^{+0.82}_{-0.84}$	$12.67^{+0.30}_{-0.31}$
$9.00 < \log_{10}M < 9.50$	96	$2.10^{+0.38}_{-0.36}$	$11.54^{+0.33}_{-0.31}$
$9.50 < \log_{10}M < 10.00$	99	$3.00^{+0.45}_{-0.41}$	$12.14^{+0.21}_{-0.19}$
$10.00 < \log_{10}M < 10.50$	60	$2.93^{+0.66}_{-0.55}$	$12.11^{+0.31}_{-0.26}$
$10.50 < \log_{10}M < 11.00$	53	$3.06^{+0.62}_{-0.55}$	$12.18^{+0.28}_{-0.25}$
Hβ+[OIII] $z = 2.23$ ($\log_{10}L^\star = 42.66^{+0.13}_{-0.13}$)			
$42.30 < \log_{10}L_{\mathrm{line}} < 42.66$	136	$2.66^{+0.44}_{-0.44}$	$11.77^{+0.28}_{-0.28}$
$42.66 < \log_{10}L_{\mathrm{line}} < 42.74$	56	$5.15^{+0.64}_{-0.68}$	$12.74^{+0.16}_{-0.17}$
$42.74 < \log_{10}L_{\mathrm{line}} < 43.10$	57	$7.38^{+0.88}_{-0.90}$	$13.17^{+0.14}_{-0.14}$
$9.25 < \log_{10}M < 10.00$	120	$3.08^{+0.47}_{-0.45}$	$11.89^{+0.26}_{-0.25}$
$10.00 < \log_{10}M < 10.50$	66	$3.22^{+0.50}_{-0.50}$	$11.97^{+0.27}_{-0.27}$
$10.50 < \log_{10}M < 11.00$	41	$3.48^{+0.91}_{-0.90}$	$12.08^{+0.35}_{-0.34}$
Hβ+[OIII] $z = 3.24$ ($\log_{10}L^\star = 42.83^{+0.19}_{-0.17}$)			
$42.30 < \log_{10}L_{\mathrm{line}} < 42.67$	68	$3.24^{+0.51}_{-0.53}$	$11.77^{+0.24}_{-0.25}$
$42.67 < \log_{10}L_{\mathrm{line}} < 42.83$	67	$5.56^{+0.74}_{-0.73}$	$12.52^{+0.17}_{-0.17}$
$42.83 < \log_{10}L_{\mathrm{line}} < 43.18$	44	$6.98^{+1.12}_{-1.00}$	$12.80^{+0.19}_{-0.17}$
$9.20 < \log_{10}M < 9.70$	56	$5.09^{+0.69}_{-0.63}$	$12.29^{+0.18}_{-0.17}$
$9.70 < \log_{10}M < 10.30$	80	$4.35^{+0.65}_{-0.55}$	$12.08^{+0.20}_{-0.17}$
$10.30 < \log_{10}M < 11.00$	29	$5.02^{+1.21}_{-1.04}$	$12.27^{+0.32}_{-0.28}$

Table 4.4: The clustering properties of [OII] as a function of line luminosity and stellar mass. Table description is the same as that of Table 4.3. The $z = 3.34$ and 4.69 measurements are not included in this table as the sample sizes were too small to divide in line luminosity and stellar mass bins. The measurements corresponding to the full samples are shown in Table 4.2.

Subsample	N_D	$r_{0,\mathrm{exact}}$ (Mpc h^{-1})	$\log_{10}$ $\mathrm{M_{min}}$ ($\mathrm{M_\odot}$ h^{-1})
[OII] $z = 1.47$ ($\log_{10}L^\star = 41.86^{+0.03}_{-0.03}$)			
$41.05 < \log_{10}L_{\mathrm{line}} < 41.15$	200	$1.34^{+0.27}_{-0.22}$	$10.47^{+0.61}_{-0.51}$
$41.15 < \log_{10}L_{\mathrm{line}} < 41.25$	501	$1.41^{+0.18}_{-0.18}$	$10.62^{+0.37}_{-0.36}$
$41.25 < \log_{10}L_{\mathrm{line}} < 41.45$	761	$1.74^{+0.20}_{-0.20}$	$11.16^{+0.27}_{-0.28}$
$41.45 < \log_{10}L_{\mathrm{line}} < 41.65$	638	$2.47^{+0.29}_{-0.29}$	$11.89^{+0.21}_{-0.22}$
$41.65 < \log_{10}L_{\mathrm{line}} < 41.85$	667	$2.76^{+0.32}_{-0.32}$	$12.08^{+0.20}_{-0.20}$
$41.85 < \log_{10}L_{\mathrm{line}} < 42.00$	292	$3.34^{+0.40}_{-0.40}$	$12.39^{+0.19}_{-0.19}$
$42.00 < \log_{10}L_{\mathrm{line}} < 42.10$	101	$3.23^{+0.46}_{-0.49}$	$12.34^{+0.23}_{-0.24}$
$42.10 < \log_{10}L_{\mathrm{line}} < 42.20$	68	$3.32^{+0.49}_{-0.50}$	$12.38^{+0.23}_{-0.24}$
$42.20 < \log_{10}L_{\mathrm{line}} < 42.60$	56	$4.06^{+0.88}_{-0.70}$	$12.68^{+0.31}_{-0.25}$
$8.40 < \log_{10}M < 8.80$	217	$1.51^{+0.23}_{-0.23}$	$10.84^{+0.49}_{-0.49}$
$8.80 < \log_{10}M < 9.20$	671	$2.04^{+0.24}_{-0.24}$	$11.48^{+0.21}_{-0.21}$
$9.20 < \log_{10}M < 9.40$	429	$1.88^{+0.24}_{-0.24}$	$11.33^{+0.24}_{-0.23}$
$9.40 < \log_{10}M < 9.85$	840	$2.20^{+0.26}_{-0.25}$	$11.61^{+0.21}_{-0.21}$
$9.85 < \log_{10}M < 10.30$	492	$2.46^{+0.29}_{-0.29}$	$11.81^{+0.21}_{-0.21}$
$10.30 < \log_{10}M < 10.51$	163	$2.30^{+0.33}_{-0.33}$	$11.69^{+0.25}_{-0.26}$
$10.51 < \log_{10}M < 10.85$	203	$2.61^{+0.36}_{-0.35}$	$11.92^{+0.25}_{-0.24}$
$10.85 < \log_{10}M < 11.05$	97	$2.54^{+0.37}_{-0.39}$	$11.86^{+0.27}_{-0.28}$
[OII] $z = 2.25$ ($\log_{10}L^\star = 42.34^{+0.04}_{-0.03}$)			
$42.40 < \log_{10}L_{\mathrm{line}} < 42.57$	102	$2.97^{+0.42}_{-0.42}$	$11.95^{+0.22}_{-0.22}$
$42.57 < \log_{10}L_{\mathrm{line}} < 43.21$	35	$4.49^{+0.75}_{-0.73}$	$12.55^{+0.23}_{-0.22}$
$9.50 < \log_{10}M < 10.25$	61	$3.21^{+0.66}_{-0.54}$	$11.95^{+0.36}_{-0.29}$
$10.25 < \log_{10}M < 11.80$	43	$5.01^{+0.76}_{-0.73}$	$12.56^{+0.21}_{-0.20}$

line luminosity-stellar mass grid and calculate the halo mass following the same methodology highlighted in §4.3.2. Each realization is a rectangular box randomly placed in the grid and must have > 50 sources. The results are shown in Figure 4.10 for only the NB921 samples (Hβ+[OIII] $z = 0.84$ and [OII] $z = 1.47$) as these are the most populated samples and are much easier to investigate the dual dependency of line luminosity and stellar mass with the halo mass. We find that for increasing line luminosity and stellar mass, the halo mass is increasing from as low as 10^8 to 10^{13} $M_\odot$, although there is a significant scatter such that to assess which property dominates the dependency with halo mass requires a look at how stellar mass (line luminosity) is dependent on halo mass for a fixed line luminosity (stellar mass).

We first investigate if there is a line luminosity dependency for a fixed stellar mass. We find a strong dependency between halo mass and line luminosity in Hβ+[OIII] emitters with fixed stellar masses of $10^{8.5-9.5}$ $M_\odot$ where the halo mass is found to increase from $\sim 10^{8.0}$ $M_\odot$ to $\sim 10^{12.5-13.0}$ $M_\odot$. Beyond $> 10^{9.5}$ $M_\odot$ the halo mass is consistent with $10^{12.5-13}$ $M_\odot$ for all observed line luminosities, although this is primarily due to a small sample size (~ 300 sources, see Table 4.3) and a limiting range of line luminosities, especially at higher stellar masses.

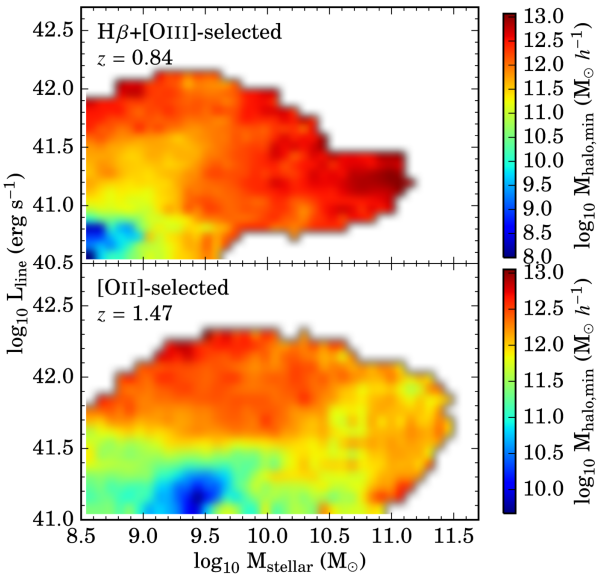

Figure 4.10: Shown is the halo mass dependency on line luminosity and stellar mass. Only the NB921 samples are used (z = 0.84 Hβ+[OIII] and z = 1.47 [OII]) as these are the most populated ($\sim 2500 - 3000$ sources each). All the measurements were done by randomly sampling the grid 10000 times and going through the clustering analysis to measure the halo mass. Overall, we find that the halo mass correlation with line luminosity is stronger than with stellar mass.

For the $z = 1.47$ [OII] emitters, we find that for fixed stellar masses of $10^{8.5-11}$ $M_\odot$, there is a strong dependency with line luminosity such that the halo mass increases from $\sim 10^{9.5}$ $M_\odot$ to 10^{13} $M_\odot$with increasing line luminosity.

Interestingly, the dependency is found for a wider range of fixed stellar masses in comparison to the Hβ+[OIII] sample and this could be due to the [OII] sample selecting more higher mass galaxies with low SFRs and ionization parameters compared to Hβ+[OIII].

In the case of a fixed line luminosity, we find that there is only a stellar mass dependency with halo mass for Hβ+[OIII] emitters with $L \lesssim 10^{41.5}$ erg s^{-1} and it becomes more prevalent at $L \lesssim 10^{41.0}$ erg s^{-1}. The stellar mass dependency in the $L_{\mathrm{H}\beta+[\mathrm{OIII}]} \sim 10^{41.0-41.5}$ erg s^{-1} regime is probably due to contaminants, such as high-mass AGNs, that reside in halos of $\sim 10^{13}$ M$_\odot$. If we disregard this subpopulation of high mass sources, then the dependency breaks down. At $L_{\mathrm{H}\beta+[\mathrm{OIII}]} \lesssim 10^{41.0}$ erg s^{-1}, we find the dependency is the strongest where emitters with stellar masses $> 10^{8.6}$ M$_\odot$ reside in increasingly higher mass halos.

Figure 4.10 shows no significant stellar mass dependency for $z = 1.47$ [OII] emitters at a given line luminosity $> 10^{41.6}$ erg s^{-1}. We only find a stellar mass dependency in the case that $L_{[\mathrm{OII}]} \lesssim 10^{41.3}$ erg s^{-1} where the halo mass is between $10^{11-11.5}$ M$_\odot$ for $8.5 < \log_{10} \mathrm{M}_{\mathrm{stellar}}/\mathrm{M}_\odot < 9$, drops to halo masses of $10^{9.5-11}$ M$_\odot$ for $9 < \log_{10} \mathrm{M}_{\mathrm{stellar}}/\mathrm{M}_\odot < 9.5$, and then increases to halo mass of 10^{12} M$_\odot$ with increasing stellar mass.

We find that for both Hβ+[OIII] and [OII] emitters, a stellar mass dependency appears for the case of faint line luminosities as opposed to the line luminosity dependency which appears for the full stellar mass range. This could suggest that the trend between halo mass and line luminosity is more significant than with stellar mass, such that the correlations we observed in stellar mass could be a result of the halo mass correlation with line luminosity for our samples. Sobral et al. (2010) came to a similar conclusion using a sample of $z = 0.84$ Hα emitters and the rest-frame K-band luminosity as a proxy for stellar mass. Cochrane et al. (2017) also came to a similar conclusion using samples of $z = 0.84$, 1.47, and 2.23 Hα emitters.

4.5 Discussion

In the previous sections, we found that there is a strong, redshift-independent relationship between line luminosity and minimum halo mass (relatively independent of stellar mass for $z = 0.84$ and 1.47 Hβ+[OIII] and [OII] emitters, respectively) up to $L \sim L^{\star}$ for Hα, Hβ+[OIII], and [OII] emitters. For the $L > L^{\star}$ regime, we find that the dependency becomes shallower and is consistent with minimum halo masses between $10^{12.5}$ $M_{\odot}$ and 10^{13} $M_{\odot}$. In this section, we discuss potential physical reasons for the flat/shallower slope of this relationship for the brightest emitters with the understanding that the emission lines observed trace the underlying star formation activity.

4.5.1 Transitional Halo Mass

Current models of galaxy formation suggest that the star formation efficiency is tied to the host halo mass with a peak efficiency found in $\sim 10^{12}$ $M_{\odot}$ halos (e.g., Behroozi et al. 2013a). For $> 10^{12}$ $M_{\odot}$ halos, models predict that the star formation activity in galaxies diminishes as external quenching mechanisms (e.g., shock heating of infalling gas; Dekel & Birnboim 2006) become stronger and are accompanied by internal quenching mechanisms (e.g., AGN feedback; Best et al. 2006). This is referred to as 'halo quenching', where a specific global halo mass is related to galaxy quenching. We note that this is still debatable where, observationally, some studies have found that external quenching is mainly a local phenomenon (e.g., Darvish et al. 2016) and does not depend significantly on the global halo mass (e.g., Peng et al. 2012; Carollo et al. 2013). Other observational studies find that galaxy quenching does depend on halo mass (e.g., Prescott et al. 2011; also see references in Darvish et al. 2017).

A consequence of the halo quenching predictions is a possible transitional halo mass for which the fraction of star-forming galaxies drops and the fraction of passive galaxies increases sharply. Current predictions place this redshift-independent mass scale at a few $\times$ 10^{12} $M_{\odot}$ to

10^{13} $M_\odot$ (Croton et al., 2006; Dekel & Birnboim, 2006; Cen, 2011; Bower et al., 2017) and observations measure it at $\sim 5-8\times10^{12}$ $M_\odot$ (e.g., Hartley et al. 2013; Dolley et al. 2014).

A transitional halo mass would imply that the probability of finding a star-forming galaxy above this mass scale diminishes considerably. Therefore, one would find that above a certain line luminosity, all star forming galaxies would typically reside in halos of a specific mass. We find such a feature in Figure 4.9 where $L > L^\star$ emitters have a flat/shallower line luminosity dependency consistent with halo masses between 3×10^{12} $M_\odot$ and 10^{13} $M_\odot$ up to $z\sim5$, in agreement with predictions of a transitional halo mass.

Although we find evidence for a transitional halo mass, it raises the question of how the brightest emitters reside in 10^{13} $M_\odot$ halos. Since line luminosity traces star-formation activity, it then seems puzzling that systems with such high SFRs are found in massive halos well past the scale where peak SF efficiency occurs. One possibility is that $L > L^\star$ emitters have their emission lines powered by AGN activity. Studies of $z\sim0.8-2.2$ Hα emitters find increasing AGN fractions with increasing line luminosity (Sobral et al. 2016b). Typical $z\sim1.5$ X-ray and radio-selected AGNs are also found to reside in halos of $\sim10^{13}$ $M_\odot$ (Hickox et al., 2009; Koutoulidis et al., 2013; Mendez et al., 2016), consistent with the constant halo mass for $L > L^\star$ Hβ+[OIII] and [OII] emitters. It is then quite possible that the brightest emitters in our samples are AGNs, although we require future spectroscopic confirmation.

Another possibility is that a fraction of the brightest emitters can have their emission lines powered by major merging events, such that these systems are currently undergoing a starburst phase. Simulations of major mergers predict elevated levels of star-formation activity (e.g., Mihos & Hernquist 1996; Di Matteo et al. 2008; Bournaud et al. 2011) and observations have thus far found evidence to support this (e.g., Hung et al. 2013). Semi-analyical models have also predicted that the stellar mass assembly in high-mass halos is merger-driven (e.g., Zehavi et al. 2012). A detailed morphological study of the fraction of mergers as a function of line luminosity would help in addressing this issue and we plan to explore this in the future.

It could also be possible that enhanced gas inflows could allow for the presence of $> L^{\star}$ emitters in massive halos. Dekel & Birnboim (2006) used simulations and predict that cold filamentary streams can penetrate the shock heated halo gas in $> 3 \times 10^{12}$ $M_{\odot}$ halos and fuel star-formation activity in $L > L^{\star}$ galaxies above $z > 2$. To support this level of star-formation activity requires large cold gas accretion rates and a recent ALMA study by Scoville et al. (2017) estimated the rate to be > 100 $M_{\odot}$ yr^{-1} for $z > 2$ to maintain galaxies along the main-sequence.

Overall, we find evidence for a possible transitional halo mass for which star-forming galaxies become less common and halos are increasingly populated by passive galaxies. A likely possibility is that the $L > L^{\star}$ emitters are a mixture of AGN- and star-formation-dominated systems. This is also suggested by Kauffmann et al. (2003) in the local Universe (up to $z \sim 0.3$) where they find that galaxies with AGN and bright [OIII] lines also include young stellar populations due to a recent phase of star-formation activity. Future spectroscopic and morphological studies can shed light on the physical processes involved that are powering nebular emission lines in such massive halos and provide us with valuable insight on the quenching mechanisms that are occurring at this transitional halo mass.

4.5.2 Clustering more dependent on line luminosity than stellar mass?

In §4.4.2 and §4.4.4 we found that the dependency of clustering on line luminosity was more significant than on stellar mass. We also concluded, based on the results of our $z = 0.84$ Hβ+[OIII] and $z = 1.47$ [OII] samples in §4.4.4, the stellar mass dependency may be a result of the line luminosity dependency. This is a similar conclusion made by Sobral et al. (2010) where they used a $z = 0.84$ Hα-selected sample and found that the line luminosity dependency was more significant than the dependency with stellar mass. Coil et al. (2017) came to a similar conclusion where they found that the clustering amplitude was a stronger function of the specific star formation rate than stellar mass and that the clustering strength for a given specific star formation rate was found to be independent of stellar mass. Cochrane et al. (2017) used

Hα-selected narrowband samples at $z = 0.84$, 1.47, and 2.23 and found that the line luminosity dependency was not driven/independent of stellar mass.

We note that the lack of a strong stellar mass dependency with clustering strength/dark matter halo mass could be mainly caused by sample selection. As mentioned before, our samples are line flux-selected such that they are complete in line luminosity down to a completeness limit. Our samples are then not stellar mass complete, especially for the low stellar mass range ($< 10^9$ M$_\odot$; see Khostovan et al. 2016 for the stellar mass functions of our samples). We can only conclude that for narrowband-selected samples, the clustering strength dependency with stellar mass seems to be less significant than the dependency with line luminosity and may also be a result of it as well.

4.6 Conclusions

We have presented our Hβ+[OIII] and [OII] clustering measurements up to $z \sim 3.3$ and ~ 4.7, respectively. The main results of this study are:

1. We find that the power law slopes of the angular correlation functions are consistent with $\beta \sim -0.80$. Using the exact Limber equation, we find typical r_0 between $1.45 - 4.01\ h^{-1}$ Mpc and $1.99 - 8.25\ h^{-1}$ Mpc for Hβ+[OIII] and [OII] emitters, respectively. These correspond to minimum halo masses between $10^{10.70-12.08}$ M$_\odot$ and $10^{11.46-12.62}$ M$_\odot$, respectively.

2. A r_0-line luminosity dependency is found where the brightest emitters are more clustered compared to the faintest emitters. This dependency is found to be redshift-dependent but is biased due to the line luminosity function evolution. When rescaling based on $L^\star(z)$ and using model predictions of halo mass given r_0, we find a strong, increasing dependency between minimum halo mass and line luminosity that is independent of redshift with the faintest Hβ+[OIII] ([OII]) emitters found in $10^{9.5}$ M$_\odot$ ($10^{10.5}$ M$_\odot$) halos and the brightest Hβ+[OIII] ([OII]) emitters in 10^{13} M$_\odot$ ($10^{12.5}$ M$_\odot$) halos.

3. We find a redshift-independent dependency between stellar and halo mass. We find that Hβ+[OIII] emitters with stellar masses $> 10^{9.75}$ $M_\odot$ reside in $10^{12.3}$ $M_\odot$ halos between $z = 0.84$ and 3.24. The [OII] samples also show a dependency for the full stellar mass range.

4. We find that halo mass is strongly correlated with line luminosity than stellar mass when investigating the respective trends in a line luminosity-stellar mass grid space.This then suggests a simple connection between the nebular emission line properties of galaxies and their host halo mass.

5. The line luminosity-halo mass dependency shows an increase from the faintest emitters observed to $L \sim L^\star(z)$. For emitters brighter that $L^\star$, we find that the trend is consistent with halos between $10^{12.5-13}$ $M_\odot$, which is consistent with predictions of a transitional halo mass scale. The bright emitters residing in such halo masses seem to have their strong emission lines attributed to AGN activity, galaxy merging, and enhanced gas inflow.

Our results suggest a simple connection between the clustering/dark matter halo properties and nebular emission line properties of star-forming/'active' galaxies up to $z \sim 5$. This has implications for future theoretical studies that model this connection since previous constraints were up to $z \sim 2$ for only Hα emitters. On the observational side, future spectroscopic studies of bright, emission line-selected galaxies can allow us to investigate the dependency between the ISM properties (internal mechanisms) of galaxies and massive halos (external mechanisms). Morphological studies of our samples can also test to see if the shape of galaxies is connected with the host halo properties. Future space-based (e.g., *JWST*, *WFIRST*, *Euclid*) and ground-based observatories (e.g., European Extremely Large Telescope, Thirty Meter Telescope), can also allow us to study the clustering properties of emission line-selected galaxies at higher redshifts and larger comoving volumes. This would allow us to see when the following redshift-independent trends that seem to have been in place since $z \sim 5$ were first established, which would present a new scaling relation for galaxy formation and evolution models. Our results also are prelude

to large-scale spectroscopic surveys using the upcoming Subaru/PFS (Takada et al., 2014), VISTA/4MOST (de Jong et al., 2016), and Mayall/DESI (DESI Collaboration et al., 2016) instruments that will observe galaxy emission lines in large comoving volumes at redshifts up to $z \sim 2.5$.

4.7 Appendix

4.7.1 Effects of Halo Model Assumptions

Various prescriptions of the halo bias and mass functions exist in the literature. In this section, we explore the effects of assuming a Tinker et al. (2010) halo bias function and Tinker et al. (2008) halo mass function as opposed to other prescriptions. We consider four cases with the following mass and bias functions, respectively: 1) Press & Schechter (1974) + Mo & White (1996), 2) Sheth et al. (2001) for both, 3) Tinker et al. (2008) + Jose et al. (2016), and 4) Despali et al. (2016) + Comparat et al. (2017).

Figure 4.11 shows a comparison between our predictions of halo mass (M_{DMH}) and the predictions from the four cases highlighted above (M_{model}) for a given r_0 measurement at $z \sim 1.5$ and ~ 3.2. We find the offsets are $\sim \pm 0.2$ dex for $r_0 > 3$ Mpc h^{-1} and increase to ± 0.4 dex for lower clustering lengths. The third case best matches our predictions, which is not surprising as it uses the Tinker et al. (2008) halo mass function (same as the one we assumed) and the Jose et al. (2016) bias function, which is an update of the Tinker et al. (2010) bias function. Based on Figure 4.11, we caution the reader that halo mass measurements, be it from our model or any HOD/abundance matching model, can be sensitive to the assumed halo prescriptions.

4.7.2 Minimum or Effective Halo Mass?

We presented our dark matter halo model in §4.3.5 where we use the effective bias using a one-to-one galaxy-halo occupation distribution above a minimum halo mass to connect halo mass

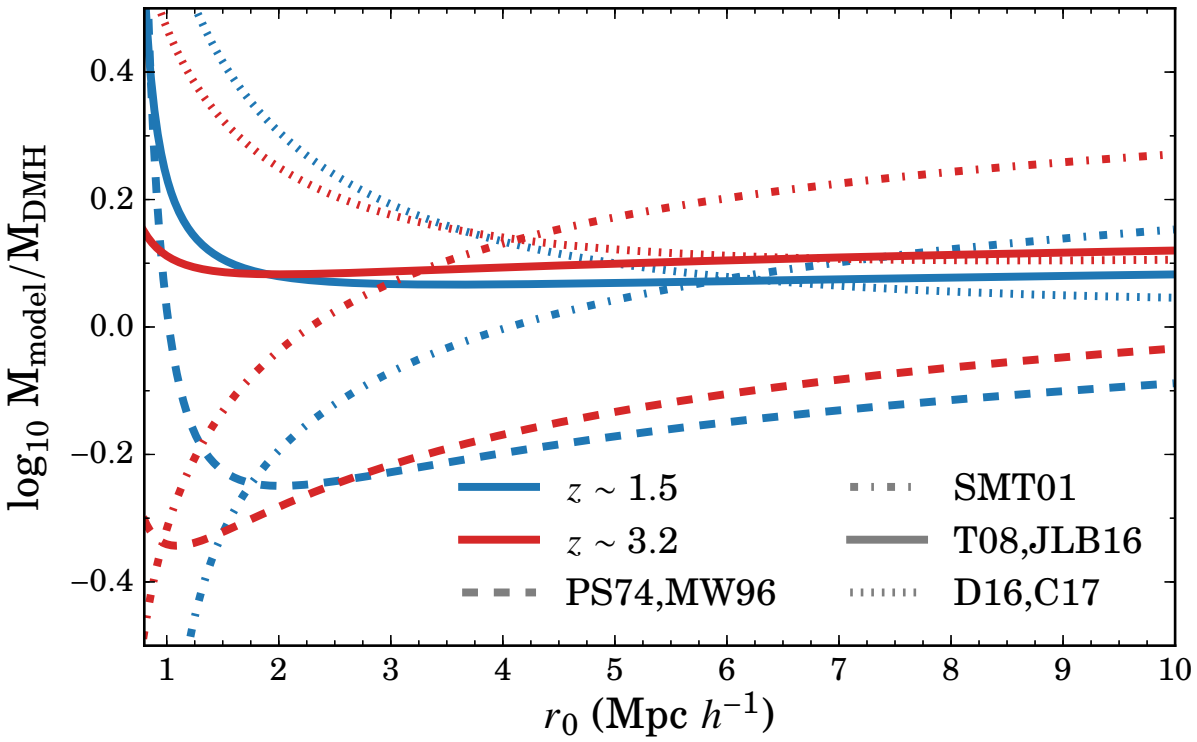

Figure 4.11: Comparison of the predicted minimum halo masses for a given r_0 between our assumed halo bias (Tinker et al., 2010) and mass (Tinker et al., 2008) functions against other assumptions. The cases are as follows (mass function, bias function): (1) Press & Schechter (1974) and Mo & White (1996), (2) Sheth et al. (2001), (3) Tinker et al. (2008) and Jose et al. (2016), and (4) Despali et al. (2016) and Comparat et al. (2017). We show the difference for $z \sim 1.5$ and ~ 3.2 with M_{model}/M_{DMH} being the ratio of one of the cases highlighted above (M_{model}) and our model (M_{DMH}). We find that assuming different prescriptions for halo properties can introduce offsets of $\sim \pm 0.2$ dex for $r_0 > 3$ Mpc h^{-1} and ± 0.4 dex by $r_0 \sim 1$ Mpc h^{-1}.

with r_0 (our observable). This is a simplified approach of measuring halo mass in comparison to typical clustering/dark matter halo studies. Assuming a one-to-one galaxy-halo occupation distribution is not entirely correct, especially for emission line-selected galaxies that form a subset of the total star-forming galaxy population, which forms also a subset of the global population of galaxies. We refer the reader to Cochrane et al. (2017) and Favole et al. (2016) for discussions regarding halo occupation distributions of Hα and [OII] emitters, respectively.

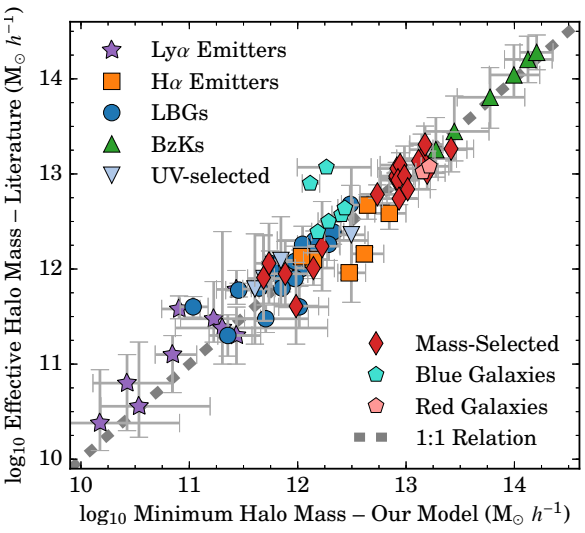

Figure 4.12: A comparison between the effective halo mass, M_{eff}, drawn from the literature and the minimum halo mass, M_{min}, measured using the clustering lengths from the literature in conjunction with our r_0-M_{min} halo model as described in §4.3.5. We find that our simplified model (one-to-one galaxy-halo occupation) produces M_{min} that is consistent with M_{eff} when compared to studies using complex prescriptions for HOD models.

Comparing the stellar mass densities of the global and emission line-selected galaxies from Khostovan et al. (2016) can give us a general idea of what percentage halos are populated by our samples. We find that Hβ+[OIII] emitters reside in $\sim$**40**, **65**, **35**, and **35** percent of halos at $z = 0.84$, **1.42**, **2.23**, and **3.24**, respectively. [OII] emitters are found to reside in $\sim$**70**, **35**, and **15** percent of halos at $z = 1.47$, **2.25**, and **3.34** (there was no $z = 4.69$ stellar mass density measurement in Khostovan et al. (2016) due to the small sample size). It is clear then that our emission line galaxies will not reside in every halo.

It is clear then that our emission line galaxies will not reside in every halo, such that our "minimum" halo masses will be systematically higher. To understand what halo mass is actually being measured using our approach, we compare the predictions from our model with the literature in Figure 4.12 by using r_0 reported in the literature and apply our model to measure M_{min}. Figure 4.12 shows that our measurements of M_{min} are strongly consistent with the effective halo mass reported in studies of Lyα emitters (Ouchi et al. 2010; Bielby et al. 2016; Ouchi et al. 2018), Hα emitters (Geach et al. 2012; Cochrane et al. 2017; Kashino et al. 2017), LBGs (Hildebrandt et al. 2005; Ouchi et al. 2005; Lee et al. 2006), ***BzKs*** (Hayashi et al. 2007), UV continuum-selected (Durkalec et al. 2018), mass-selected (Wake et al. 2011; Durkalec et al. 2015, 2018, Blue galaxies (Mostek et al. 2013), and Red galaxies (Blake et al. 2008; Mostek et al. 2013).

The strong agreement over different sample types and redshifts ranging between local and $z \sim 7$ suggests that, due to our one-to-one galaxy-halo occupation assumption, our model predictions for halo mass are consistent with being effective halo masses rather than minimum halo masses. With this caveat, we still report our halo masses as "minimum" as defined by our model, but note that due to our assumption regarding the occupation distribution, they better represent the effective halo mass.

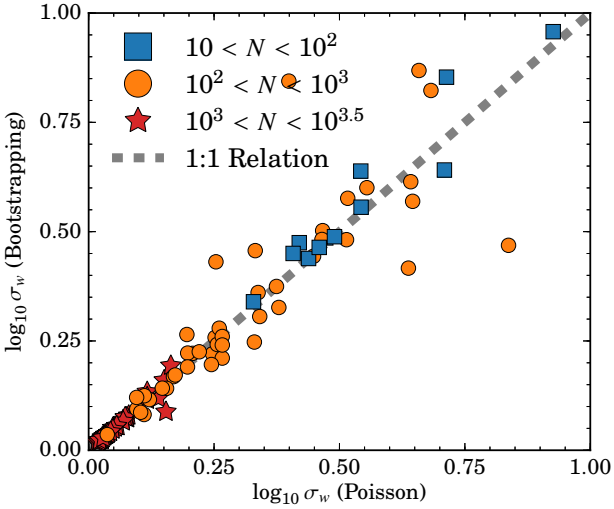

Figure 4.13: Error measurement comparison between Poisson and Bootstrapping errors. The Poisson errors measured are for single realization as described in §4.3.2. The bootstrapped errors are based on resampling a single realization of $w(\theta)$ 2000 times. For both assessments, the bin size and centers were the same in order to ensure a direct comparison. We find that for different sample sizes, N, the errors between Poisson and Bootstrapping are consistent.

4.7.3 Bootstrapping and Poisson Errors

There are three main error estimators that are typically employed in clustering studies: bootstrapping, jackknifing, and Poisson. In the case that Poisson errors are assumed, then the errors are defined as shown in Equation 5.3. Norberg et al. (2009) studied these three estimators to see how reliably each measures the 'true' errors of the ACFs. They found that bootstrapping overestimates the errors by $\sim$40 percent and jackknifing fails at small-scales but can reproduce the errors at large-scales, while Poisson errors were found to underestimate the errors.

We note that the results of Norberg et al. (2009) are based on simulations that have sample sizes comparable to SDSS (10^{5-6} sources) such that the Poisson errors, which are proportional to sample sizes, would severely underestimate the 'true' errors. This may not be true for our samples, which typically consist of 10^{2-3} sources. To test this, we measure the ACF for all the full samples with a fixed bin size and center assuming: 1) Poisson errors and 2) resampling the

ACF 2000 times to measure the errors via bootstrapping.

Figure 4.13 shows the comparison between the assumption of Poisson errors and bootstrapping for all our full samples. We find that our measurements assuming Poisson errors is strongly consistent with bootstrapping up to sample sizes of 10^3. Note that we assume Poisson errors for each individual ACF but also take into account binning effects by repeating our measurements of the ACF with varying bin sizes and centers such that our final measurements are based on the distributions of these realizations.

CHAPTER 5

The clustering of typical Lyα emitters from $z \sim 2.5-6$: host halo masses depend on Lyα and UV luminosities

Abstract

We investigate the clustering and halo properties of ~ 4000 Lyα-selected emission line galaxies (LAEs) from the Slicing COSMOS 4K (SC4K) in 15 discrete redshift slices between $z \sim 2.5-6$. We measure clustering lengths of $r_0 \sim 3-6\ h^{-1}$ Mpc and typical halo masses of $\sim 10^{11}$ $M_\odot$ for our narrowband-selected LAEs with $L_{Ly\alpha} \sim 10^{42}$ erg s^{-1} and $r_0 \sim 3.5-15\ h^{-1}$ Mpc with typical halo masses of $\sim 10^{11-12}$ $M_\odot$ for our intermediate band-selected LAEs with $L_{Ly\alpha} \sim 10^{43}$ erg s^{-1}. We find a strong, redshift-independent trend between halo mass and Lyα luminosity normalized by the characteristic line luminosity, $L^\star(z)$. The faintest LAEs ($L \sim 0.1\ L^\star(z)$) typically found by deep narrowband surveys are found in 10^{10} $M_\odot$ halos and the brightest LAEs ($L \sim 7\ L^\star(z)$) are found in $\sim 5 \times 10^{12}$ $M_\odot$ halos. A dependency with the rest-frame 1500 Å UV luminosity, M_{UV}, is also found where the halo masses increases from 10^{11} $M_\odot$ to 10^{13} $M_\odot$ for $M_{UV} \sim -19$ mag to -23.5 mag. Halo mass is also observed to increase from $10^{9.8}$ $M_\odot$ to $10^{12.3}$ $M_\odot$ for UV

star formation rates from ~ 0.6 $M_\odot$ yr^{-1} to 10 $M_\odot$ yr^{-1} and continues to increase up to $10^{13.5}$ $M_\odot$ in halo mass, although the majority of those sources are AGN. All the trends we observe are found to be redshift-independent. Our results highlight LAEs as likely progenitors of a wide range of galaxies, from dwarf-like, to Milky Way-type, to bright cluster galaxies making LAEs great tools in investigating the early formation and evolution of the galaxies we see in the local Universe.

5.1 Introduction

The current state of galaxy formation and evolution theory suggests that galaxies formed with the assistance of their host dark matter halos, where deep gravitational potential wells allowed for the accretion of cold gas to form the galaxies and fuel star formation activity (see Benson 2010 and Somerville & Davé 2015 for a review). The era between cosmic noon ($z \sim 2$) and the 'end' of the epoch of reionization ($z \sim 6$) constitutes an important time period in the Universe' history. It is within that time (~ 2 Gyr) that galaxies rapidly evolved with their typical star formation rates increasing by an order of magnitude (e.g., Madau & Dickinson 2014; Khostovan et al. 2015). Since galaxies reside and evolve within dark matter halos, the host halos likely play a fundamental role in the overall evolution of galaxies. How do galaxies and their host halos co-evolve?

Addressing such a fundamental question requires representative samples of high-z star-forming galaxies to study their observed clustering properties. Since galaxies reside in dark matter halos, their clustering properties directly trace their dark matter halo properties, although with a few assumptions (e.g., halo mass and bias functions, occupation distributions; see Cooray & Sheth 2002 for a review). Samples of Lyα emitters (LAEs) selected via narrowband surveys provide one efficient and robust window in probing the high-z Universe (e.g., Ouchi et al. 2008; Nilsson et al. 2009). Narrowband surveys have the added advantage of forming large samples of

galaxies by directly observing emission lines associated with star formation and AGN activity using specially designed photometric filters. Because the filter widths are quite narrow (between $50-200$ Å in FWHM), emission line galaxies selected in narrowband surveys have reliable redshifts within $1-2$ percent error (albeit with typical $5-10$ percent contamination; Sobral et al. 2018a).

Previous narrowband surveys have surveyed for LAEs between $z \sim 2-7$ (e.g., Cowie & Hu 1998; Rhoads et al. 2000; Gronwall et al. 2007; Ouchi et al. 2008; Matthee et al. 2015; Santos et al. 2016; Konno et al. 2018), but only a few have investigated their clustering properties. The earliest work on LAE clustering was done by Ouchi et al. (2003), which observed 87 LAEs at $z = 4.86$ in the 543 arcmin^2 Subaru Deep Field and reported the first angular correlation functions and clustering lengths for LAEs ($r_0 = 3.5 \pm 0.3\ h^{-1}$ Mpc). Subsequent narrowband surveys have allowed for measurements of LAE clustering properties between $z \sim 2-7$ (e.g., Shimasaku et al. 2004; Kovač et al. 2007; Ouchi et al. 2010; Zheng et al. 2016; Ouchi et al. 2018). Guaita et al. (2010) presented the first $z \sim 2.1$ measurement using a sample of 250 LAEs in the 0.36 deg^2 ECDF-S field and found $r_0 = 4.8 \pm 0.9$ Mpc h^{-1} and a typical halo mass of $\sim 3.2 \times 10^{11}$ M$_\odot$. The recent $z \sim 2$ measurements of Kusakabe et al. (2018) presented the latest constraints using a sample of ~ 1250 LAEs in four separate fields for a total survey area of 1 deg^2 and found $r_0 = 2.38^{+0.34}_{-0.39}$ Mpc h^{-1} and a typical halo mass of 4×10^{10} M$_\odot$. Both surveys cover the same redshift, but both measure significantly different results. In respect to Guaita et al. (2010), the survey area of Kusakabe et al. (2018) is about 3 times larger and 2.2 times fainter in line flux, which signifies the importance of investigating the clustering properties in terms of their Lyα luminosities.

Although the past two decades have produced a handful of LAE clustering measurements, only a few have focused on how the measured clustering/halo properties are related/correlated to the physical properties of the LAEs (e.g., line luminosity, stellar mass, star formation rates). Ouchi et al. (2003) measured the angular correlation functions subdivided into a bright and

faint sample divided at $L_{\mathrm{Ly}\alpha} \simeq 10^{42.2}$ erg s^{-1} and showed that the brightest LAEs tend to be more clustered in comparison to the faint sample. Bielby et al. (2016) presented clustering measurements of $z \sim 3.1$ LAEs in bins of R-band limiting magnitude (corresponds to the 1500Å UV continuum luminosity, $\mathrm{M_{UV}}$) and found $r_0 \sim 3\ h^{-1}$ Mpc at $R_{lim} = 27.5$ mag and $r_0 \sim 4.5\ h^{-1}$ Mpc at $R_{lim} = 26.00$ mag, such that LAEs with bright $\mathrm{M_{UV}}$ are more strongly clustered. Recently, Kusakabe et al. (2018) used archival NB387 imaging to select about 1250 $z \sim 2$ LAEs across 1 deg^2 and found a weak correlation between Lyα line luminosity limit and clustering length/halo mass. The culmination of these works have suggested possible links between the physical properties of galaxies and their host halo properties.

Besides Lyα studies, narrowband surveys focused on Hα (Sobral et al., 2010; Cochrane et al., 2017, 2018), [OIII] (Khostovan et al., 2018), and [OII] (Khostovan et al., 2018) emission line-selected galaxies have also found strong trends between the physical properties of star-forming/active galaxies and their host halo properties. These surveys reveal strong correlations between halo mass and line luminosity (proxy for star formation rate) up to $z \sim 2.23$ (Hα), $z \sim 3.3$ ([OIII]), and $z \sim 4.7$ ([OII]). Interestingly, Khostovan et al. (2018) found that these trends are redshift-independent once the evolution in typical line luminosity is taken into account suggesting that the host halo and residing galaxy co-evolve in unison over cosmic time. Sobral et al. (2010) was the first to notice this trend up to $z \sim 2.23$ using the Hα sample drawn from the High-z Emission Line Survey (HiZELS) followed by the recent measurements of Cochrane et al. (2017), while Khostovan et al. (2018) extended this work to incorporate [OIII] and [OII] emission-line galaxies up to $z \sim 4.7$ using the same narrowband survey.

Although much work has been done on quantifying the clustering/halo properties and its relation to the physical properties of star-forming galaxies, not much focus has been applied to such analysis with Lyα-selected samples, which allow for observing such trends up to the era of reionization. In this paper, we use the Slicing COSMOS 4K (SC4K) survey to investigate the clustering properties of LAEs in 15 discrete redshift slices between $z \sim 2.5-5.8$ with a total of

~ 4000 LAEs within the 2 deg^2 COSMOS and 1.3 deg^2 SA22 fields.

The paper is organized as follows: In §5.2, we describe the sample of LAEs. In §5.3, we present how we generate our random samples, the methodology in measuring the angular correlation functions, the clustering length, and halo masses, as well as corrections for cosmic variance and a discussion on contamination. In §5.4, we show our methodology in measuring the UV continuum luminosity and slope, as well as the UV star formation rates. In §5.5, we present our main results with discussion regarding its interpretation. Finally, §6.4 highlights the main points of this paper and our final remarks.

Throughout this paper we assume a ΛCDM cosmology with $H_0 = 70$ km s^{-1} Mpc^{-1}, $\Omega_m = 0.3$, and $\Omega_\Lambda = 0.7$. Our reported values for halo masses and $r_0$are in units of $M_\odot\ h^{-1}$ and Mpc h^{-1}, respectively, unless otherwise specified.

5.2 Lyα Sample

5.2.1 Slicing COSMOS 4K

Our sample is drawn from the publicly available Slicing COSMOS 4K (SC4K; Paulino-Afonso et al. 2018; Sobral et al. 2018a), containing 3908 Lyα emitters (LAEs). The survey uses archival Subaru imaging from 12 intermediate bands (Capak et al., 2007; Taniguchi et al., 2007, 2015) in the ~ 2 deg^2 COSMOS field (Scoville et al., 2007; Capak et al., 2007) that are re-reduced following the procedures outlined in Sobral et al. (2018a). The SC4K survey also includes imaging using four narrowband filters: NB392 ($z = 2.2$; Sobral et al. 2017; Matthee et al. 2017b), NB501 ($z = 3.1$; Matthee et al. 2017b), NB711 ($z = 4.8$; Perez et al., in prep), and NB816 ($z = 5.7$; Santos et al. 2016). We restrict our analysis to the samples with $z \gtrsim 2.5$ and also those samples for which the image-to-image variation is negligible and spatially contiguous. This includes all 12 intermediate bands and the NB711 and NB816 narrowband samples.

We refer the reader to Sobral et al. (2018a) for details regarding the sample selection. In

brief, initial emission line galaxy candidates were selected by applying a rest-frame equivalent width cut of **25** Å and **50** Å for intermediate bands and narrowbands, respectively, along with a nebular excess significance cut of $\Sigma > 3$. A combination of spectroscopic redshifts, photometric redshifts, and color-color diagnostics were used to select potential LAEs. These candidates were then visually checked to remove any contaminants arising from artifacts not removed in the data reduction pipeline (e.g., diffraction patterns, edge effects resulting in poor S/N) and sources that have their narrow or intermediate band photometry boosted by the presence of a bright halo from a nearby star in the image. In total, a final sample size of 3908 LAEs spanning between $z \sim 2.5-6$ were selected for which we use 3704 of them due to discarding the NB392 and NB501 samples. In total, 112 of the 3908 LAEs have spectroscopic confirmation with future follow-up observations planned.

Table 5.1 highlights the redshifts and sample sizes of all the LAE samples. To take advantage of larger sample sizes, especially at the high-z end (e.g. IA767 and IA827), we combine the intermediate band samples to form five larger samples as described at the bottom of Table 5.1. The choice of combinations was based on maximizing the sample size, with the different completeness limits per individual sample taken into account, while keeping the redshift widths minimized so as to remove possible cosmic evolutionary effects when using the samples in our clustering measurements.

5.2.2 SA22 NB497

In addition to the SC4K sample, we also use a sample of 1198 $z = 3.1$ LAEs observed in the **1.38** deg^2 SA22 field using archival Subaru Suprime-Cam NB497 imaging (Yamada et al., 2012). The observations were done using Suprime-Cam on the Subaru 8.2 m telescope and consisted of 7 contiguous, homogeneous pointings using three filters: NB497, B, and V, for which the last two were used as the corresponding broadband filters to measure the nebular color excess. These images were re-reduced following the procedures of Sobral et al. (2018a) and the source selection

done by Matthee et al., in prep?. Of the 1198 $z = 3.1$ LAEs, 54 of them are spectroscopically confirmed.

5.3 Clustering Measurements

5.3.1 Random Sample

We follow the approach used in Khostovan et al. (2018), which followed Sobral et al. (2010) to generate random samples. For each narrowband and intermediate band sample, we use the corresponding masked regions maps (see Sobral et al. 2018a). These masked regions remove parts of the survey where the imaging is poor in quality and bright diffraction patterns around bright stars are found. Figure 5.1 shows an example of the masked regions overlaid with our $z = 4.13$ IA624 LAE sample. The bluer intermediate bands (IA427 - IA574) also include an extra ~ 0.02 deg^2 masking due to the lack of u-band imaging. Each sample is homogeneous in depth throughout the COSMOS field, as well as in the SA22 field where we have NB497 imaging. This allows us to exclude the effects of variable depth in generating the mock random samples. In total, our random samples consist of $\sim 10^6$ mock sources per corresponding intermediate/narrowband sample which a subset is selected randomly when making measurements of the angular correlation functions (see below).

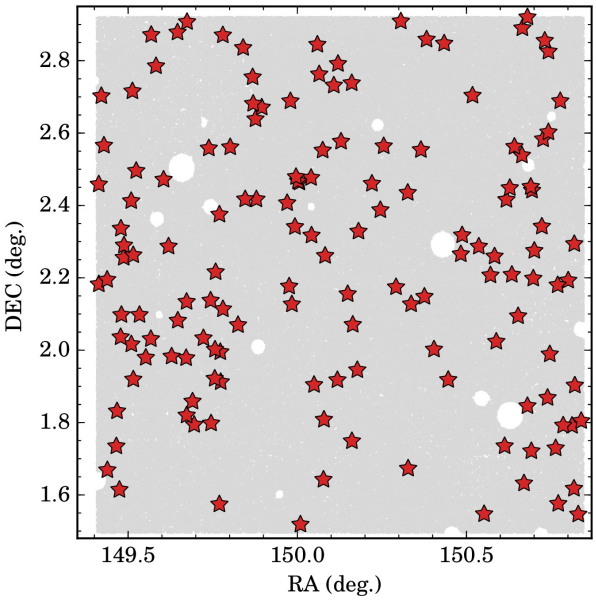

Figure 5.1: The on-sky distribution of the $z = 4.13$ IA624 sample of LAEs shown as red stars. Specific regions are masked throughout the field to account for bright stars and various artifacts. These masked regions are taken into account when generating the random catalogs. The flux depths throughout the images are homogeneous which decreases the effects of image-to-image variations in the clustering measurements.

5.3.2 Angular Correlation Function

A correlation function is a statistical tool that traces the clustering properties of a given sample by comparing the angular (or spatial) distribution to a random distribution (Peebles, 1980). This is typically defined as:

$$dP_{12} = N(1 + w(\theta_{12}))d\Omega_1 d\Omega_2 \tag{5.1}$$

where dP_{12} is the probability of finding two galaxies at positions Ω_1 and Ω_2 with an angular separation of θ_{12} for a complete sample with number density, N. In the case that no angular/spatial correlation exists, then $w(\theta) = 0$ and the probability reduces into a uniform distribution. Therefore, to observe the clustering of galaxies requires a non-zero correlation function.

To measure the angular correlation function, we use the unique methodology as proposed by Sobral et al. (2010) and modified by Khostovan et al. (2018). Similar to many studies, this methodology uses the Landy & Szalay (1993, LS) estimator to measure the observed correlation function described as:

$$w(\theta) = 1 + \left(\frac{N_R}{N_D}\right)^2 \frac{DD(\theta)}{RR(\theta)} - 2\left(\frac{N_R}{N_D}\right)\frac{DR(\theta)}{RR(\theta)} \tag{5.2}$$

where DD, DR, and RR are the real-real, real-random, and random-random galaxy pairs, respectively, and N_R and N_D are the number of random and real galaxies, respectively. The errors are described as:

$$\Delta w(\theta) = \frac{1 + w(\theta)}{\sqrt{DD(\theta)}} \tag{5.3}$$

and are assumed to be Poisson errors. Norberg et al. (2009) showed that Poisson statistics underestimates the "true" errors and suggests using bootstrapping. We note that this result is based on sample sizes of the order of 10^7 and that Khostovan et al. (2018) find no significant difference between Poisson and bootstrapping error measurements for sample sizes similar to the one used in this study (see Appendix C of Khostovan et al. 2018).

We use the following fitting function:

$$w(\theta) = A_w\left(\theta^{\beta} - \frac{\sum RR\theta^{\beta}}{\sum RR}\right) \tag{5.4}$$

where the second term is the integral constraint (IC) that takes into account the underestimation of $w(\theta)$ at large angular separations and A_w and β are the clustering amplitude and slope, respectively. Since our sample sizes are not large enough to constrain the slope, we assume $\beta = -0.8$ (fiducial) for all our measurements.

As described in Khostovan et al. (2018), we measure the correlation function by randomly selecting a starting bin center between $1'' - 5''$ (e.g. $8-40$ kpc at $z \sim 2.5$, $6-30$ kpc at $z \sim 5.7$), constant bin sizes of $\log_{10}\Delta\theta \sim 0.1-0.3$, and a maximum angular separation of $7200''$ (e.g., 58 Mpc at $z \sim 2.5$, 43 Mpc at $z \sim 5.7$). The random sample is drawn from our large mock catalog mentioned in §5.3.1 and we randomly select the number of mock galaxies to be $10-500$ times the number of LAEs. With both the real and random samples, we measure the $w(\theta)$ via the LS estimator as described in Equation 5.2. We then fit our power law model as described in Equation 5.4 to measure the clustering amplitude.

This whole process is iterated 2000 times where the bin sizes, centers, and random sample size vary. The reported clustering amplitude measurements and its associated errors are based on the distribution of A_w drawn from all realizations. The importance of this approach, as highlighted by Khostovan et al. (2018), is that it takes into account the systematic effects due to bin selection (e.g., centers, widths), especially for the low sample sizes.

5.3.3 Real Space Correlation Function

The real space correlation function, $\xi(r)$, measures the spatial clustering of galaxies and is typically described as power law of the form $\xi(r) = (r/r_0)^{\gamma}$, where r_0 is the clustering length and γ is the slope of the correlation function. The angular correlation function (see §5.3.2) is a projection of the spatial correlation function and typical clustering studies relate the two using

the Limber approximation (Limber, 1953). Although this works for typical redshift surveys, Simon (2007) showed quantitatively that the approximation fails, especially at large angular separations, when the widths of the redshift distributions become similar to a delta function. As a consequence, at large angular separations the slope of the angular correlation function changes from $\gamma+1$ to γ, such that $w(\theta)$ is a rescaled version of $\xi(r)$. Various narrowband studies have observed this rescaling (e.g., Gawiser et al. 2007; Guaita et al. 2010; Sobral et al. 2010; Cochrane et al. 2017; Khostovan et al. 2018; Kusakabe et al. 2018; Ouchi et al. 2018).

To properly measure the spatial correlation function for our samples requires that we use the exact form of the Limber equation. We follow the methodology of Khostovan et al. (2018) which uses the exact Limber equation as defined by Simon (2007):

$$w(\theta) = \frac{r_0^{-\gamma}}{1+\cos\theta}\int_0^{\infty}\int_{\bar{r}\sqrt{2(1-\cos\theta)}}^{2\bar{r}} \frac{2p(\bar{r}-\Delta)p(\bar{r}+\Delta)]}{R^{-\gamma-1}\Delta} dR\,d\bar{r}$$
$$\Delta = \sqrt{\frac{R^2 - 2\bar{r}^2(1-\cos\theta)}{2(1+\cos\theta)}} \tag{5.5}$$

where p describes the redshift distribution which is essentially the filter profile in units of comoving distance, R is the distance between two sources, and $\bar{r}$ is the mean spatial position of two sources. As discussed in §5.3.2, our samples are not large enough to constrain the slopes of the correlation functions. Therefore, we fix the slopes such that $\beta = -0.8$ and $\gamma = -1.8$ (fiducial; $\beta = \gamma + 1$). We use the exact filter profiles associated per each narrow/intermediate band sample and use Equation 5.5 along with our observed measurements of $w(\theta)$ to measure the clustering length, r_0, per each iteration as described in §5.3.2.

The redshift distributions of the combined intermediate samples are modeled as the combination of all the filter profiles associated with the respective sample. We also weight the redshift distributions by the number of LAEs specific to a intermediate band sample. For example, the $z \sim 2.8$ sample consists of 1577 LAEs for which 634, 286, and 657 emitters are from the IA427, IA464, and IA484 samples, respectively. Since the number of LAEs is then not homogeneous per

intermediate band sample, the final redshift distribution for the combined sample is weighted by the number of emitters in each intermediate sample.

When we measure the clustering properties in bins of galaxy properties (e.g., line luminosity, UV continuum) we are essentially selecting a subsample from the full redshift distribution. Therefore, to properly measure the spatial correlation function, we must augment the weighting of the redshift distributions which is done using the same approach as described above via the total number of LAEs within each specific bin. For example, the $z \sim 2.8$ has 40, 18, and 42 percent of the sample consists of IA427, IA464, and IA484-selected LAEs, respectively, but for a specific bin in line luminosity that consists of 383 LAEs, the ratios can change such that 28, 19, and 53 percent are from respective intermediate samples. We follow this approach for all measurements of the spatial correlation function.

5.3.4 Dark Matter Halo Model

The spatial clustering of galaxies is related to the overall dark matter distribution as:

$$b_{eff}^2 = \frac{\xi_{gg}(r)}{\xi_{mm}(r)} \tag{5.6}$$

where b_{eff} is the effective galaxy bias, ξ_{gg} and ξ_{mm} are the galaxy-galaxy and matter-matter spatial correlation functions, respectively. The effective galaxy bias is related to the halo occupation distribution by:

$$b_{eff}(z) = \frac{\int_{M_{min}}^{\infty} b_h(M,z) n_h(M,z) \langle N_g(M,z) \rangle \, dM}{\int_{M_{min}}^{\infty} n_h(M,z) \langle N_g(M,z) \rangle \, dM} \tag{5.7}$$

where b_h and n_h are the halo bias and mass functions, respectively, $N_g(M,z)$ is the galaxy-halo occupation function, and $\mathrm{M_{min}}$ is the minimum dark matter halo mass. The effective halo mass can then be calculated as:

$$M_{eff} = \frac{\int_{M_{min}}^{\infty} M n_h(M,z) \langle N_g(M,z) \rangle \, dM}{\int_{M_{min}}^{\infty} n_h(M,z) \langle N_g(M,z) \rangle \, dM} \tag{5.8}$$

for a given sample at a specific redshift.

There are numerous prescriptions for the galaxy-halo occupation that ranges from simple one-to-one occupation to 3 parameter models (e.g., Kravtsov et al. 2004), to 5 parameter models (e.g., Zheng et al. 2005), and can be as complex as 12 parameter models (e.g., Geach et al. 2012).

Since many of our samples are not large enough to properly constrain multiparameter halo occupation distribution models, we assume a simple one-to-one occupation model ($\langle N_g(M,z)\rangle = 1$) where each LAE is a central galaxy hosted by a dark matter halo by a minimum halo mass, $M_{\rm min}$. We use the Colossus package (Diemer, 2017) in order to measure ξ_{mm} at the redshifts corresponding to our samples. The effective bias is measured at $r = 8\ h^{-1}$ Mpc which corresponds to the regime for which the linear matter power spectrum dominates. The Tinker et al. (2010) halo bias and Tinker et al. (2008) halo mass functions are used for b_h and n_h in Equation 5.7, respectively.

Throughout this paper, we refer to the effective halo mass as 'halo mass' unless otherwise stated.

5.3.5 Cosmic (Sample) Variance

One of the major systematic uncertainties that we take into account in our measurements is the effects of cosmic or selection variance which arises from the limited survey area. Sobral et al. (2010) measured the effects of cosmic variance on the clustering amplitude using their Hα sample at $z = 0.84$ by sampling areas between 0.05 deg^2 to 0.5 deg^2 in their 1.3 deg^2 coverage of the COSMOS field. They find that the uncertainties in the clustering amplitude as a function of area scales as $20 \times \Omega^{-0.35}$, with Ω being the survey size in deg^2. For the case of our 2 deg^2 survey, the uncertainties in the clustering amplitude is ~ 16 percent of A_w which corresponds to ~ 11 percent of the clustering length, r_0. We incorporate these systematic errors by adding them in quadrature to the measured uncertainites.

Table 5.1: List of the filters corresponding to rest-frame 1500Å for each intermediate and narrowband sample. The central wavelength and widths are the rest-frame parameters of the corresponding filters. All photometry used in measuring β are shown in the β Filters column, where the number in parenthesis denotes the total number of filters used.

Sample	z	N_g	Filter	Eff. Wave. (Å)	FWHM (Å)	β Filters	$N_{\rm filters}$
IA427	2.51 ± 0.08	748	V_{540}	1548.31	141.45	$BVgri$, IA464 – IA827, NB711, NB816	20
IA464	2.81 ± 0.09	313	V_{540}	1426.40	130.31	$VrizY$, IA484 – IA827, NB711, NB816	17
IA484	2.99 ± 0.09	713	r_{645}	1628.59	147.45	$VrizYJ$, IA505 – IA827, NB711, NB816	17
IA505	3.17 ± 0.09	484	r_{645}	1558.30	141.09	$VrizYJ$, IA527 – IA827, NB711, NB816	16
IA527	3.33 ± 0.10	642	r_{645}	1500.72	135.87	$VrizYJ$, IA574 – IA827, NB711, NB816	15
IA574	3.74 ± 0.11	98	i_{790}	1682.64	148.11	$rizYJ$, IA624 – IA827, NB711, NB816	13
IA624	4.13 ± 0.12	143	i_{790}	1554.72	136.85	$izYJ$, IA679 – IA827, NB711, NB816	11
IA679	4.58 ± 0.14	80	z_{915}	1429.34	125.81	$izYJH$, IA709 – IA827, NB711, NB816	11
IA709	4.82 ± 0.13	63	z_{915}	1579.84	120.60	$izYJH$, IA738 – IA827, NB816	9
IA738	5.06 ± 0.13	79	z_{915}	1517.28	115.83	$izYJH$, IA767 – IA827, NB816	8
IA767	5.33 ± 0.15	33	z_{915}	1452.56	110.89	$zYJH$, IA827, NB816	6
IA827	5.78 ± 0.14	36	Y_{1029}	1517.51	76.17	$zYJHK$	5
NB497	3.10 ± 0.02	1198	r_{645}	1584.90	143.49	$grizJ$	5
NB711	4.86 ± 0.03	78	z_{915}	1569.06	119.78	$izYJH$, IA738 – IA827	9
NB816	5.71 ± 0.04	192	Y_{1029}	1535.60	77.10	$zYJH$	4
IA427 - IA484	$2.75^{+0.33}_{-0.33}$	1577	—	—	—	—	—
IA505 - IA527	$3.25^{+0.18}_{-0.17}$	1074	—	—	—	—	—
IA574 - IA624	$3.94^{+0.32}_{-0.31}$	185	—	—	—	—	—
IA679 - IA738	$4.82^{+0.37}_{-0.38}$	192	—	—	—	—	—
IA767 - IA827	$5.56^{+0.37}_{-0.38}$	53	—	—	—	—	—

5.3.6 Contamination

The effect off contamination is typically assumed to cause an underestimation of the observed clustering signal. The general idea is that contaminants will form a fraction of the underlying and will be randomly distributed, hence the underestimation. Quantitatively, the clustering signal, A_w, will be underestimated by a factor of $(1-f)^2$, with f being the contamination fraction. This translates to a factor of $(1-f)^{2/|\gamma|}$ for r_0 (the clustering length).

As discussed in Khostovan et al. (2018), the effects of contamination is not as straightforward since the contaminants are other emission line-selected galaxies. In the case of this study, our contaminants will be primarly low-z interlopers, such as [OII], [OIII], and Hα emitters. These low-z interlopers also exhibit non-random clustering (e.g., Shioya et al. 2008; Sobral et al. 2010; Stroe & Sobral 2015; Cochrane et al. 2017; Khostovan et al. 2018) and, therefore, can either cause an overestimation or underestimation of the clustering signal.

Sobral et al. (2018a) investigated the contamination fraction for the SC4K sample using the available spectroscopic measurements. Of the 132 sources with spectroscopic redshifts, 112 were confirmed to be LAEs suggesting a contamination fraction of ~ 15 percent, which is typically of large-area Lyα NB surveys. Sobral et al. (2018a) also investigated whether this contamination was dependent on redshift, Lyα luminosity, and rest-frame EW and found that it is constant around 10 - 20 percent. Using the simple $(1-f)^2$ factor, a contamination fraction of 15 percent would increase A_w by ~ 38 percent and r_0 by ~ 20 percent, but with the assumption that these contaminants are randomly distributed, which, as discussed above, may well not be the case. We instead omit from correcting the clustering measurements for contamination effects, but cite the numbers above as the maximum effect contaminants can have on the clustering signal.

5.4 Rest-Frame UV Properties

5.4.1 Determining M_{UV} and β

The typical shape of the SED of star-forming galaxies at $1300\text{Å} < \lambda < 2800\text{Å}$ can be best fit by a power law of the form $f_\lambda \propto \lambda^\beta$, where f_λ is the flux density in units of erg s^{-1} cm^{-2} Å^{-1} and β is the UV spectral slope. Since the cross-section of dust grains better absorbs UV light, the shape of the SED via β can be used to measure the amount of dust attenuation (e.g, Calzetti et al. 1994; Meurer et al. 1999), although it should be noted that redder UV slopes ($\beta > -2$) can also signify galaxies with mature, evolved stellar populations. We expect this degeneracy in

interpreting β to be negligible as our samples are emission line-selected and are then biased towards populations of actively star-forming galaxies.

We measure β by fitting the power law described above using the available photometry in the rest-frame range of $1300\text{Å} < \lambda < 2800\text{Å}$ and measure the 1500 Å UV continuum magnitudes (M_{UV}). Table 5.1 shows the corresponding observer-frame photometric band used to measure M_{UV} , the rest-frame effective wavelength and FWHM of the filter, and the observer-frame filters used in measuring β. Although the filters cover 1500Å within the FWHM, their effective wavelengths are off-centered by a maximum of ~ 130Å which causes an offset in our measurements of M_{UV}. We calculate the maximum offsets to be ~ -0.04, -0.09, and -0.14 mag for UV spectral slopes of $\beta = -1.5$, -1, -0.5. In principle, the offset can be taken into account by applying the correction, $-2.5(\beta+2)\log_{10}(\lambda/1500\text{Å})$, to M_{UV}. Since our LAEs typically have blue spectral slopes, especially for the higher redshift samples, the offsets are negligible. For the case of our sources with red spectral slopes ($\beta > -2$), we find the uncertainties in M_{UV} are larger than the offsets.

Since our samples are emission line-selected, we are prone to detect low stellar mass sources for which the stellar continuum is below the survey detection limit. In such cases, we apply a lower limit to M_{UV} by using the 3σ detection limit of the photometry. The lack of stellar continuum also means that we are not able to measure β for a subset of our sources. There are also sources for which the uncertainties in β are quite high due to weak stellar continuum measurements. To take this effects into account, we take all measurements of β that have a S/N ($|\beta/\Delta\beta|$) > 3 and measure the median. This is then used as the median stacked spectral slope for those that have S/N < 3 or no β measurements.

5.4.2 Star Formation Rates of LAEs

Typically, narrow band surveys measure star formations rates using the observed or dust-corrected emission line luminosity in conjunction with a star formation calibration. In the case

of LAEs, measuring star formation rates using the Lyα line introduces several caveats. Even though Lyα traces the ionizing radiation of star formation activity, it is severely attenuated by dust and is easily absorbed/scattered by neutral hydrogen such that not all of the Lyα photons reach the observer.

To measure the star formation rates of our LAEs, we instead use the UV continuum luminosities, M_{UV}, as described in §5.4.1, which traces the population of short-lived, massive *O*, *B*, and *A* type stars covering a star formation activity timescale of ~ 100 Myr. We assume the Kennicutt (1998) SFR(UV) calibration:

$$\mathrm{SFR(UV)} = 1.4 \times 10^{-28} \left(\frac{L_\nu}{erg\ s^{-1}\ Hz^{-1}} \right) M_\odot\ yr^{-1} \tag{5.9}$$

where L_ν is the UV luminosity per unit frequency. This calibration is valid for the range of 1500 Å to 2800 Å, where L_ν is consistently flat (assuming $\beta \sim -2$). We assume the Meurer et al. (1999) calibration to dust correct M_{UV}:

$$A_{UV} = 4.43 + 1.99\beta \tag{5.10}$$

where A_{UV} is the UV dust extinction and β is the UV spectral slope described in §5.4.1.

5.5 Results & Discussion

5.5.1 Clustering Properties of LAEs

The angular correlation functions are shown for all our narrowband, intermediate band, and combined samples in Figures 5.2, 5.3, and 5.4, respectively, and are in order in redshift from left to right. Each bin in angular separation encompasses the median measurement of $w(\theta)$ for all 2000 realizations and the errors includes the scatter in $w(\theta)$ and the median Poisson error described in Equation 5.3. In this respect, we are taking into account the effects of selecting some arbitrary fixed bin size and bin width in making our final ACF measurements. We overlay

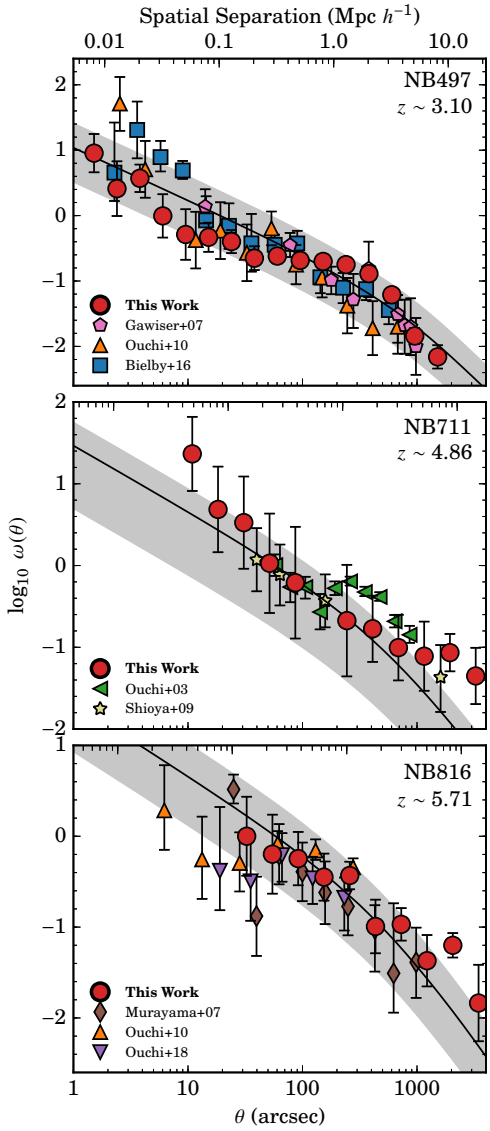

Figure 5.2: The angular correlation functions for each narrowband sample. The *red circles* are the median observed measurements for $w(\theta)$ based on all 2000 iterations. The *black line* shows the best-fit model as described in Equation 5.5 with the 1σ uncertainty represented as the *grey*. We only detect the 1−halo term at $\theta < 10''$ ($r < 53$ kpc h^{-1}) for our $z \sim 3.1$ sample, which suggests that our sample does contain satellites. We ruled out the large overdensity in the SA22 field as the source of the 1−halo term (see Appendix 5.7.1). Overlaid are the ACFs from various narrowband surveys that are consistent with our redshift samples.

the fits based on the measured r_0 in Equation 5.5 and shown in Table 5.2 and find that it is consistent with the median ACFs. Note that, as described above, the measured r_0 is based on the distribution of 2000 r_0 measurements that correspond to each individual ACF.

As described in §5.3.2, we use the exact form of the Limber Equation as outlined by Simon (2007) to fit the ACFs and find that it best represents the observed measurements, especially at higher angular separations where the deviation from a simple power law occurs. This is more pronounced in the $z \sim 3.1$ NB497 ACF at angular separations greater than $600''$, which corresponds to comoving separations of ~ 3.4 Mpc h^{-1}, as shown in the top panel of Figure 5.2. Previous narrowband studies have also observed deviations from the simple power law form at high angular separations (e.g., Sobral et al. 2010; Cochrane et al. 2017; Khostovan et al. 2018).

Figure 5.2 includes the observed ACFs from various clustering studies of LAEs (Ouchi et al., 2003; Gawiser et al., 2007; Murayama et al., 2007; Shioya et al., 2009; Ouchi et al., 2010; Bielby et al., 2016; Ouchi et al., 2018).

We find that in, general, our ACFs and fits are in agreement with the literature. Note that the ACFs shown are not corrected for cosmic variance effects, which would severely affect $\sim$ arcmin^2 measurements such as those of Ouchi et al. (2003) and Gawiser et al. (2007) (see Table 5.3 for survey size). This is probably why the $z \sim 4.86$, 543 arcmin^2 Subaru Deep Survey measurements of Ouchi et al. (2003) are systematically above our measurements, but still within 1σ.

5.5.1.1 Effects of the 1-halo Term

Typically, ACFs trace two distinct clustering scenarios. The first is the galaxy-galaxy angular correlation within a single dark matter halo, referred to as the 1-halo term. The second is the galaxy-galaxy angular correlation with both galaxies residing in separate dark matter halos, which is referred to as the 2-halo term. The 1-halo term signal is observed at low angular separations and traces the clustering properties of both central and satellite galaxies, while the 2-halo term is observed at larger angular separations. Evidence for a 1-halo term would be seen as a deviation from a power law at low angular separations.

We find that all our samples show no significant detection of the 1-halo term, except for the $z \sim 3.1$ NB497 sample, which suggests that the LAEs in our sample are primarily centrals and have low/negligible satellite fractions. This could be due to selection bias as we are selecting LAEs with strong emission lines are missing the faint, low-mass population that form the bulk of the satellite population.

We detect the 1−halo term in the $z \sim 3.1$ NB497 sample at angular (comoving) separations of $\sim 10''$ (~ 50 kpc h^{-1}), although we note that the observed ACFs are still consistent with the exact Limber equation fits. One possible reason for the detection of the 1−halo term is the presence of a significant overdense region in the SA22 field which, in principle, would cause elevated correlation function measurements at low angular resolutions. We test this idea in Appendix 5.7.1 by masking the overdense region and repeating our measurements. We find no significant difference between the ACFs for the full SA22 field and the case where the overdense

region is masked.

Another possibility is that the $z \sim 3.1$ NB497 sample is deep enough in line luminosity to observe satellite LAE galaxies. We test this idea as well in Appendix 5.7.1 by applying varying line luminosity thresholds and find that the 1−halo term disappears at $L_{\mathrm{Ly}\alpha} \gtrsim 0.4\ L^{\star}$, such that the satellite fraction is negligible beyond this threshold. Although we like to point out that studies of emission line galaxies (Cochrane et al., 2017) and LBGs (Harikane et al., 2018) show that the satellite fractions are typically $\lesssim 5$ percent, such that they are negligible. Since measurements of the satellite population is not the main focus of this paper, we defer further discussion but assume based on past works and our own observations that such a population has minimal effects on our measurements.

5.5.1.2 Clustering Length

With the observed ACFs, we measure the spatial clustering lengths using our approach highlighted in §5.3.3. Figure 5.5 shows the redshift evolution of the clustering length, r_0, for all our LAE samples. Although there is a distinct difference between the NB- and IB (combined IB)-selected results which arises primarily due to sample bias, both show an increasing r_0 with increasing redshift and are shown in Table 5.2. Comparing the NB- and IB-samples yields an apparently different redshift evolution where by $z = 5.7$, the IB-samples are three times as clustered. A similar result is seen when comparing the NB- and combined IB-samples. The main cause of this difference is due to sample selection and survey parameters (e.g., IB samples are shallower in depth and have a rest-frame EW cut two times higher than the NB samples).

The issue of sample selection effects on the clustering results become evident when comparing IB-to-IB samples. For example, the $z = 2.8$ IA464 sample is shallower in depth in comparison to the $z = 2.5$ IA427 and $z = 3.0$ IA484 sample and is found to be more clustered by a factor of two. This suggests that the clustering signal is dependent on Lyα luminosity and to properly compare clustering properties requires that we take this effect into account, as suggested by

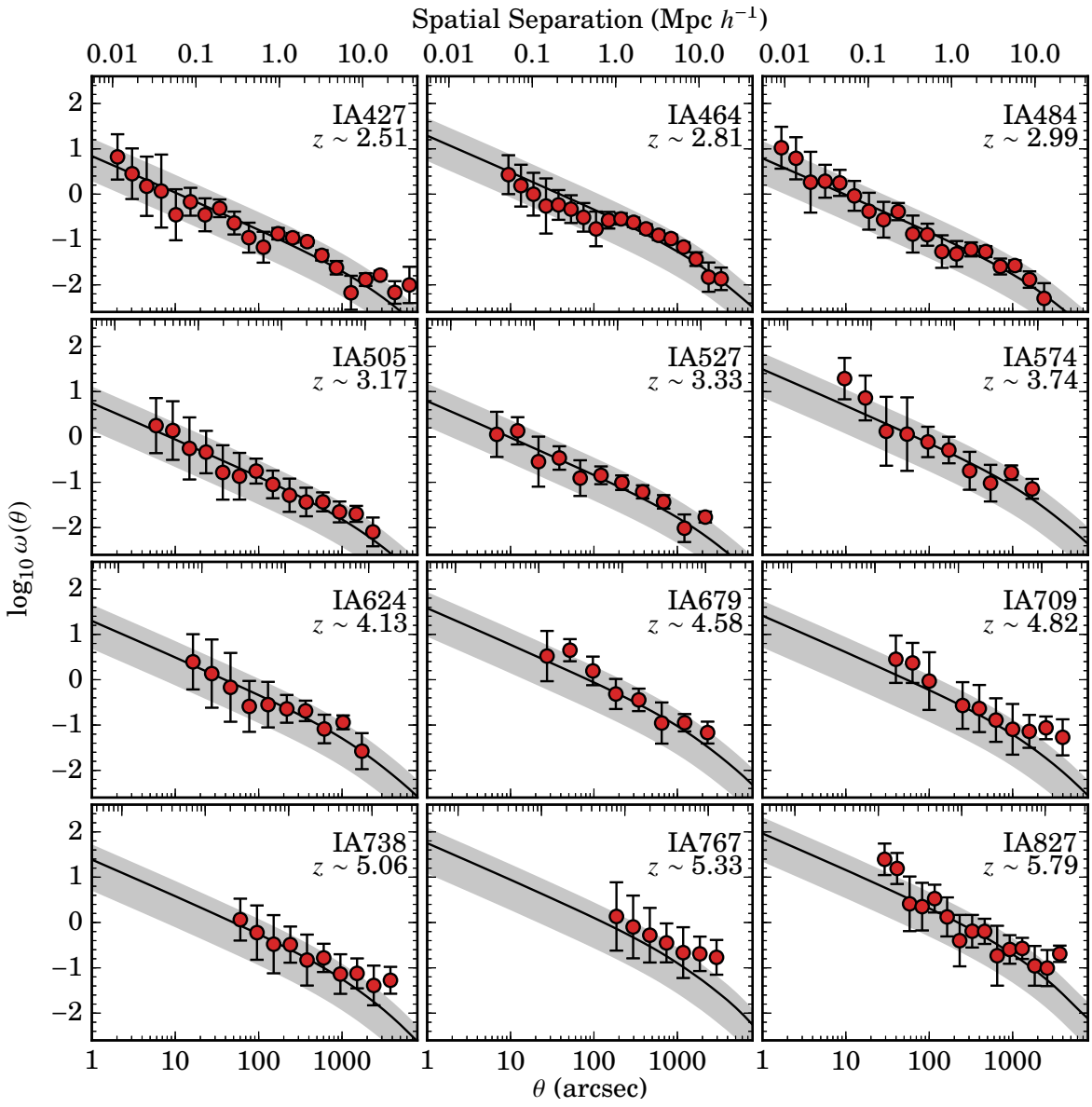

Figure 5.3: Same description as in Figure 5.2 but for the intermediate samples. We find no significant detections of the 1-halo term implying that satellite fractions are negligible for these LAEs. Note that the IB samples are biased towards the brightest LAEs (typically $L > L^{\star}(z)$ galaxies).

Table 5.2: The clustering properties for the full population of LAEs per sample. Shown are the redshifts, filter names, number of LAEs per sample, the corresponding survey area in deg^2, the characteristic line luminosity ($L^\star(z)$), the clustering amplitude measured from the observed ACFs, the exact clustering length, r_0, measured using Equation 5.5, and the effective halo mass measured using our model described in §5.3.4. Each sample presented are within the ~ 2 deg^2 field, except for the 1.38 deg^2 SA22 NB497 sample. All $L^\star(z)$ measurements are from Sobral et al. (2018a) except for the narrowband samples. The NB816 $L^\star$ is measured by Santos et al. (2016). We use the redshift evolution of $L^\star(z)$ from the SC4K samples measured in Sobral et al. (2018a) to measure $L^\star(z)$ for the NB497 and NB711 samples. Our NB711 $L^\star(z)$ measurement is consistent with Shioya et al. (2009) which measured $\log_{10} L^\star = 42.9^{+0.5}_{-0.3}$ erg s^{-1}, although with large error bars.

z	Filter	$N_{\rm gal}$	Area (deg^2)	$\log_{10}\ L^\star(z)$ (erg s^{-1})	A_w (arcsec$^{-0.8}$)	$r_0^{\rm exact}$ (Mpc h^{-1})	$\log_{10}$ Halo Mass ($M_\odot\ h^{-1}$)
2.51	IA427	748	1.94	$42.76^{+0.07}_{-0.07}$	$6.47^{+1.25}_{-1.2}$	$4.13^{+0.42}_{-0.42}$	$11.59^{+0.16}_{-0.16}$
2.81	IA464	313	1.94	$42.83^{+0.36}_{-0.19}$	$15.51^{+3.10}_{-2.93}$	$7.24^{+0.76}_{-0.74}$	$12.28^{+0.13}_{-0.13}$
2.99	IA484	713	1.94	$42.64^{+0.06}_{-0.05}$	$4.86^{+1.13}_{-1.08}$	$3.85^{+0.46}_{-0.45}$	$11.30^{+0.20}_{-0.19}$
3.17	IA505	484	1.94	$42.80^{+0.09}_{-0.07}$	$4.46^{+1.42}_{-1.09}$	$3.62^{+0.54}_{-0.50}$	$11.14^{+0.25}_{-0.23}$
3.33	IA527	642	1.94	$42.68^{+0.07}_{-0.06}$	$5.94^{+1.13}_{-1.13}$	$3.89^{+0.43}_{-0.42}$	$11.20^{+0.18}_{-0.18}$
3.74	IA574	98	1.96	$43.03^{+0.18}_{-0.15}$	$23.39^{+7.97}_{-6.13}$	$9.56^{+1.50}_{-1.26}$	$12.31^{+0.19}_{-0.16}$
4.13	IA624	143	1.96	$42.83^{+0.17}_{-0.15}$	$15.59^{+5.09}_{-4.68}$	$7.49^{+1.17}_{-1.22}$	$11.89^{+0.20}_{-0.21}$
4.58	IA679	80	1.96	$43.15^{+0.16}_{-0.15}$	$37.35^{+10.52}_{-10.51}$	$10.81^{+1.79}_{-1.66}$	$12.21^{+0.20}_{-0.18}$
4.82	IA709	63	1.96	$42.98^{+0.17}_{-0.14}$	$24.38^{+11.39}_{-8.69}$	$8.26^{+1.79}_{-1.87}$	$11.81^{+0.28}_{-0.29}$
5.06	IA738	79	1.96	$43.30^{+0.23}_{-0.19}$	$19.68^{+8.13}_{-5.54}$	$7.79^{+1.61}_{-1.10}$	$11.67^{+0.27}_{-0.19}$
5.33	IA767	33	1.96	$43.30^{+0.28}_{-0.20}$	$39.53^{+19.24}_{-18.98}$	$12.74^{+2.50}_{-2.62}$	$12.21^{+0.23}_{-0.24}$
5.79	IA827	36	1.96	$43.35^{+0.24}_{-0.19}$	$76.99^{+25.06}_{-24.01}$	$15.56^{+2.51}_{-2.71}$	$12.34^{+0.18}_{-0.20}$
3.10	NB497	1198	1.38	42.77	$8.95^{+1.54}_{-1.55}$	$3.11^{+0.30}_{-0.29}$	$10.89^{+0.18}_{-0.17}$
4.86	NB711	78	1.96	43.15	$17.85^{+10.81}_{-7.43}$	$4.57^{+1.24}_{-1.33}$	$10.97^{+0.42}_{-0.45}$
5.71	NB816	172	1.96	$43.25^{+0.09}_{-0.06}$	$19.18^{+4.07}_{-3.83}$	$5.04^{+0.55}_{-0.56}$	$10.87^{+0.17}_{-0.17}$
2.75	—	1577	—	—	$2.89^{+0.63}_{-0.59}$	$4.50^{+0.54}_{-0.51}$	$11.63^{+0.18}_{-0.17}$
3.25	—	1074	—	—	$3.17^{+0.85}_{-0.74}$	$3.75^{+0.52}_{-0.50}$	$11.17^{+0.23}_{-0.22}$
3.94	—	185	—	—	$10.41^{+4.26}_{-3.52}$	$7.62^{+1.56}_{-1.48}$	$11.97^{+0.26}_{-0.25}$
4.82	—	192	—	—	$12.71^{+4.36}_{-3.98}$	$9.24^{+1.94}_{-1.93}$	$11.96^{+0.26}_{-0.26}$
5.56	—	53	—	—	$44.55^{+19.63}_{-15.12}$	$16.16^{+3.80}_{-3.52}$	$12.43^{+0.26}_{-0.24}$

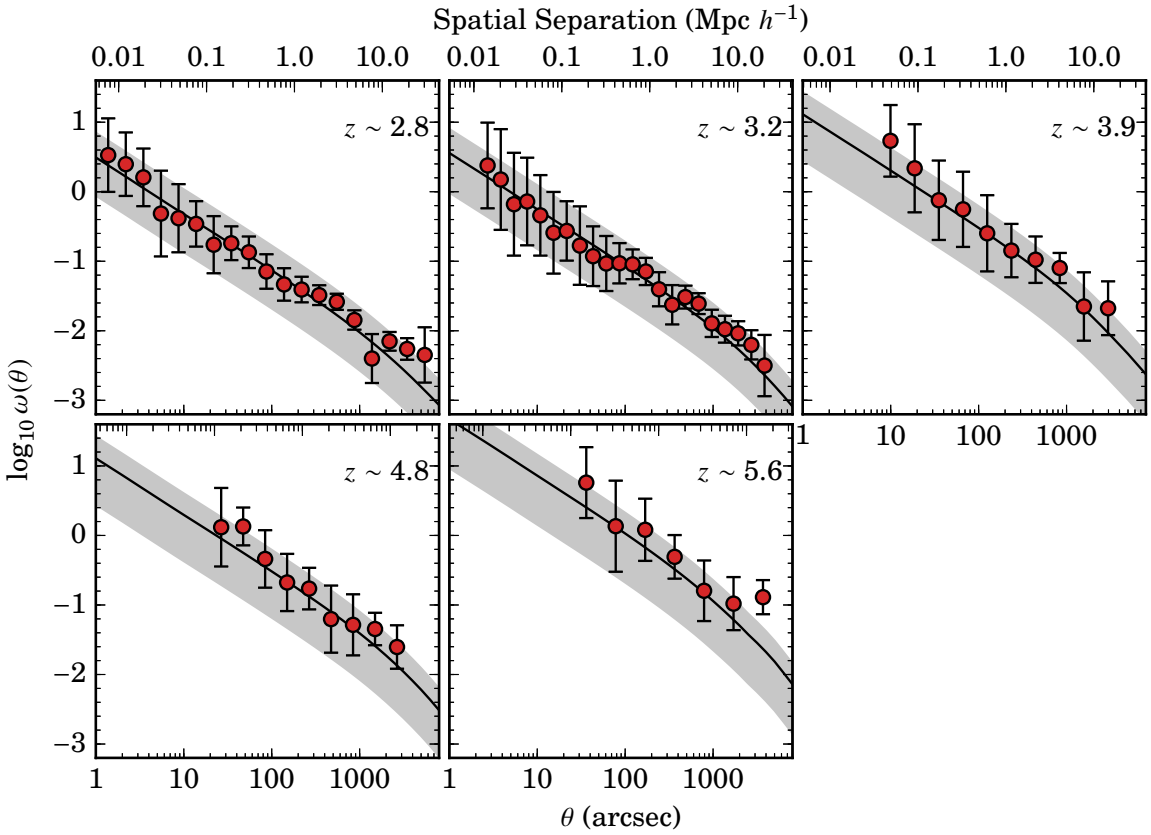

Figure 5.4: Same description as in Figure 5.2 but for the combined intermediate samples. The main importance of the combined IB samples is the large increase in sample sizes, especially at $z > 4$ where the individual IB samples contain $\sim 30-100$ LAEs each. As found in Figure 5.3, we find no significant detection of a 1−halo term such that the satellite fraction in these LAE samples are negligible.

Khostovan et al. (2018).

Figure 5.5 also includes the clustering lengths associated with minimum halo masses between 10^{8-12} $M_\odot$ host dark matter halos as a function of redshift. We find that our IB-selected LAEs typically reside in host halos with a minimum mass range of $\sim 10^{11-12}$ $M_\odot$ and the NB-selected LAEs show a consistent minimum host halo mass of $\sim 10^{11}$ $M_\odot$ for all redshifts observed. There is no redshift evolution observed in host halo mass, which suggests that LAEs at different redshifts reside in halos of similar physical properties. Table 5.2 highlights the effective host halo masses per sample.

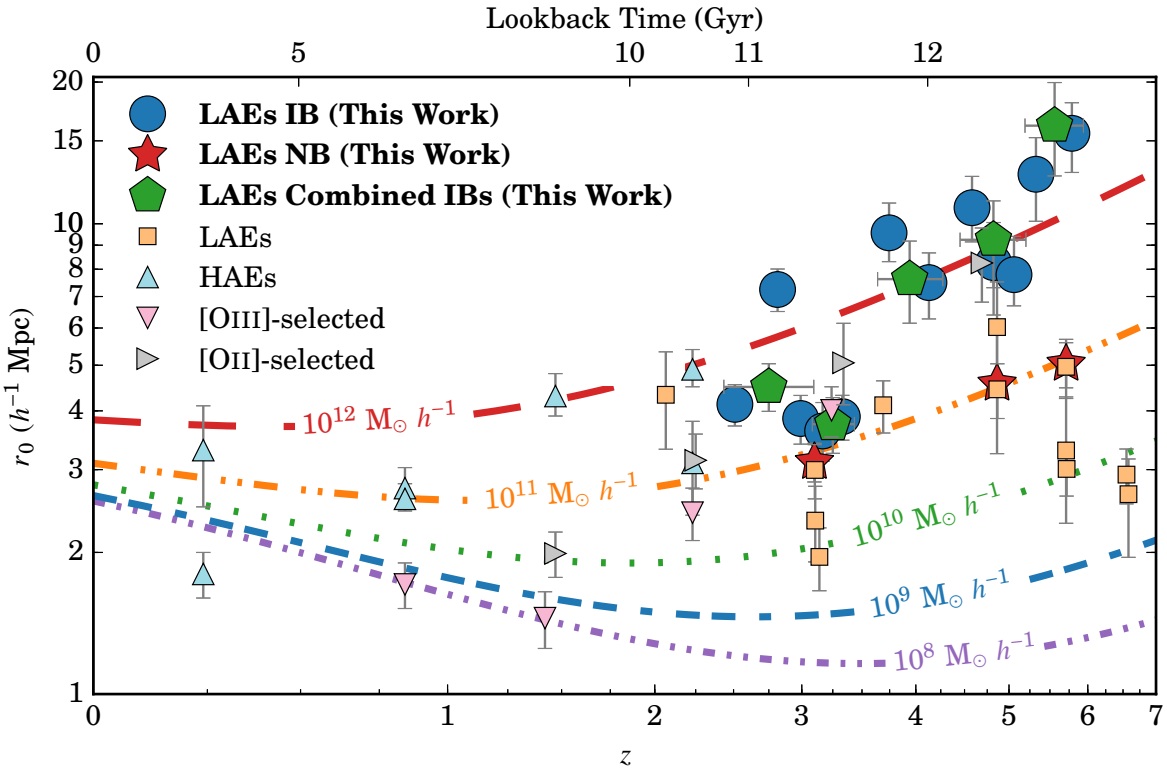

Figure 5.5: The redshift evolution of the clustering length, r_0, for our intermediate band, combined, and narrowband-selected Lyα emitters. We find that r_0 increases with increasing redshift up to $z \sim 6$ for our intermediate band and combined samples. Our narrowband-selected measurements show a constant r_0 with redshift. The systematic offset in r_0 between our intermediate and narrowband-selected samples is attributed to sample bias (e.g., depth of each sample). The redshift evolutions of host dark matter halos are also shown for minimum halo masses between 10^{8-12} M$_\odot$ h^{-1}. Our intermediate band-selected LAEs are found to be hosted by 10^{11-12} M$_\odot$ halos, while our narrowband-selected LAEs are hosted by $\sim 10^{11}$ M$_\odot$ halos for all redshifts. We also compare to Hα, [OII], and [OIII] narrowband studies and find that, for the overlapping redshift ranges, we are in agreement, suggesting that the various emission line-selected galaxies reside in similar clustering environments and host dark matter halos.

We also include the r_0 measurements of NB-selected LAEs drawn from the literature in Figure 5.5 (Ouchi et al., 2003; Murayama et al., 2007; Guaita et al., 2010; Ouchi et al., 2010; Bielby et al., 2016; Ouchi et al., 2018). Differences in measuring clustering lengths and halo masses in comparison to our approach are taken into account and described in Appendix 5.7.2. Figure 5.5 also includes Hα (Shioya et al., 2008; Sobral et al., 2010; Stroe & Sobral, 2015; Cochrane et al., 2017; Kashino et al., 2017), [OIII] (Khostovan et al., 2018), and [OII] emitters (Takahashi et al., 2007; Khostovan et al., 2018).

We find an excellent agreement between our measurement of $r_0 = 3.11^{+0.30}_{-0.29}$ Mpc h^{-1} for our $z \sim 3.1$ NB497 sample and $r_0 = 2.99 \pm 0.40$ Mpc h^{-1} from the VLT LBG redshift survey of Bielby et al. (2016). Both our work and Bielby et al. (2016) use a similar NB497 filter and are somewhat similar in survey parameters and selection, although their sample size is smaller (~ 600 LAEs) and they apply a higher rest-frame equivalent width cut (65Å). We find that the other $z \sim 3.1$ studies report a lower r_0 with a $> 1\sigma$ deviation with the ECDF-S MUSYC imaging survey of Gawiser et al. (2007) measuring an $r_0 = 2.34 \pm 0.43$ Mpc h^{-1} and Ouchi et al. (2010) measuring $r_0 = 1.96 \pm 0.30$ Mpc h^{-1} for LAEs in the SXDS field. The Ouchi et al. (2010) $z \sim 3.1$ sample is somewhat deeper than our NB497 sample with a limiting flux of $\sim 1.2 \times 10^{-17}$ erg s^{-1} cm^{-2}. The Gawiser et al. (2007) sample is also somewhat deeper with a limiting flux of $\sim 1.5 \times 10^{-17}$ erg s^{-1} cm^{-2}, such that the discrepancy is most likely due to the fainter LAEs being picked up by the two respective studies.

Our $z = 4.86$ NB711 r_0 measurement is found to be in agreement with the Shioya et al. (2009) 1.83 deg^2 COSMOS measurement of $r_0 = 4.44 \pm 0.59$ Mpc h^{-1}, despite the different source extraction and sample selection used by Sobral et al. (2018a). Ouchi et al. (2003) did an earlier clustering analysis of LAEs in the 543 arcmin^2 Subaru Deep Field using a similar NB711 filter and reported a $r_0 = 6.03 \pm 1.49$ Mpc h^{-1}, which is within 1σ agreement with our results.

We also find an agreement within 1σ between our $z = 5.71$ NB816 r_0 measurement and that of the 1.95 deg^2 COSMOS measurement of Murayama et al. (2007), while the SXDS measurements of Ouchi et al. (2010) and the HSC SILVERRUSH measurements of Ouchi et al. (2018) are lower. The cause of the difference is due to survey depth (Lyα luminosity; e.g., the SXDS measurements are close to 1 mag deeper in terms of 5σ NB detection limits) and also cosmic variance (the HSC SILVERRUSH measurements covers more than 10 times the survey area than our survey). The striking difference between these measurements shows the need to investigate the clustering and halo properties of emission line galaxies as a function of line luminosity.

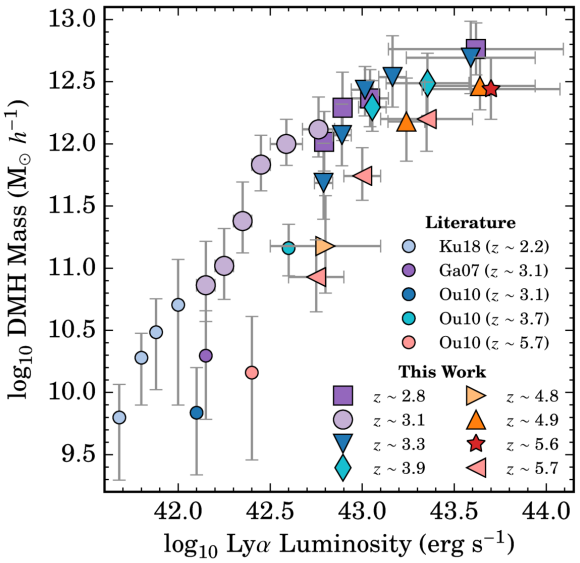

Figure 5.6: Halo mass in terms of Lyα luminosity. For each redshift sample, we see that halo mass increases with increasing line luminosity. Between $z \sim 2-3$, our measurements along with the literature show an increase in halo mass from $10^{9.7-12.8}$ $M_\odot$ for Lyα luminosities between $10^{41.7-43.6}$ erg s^{-1}. Similar trends are also seen at $z > 3$, but are shifted to higher line luminosities in comparison to the $z \sim 2-3$ samples. This is primarily due to the cosmic evolution of the Lyα luminosity functions and highlights the need to correct for this evolution in order to see if there is any evolution in regards to the clustering/halo properties of LAEs.

5.5.2 Line Luminosity

Motivated by the results of Sobral et al. (2010), Cochrane et al. (2017), and Khostovan et al. (2018), we investigate the trends between Lyα luminosity and host dark matter halo mass. Throughout the rest of this paper, we will use our combined intermediate band samples to increase the sample statistics while also ensuring that the redshift range per sample is small enough that any redshift evolution within each combined sample is negligible.

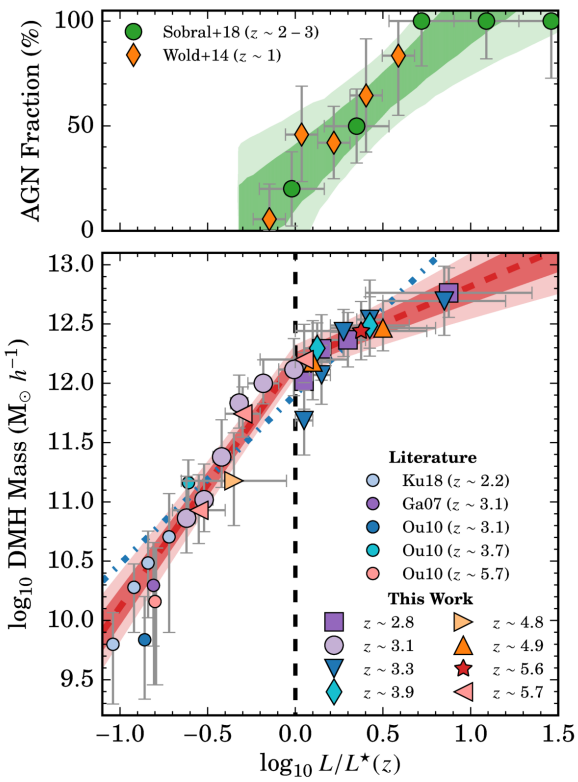

Figure 5.7: Host halo mass and Lyα luminosity normalized by the characteristic line luminosity, $L^\star(z)$. We find a strong, redshift-independent trend between host halo mass and line luminosity similar to previous narrowband works for Hα-, [OII]-, and [OIII]-selected emission line galaxies (Sobral et al., 2010; Cochrane et al., 2017; Khostovan et al., 2018). We find that the observed trends become shallower at $L > L^\star(z)$, which is a signature of a transitional halo mass where it becomes increasingly improbable that a star-forming galaxy resides in higher host halo masses. The continuous, shallower increase can also be a sign of AGN contribution at the brightest Lyα luminosities. Recent work by Sobral et al. (2018b) find that for $L > 2L^\star(z)$, the AGN fraction per Lyα luminosity is essentially 50 percent.

We show the host halo mass in terms of Lyα luminosity in Figure 5.6. For all redshift samples, we find that host halo mass increases with increasing Lyα luminosity. Including the $z = 2.2$ Kusakabe et al. (2018) measurements and the $z = 3.1$ Gawiser et al. (2007) and Ouchi et al. (2010) measurements, along with our $z \sim 2-3$ samples, we find that halo mass increases from $10^{9.7-12.8}$ $M_\odot$ between $10^{41.7-43.6}$ erg s^{-1} in Lyα luminosity. We find similar results when looking at the higher redshift samples, in conjunction with measurements from the literature. The main difference between the redshift samples is that their is an offset in Lyα luminosity with the high-z measurements shifted to higher Lyα luminosities. This is due to the cosmic evolution in the Lyα luminosity functions, which must be taken into account in order to investigate the evolution of clustering/halo properties of LAEs.

Figure 5.7 shows host halo mass in terms of Lyα luminosity normalized by the characteristic line luminosity, $L^\star(z)$. The measurements of $L^\star(z)$ used are shown in Table 5.2 and are taken from Sobral et al. (2018a). Since we combine our intermediate band samples, we carefully take into account the variation in $L^\star(z)$ between each individual intermediate band sample by first applying the corresponding $L^\star(z)$ and then

binning in terms of $L^\star(z)$.

We find a strong, increasing trend between host halo mass and $L/L^\star(z)$ from $z \sim 2.8-5.7$ covering 1.3 Gyr of cosmic history from the end of reionization to the peak of cosmic star formation. Our faintest LAEs ($L \sim 0.25L^\star(z)$) are observed to reside in $10^{10.8}$ $M_\odot$ halos and our brightest LAEs ($L \sim 7L^\star(z)$) reside in $10^{12.8}$ $M_\odot$ halos. The typical $L^\star$ galaxy is observed to be found in $\sim 10^{12}$ $M_\odot$ host dark matter halos. Surprisingly, these are found to be redshift-independent suggesting that LAEs of the same $L^\star(z)$ type at different redshifts reside in similar halo masses.

Figure 5.7 also includes Lyα luminosity threshold measurements drawn from the literature at various redshifts (Gawiser et al., 2007; Ouchi et al., 2010; Kusakabe et al., 2018). Due to the nature of these measurements, they help constrain the faint-end of Figure 5.7 and are primarily single measurements per redshift, except for Kusakabe et al. (2018), which made five measurements (although we only show four as their deepest measurement is poorly constrained). The literature measurements, along with our own observations, show significantly strong, redshift-independent trends between Lyα luminosity and effective halo mass. Similar trends have also been observed for Hα, [OIII], and [OII] emitters (Sobral et al., 2010; Cochrane et al., 2017; Khostovan et al., 2018) up to $z \sim 5$.

To quantify the trends seen in Figure 5.7, we fit two different models: a single power law and a piecewise power law with the pivot point at $L^\star$. The best-fit single power law was:

$$\frac{M_{halo}}{M_\odot/h} = 10^{11.91^{+0.05}_{-0.05}} \left(\frac{L}{L^\star(z)}\right)^{1.44^{+0.14}_{-0.12}} \tag{5.11}$$

with a slope near unity. Although the single power law seems to represent the observations around $L \sim L^\star(z)$, there is a deviation towards lower and higher line luminosities. Based on this

deviation, we use a piecewise power law that is separated at $L^\star(z)$ with a best-fit of:

$$\frac{\mathrm{M_{halo}}}{\mathrm{M_\odot}/h} = 10^{12.19^{+0.06}_{-0.06}} \begin{cases} \left(\frac{L}{L^\star(z)}\right)^{2.08^{+0.12}_{-0.12}} & L < L^\star \\ \left(\frac{L}{L^\star(z)}\right)^{0.63^{+0.12}_{-0.12}} & L > L^\star \end{cases} \tag{5.12}$$

where the slopes above and below $L^\star(z)$ are quite different.

The best-fits show a steeply increasing halo mass with line luminosity up to $L^\star(z)$ with a slope of 2.08 ± 0.12 followed by a slowly increasing halo mass at brighter line luminosities with a slope of 0.63 ± 0.12 and a typical halo mass of $10^{12.19 \pm 0.06}$ $\mathrm{M_\odot}$ at $L^\star(z)$. Interestingly, the trend change occurs at the point where star formation efficiency is at it's peak (e.g., Behroozi et al. 2013b), which is tied to how the cold gas accretion occurs at varying halo masses.

5.5.2.1 What causes the trend change at $L > L^\star(z)$?

The slope change that is seen in Figure 5.7 could be due to a changing population of LAEs where Lyα emission is no longer driven by star formation but by AGN activity. This would result in the fraction of star-forming galaxies to decrease with increasing luminosity. Above 10^{12} $\mathrm{M_\odot}$, the star formation efficiency decreases due to accelerated gas accretion caused by the deeper gravitational potentials of higher mass halos resulting in fewer star-forming galaxies with increasing halo mass (e.g., Dekel & Birnboim 2006; Bower et al. 2017). This idea of a transitional or characteristic halo mass has been observed for Hα, [OIII], and [OII]-selected emitters between $z \sim 0.4-5$ (Khostovan et al., 2018) and by studies of star-forming and passive galaxies (e.g., Hartley et al. 2013; Dolley et al. 2014).

To understand whether AGN contribution could be causing a trend change at $L > L^\star(z)$, we include the $z \sim 2-3$ AGN fraction measurements of Sobral et al. (2018b) and $z \sim 1$ measurements of Wold et al. (2014) in the top panel of Figure 5.7. About 20 percent of $z \sim 1-3$ LAEs are found to be AGNs around $L^\star$ and by 2 $L^\star(z)$, half of the population of LAEs are AGNs. Although their results are for $z \sim 1-3$ LAEs which overlap with a few of our samples, the

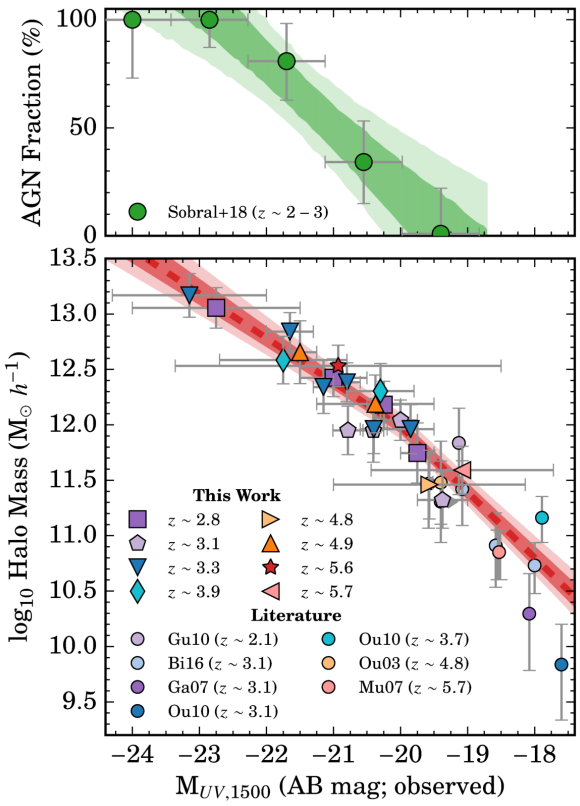

Figure 5.8: Shown is the host halo mass versus the rest-frame 1500 Å UV continuum luminosity per each redshift sample. Note that these are not corrected for dust extinction. We observe a strong, redshift-independent trend for the full range of UV luminosities observed where galaxies with the brightest continuum reside in massive halos. Included are the M_{UV} limit measurements from the literature. Bielby et al. (2016) covered multiple M_{UV} limits and also found a similar trend and even extend our observed trends down to $M_{UV} \sim -18$.

implications it has for our higher redshift samples is that our bright LAE samples are most likely AGN-dominated. Calhau et al., in prep, found a strong correlation between the fraction of X-ray detected AGNs and Lyα luminosity with 100 percent X-ray AGN fraction at the brightest LAEs in the SC4K sample. Matthee et al. (2017b) found that $z \sim 2.3$ LAEs are about 50 percent X-ray AGNs at $> 10^{44}$ erg s^{-1} (see also Konno et al. 2016). The halo masses measured for our $> 2\ L^\star(z)$ samples are also consistent with previous AGN clustering studies (e.g., halo masses of $\gtrsim 10^{12.5}$ $M_\odot$; Hickox et al. 2009; Koutoulidis et al. 2013; Allevato et al. 2016; Mendez et al. 2016; Hale et al. 2018).

5.5.3 Rest-Frame UV Continuum

In the previous section, we found that the line luminosity properties of LAEs is correlated with the host halo regardless of redshift such that the brightest LAEs reside in the most massive halos, regardless of redshift. Here we explore how the host halo mass can depend on the rest-frame UV properties, specifically the 1500Å UV continuum luminosity (M_{UV}) and the UV-measured star formation rate. Our method of measuring both properties is described in §5.4.

Figure 5.8 shows how the observed (not corrected for dust) M_{UV} and the host halo mass

are correlated. We find a strong trend where the host halo mass increases with increasing UV luminosity. The most UV-bright LAEs ($M_{UV} < -22$) are found to reside in 10^{13} $M_\odot$ halos. Fainter than $M_{UV} > -20$, we find our LAEs are hosted in $< 10^{11.5}$ $M_\odot$ and are primarily from our narrowband samples. Interestingly, the trend is also redshift-independent as seen for the host halo mass - Lyα luminosity results shown in §5.5.2. Note that we do not normalize by the characteristic UV luminosity, $M^\star_{UV}$, as previous work have shown it to be constant for the redshift ranges we probe (e.g., Oesch et al. 2010).

We also include M_{UV}-limit measurements from the literature which cover the faintest end of Figure 5.8 (Ouchi et al., 2003; Gawiser et al., 2007; Murayama et al., 2007; Guaita et al., 2010; Ouchi et al., 2010). Presently, Bielby et al. (2016) is the only work that covered multiple M_{UV}-limit thresholds for which they measured halo masses. Their measurements cover the range $-18 < M_{UV} < -20$ and show an increasing trend between M_{UV} and halo mass in perfect agreement with the trends we observe with our samples. Furthermore, their $M_{UV} > -19$ measurements complement ours by showing that the trends seen at brighter UV luminosities continues down to $M_{UV} \sim -18$. We find then that not only are the observed trends redshift-independent, but also that the host halo masses of LAEs depends on a wide range of M_{UV}.

Using both our measurements and those from the literature, we fit a piecewise power law:

$$\frac{M_{halo}}{M_\odot/h} = \begin{cases} 10^{11.99^{+0.05}_{-0.06} - 0.40^{+0.03}_{-0.04}\left(M_{UV}+20\right)} & M_{UV} > -20 \\ 10^{11.99^{+0.05}_{-0.06} - 0.60^{+0.10}_{-0.13}\left(M_{UV}+20\right)} & M_{UV} < -20 \end{cases} \tag{5.13}$$

with the pivot at $M_{UV} = -20$ mag, which is consistent with a changing slope towards fainter UV luminosities as shown by the literature measurements. The different slopes are statistically significant ($> 1\sigma$) and show a typical host halo mass of $\sim 10^{12}$ $M_\odot$ at $M_{UV} \sim -20$ mag. This is similar to what we find for typical $L^\star(z)$ galaxies as shown in Figure 5.7, although the trend change is not as statistically significant.

We also include the AGN fraction measurements of Sobral et al. (2018b) in the top panel of Figure 5.8. More than 50 percent of LAEs are AGNs for $M_{UV} < -21$ mag, which corresponds to measured halo masses of $> 10^{12.5}$ $M_\odot$, consistent with measurements from AGN studies (e.g., Hickox et al. 2009; Mendez et al. 2016).

5.5.4 Star Formation Rate

The results in Figure 5.8 are based on the observed M_{UV} for which the UV luminosity is not corrected for dust. To explore how host halo mass depends directly on the star formation rate, we dust correct M_{UV} using the UV slope, β, and use the Kennicutt (1998) calibration as described in §5.4.

Figure 5.9 shows the host halo mass for each LAE sample in bins of UV star formation rate. We find that the host halo mass increases with increasing star formation rate at all redshifts. The trends observed are also found to be redshift independent, similar to the other trends with galaxy properties that have been noted in this paper. The range of dark matter halo masses shown vary greatly with the least active galaxies (SFR ~ 1.6 $M_\odot$ yr^{-1}) residing in $10^{11.2}$ $M_\odot$ halos and the most active (SFR ~ 100 $M_\odot$ yr^{-1}) residing in 10^{13} $M_\odot$ halos. SFRs > 100 $M_\odot$ yr^{-1} primarily have their UV continuum emission powered by AGNs as we saw in Figure 5.8 and, therefore, are not physical. This region is highlighted in Figure 5.9.

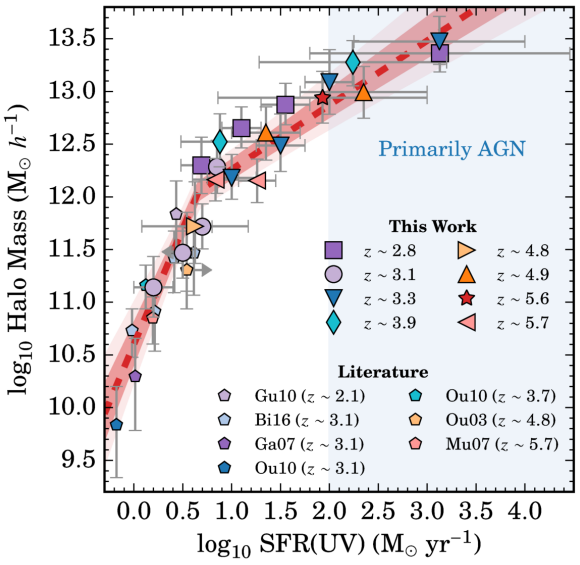

Figure 5.9: The host halo mass as measured in bins of dust-corrected rest-frame UV star formation rate. We find that an increasing, redshift-independent trend between increasing halo mass and increasing star formation rate. Included are the dust-corrected M_{UV}-limit literature measurements from various narrowband surveys. Bielby et al. (2016) covers multiple star formation rate bins and also shows a similar trend in comparison to our observations, although for a limited star formation rate range. Above 10 $M_\odot$ yr^{-1} and halo masses of 10^{12} $M_\odot$, the observed trends become shallower, similar to our observations of the halo mass - Lyα luminosity trends.

Included in Figure 5.9 are the M_{UV}-limit measurements from $z \sim 2-6$ studies found in the literature (Ouchi et al., 2003; Gawiser et al., 2007; Murayama et al., 2007; Guaita et al., 2010; Ouchi et al., 2010; Bielby et al., 2016). The measurements were redone to match with the assumptions made in this work (see Appendix 5.7.2 for details) and converted to SFR using Equation 5.9. The typical β slope for these samples are bluer than $\beta \sim -2$, which implies zero to minimal dust attenuation (e.g., see Figure 2 of Ono et al. (2010)). Because these measurements are M_{UV} (SFR)-limit studies, they help to constrain the least active end (SFR $\lesssim 1.6$ $M_\odot$ yr^{-1}) of Figure 5.9.

We find that two trends are present in Figure 5.9 where the halo mass increases rapidly from low SFR to ~ 4.5 $M_\odot$ yr^{-1} and continues to increase with a shallower slope to higher SFRs. To quantify these trends, we fit our measurements and those from the literature with a piecewise power law. The best fit is:

$$\frac{M_{halo}}{M_\odot/h} = 10^{12.05^{+0.08}_{-0.09}} \begin{cases} \left(\frac{SFR}{4.5}\right)^{2.19^{+0.25}_{-0.23}} & SFR < 4.5 \ \frac{M_\odot}{yr} \\ \left(\frac{SFR}{4.5}\right)^{0.61^{+0.09}_{-0.05}} & SFR > 4.5 \ \frac{M_\odot}{yr} \end{cases} \tag{5.14}$$

with a typical halo mass of $10^{12.05^{+0.08}_{-0.09}}$ $M_\odot$ at SFR ~ 4.5 $M_\odot$ yr^{-1}, which is the point for which we visually see a change in the trend in Figure 5.9.

In comparison to the halo mass - $L_{Ly\alpha}$ trend we measured, there are many important similarities. The pivot point in the piecewise has similar halo masses and the slopes of both trends are very much similar. This could suggest that $L_{Ly\alpha}$ is indeed tracing the star formation activity, despite the many caveats surrounding using Lyα as a star formation indicator (see Dijkstra (2017) for a review).

The typical halo mass measured at 4.5 $M_\odot$ yr^{-1} is consistent with the peak of star formation efficiency found in halos of $\sim 10^{12}$ $M_\odot$. This is similar to what we also find for the halo mass - $L_{Ly\alpha}$ results. The changing slope seen above 4.5 $M_\odot$ yr^{-1} is most likely due to the combining

effects of a larger population of AGNs and the existence of LAEs that are undergoing an intense period of star formation activity.

The observed trends suggests that the processes that govern star formation activity and the production of the Lyα line in LAEs is strongly tied to the host halo mass properties. The redshift independence reinforces the idea that this connection is independent of time such that halos and their residing galaxies co-evolve with each other in unison. This would then suggest that one of the most important characteristics that governs the evolution of a galaxy is the host dark matter halo mass.

5.6 Conclusion

We present a comprehensive investigation of the clustering and halo properties of LAEs and explore their dependences on Lyα luminosity, UV continuum luminosity, and UV star formation rate in multiple redshift slices between $z \sim 2.5-6$. We highlight the main results of this study here:

1. We measure the angular correlation functions and clustering lengths of every redshift sample. The clustering lengths of the narrowband samples are shown to increase from $r_0 \sim 3.1-5.0$ Mpc h^{-1} between $z \sim 3.1-5.7$. The intermediate band and combined intermediate band samples show a more rapid increase in r_0 from ~ 4.5 Mpc h^{-1} at $z \sim 2.5$ to ~ 16 Mpc h^{-1} by $z \sim 5.8$. The typical halo masses of the narrowband samples are found to be $\sim 10^{11}$ $M_\odot$, while the intermediate band samples range between $\sim 10^{11-12}$ $M_\odot$.

2. Host halo mass is found to scale with Lyα luminosity at all redshifts probed. Initial analysis of this trend shows a redshift evolution, but this is found to be caused by the cosmic evolution of the Lyα luminosity function. Taking this into account by normalizing Lyα luminosity by $L^\star(z)$ shows a redshift-independent trend with host halo mass. LAEs are found to reside in

a wide range of host halos ranging from $10^{9.75}$ $M_\odot$ at $\sim 0.1L^\star(z)$ to $10^{12.1}$ $M_\odot$ at $L^\star(z)$ and $10^{12.8}$ $M_\odot$ at $\sim 10L^\star(z)$.

3. We find a strong, redshift-independent trend between host halo mass and observed 1500Å UV continuum luminosity. LAEs with $M_{UV} \sim -18$ mag are found to reside in $10^{10.5}$ $M_\odot$ halos and $M_{UV} \sim -23$ mag in 10^{13} $M_\odot$ halos.

4. We also find a strong, redshift-independent trend between host halo mass and dust-corrected UV star formation rate. We find that LAEs with SFR ~ 1 $M_\odot$ yr^{-1} reside in 10^{10} $M_\odot$ halos and ~ 100 $M_\odot$ yr^{-1} reside in $10^{12.8}$ $M_\odot$ halos.

5. For both Lyα luminosity and UV SFR, we observe sharp trend changes. In the case of Lyα luminosity, we find that the host halo mass scales as $(L/L^\star(z))^{2.08}$ and $(L/L^\star(z))^{0.63}$ for below and above $L^\star(z)$, respectively. A similar trend is seen between halo mass and SFR with the trend change occurring at ~ 4.5 $M_\odot$ yr^{-1}. This is attributed to a changing population of LAEs where the brightest LAEs, in terms of line luminosity and SFRs, primarily have their emission powered by AGNs and not star formation activity.

Our results highlights the significant connection that host halos and galaxies share from the end of the epoch of reionization to the peak of cosmic star formation. The redshift-independent trends with halo mass signifies the co-evolution of galaxies and their host halos and that the host halo mass is a defining factor in how the residing galaxy evolves.

At all redshift slices, we find the LAEs in our samples cover a wide range in host halo masses. But what are the present-day descendants of these types of galaxies? In the grand scheme of galaxy evolution, we wish to understand what became of the galaxies we observe. Figure 5.10 shows the present-day halo masses of our full LAE samples measured using the halo mass accretion tracks of Behroozi et al. (2013b). Given the wide range in halo masses we have observed throughout this study, we find that LAEs cover a wide range of present-day

descendants from dwarf-like ($M_{\rm halo} \sim 10^{11}$ M$_\odot$), to Milky Way-like ($M_{\rm halo} \sim 10^{12}$ M$_\odot$), and galaxies residing in cluster-like environments ($M_{\rm halo} > 10^{13}$ M$_\odot$). The wide range in the type of descendants shows that LAEs are great tools in studying how galaxies formed and evolved to the ones we currently see in the local Universe.

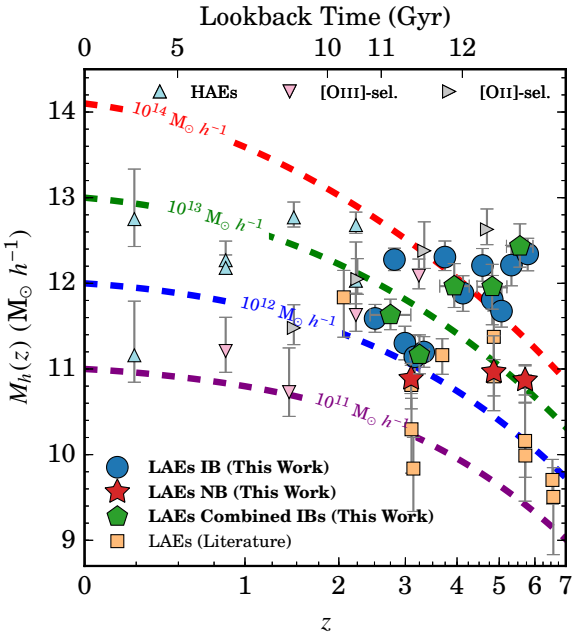

Figure 5.10: The present-day descendants of emission line-selected galaxies. The *dashed lines* are the evolutionary tracks of present-day 10^{11-14} M$_\odot$ host halos assuming the halo mass accretion model of Behroozi et al. (2013b). Our narrowband-selected LAEs are found to be progenitors of galaxies in present-day 10^{12-13} M$_\odot$ halos, while our intermediate band samples are in more massive present-day halos ($> 10^{13}$ M$_\odot$ halos). Other LAE narrowband surveys show a similar result such that Lyα emiters are the progenitors of a wide range of present-day galaxies, similar to what is found for Hα-, [OII]-, and [OIII]-selected galaxies.

5.7 Appendix

5.7.1 Effects of the SA22 Overdense Region

Previous work on the SA22 field has identified and extensively studied a significant overdense region (protocluster) comprised of Lyα emitters and LBGs at $z \sim 3.1$ (e.g., Steidel et al. 1998, 2000; Hayashino et al. 2004; Webb et al. 2009; Nestor et al. 2011; Yamada et al. 2012; Kubo et al. 2015, 2016; Saez et al. 2015; Topping et al. 2016). Figure 5.11 shows a 0.12 deg^2 cutout centered on the position of the overdense region highlighted by the source isodensity levels from Hayashino et al. (2004). We include the distribution of our $z \sim 3.1$ LAEs and find that it traces the underlying overdensity. The main question that needs to be addressed is how does the overdense region affect our observed angular correlation functions as shown in the top panel of Figure 5.2?

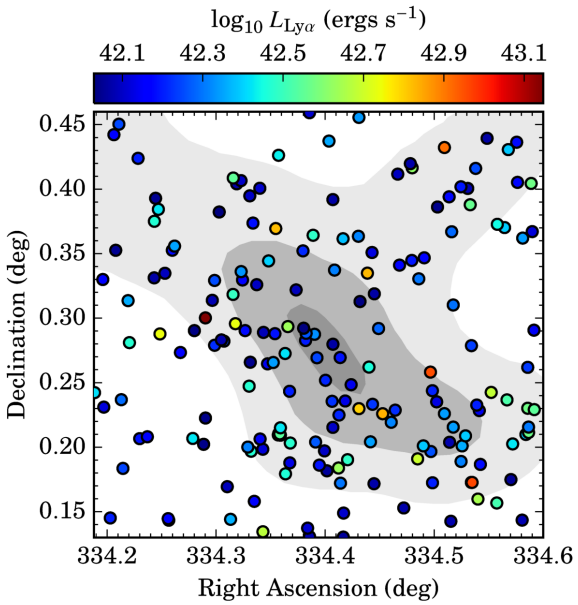

Figure 5.11: A $24' \times 18'$ cutout of the SA22 field centered on the $z \sim 3.1$ protocluster. The *circles* represent the angular positions of our NB497-selected LAEs with the color scale related to their line luminosities. The *grey shaded regions* are the source isodensity levels from Hayashino et al. (2004) and compiled by Saez et al. (2015) that highlight the location of the SA22 overdense region. The $z = 3.1$ LAEs that seem to primarily populate the overdense region have line luminosities of $\lesssim 10^{42.4}$ erg s^{-1}, which are the faintest LAEs in the sample.

As described in §5.3.2, there is a signature of a 1−halo term in the NB497 ACFs which would suggest a satellite fraction of LAEs. We investigate if this is due to the presence of the significant overdense region discussed above by measuring the ACFs using the same methodology used throughout this paper and masking the 0.12 deg^2 field shown in Figure 5.11. Note that we also mask the random maps as well to ensure a consistent survey geometry.

Figure 5.12 shows the comparison between the ACFs for the full field and for the case where the overdense region is masked. We find that there is no difference between the two correlation functions such that the overdensity does not significantly affect the overall clustering measurements. Hayashino et al. (2004) also found the overdense region to have a weak clustering signal relative to the whole SA22 field.

We next investigate if the cause for the 1−halo term is due to flux depth of the sample. Figure 5.11 shows the spatial and luminosity distribution of the $z \sim 3.1$ LAEs where concentrations of faint LAEs are found within the overdense region. To test if the 1−halo term arises from faint LAEs that comprise the satellite population, we measure the ACFs for the full SA22 field with varying line luminosity thresholds. Figure 5.12 shows the 1−halo term disappears by $L_{\mathrm{Ly}\alpha} \gtrsim 0.4\ L^\star$, which is consistent with the spatial/luminosity distribution shown in Figure 5.11.

Although a detailed analysis of the satellite fractions is beyond the scope of this work, we find that all our samples do not exhibit signatures of population of satellite galaxies except for the NB497 sample, which we find to also have negligible satellite fraction effects above $0.4L^\star$. If the satellite fractions do affect our measurements, then it would be primarily isolated to the lowest line luminosity ranges of our samples and would result in overestimations of their host dark matter halos. Lastly, the most comprehensive study of satellite fractions of emission line-selected galaxies was done by Cochrane et al. (2017) for their $z = 0.4$, 0.8, 1.5, and 2.2 NB-selected Hα samples where they find that, on average, $3-5$ percent of the sample are satellites. In comparison to LBG samples, the recent 100 deg^2 HSC survey found satellite fractions of $\lesssim 5$ percent between $z \sim 4-6$ (Harikane et al., 2018). Throughout the rest of this paper, we neglect the effects of the satellite population.

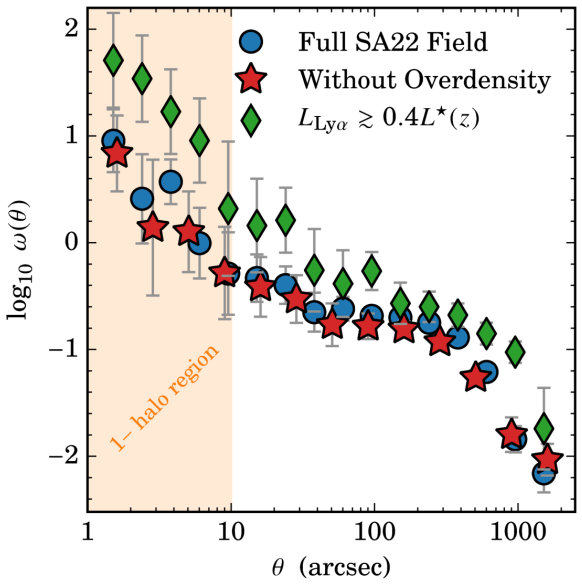

Figure 5.12: Comparison of the ACF for the Full SA22 field (*blue circles*) and for the case where the overdensity is masked (*red stars*). We find that both ACFs are consistent with each other such that the $z \sim 3.1$ protocluster is not affecting our clustering measurements and that the 1–halo term still exists in both cases (region highlighted in *orange*). The *green diamonds* show the ACF for the Full SA22 field with the added condition of a line luminosity threshold $\gtrsim 0.4L^\star$. We find that above this threshold, the deviation from a simple power law associated with the detection of a 1–halo term disappears, suggesting that the satellite fraction of galaxies is close to zero above $0.4L^\star$.

5.7.2 Clustering Measurements from the Literature

We have used several narrowband studies for the purpose of comparison throughout this paper. Due to our unique approach and the varying assumptions between each measurement drawn from the literature, we have to be careful on how we are comparing our measurements to the literature. To resolve this issue, we have to normalize the methodology between our clustering

Table 5.3: Clustering Measurements of Lyα Emitters from the Literature. Shown are the referred narrowband studies, redshifts per each sample, the corresponding narrowband filter identification, the survey area, the r_0 reported in the respective study, our measurement of r_0 based on our assumptions and methodology using the observed angular correlation functions, and the host halo mass using our own r_0-halo mass model.

Study	Redshift	Filter	Area (deg^2)	$r_{0,\mathrm{reported}}$ (Mpc h^{-1})	$r_{0,\mathrm{measured}}$ (Mpc h^{-1})	$\log_{10}$ Halo Mass ($\mathrm{M}_\odot$ h^{-1})
Bielby et al. (2016)	3.10 ± 0.03	NB497	1.07	$2.86^{+0.33}_{-0.33}$	$2.99^{+0.40}_{-0.40}$	$10.81^{+0.23}_{-0.28}$
Gawiser et al. (2007)	3.11 ± 0.02	NB4990	0.27	$2.52^{+0.56}_{-0.70}$	$2.34^{+0.43}_{-0.43}$	$10.30^{+0.36}_{-0.51}$
Guaita et al. (2010)	2.07 ± 0.02	NB3727	0.36	$4.80^{+0.90}_{-0.90}$	$4.33^{+1.01}_{-1.01}$	$11.84^{+0.31}_{-0.46}$
Murayama et al. (2007)	5.71 ± 0.04	NB816	1.95	—	$4.96^{+0.71}_{-0.71}$	$10.85^{+0.20}_{-0.25}$
Ouchi et al. (2003)	4.86 ± 0.03	NB711	0.15	—	$6.03^{+1.49}_{-1.49}$	$11.37^{+0.30}_{-0.43}$
Ouchi et al. (2010)	3.14 ± 0.03	NB503	0.98	$1.70^{+0.39}_{-0.46}$	$1.96^{+0.30}_{-0.30}$	$9.84^{+0.50}_{-0.36}$
Ouchi et al. (2010)	3.69 ± 0.03	NB570	0.96	$2.74^{+0.58}_{-0.72}$	$4.11^{+0.52}_{-0.52}$	$11.16^{+0.19}_{-0.22}$
Ouchi et al. (2010)	5.71 ± 0.04	NB816	1.03	$3.12^{+0.33}_{-0.36}$	$3.29^{+0.99}_{-0.99}$	$10.16^{+0.45}_{-0.70}$
Ouchi et al. (2010)	6.55 ± 0.05	NB921	0.90	$2.31^{+0.65}_{-0.85}$	$2.93^{+0.39}_{-0.39}$	$9.70^{+0.24}_{-0.28}$
Ouchi et al. (2018)	5.72 ± 0.05	NB816	13.8	$3.01^{+0.35}_{-0.35}$	$3.01^{+0.37}_{-0.37}$	$9.99^{+0.22}_{-0.25}$
Ouchi et al. (2018)	6.58 ± 0.05	NB921	21.2	$2.66^{+0.49}_{-0.70}$	$2.66^{+0.50}_{-0.71}$	$9.50^{+0.34}_{-0.67}$
Shioya et al. (2009)	4.86 ± 0.03	NB711	1.83	$4.40^{+1.30}_{-1.50}$	$4.44^{+0.59}_{-0.59}$	$10.91^{+0.20}_{-0.23}$

measurements and those from the literature. We achieve this by taking the observed angular correlation functions from each narrowband study, fit Equation 5.5 to measure r_0 and use the narrowband filter attributed to that study as the proxy for the redshift distribution, and include the errors associated with cosmic variance by using the empirical relation measured by Sobral et al. (2010).

Table 5.3 shows our recalculations of r_0 for each narrowband study used in this paper for comparison purposes. We also include the measured halo masses in Table 5.3, which are based on the same assumptions described in §5.3.4. In comparison to the measurements reported in each study, the error bars we measure are typically larger than that reported in the literature due to the inclusion of cosmic variance effects.

We like to emphasis on a few of these studies as we had to apply specific corrections/extensions.

For the Ouchi et al. (2003) study, only a measurement of the clustering amplitude and slope was reported for which we have extended this work by making measurements of r_0 and halo mass. The Murayama et al. (2007) angular correlation functions did not include an integral constraint correction. Since the survey size and sample is essentially the same as our NB816 sample (note that we used the archival NB816 images which are the same used in Murayama et al. 2007), we use our integral constraint to correct their angular correlation functions. For the Shioya et al. (2009), we report their measurement of $4.4^{+1.3}_{-1.5}$ Mpc h^{-1} which assumes a slope of $\gamma = -1.90 \pm 0.22$. In our recalculation of their measurement, we keep γ fixed on -1.80, which is consistent with their measured slope.

CHAPTER 6

Conclusions

I present the main conclusions of each chapter that was presented in this thesis. Each chapter corresponds to a paper that has been peer-reviewed and published within the Monthly Notices of the Royal Astronomical Society.

6.1 The Luminosity Functions and Star Formation History of Emission Line Galaxies

We have presented the largest sample of Hβ+[OIII] and [OII] emitters between $z \sim 0.8-5$ that have been selected based on a robust and self-consistent technique, backed up by a wide array of spectroscopic emitters. We have used the HiZELS UKIRT and Subaru narrow-band catalogs, along with multi-wavelength data from the COSMOS and UDS fields, to create a clean and well-defined sample of star-forming galaxies. The main results of this paper are as follows:

1. We have robustly selected a total of 2477, 371 , 270, 179 Hβ+[OIII] emitters at $z = 0.84$,

1.42, 2.23, and 3.24 and 3285, 137, 35, 18 [OII] emitters at $z = 1.47$, 2.25, 3.34, and 4.69 in the combined COSMOS and UDS fields. These are the largest samples of Hβ+[OIII] and [OII] emitters to have been detected in this redshift range.

2. We have extended the luminosity function in the literature to higher-z, as well as refined the lower-z measurements for both types of emitters. For the Hβ+[OIII] emitters, we find that the bright-end of our $z = 1.42$ and $z = 2.23$ LFs are in agreement with the grism spectroscopy-based luminosity functions of Colbert et al. (2013); hence, this increases the reliability of our sample being dominantly [OIII] emitters in the bright-end. We also find from our predictions of the [OIII] LFs that our sample is dominated by [OIII] emitters at the bright-end. The faint-end is dominated by Hβ emitters. We also find that the normalization of the [OIII] LFs are the same such that the relative contribution of Hβ emitters is the same between $z \sim 0.8 - 2.2$.

3. The evolution of $L^\star$ and $\phi_\star$ for Hβ+[OIII] is found to have a strong increasing/decreasing evolution, respectively, up to $z \sim 3$. For our [OII] sample, we find that $L^\star$ increases strongly up to $z \sim 5$ and $\phi_\star$ is strongly dropping up to the same redshift.

4. We have discussed that our luminosity functions are reliable to be used in making predictions of the number of emitters to be detected by future wide-surveys, such as *Euclid* and WFIRST. Furthermore, our luminosity functions can also determine the number of low-z interlopers in Lyα studies, such that the level of contamination by low-z sources can be reduced in such studies.

5. The SFRD has been constrained using [OII] measurements up to $z \sim 5$ for the first time. We find that the peak of the cosmic SFRD is located around $z \sim 3$ and is in agreement with our large compilation of UV, IR, radio, and nebular emission studies. We find that for $z > 2$, our SFRD fit drops slightly faster in comparison to the UV dropout studies in this redshift

regime. However, we find that the UV measurements are within the 1-σ error bar range of our SFRD fit. Future space-based narrow-band surveys, such as *JWST* and *WISH*, will be able to extend the range of [OII] detection out to $z \sim 12$ so that we can compare and confirm or invalidate the UV dropout measurements.

6. We also find that the Hβ+[OIII] SFRD measurements are nicely in line with our [OII] sample and other star-formation tracers. This then brings to question of whether the Hβ+[OIII] calibration is more "reliable" as a tracer of star-formation than previously thought. With our large sample of these emitters, we will have the ability to explore this issue in detail.

7. By integrating the SFRD, we have made estimates of the stellar mass density evolution and find that it steeply rose up to $z \sim 2$ and flattened out up to the present-day. This is also confirmed by the wealth of measurements in the literature.

The results in the paper have implications in the evolution of galaxies and the star-formation activity occurring in said galaxies. Despite the robustness of our sample, there is still room for improvement. Our measurements have done well to constrain the bright-end, while keeping the faint-end fixed based on measurements from the literature. We will require deeper narrow-band and broad-band measurements in order to constrain the faint-end slope of the LF. Spectroscopic follow-up will also be necessary to accurately measure the extent of AGN contamination in our sample. Although, our color-color selections have shown (see figure 2.11) that they are quite reliable due to the large set of spectroscopic measurements confirming this reliability. That being said, spectroscopic measurements of our sample will help in separating the Hβ and [OIII] samples to measure separate luminosity functions. Lastly, future narrow-band surveys, such as the proposed *WISH* telescope, will be able to extend the redshift window of Hβ+[OIII] and [OII] studies up to $z \sim 12$, which can be used to confirm the UV dropout studies at higher-z. Despite all these improvements and potential future progresses, our sample has reliably (given all the limitations) and robustly traced the evolution of star-forming activity in the universe.

6.2 Stellar Mass Functions and Equivalent Width Evolutions

We have presented the evolution of the stellar mass functions and densities up to $z \sim 3$, the evolution of the rest-frame equivalent widths up to $z \sim 5$, and the evolution of the ionization parameter as described by the [OIII]/[OII] ratio up to $z \sim 3$. The main results of this study are the following:

1. In conjunction with the widely used UVJ colour-colour classification scheme, we find that $\sim 98\%$ of all Hβ+[OIII] and [OII] emitters are classified as "active" (star-forming or AGN) galaxies.

2. The stellar mass functions of Hβ+[OIII] emitters show a strong, increasing evolution in $M_\star$ from $10^{10.96^{+0.15}_{-0.08}}$ $M_\odot$ to $10^{11.60^{+0.29}_{-0.13}}$ $M_\odot$ and a weak, increasing evolution in $\phi_\star$ from $10^{-4.16\pm0.08}$ Mpc^{-3} to $10^{-3.87^{+0.06}_{-0.11}}$ Mpc^{-3} with decreasing redshift. Similar trends are seen for the stellar mass functions of [OII] emitters from $z = 1.47$ to $z = 3.34$ where an unchanging $M_\star \sim 10^{11.60}$ $M_\odot$ is seen for all redshifts sampled and a strong, increasing evolution in $\phi_\star$ from $10^{-5.18^{+0.09}_{-0.13}}$ Mpc^{-3} to $10^{-3.92\pm0.05}$ Mpc^{-3} with decreasing redshift.

3. The similarity between the $z = 0.84$ and 1.42 Hβ+[OIII] SMFs and the rise in the SMFs between $z = 3.24$ to $z = 1.42$ is probable evidence for the rapid stellar mass build-up followed by its decay due to the decrease of star-formation activity in the Universe. The stellar mass functions of the [OII] emitters all shows rapid build-up of stellar masses from $z = 3.34$ to $z = 1.47$ for [OII]-selected galaxies.

4. Stellar mass densities of our Hβ+[OIII] and [OII] emitters, in conjunction with the HiZELS Hα SMDs of Sobral et al. (2014), show how the evolution in the SMDs traces that of the full sample (passive + active) as found in the literature. By $z = 0.84$, we find that the SMDs deviate from the full population implying the transition of active galaxies into passive galaxies. This ties into the picture of decreasing star-formation activity in the Universe.

5. The relationship between EW_{rest} and stellar mass for Hβ+[OIII] and [OII] emitters up to $z \sim 3$ and ~ 5, respectively, is studied for the first time where we find a power-law relationship between the two physical properties as seen in Hα studies (e.g., Fumagalli et al. 2012; Sobral et al. 2014). We find that all our Hβ+[OIII] samples are best represented by $EW_{rest} \propto M^{-0.35}$ and the [OII] samples as $\propto M^{-0.45}$. The $z = 1.47$ [OII] sample has a shallower trend best fit as $\propto M^{-0.23}$.

6. We find that the Hβ+[OIII] EW_{rest} increases from $z = 0$ to $z \sim 2$ by a factor of ~ 100. From $z \sim 2$ to ~ 8, we find evidence for a shallower trend by using the *Spitzer* IRAC measurements of Labbé et al. (2013) and Smit et al. (2014, 2015) as upper limits and also the deviation from the $z = 0 - 2$ power-law seen by our $z = 3.24$ EW_{rest} and the $z \sim 3.5$ Keck/MOSFIRE EW_{rest} measurement of Schenker et al. (2013b).

7. We present the first measurement of the [OII] EW_{rest} out to $z \sim 5$. We find that the [OII] EW_{rest} increases by a factor of ~ 60, followed by a decrease in EW_{rest} to higher redshift. This could be one reason why no high-z measurements of [OII] exists in the $z > 5$ regime from UV studies that are finding ubiquitous high Hβ+[OIII] EW sources.

8. We study the evolution of the ionization state of the gas using the [OIII]/[OII] line ratio. The line ratio increases beyond $z \sim 3$ such that the higher the redshift, the higher the ionization parameter. This could explain the lack of [OII] detections at high-z. If the higher ionization parameter is due to a harder ionizing source (e.g., high energy photons coming from massive stars), then it could suppress the [OII] line while producing a stronger [OIII] line as the doubly-ionized oxygen atoms are bombarded with highly energetic photons and free electrons such that they can not make the transition to produce an [OII] line. The higher ionization parameter can also explain the recent detections of emission lines with high ionization potentials at $z \sim 5$ to ~ 7 (e.g., CIII], CIV, HeII, NIV). The physical reason for a higher

ionization parameter is still in debate and can be explained by a harder ionizing radiation field, electron densities, and metallicities.

Our results present a clearer picture of the EW_{rest} of the Hβ+[OIII] and [OII] lines, as well as an understanding of how the strengths of these lines and its dependency on the changes in the ionization state of the gas can explain the recent developments in detecting Hβ+[OIII] at $z \sim 6-8$ and other emission lines that arise from transitions involving high ionization potentials. The results highlighted in this paper prepare for the next-generation of ground-based telescopes (e.g., Thirty Meter Telescope) and state-of-the-art space-based observatories (e.g., *JWST*, *EUCLID*, *WFIRST*) by presenting an outline of the evolution of the EW_{rest} and the [OIII]/[OII] line ratio and predictions for the high-z Universe that can better our understanding of the physical conditions for which forms the observed EW_{rest} and [OIII]/[OII] line ratios.

6.3 Clustering Properties of Hβ+[OIII] and [OII] Emission Line Galaxies

We have presented our Hβ+[OIII] and [OII] clustering measurements up to $z \sim 3.3$ and ~ 4.7, respectively. The main results of this study are:

1. We find that the power law slopes of the angular correlation functions are consistent with $\beta \sim -0.80$. Using the exact Limber equation, we find typical r_0 between $1.45-4.01\ h^{-1}$ Mpc and $1.99-8.25\ h^{-1}$ Mpc for Hβ+[OIII] and [OII] emitters, respectively. These correspond to minimum halo masses between $10^{10.70-12.08}$ $M_\odot$ and $10^{11.46-12.62}$ $M_\odot$, respectively.

2. A r_0-line luminosity dependency is found where the brightest emitters are more clustered compared to the faintest emitters. This dependency is found to be redshift-dependent but is biased due to the line luminosity function evolution. When rescaling based on $L^\star(z)$ and using model predictions of halo mass given r_0, we find a strong, increasing dependency

between minimum halo mass and line luminosity that is independent of redshift with the faintest Hβ+[OIII] ([OII]) emitters found in $10^{9.5}$ $M_\odot$ ($10^{10.5}$ $M_\odot$) halos and the brightest Hβ+[OIII] ([OII]) emitters in 10^{13} $M_\odot$ ($10^{12.5}$ $M_\odot$) halos.

3. We find a redshift-independent dependency between stellar and halo mass. We find that Hβ+[OIII] emitters with stellar masses $> 10^{9.75}$ $M_\odot$ reside in $10^{12.3}$ $M_\odot$ halos between $z = 0.84$ and 3.24. The [OII] samples also show a dependency for the full stellar mass range.

4. We find that halo mass is strongly correlated with line luminosity than stellar mass when investigating the respective trends in a line luminosity-stellar mass grid space.This then suggests a simple connection between the nebular emission line properties of galaxies and their host halo mass.

5. The line luminosity-halo mass dependency shows an increase from the faintest emitters observed to $L \sim L^\star(z)$. For emitters brighter that $L^\star$, we find that the trend is consistent with halos between $10^{12.5-13}$ $M_\odot$, which is consistent with predictions of a transitional halo mass scale. The bright emitters residing in such halo masses seem to have their strong emission lines attributed to AGN activity, galaxy merging, and enhanced gas inflow.

Our results suggest a simple connection between the clustering/dark matter halo properties and nebular emission line properties of star-forming/'active' galaxies up to $z \sim 5$. This has implications for future theoretical studies that model this connection since previous constraints were up to $z \sim 2$ for only Hα emitters. On the observational side, future spectroscopic studies of bright, emission line-selected galaxies can allow us to investigate the dependency between the ISM properties (internal mechanisms) of galaxies and massive halos (external mechanisms). Morphological studies of our samples can also test to see if the shape of galaxies is connected with the host halo properties. Future space-based (e.g., *JWST*, *WFIRST*, *Euclid*) and ground-based observatories (e.g., European Extremely Large Telescope, Thirty Meter Telescope), can also

allow us to study the clustering properties of emission line-selected galaxies at higher redshifts and larger comoving volumes. This would allow us to see when the following redshift-independent trends that seem to have been in place since $z \sim 5$ were first established, which would present a new scaling relation for galaxy formation and evolution models. Our results also are prelude to large-scale spectroscopic surveys using the upcoming Subaru/PFS (Takada et al., 2014), VISTA/4MOST (de Jong et al., 2016), and Mayall/DESI (DESI Collaboration et al., 2016) instruments that will observe galaxy emission lines in large comoving volumes at redshifts up to $z \sim 2.5$.

6.4 Clustering Properties of Typical Lyα Emitters

We present a comprehensive investigation of the clustering and halo properties of LAEs and explore their dependences on Lyα luminosity, UV continuum luminosity, and UV star formation rate in multiple redshift slices between $z \sim 2.5-6$. We highlight the main results of this study here:

1. We measure the angular correlation functions and clustering lengths of every redshift sample. The clustering lengths of the narrowband samples are shown to increase from $r_0 \sim 3.1-5.0$ Mpc h^{-1} between $z \sim 3.1-5.7$. The intermediate band and combined intermediate band samples show a more rapid increase in r_0 from ~ 4.5 Mpc h^{-1} at $z \sim 2.5$ to ~ 16 Mpc h^{-1} by $z \sim 5.8$. The typical halo masses of the narrowband samples are found to be $\sim 10^{11}$ $M_\odot$, while the intermediate band samples range between $\sim 10^{11-12}$ $M_\odot$.

2. Host halo mass is found to scale with Lyα luminosity at all redshifts probed. Initial analysis of this trend shows a redshift evolution, but this is found to be caused by the cosmic evolution of the Lyα luminosity function. Taking this into account by normalizing Lyα luminosity by $L^\star(z)$ shows a redshift-independent trend with host halo mass. LAEs are found to reside in

a wide range of host halos ranging from $10^{9.75}$ $M_\odot$ at $\sim 0.1L^\star(z)$ to $10^{12.1}$ $M_\odot$ at $L^\star(z)$ and $10^{12.8}$ $M_\odot$ at $\sim 10L^\star(z)$.

3. We find a strong, redshift-independent trend between host halo mass and observed 1500Å UV continuum luminosity. LAEs with $M_{UV} \sim -18$ mag are found to reside in $10^{10.5}$ $M_\odot$ halos and $M_{UV} \sim -23$ mag in 10^{13} $M_\odot$ halos.

4. We also find a strong, redshift-independent trend between host halo mass and dust-corrected UV star formation rate. We find that LAEs with SFR ~ 1 $M_\odot$ yr^{-1} reside in 10^{10} $M_\odot$ halos and ~ 100 $M_\odot$ yr^{-1} reside in $10^{12.8}$ $M_\odot$ halos.

5. For both Lyα luminosity and UV SFR, we observe sharp trend changes. In the case of Lyα luminosity, we find that the host halo mass scales as $(L/L^\star(z))^{2.08}$ and $(L/L^\star(z))^{0.63}$ for below and above $L^\star(z)$, respectively. A similar trend is seen between halo mass and SFR with the trend change occurring at ~ 4.5 $M_\odot$ yr^{-1}. This is attributed to a changing population of LAEs where the brightest LAEs, in terms of line luminosity and SFRs, primarily have their emission powered by AGNs and not star formation activity.

Our results highlights the significant connection that host halos and galaxies share from the end of the epoch of reionization to the peak of cosmic star formation. The redshift-independent trends with halo mass signifies the co-evolution of galaxies and their host halos and that the host halo mass is a defining factor in how the residing galaxy evolves.

At all redshift slices, we find the LAEs in our samples cover a wide range in host halo masses. But what are the present-day descendants of these types of galaxies? In the grand scheme of galaxy evolution, we wish to understand what became of the galaxies we observe. Figure 5.10 shows the present-day halo masses of our full LAE samples measured using the halo mass accretion tracks of Behroozi et al. (2013b). Given the wide range in halo masses we have observed throughout this study, we find that LAEs cover a wide range of present-day

descendants from dwarf-like ($M_{\rm halo} \sim 10^{11}$ $M_\odot$), to Milky Way-like ($M_{\rm halo} \sim 10^{12}$ $M_\odot$), and galaxies residing in cluster-like environments ($M_{\rm halo} > 10^{13}$ $M_\odot$). The wide range in the type of descendants shows that LAEs are great tools in studying how galaxies formed and evolved to the ones we currently see in the local Universe.

Bibliography

Adams J. J., et al., 2011, ApJS, 192, 5

Adelberger K. L., Steidel C. C., Pettini M., Shapley A. E., Reddy N. A., Erb D. K., 2005, ApJ, 619, 697

Alavi A., et al., 2014, ApJ, 780, 143

Alavi A., et al., 2016, ApJ, 832, 56

Allevato V., et al., 2016, ApJ, 832, 70

Arnouts S., et al., 2005, ApJL, 619, L43

Arnouts S., et al., 2007, A&A, 476, 137

Baldry I. K., Balogh M. L., Bower R. G., Glazebrook K., Nichol R. C., Bamford S. P., Budavari T., 2006, MNRAS, 373, 469

Barone-Nugent R. L., et al., 2014, ApJ, 793, 17

Bauer A. E., et al., 2013, MNRAS, 434, 209

Bayliss K. D., McMahon R. G., Venemans B. P., Ryan-Weber E. V., Lewis J. R., 2011, MNRAS, 413, 2883

Bayliss K. D., McMahon R. G., Venemans B. P., Banerji M., Lewis J. R., 2012, MNRAS, 426, 2178

Behroozi P. S., Wechsler R. H., Conroy C., 2013a, ApJL, 762, L31

Behroozi P. S., Wechsler R. H., Conroy C., 2013b, ApJ, 770, 57

Bell E. F., McIntosh D. H., Katz N., Weinberg M. D., 2003, ApJS, 149, 289

Benson A. J., 2010, , 495, 33

Best P. N., Kaiser C. R., Heckman T. M., Kauffmann G., 2006, MNRAS, 368, L67

Best P., et al., 2013, Astrophysics and Space Science Proceedings, 37, 235

Bielby R., et al., 2012, A&A, 545, A23

Bielby R. M., et al., 2016, MNRAS, 456, 4061

Birnboim Y., Dekel A., 2003, MNRAS, 345, 349

Blake C., Collister A., Lahav O., 2008, MNRAS, 385, 1257

Bolzonella M., et al., 2010, A&A, 524, A76

Bongiorno A., et al., 2010, A&A, 510, A56

Boselli A., Gavazzi G., 2006, PASP, 118, 517

Bournaud F., et al., 2011, ApJ, 730, 4

Bouwens R. J., et al., 2011, ApJ, 737, 90

Bouwens R. J., et al., 2012a, ApJL, 752, L5

Bouwens R. J., et al., 2012b, ApJ, 754, 83

Bouwens R. J., et al., 2014, ApJ, 795, 126

Bouwens R. J., et al., 2015, ApJ, 803, 34

Bouwens R. J., et al., 2016, ApJ, 830, 67

Bower R. G., Schaye J., Frenk C. S., Theuns T., Schaller M., Crain R. A., McAlpine S., 2017, MNRAS, 465, 32

Bradshaw E. J., et al., 2013, MNRAS, 433, 194

Brammer G. B., van Dokkum P. G., Coppi P., 2008, ApJ, 686, 1503

Brammer G. B., et al., 2011, ApJ, 739, 24

Bridge J. S., et al., 2015, ApJ, 799, 205

Bruzual G., Charlot S., 2003, MNRAS, 344, 1000

Bundy K., et al., 2006, ApJ, 651, 120

Bunker A. J., Warren S. J., Hewett P. C., Clements D. L., 1995, MNRAS, 273, 513

Calzetti D., 2013, Star Formation Rate Indicators. p. 419

Calzetti D., Kinney A. L., Storchi-Bergmann T., 1994, ApJ, 429, 582

Calzetti D., Armus L., Bohlin R. C., Kinney A. L., Koornneef J., Storchi-Bergmann T., 2000, ApJ, 533, 682

Capak P., et al., 2007, ApJS, 172, 99

Cappelluti N., et al., 2009, A&A, 497, 635

Caputi K. I., Cirasuolo M., Dunlop J. S., McLure R. J., Farrah D., Almaini O., 2011, MNRAS, 413, 162

Carollo C. M., et al., 2013, ApJ, 776, 71

Cen R., 2011, ApJ, 741, 99

Chabrier G., 2003, PASP, 115, 763

Charlot S., Fall S. M., 2000, ApJ, 539, 718

Ciardullo R., et al., 2013, ApJ, 769, 83

Cirasuolo M., et al., 2007, MNRAS, 380, 585

Cochrane R. K., Best P. N., Sobral D., Smail I., Wake D. A., Stott J. P., Geach J. E., 2017, MNRAS, 469, 2913

Cochrane R. K., Best P. N., Sobral D., Smail I., Geach J. E., Stott J. P., Wake D. A., 2018, MNRAS, 475, 3730

Coil A. L., et al., 2008, ApJ, 672, 153

Coil A. L., et al., 2011, ApJ, 741, 8

Coil A. L., Mendez A. J., Eisenstein D. J., Moustakas J., 2017, ApJ, 838, 87

Colbert J. W., et al., 2013, ApJ, 779, 34

Colless M., et al., 2001, MNRAS, 328, 1039

Comparat J., Prada F., Yepes G., Klypin A., 2017, MNRAS, 469, 4157

Conroy C., Wechsler R. H., 2009, ApJ, 696, 620

Cooray A., Sheth R., 2002, , 372, 1

Coupon J., et al., 2015, MNRAS, 449, 1352

Cowie L. L., Hu E. M., 1998, AJ, 115, 1319

Croton D. J., et al., 2006, MNRAS, 365, 11

Cucciati O., et al., 2012, A&A, 539, A31

DESI Collaboration et al., 2016, preprint, (arXiv:1611.00036)

Daddi E., Cimatti A., Renzini A., Fontana A., Mignoli M., Pozzetti L., Tozzi P., Zamorani G., 2004, ApJ, 617, 746

Daddi E., et al., 2007, ApJ, 670, 156

Damen M., Labbé I., Franx M., van Dokkum P. G., Taylor E. N., Gawiser E. J., 2009, ApJ, 690, 937

Darvish B., Sobral D., Mobasher B., Scoville N. Z., Best P., Sales L. V., Smail I., 2014, ApJ, 796, 51

Darvish B., Mobasher B., Sobral D., Scoville N., Aragon-Calvo M., 2015a, ApJ, 805, 121

Darvish B., Mobasher B., Sobral D., Hemmati S., Nayyeri H., Shivaei I., 2015b, ApJ, 814, 84

Darvish B., Mobasher B., Sobral D., Rettura A., Scoville N., Faisst A., Capak P., 2016, ApJ, 825, 113

Darvish B., Mobasher B., Martin D. C., Sobral D., Scoville N., Stroe A., Hemmati S., Kartaltepe J., 2017, ApJ, 837, 16

Davé R., Oppenheimer B. D., Finlator K., 2011, MNRAS, 415, 11

Davé R., Finlator K., Oppenheimer B. D., 2012, MNRAS, 421, 98

Davidzon I., et al., 2015, preprint, (arXiv:1511.01145)

Davis M., et al., 2003, in Guhathakurta P., ed., Vol. 4834, Discoveries and Research Prospects from 6- to 10-Meter-Class Telescopes II. pp 161–172 (arXiv:astro-ph/0209419), doi:10.1117/12.457897

Dawson K. S., et al., 2013, AJ, 145, 10

Dawson K. S., et al., 2016, AJ, 151, 44

Dekel A., Birnboim Y., 2006, MNRAS, 368, 2

Despali G., Giocoli C., Angulo R. E., Tormen G., Sheth R. K., Baso G., Moscardini L., 2016, MNRAS, 456, 2486

Di Matteo P., Bournaud F., Martig M., Combes F., Melchior A.-L., Semelin B., 2008, A&A, 492, 31

Dickinson M., 1998, in Livio M., Fall S. M., Madau P., eds, The Hubble Deep Field. p. 219 (arXiv:astro-ph/9802064)

Diemer B., 2017, preprint, (arXiv:1712.04512)

Diemer B., Kravtsov A. V., 2015, ApJ, 799, 108

Dijkstra M., 2017, preprint, (arXiv:1704.03416)

Dijkstra M., Gronke M., Sobral D., 2016, preprint, (arXiv:1602.07695)

Dolley T., et al., 2014, ApJ, 797, 125

Drake A. B., et al., 2013, MNRAS, 433, 796

Driver S. P., et al., 2011, MNRAS, 413, 971

Drory N., Alvarez M., 2008, ApJ, 680, 41

Durkalec A., et al., 2015, A&A, 583, A128

Durkalec A., et al., 2018, A&A, 612, A42

Eisenstein D. J., Hu W., 1998, ApJ, 496, 605

Elsner F., Feulner G., Hopp U., 2008, A&A, 477, 503

Elvis M., et al., 2009, ApJS, 184, 158

Erb D. K., Steidel C. C., Shapley A. E., Pettini M., Reddy N. A., Adelberger K. L., 2006, ApJ, 647, 128

Fabian A. C., 2012, ARA&A, 50, 455

Faisst A. L., et al., 2016, preprint, (arXiv:1601.07173)

Favole G., Rodríguez-Torres S. A., Comparat J., Prada F., Guo H., Klypin A., Montero-Dorta A. D., 2016, preprint, (arXiv:1611.05457)

Finkelstein S. L., et al., 2015, ApJ, 810, 71

Forrest B., et al., 2017, ApJL, 838, L12

Förster Schreiber N. M., et al., 2009, ApJ, 706, 1364

Fujita S. S., et al., 2003, ApJL, 586, L115

Fumagalli M., et al., 2012, ApJL, 757, L22

Furlong M., et al., 2015, MNRAS, 450, 4486

Gallazzi A., Brinchmann J., Charlot S., White S. D. M., 2008, MNRAS, 383, 1439

Gallego J., García-Dabó C. E., Zamorano J., Aragón-Salamanca A., Rego M., 2002, ApJL, 570, L1

Garilli B., et al., 2014, A&A, 562, A23

Garn T., et al., 2010, MNRAS, 402, 2017

Gawiser E., et al., 2007, ApJ, 671, 278

Geach J. E., Smail I., Best P. N., Kurk J., Casali M., Ivison R. J., Coppin K., 2008, MNRAS, 388, 1473

Geach J. E., Sobral D., Hickox R. C., Wake D. A., Smail I., Best P. N., Baugh C. M., Stott J. P., 2012, MNRAS, 426, 679

Giavalisco M., 2002, ARA&A, 40, 579

Giodini S., et al., 2012, A&A, 538, A104

Glazebrook K., Tober J., Thomson S., Bland-Hawthorn J., Abraham R., 2004, AJ, 128, 2652

González V., Labbé I., Bouwens R. J., Illingworth G., Franx M., Kriek M., Brammer G. B., 2010, ApJ, 713, 115

González V., Labbé I., Bouwens R. J., Illingworth G., Franx M., Kriek M., 2011, ApJL, 735, L34

González V., Bouwens R., Illingworth G., Labbé I., Oesch P., Franx M., Magee D., 2014, ApJ, 781, 34

Grazian A., et al., 2015, A&A, 575, A96

Gronwall C., et al., 2007, ApJ, 667, 79

Gruppioni C., et al., 2013, MNRAS, 432, 23

Guaita L., et al., 2010, ApJ, 714, 255

Gunawardhana M. L. P., et al., 2013, MNRAS, 433, 2764

Guo H., et al., 2013, ApJ, 767, 122

Guo H., et al., 2014, MNRAS, 441, 2398

Guth A. H., 1981, , 23, 347

Hale C. L., Jarvis M. J., Delvecchio I., Hatfield P. W., Novak M., Smolčić V., Zamorani G., 2018, MNRAS, 474, 4133

Hammer F., et al., 1997, ApJ, 481, 49

Hao C.-N., Kennicutt R. C., Johnson B. D., Calzetti D., Dale D. A., Moustakas J., 2011, ApJ, 741, 124

Harikane Y., et al., 2016, ApJ, 821, 123

Harikane Y., et al., 2018, PASJ, 70, S11

Hartley W. G., et al., 2008, MNRAS, 391, 1301

Hartley W. G., et al., 2013, MNRAS, 431, 3045

Hayashi M., Shimasaku K., Motohara K., Yoshida M., Okamura S., Kashikawa N., 2007, ApJ, 660, 72

Hayashi M., Sobral D., Best P. N., Smail I., Kodama T., 2013, MNRAS, 430, 1042

Hayashi M., et al., 2015, PASJ, 67, 80

Hayashino T., et al., 2004, AJ, 128, 2073

Hemmati S., Mobasher B., Darvish B., Nayyeri H., Sobral D., Miller S., 2015, ApJ, 814, 46

Henriques B. M. B., White S. D. M., Thomas P. A., Angulo R., Guo Q., Lemson G., Springel V., Overzier R., 2015, MNRAS, 451, 2663

Hickox R. C., et al., 2009, ApJ, 696, 891

Hicks E. K. S., Malkan M. A., Teplitz H. I., McCarthy P. J., Yan L., 2002, ApJ, 581, 205

Hildebrandt H., et al., 2005, A&A, 441, 905

Hogg D. W., Cohen J. G., Blandford R., Pahre M. A., 1998, ApJ, 504, 622

Hopkins A. M., Beacom J. F., 2006, ApJ, 651, 142

Hopkins P. F., Kereš D., Oñorbe J., Faucher-Giguère C.-A., Quataert E., Murray N., Bullock J. S., 2014, MNRAS, 445, 581

Hung C.-L., et al., 2013, ApJ, 778, 129

Ilbert O., et al., 2009, ApJ, 690, 1236

Ilbert O., et al., 2010, ApJ, 709, 644

Ilbert O., et al., 2013, A&A, 556, A55

Ishikawa S., Kashikawa N., Toshikawa J., Onoue M., 2015, MNRAS, 454, 205

Johnston R., 2011, A&AR, 19, 41

Jose C., Lacey C. G., Baugh C. M., 2016, MNRAS, 463, 270

Kajisawa M., et al., 2009, ApJ, 702, 1393

Karim A., et al., 2011, ApJ, 730, 61

Kashino D., et al., 2013, ApJL, 777, L8

Kashino D., et al., 2017, preprint, (arXiv:1703.08326)

Kauffmann G., et al., 2003, MNRAS, 346, 1055

Kennicutt Jr. R. C., 1998, ARA&A, 36, 189

Kennicutt R. C., Evans N. J., 2012, ARA&A, 50, 531

Kerscher M., Szapudi I., Szalay A. S., 2000, ApJL, 535, L13

Kewley L. J., Geller M. J., Jansen R. A., 2004, AJ, 127, 2002

Kewley L. J., Dopita M. A., Leitherer C., Davé R., Yuan T., Allen M., Groves B., Sutherland R., 2013, ApJ, 774, 100

Kewley L. J., Zahid H. J., Geller M. J., Dopita M. A., Hwang H. S., Fabricant D., 2015, ApJL, 812, L20

Khostovan A. A., Sobral D., Mobasher B., Best P. N., Smail I., Stott J. P., Hemmati S., Nayyeri H., 2015, MNRAS, 452, 3948

Khostovan A. A., Sobral D., Mobasher B., Smail I., Darvish B., Nayyeri H., Hemmati S., Stott J. P., 2016, MNRAS, 463, 2363

Khostovan A. A., et al., 2018, MNRAS, 478, 2999

Kobulnicky H. A., Kewley L. J., 2004, ApJ, 617, 240

Konno A., Ouchi M., Nakajima K., Duval F., Kusakabe H., Ono Y., Shimasaku K., 2016, ApJ, 823, 20

Konno A., et al., 2018, PASJ, 70, S16

Koutoulidis L., Plionis M., Georgantopoulos I., Fanidakis N., 2013, MNRAS, 428, 1382

Kovač K., Somerville R. S., Rhoads J. E., Malhotra S., Wang J., 2007, ApJ, 668, 15

Kravtsov A. V., Berlind A. A., Wechsler R. H., Klypin A. A., Gottlöber S., Allgood B., Primack J. R., 2004, ApJ, 609, 35

Kubo M., Yamada T., Ichikawa T., Kajisawa M., Matsuda Y., Tanaka I., 2015, ApJ, 799, 38

Kubo M., Yamada T., Ichikawa T., Kajisawa M., Matsuda Y., Tanaka I., Umehata H., 2016, MNRAS, 455, 3333

Kusakabe H., et al., 2018, PASJ, 70, 4

Labbé I., et al., 2013, ApJL, 777, L19

Lamareille F., et al., 2009, A&A, 495, 53

Landy S. D., Szalay A. S., 1993, ApJ, 412, 64

Lawrence A., et al., 2007, MNRAS, 379, 1599

Le Fèvre O., et al., 2005, A&A, 439, 845

Le Fèvre O., et al., 2013, A&A, 559, A14

Leauthaud A., Tinker J., Behroozi P. S., Busha M. T., Wechsler R. H., 2011, ApJ, 738, 45

Leauthaud A., et al., 2012, ApJ, 744, 159

Lee K.-S., Giavalisco M., Gnedin O. Y., Somerville R. S., Ferguson H. C., Dickinson M., Ouchi M., 2006, ApJ, 642, 63

Lee J. C., et al., 2011, ApJS, 192, 6

Lee K.-S., et al., 2012, ApJ, 752, 66

Li C., White S. D. M., 2009, MNRAS, 398, 2177

Lilly S. J., Le Fevre O., Hammer F., Crampton D., 1996, ApJL, 460, L1

Lilly S. J., et al., 2007, ApJS, 172, 70

Limber D. N., 1953, ApJ, 117, 134

Lin L., et al., 2012, ApJ, 756, 71

Liu X., Shapley A. E., Coil A. L., Brinchmann J., Ma C.-P., 2008, ApJ, 678, 758

Ly C., et al., 2007, ApJ, 657, 738

Ly C., Lee J. C., Dale D. A., Momcheva I., Salim S., Staudaher S., Moore C. A., Finn R., 2011, ApJ, 726, 109

Madau P., Dickinson M., 2014, ARA&A, 52, 415

Madau P., Ferguson H. C., Dickinson M. E., Giavalisco M., Steidel C. C., Fruchter A., 1996, MNRAS, 283, 1388

Marchesini D., van Dokkum P. G., Förster Schreiber N. M., Franx M., Labbé I., Wuyts S., 2009, ApJ, 701, 1765

Markwardt C. B., 2009, in Bohlender D. A., Durand D., Dowler P., eds, Astronomical Society of the Pacific Conference Series Vol. 411, Astronomical Data Analysis Software and Systems XVIII. p. 251 (arXiv:0902.2850)

Marmol-Queralto E., McLure R. J., Cullen F., Dunlop J. S., Fontana A., McLeod D. J., 2015, preprint, (arXiv:1511.01911)

Marulli F., et al., 2013, A&A, 557, A17

Matarrese S., Coles P., Lucchin F., Moscardini L., 1997, MNRAS, 286, 115

Matthee J., Sobral D., Santos S., Röttgering H., Darvish B., Mobasher B., 2015, MNRAS, 451, 400

Matthee J., Sobral D., Oteo I., Best P., Smail I., Röttgering H., Paulino-Afonso A., 2016, MNRAS, 458, 449

Matthee J., Schaye J., Crain R. A., Schaller M., Bower R., Theuns T., 2017a, MNRAS, 465, 2381

Matthee J., Sobral D., Best P., Smail I., Bian F., Darvish B., Röttgering H., Fan X., 2017b, MNRAS, 471, 629

McCracken H. J., et al., 2010, ApJ, 708, 202

McCracken H. J., et al., 2015, MNRAS, 449, 901

McLure R. J., et al., 2013, MNRAS, 428, 1088

Mendez A. J., et al., 2016, ApJ, 821, 55

Meneux B., et al., 2008, A&A, 478, 299

Meneux B., et al., 2009, A&A, 505, 463

Meurer G. R., Heckman T. M., Calzetti D., 1999, ApJ, 521, 64

Mihos J. C., Hernquist L., 1996, ApJ, 464, 641

Mo H. J., White S. D. M., 1996, MNRAS, 282, 347

Mobasher B., et al., 2015, ApJ, 808, 101

Mortlock A., et al., 2015, MNRAS, 447, 2

Moscardini L., Coles P., Lucchin F., Matarrese S., 1998, MNRAS, 299, 95

Mostek N., Coil A. L., Cooper M., Davis M., Newman J. A., Weiner B. J., 2013, ApJ, 767, 89

Moster B. P., Naab T., White S. D. M., 2013, MNRAS, 428, 3121

Moster B. P., Naab T., White S. D. M., 2017, preprint, (arXiv:1705.05373)

Moustakas J., et al., 2013, ApJ, 767, 50

Murayama T., et al., 2007, ApJS, 172, 523

Murphy E. J., et al., 2011, ApJ, 737, 67

Mutch S. J., Croton D. J., Poole G. B., 2013, MNRAS, 435, 2445

Muzzin A., et al., 2013, ApJ, 777, 18

Nakajima K., Ouchi M., 2014, MNRAS, 442, 900

Nakajima K., Ouchi M., Shimasaku K., Hashimoto T., Ono Y., Lee J. C., 2013, ApJ, 769, 3

Nayyeri H., et al., 2014, ApJ, 794, 68

Nestor D. B., Shapley A. E., Steidel C. C., Siana B., 2011, ApJ, 736, 18

Newman S. F., et al., 2014, ApJ, 781, 21

Nilsson K. K., Tapken C., Møller P., Freudling W., Fynbo J. P. U., Meisenheimer K., Laursen P., Östlin G., 2009, A&A, 498, 13

Noeske K. G., et al., 2007, ApJL, 660, L47

Norberg P., et al., 2002, MNRAS, 332, 827

Norberg P., Baugh C. M., Gaztañaga E., Croton D. J., 2009, MNRAS, 396, 19

Oesch P. A., et al., 2010, ApJL, 725, L150

Oke J. B., Gunn J. E., 1983, ApJ, 266, 713

Ono Y., Ouchi M., Shimasaku K., Dunlop J., Farrah D., McLure R., Okamura S., 2010, ApJ, 724, 1524

Orsi Á., Padilla N., Groves B., Cora S., Tecce T., Gargiulo I., Ruiz A., 2014, MNRAS, 443, 799

Osterbrock D. E., Ferland G. J., 2006, Astrophysics of gaseous nebulae and active galactic nuclei

Oteo I., Sobral D., Ivison R. J., Smail I., Best P. N., Cepa J., Pérez-García A. M., 2015, MNRAS, 452, 2018

Ouchi M., et al., 2003, ApJ, 582, 60

Ouchi M., et al., 2005, ApJL, 635, L117

Ouchi M., et al., 2008, ApJS, 176, 301

Ouchi M., et al., 2010, ApJ, 723, 869

Ouchi M., et al., 2018, PASJ, 70, S13

Pallottini A., et al., 2015, MNRAS, 453, 2465

Papovich C., et al., 2015, ApJ, 803, 26

Pascual S., 2005, PASP, 117, 120

Paulino-Afonso A., et al., 2018, MNRAS, 476, 5479

Peebles P. J. E., 1980, The large-scale structure of the universe

Peng Y.-j., et al., 2010, ApJ, 721, 193

Peng Y.-j., Lilly S. J., Renzini A., Carollo M., 2012, ApJ, 757, 4

Pérez-González P. G., et al., 2008, ApJ, 675, 234

Pirzkal N., et al., 2013, ApJ, 772, 48

Pozzetti L., et al., 2010, A&A, 523, A13

Prescott M., et al., 2011, MNRAS, 417, 1374

Press W. H., Schechter P., 1974, ApJ, 187, 425

Puglisi A., et al., 2016, A&A, 586, A83

Rasappu N., Smit R., Labbé I., Bouwens R. J., Stark D. P., Ellis R. S., Oesch P. A., 2016, MNRAS, 461, 3886

Reddy N. A., Steidel C. C., 2009, ApJ, 692, 778

Reddy N. A., Pettini M., Steidel C. C., Shapley A. E., Erb D. K., Law D. R., 2012, ApJ, 754, 25

Reddy N. A., et al., 2015, ApJ, 806, 259

Rhoads J. E., Malhotra S., Dey A., Stern D., Spinrad H., Jannuzi B. T., 2000, ApJL, 545, L85

Rigby J. R., Wuyts E., Gladders M. D., Sharon K., Becker G. D., 2011, ApJ, 732, 59

Roberts-Borsani G. W., et al., 2016, ApJ, 823, 143

Robertson B. E., et al., 2013, ApJ, 768, 71

Roche N. D., Almaini O., Dunlop J., Ivison R. J., Willott C. J., 2002, MNRAS, 337, 1282

Rodighiero G., et al., 2011, ApJL, 739, L40

Rodriguez-Gomez V., et al., 2015, preprint, (arXiv:1511.08804)

Saez C., et al., 2015, MNRAS, 450, 2615

Salim S., et al., 2007, ApJS, 173, 267

Sanders R. L., et al., 2015, ApJ, 799, 138

Sanders R. L., et al., 2016, ApJ, 816, 23

Santos S., Sobral D., Matthee J., 2016, MNRAS, 463, 1678

Schaerer D., de Barros S., 2009, A&A, 502, 423

Schaerer D., de Barros S., 2010, A&A, 515, A73

Schechter P., 1976, ApJ, 203, 297

Schenker M. A., et al., 2013a, ApJ, 768, 196

Schenker M. A., Ellis R. S., Konidaris N. P., Stark D. P., 2013b, ApJ, 777, 67

Schreiber C., et al., 2015, A&A, 575, A74

Scoville N., et al., 2007, ApJS, 172, 1

Scoville N., et al., 2017, ApJ, 837, 150

Sheth R. K., Mo H. J., Tormen G., 2001, MNRAS, 323, 1

Shim H., Chary R.-R., Dickinson M., Lin L., Spinrad H., Stern D., Yan C.-H., 2011, ApJ, 738, 69

Shimasaku K., et al., 2004, ApJL, 605, L93

Shioya Y., et al., 2008, ApJS, 175, 128

Shioya Y., et al., 2009, ApJ, 696, 546

Shirazi M., Brinchmann J., Rahmati A., 2014, ApJ, 787, 120

Shivaei I., Reddy N. A., Steidel C. C., Shapley A. E., 2015, ApJ, 804, 149

Simon P., 2007, A&A, 473, 711

Smit R., Bouwens R. J., Franx M., Illingworth G. D., Labbé I., Oesch P. A., van Dokkum P. G., 2012, ApJ, 756, 14

Smit R., et al., 2014, ApJ, 784, 58

Smit R., et al., 2015, ApJ, 801, 122

Sobral D., et al., 2009, MNRAS, 398, 75

Sobral D., Best P. N., Geach J. E., Smail I., Cirasuolo M., Garn T., Dalton G. B., Kurk J., 2010, MNRAS, 404, 1551

Sobral D., Best P. N., Smail I., Geach J. E., Cirasuolo M., Garn T., Dalton G. B., 2011, MNRAS, 411, 675

Sobral D., Best P. N., Matsuda Y., Smail I., Geach J. E., Cirasuolo M., 2012, MNRAS, 420, 1926

Sobral D., Smail I., Best P. N., Geach J. E., Matsuda Y., Stott J. P., Cirasuolo M., Kurk J., 2013a, MNRAS, 428, 1128

Sobral D., et al., 2013b, ApJ, 779, 139

Sobral D., Best P. N., Smail I., Mobasher B., Stott J., Nisbet D., 2014, MNRAS, 437, 3516

Sobral D., et al., 2015a, MNRAS, 451, 2303

Sobral D., Matthee J., Darvish B., Schaerer D., Mobasher B., Röttgering H. J. A., Santos S., Hemmati S., 2015b, ApJ, 808, 139

Sobral D., Stroe A., Koyama Y., Darvish B., Calhau J. a., Afonso A., Kodama T., Nakata F., 2016a, MNRAS,

Sobral D., Kohn S. A., Best P. N., Smail I., Harrison C. M., Stott J., Calhau J., Matthee J., 2016b, MNRAS, 457, 1739

Sobral D., et al., 2017, MNRAS, 466, 1242

Sobral D., Santos S., Matthee J., Paulino-Afonso A., Ribeiro B., Calhau J., Khostovan A. A., 2018a, MNRAS,

Sobral D., et al., 2018b, MNRAS, 477, 2817

Somerville R. S., Davé R., 2015, ARA&A, 53, 51

Stark D. P., Ellis R. S., Bunker A., Bundy K., Targett T., Benson A., Lacy M., 2009, ApJ, 697, 1493

Stark D. P., Schenker M. A., Ellis R., Robertson B., McLure R., Dunlop J., 2013, ApJ, 763, 129

Stark D. P., et al., 2014, MNRAS, 445, 3200

Stark D. P., et al., 2015a, MNRAS, 450, 1846

Stark D. P., et al., 2015b, MNRAS, 454, 1393

Steidel C. C., Pettini M., Hamilton D., 1995, AJ, 110, 2519

Steidel C. C., Adelberger K. L., Dickinson M., Giavalisco M., Pettini M., Kellogg M., 1998, ApJ, 492, 428

Steidel C. C., Adelberger K. L., Shapley A. E., Pettini M., Dickinson M., Giavalisco M., 2000, ApJ, 532, 170

Steidel C. C., et al., 2014, ApJ, 795, 165

Stott J. P., Sobral D., Smail I., Bower R., Best P. N., Geach J. E., 2013a, MNRAS, 430, 1158

Stott J. P., et al., 2013b, MNRAS, 436, 1130

Stott J. P., et al., 2014, MNRAS, 443, 2695

Stott J. P., et al., 2016, MNRAS, 457, 1888

Stroe A., Sobral D., 2015, MNRAS, 453, 242

Suzuki T. L., et al., 2016, MNRAS, 462, 181

Swinbank A. M., Sobral D., Smail I., Geach J. E., Best P. N., McCarthy I. G., Crain R. A., Theuns T., 2012a, MNRAS, 426, 935

Swinbank A. M., Smail I., Sobral D., Theuns T., Best P. N., Geach J. E., 2012b, ApJ, 760, 130

Takada M., et al., 2014, PASJ, 66, R1

Takahashi M. I., et al., 2007, ApJS, 172, 456

Taniguchi Y., et al., 2007, ApJS, 172, 9

Taniguchi Y., et al., 2015, PASJ, 67, 104

Tasca L. A. M., et al., 2015, A&A, 581, A54

Teplitz H. I., Collins N. R., Gardner J. P., Hill R. S., Rhodes J., 2003, ApJ, 589, 704

Thomas D., et al., 2013, MNRAS, 431, 1383

Tinker J., Kravtsov A. V., Klypin A., Abazajian K., Warren M., Yepes G., Gottlöber S., Holz D. E., 2008, ApJ, 688, 709

Tinker J. L., Robertson B. E., Kravtsov A. V., Klypin A., Warren M. S., Yepes G., Gottlöber S., 2010, ApJ, 724, 878

Tomczak A. R., et al., 2014, ApJ, 783, 85

Tomczak A. R., et al., 2016, ApJ, 817, 118

Topping M. W., Shapley A. E., Steidel C. C., 2016, ApJL, 824, L11

Tresse L., Maddox S. J., Le Fèvre O., Cuby J.-G., 2002, MNRAS, 337, 369

Vale A., Ostriker J. P., 2004, MNRAS, 353, 189

Vanzella E., et al., 2010, A&A, 513, A20

Villar V., Gallego J., Pérez-González P. G., Pascual S., Noeske K., Koo D. C., Barro G., Zamorano J., 2008, ApJ, 677, 169

Visbal E., Haiman Z., Bryan G. L., 2016, preprint, (`arXiv:1602.04843`)

Vulcani B., et al., 2015, preprint, (`arXiv:1509.00486`)

Wake D. A., et al., 2011, ApJ, 728, 46

Webb T. M. A., Yamada T., Huang J.-S., Ashby M. L. N., Matsuda Y., Egami E., Gonzalez M., Hayashimo T., 2009, ApJ, 692, 1561

Whitaker K. E., et al., 2014, ApJ, 795, 104

Wild V., Charlot S., Brinchmann J., Heckman T., Vince O., Pacifici C., Chevallard J., 2011, MNRAS, 417, 1760

Williams R. J., Quadri R. F., Franx M., van Dokkum P., Labbé I., 2009, ApJ, 691, 1879

Wold I. G. B., Barger A. J., Cowie L. L., 2014, ApJ, 783, 119

Wuyts S., et al., 2011, ApJ, 738, 106

Yabe K., Ohta K., Iwata I., Sawicki M., Tamura N., Akiyama M., Aoki K., 2009, ApJ, 693, 507

Yamada T., Nakamura Y., Matsuda Y., Hayashino T., Yamauchi R., Morimoto N., Kousai K., Umemura M., 2012, AJ, 143, 79

York D. G., et al., 2000, AJ, 120, 1579

Zehavi I., et al., 2005, ApJ, 630, 1

Zehavi I., et al., 2011, ApJ, 736, 59

Zehavi I., Patiri S., Zheng Z., 2012, ApJ, 746, 145

Zheng Z., et al., 2005, ApJ, 633, 791

Zheng Z.-Y., Malhotra S., Rhoads J. E., Finkelstein S. L., Wang J.-X., Jiang C.-Y., Cai Z., 2016, ApJS, 226, 23

Zhu G., Moustakas J., Blanton M. R., 2009, ApJ, 701, 86

da Cunha E., Charlot S., Elbaz D., 2008, MNRAS, 388, 1595

de Barros S., Schaerer D., Stark D. P., 2014, A&A, 563, A81

de Jong R. S., et al., 2016, in Ground-based and Airborne Instrumentation for Astronomy VI. p. 99081O, doi:10.1117/12.2232832

de los Reyes M. A., et al., 2015, AJ, 149, 79

van Dokkum P. G., et al., 2010, ApJ, 709, 1018

van der Wel A., et al., 2011, ApJ, 742, 111